FACULTY OF ENGINEERING
AND ARCHITECTURE

3D Printing Parameter Design for Styrene-Based Final Parts

Daniel Amaral Ceretti

Doctoral dissertation submitted to obtain the academic degree of
Doctor of Materials Engineering

Supervisors

Prof. Ludwig Cardon, PhD - Prof. Dagmar D'hooge, PhD

Department of Materials, Textiles and Chemical Engineering
Faculty of Engineering and Architecture, Ghent University

March 2023

GHENT
UNIVERSITY

FACULTY OF ENGINEERING
AND ARCHITECTURE

3D Printing Parameter Design for Styrene-Based Final Parts

Daniel Amaral Ceretti

Doctoral dissertation submitted to obtain the academic degree of
Doctor of Materials Engineering

Supervisors
Prof. Ludwig Cardon, PhD - Prof. Dagmar D'hooge, PhD
Department of Materials, Textiles and Chemical Engineering
Faculty of Engineering and Architecture, Ghent University

March 2023

GHENT
UNIVERSITY

ISBN 978-94-6355-697-2
NUR 971
Wettelijk depot: D/2023/10.500/29

Members of the Examination Board

Chair

Prof. Joris Degroote, PhD, Ghent University

Other members entitled to vote

Prof. Karen De Clerck, PhD, Ghent University
Prof. Mariya Edeleva, PhD, Ghent University
Prof. Mia Eeckhout, PhD, Ghent University
Prof. Jean-Marie Raquez, PhD, Université de Mons

Supervisors

Prof. Ludwig Cardon, PhD, Ghent University
Prof. Dagmar D'hooge, PhD, Ghent University

List of Publications

Full-length research articles

D. V. A. Ceretti, M. Edeleva, L. Cardon, and D. R. D'hooge, "Molecular pathways for polymer degradation during conventional processing, additive manufacturing, and mechanical recycling" *Molecules*, **2023**, 28, 5, p. 2344. (SCIE-IF 2021: 4.927)

D. V. A. Ceretti, Y. W. Marien, M. Edeleva, A. La Gala, L. Cardon, and D. R. D'hooge, "Thermal and Thermal-Oxidative Molecular Degradation of Polystyrene and Acrylonitrile Butadiene Styrene during 3D Printing Starting from Filaments and Pellets" *Sustainability*, **2022**, 14, 23, p. 15488. (SCIE-IF 2021: 3.889)

D. V. A. Ceretti, R. Fiorio, T. Van Waeleghem, A. Desmet, B. Florizoone, L. Cardon and D. R. D'hooge, "Exploiting mono- and hybrid nanocomposite materials for fused filament fabrication with acrylonitrile butadiene styrene as polymer matrix" *J. Appl. Polym. Sci.*, **2022**, 139, 41, p. 1–21. (SCIE-IF 2021: 3.057, cover article)

A. La Gala, D. V. A. Ceretti, R. Fiorio, L. Cardon, and D. R. D'hooge, "Comparing pellet- and filament-based additive manufacturing with conventional processing for ABS and PLA parts" *J. Appl. Polym. Sci.*, **2022**, 139, 44, p. 1–14. (SCIE-IF 2021: 3.057)

E. Fernandez, D. V. A. Ceretti, S. Wang, Y. Jiang, J. Zhang, D. R. D'hooge and L. Cardon, "Fused filament fabrication of copolyesters by understanding the balance of inter- and intra-layer welding," *Plast. Rubber Compos.*, **2022**, 51, 3, p. 126–132. (SCIE-IF: 1.843)

A. La Gala, R. Fiorio, D. V. A. Ceretti, M. Erkoç, L. Cardon, and D. R. D'hooge, "A Combined Experimental and Modeling Study for Pellet-Fed Extrusion-Based Additive Manufacturing to Evaluate the Impact of the Melting Efficiency" *Materials (Basel)*, **2021**, 14, 19, p. 5566. (SCIE-IF: 3.748)

Extended abstracts

D. V. A. Ceretti, R. Fiorio, A. Desmet, L. Couck, P. Cornillie, W. Van Den Broeck, L. Cardon and D. R. D'hooge, "The influence of the filament manufacturing technique on the degradation, mechanical properties, and dispersion state of ABS-graphene printed nanocomposites" on 2nd International Conference on Polymers Process Innovation. Athens, Greece, 15-16 September **2022**, poster presentation.

D. V. A. Ceretti, R. Fiorio, L. Couck, P. Cornillie, W. Van Den Broeck, L. Cardon and D. R. D'hooge, "Synergy between nanoparticles in ABS (nano)composites for 3D printing: microscopical features and rheological properties" on 2nd International Conference on Polymers Process Innovation. Athens, Greece, 15-16 September **2022**, poster presentation.

D. V. A. Ceretti, A. Verduyn, L. Cardon and D. R. D'hooge, "Morphological and mechanical characterization of 3D printed polyphenylsulfone" on 1st International Conference on Polymers Process Innovation. Virtual. 14-15 December **2021**, oral presentation.

Abstracts

D. V. A Ceretti, T. Van Waeleghem, R. Fiorio, L. Cardon, M. Edeleva and D. R. D'hooge, "The relevance of (hybrid) nanocomposites for polystyrene-based additive manufacturing" on 38th International Conference of the Polymer Processing Society. Sint-Gallen, Switzerland, 22-26 May **2023**, poster presentation. Submitted.

D. V. A. Ceretti, L. Cardon and D. R. D'hooge, "Designing ABS-based nanocomposites materials for fused filament fabrication" on Annual Meeting of the Belgian Polymer Group – 2022 (BPG 2022). Blankenberge, Belgium, 14-15 November **2022**, oral presentation.

A. La Gala, R. Fiorio, D. V. A. Ceretti, M. Erkoç, L. Cardon and D. R. D'hooge, "Extrusion-based additive manufacturing of ABS: from theory to experimental validation" on Milan Polymer Days 2021. Virtual, 6-8 July **2021**, poster presentation.

D. V. A. Ceretti, F. H. Marchesini, R. Fiorio, D. R. D'hooge and L. Cardon, "Predicting the rheological behavior of commercial polystyrene melts during isothermal degradation" on 18th International Congress on Rheology (ICR 2020). Virtual, 13-18 December **2020**, oral presentation.

Expression of gratitude

Completing a PhD thesis is a challenging task, which cannot be successfully accomplished without the support of several people. Herein I would like to express my deepest gratitude to everyone that supported me directly or indirectly during these years.

First, I would like to thank my promotors, Professor Dr. Dagmar D'hooge and Professor Dr. Ludwig Cardon, for giving me the opportunity to join CPMT as a doctoral researcher. Thank you for your open communication, patience, guidance, encouragement, and support.

Next, I would like to offer my special thanks to Professor Dr. Rudinei Fiorio. Rudi, your calmness, academic rigor, and good humor steered me through dark scientific pathways. Thanks for always proposing good ideas, innovative solutions and supporting the analysis of not always obvious data.

Also, I would like to express my deepest gratitude to Professor Dr. Mariya Edeleva. Thank you very much for the constructive feedbacks, for challenging my knowledge and helping me to enrich my academic background.

The daily working life becomes nicer when you share your office with great people, which has been my case. Therefore, I would like to thank Andrea La Gala, Dahang Tang, Sisi Wang, Zhenmin Jiao, Chiara Fiorillo, Lynn Trossart, Annabelle Verberkcmoes and Ruben Vande Ryse for sharing the office with me and for making it a fun and warm place to work. Special thanks to my office mate and friend Marah Baddour, for exchanging ideas, for the coffee breaks and the friendship.

Good research cannot be made without administrative and technical support. Thus, I would like to express my sincere gratitude to Veerle, Stefaan and Mustafa. Special thanks to Kurt for his guidance in the Additive Manufacturing lab.

I would also like to extended my gratitude to other colleagues from CPMT who were part of this journey: Sara Hubo, Willem Van De Steene, Lingyan Duan, Tom Wieme, Ellen Fernandez, Tom Van Waeleghem, Hannelore Ohnmacht, Jing Li, Khaled Sebakhy, Dixit Guleria, Maofan Zhou, Shakir Azim, Simon Debrie, Elise Caron, Laia Farràs Tasias, Laurens Delva, Nicolas Mys, Karen Van Kets, Ellen De Tandt, Ruben Demets, Gianni Vyncke, Astrid Van Belle, Amir Bashirgonbadi, Kerstin Kleinhans, Marie Grodent and Professor Dr. Kim Raegart.

I had the opportunity to join CPMT with a funding from the BOF-GOA project of Ghent University. I am thankful for the funding, which guaranteed my financial support during the PhD. In addition, I would like to express my gratitude to everyone involved in the project: Professor Dr. Geert De Schutter, Professor Dr. Pieter Cornillie, Professor Dr. Koen Dewettinck, Professor Dr. Flávio Henrique Marchesini, Dr. Davy Van de Walle, Dr. Karel Lesage, Luiza Miranda, Pablo Reyes Isaacura, and Nathaniel Hendrik.

When you move abroad to pursue a PhD, extra challenges come up, as you are new to a country in which you don't know anyone, nor speak the language. I was very fortunate to have met wonderful people in Belgium, people that became my friends and family here.

Many thanks to *le ragazze italiane*. Silvi, we met at the Dutch course and while our ability to speak the language is still debatable, our friendship grew easily during these years. Thanks for sharing the basics of Italian culture with me. I also appreciate every

occasional dinner, museum visits, spiralling moments, and the questionable series we watched together. Thanks for being an amazing company and friend. Giuli, you not only offered me amazing food (countless pizzas, lasagna and risotto) but you (and Naguino) also gave me a lot of support during this journey. Thanks a lot. I admire your strength and resilience. Cezia, your positive energy is contagious. It is extraordinary how you can combine funny and serious things in the right amount. Thank you very much for the shared moments and for the positive energy.

Also, many thanks to my Brazilian friends in the Benelux. Luiza, being part of the same project united us in the beginning of the PhD journey. I am very happy our connection grew out of the University boundaries. Thanks for being my twin in Ghent, for the uncountable brunches, for the mutual exchange and support throughout these years. Liginha, even though we randomly met, life proved us that our connection was beyond any dance floor. Thank you for your warmth, for all the *piras*, and for your sense of humor, which always makes me laugh. Julian, Rafa and Maitê, thank you for the great company, great conversations, for the briscola rounds and all the fun evenings.

I would also like to thank my friend Sara. Dear, you always made me feel comfortable around you, and we developed a very beautiful connection during these years. Thank you for exchanging ideas, insights, stories and experience. You are an incredible person.

I also offer my deepest gratitude to my friends from Brussels. Jana, thank you for your generosity and for sharing your world with me. Uhugur, thank you for being so welcoming and energetic, and for your unconditional support. Maya, thank you for teaching us how to respect the timing of others and for being such a cutie. Julia, mi

hada, you are a rock. I admire you so much for the way you choose to live your life. Thank you for letting me be part of your world.

I would also like to thank Katerina, Cris, Victor, Giulia, Carlos, Ana Paqui, Arancha, Nerea, Jaime, Gonzalo, Guena, Guille, Ginger, Mirza, Enrico, Ruth, Jolly for the lovely company, for the laughter and for the exchange of ideas.

I would also like to thank my boyfriend, Arthur. You gave me six letters and two vowels of support throughout the difficult moments, offering patience, kindness, and fun moments. I am very grateful for that. I also admire your sensibility, openness, and honesty.

Finally, I would like to thank all my family members that encouraged me to be here. Specially, my mother, Neide and my father Carlos (*in memorian*). In addition, many thanks to my siblings, Bruna and Guilherme, and to my beautiful niece, Julia.

Abstract

One of the biggest challenges of extrusion-based additive manufacturing (EAM) is to obtain 3D printed parts with final properties comparable to the ones obtained via conventional processing techniques such as injection molding. This is due to the nature of the EAM process, which relies on good interlayer and intralayer adhesion of deposited filaments and a tuned build strategy to create parts with good properties. However, anisotropic properties and the presence of voids in 3D printed parts are common. The influence of printing parameters and of material formulations on the final properties of 3D printed parts have been assessed by several researchers. Nevertheless, further research on the topic is needed to fully exploit the potential of EAM. In addition, very few research considers the influence printing technique and the printing parameters on the polymer degradation during EAM.

In the literature review of the PhD thesis, it is discussed how the combination of experimental techniques and modeling tools can be beneficial to further underpin specific degradation pathways of polymers. Furthermore, it is explained how the molecular level analysis can contribute to the comprehension of the behavior of materials undergoing structural breakdown. Nevertheless, the description of the rheological response to the irreversible time-dependent changes that the backbone of the polymer experiences during degradation has not yet been thoroughly carried out in the modeling field.

One way to describe the rheological behavior of polymers undergoing degradation is by employing rheokinetic analysis. In the first experimental part of this PhD thesis, a step towards the validation of a structural rheokinetic model is given by assessing the thermal degradation of polystyrene (PS) melts in a rheometer. To obtain the parameter

for the irreversible progress function (e.g. degradation), experimental analysis via size-exclusion chromatography (SEC) and time sweep rheological tests were carried out. The dimensionless values of the progress of the storage modulus (G'), loss modulus (G'') and the mass average molar mass M_m with ageing time were fitted to a first-order kinetic equation. A second set of parameters of the model was obtained by fitting the flow curves of virgin and aged PS to the Carreau-Yasuda equation. The nonlinear viscoelastic behavior of virgin and aged samples was assessed via constant shear rate tests. The overshoot and undershoot on the transient response of viscosity are discussed. While the overshoot is a common phenomenon observed for polymer melts, the undershoot indicates the "tumbling" effect, which is for the first time observed experimentally for aged polymer melts.

After evaluating the rheological behavior of PS undergoing thermal degradation, the degradation during EAM was assessed for polystyrene (PS) and acrylonitrile butadiene styrene (ABS). Fused filament fabrication (FFF) and pellet-based additive manufacturing (PBAM) were employed, and the degradation was assessed via a combined set of experimental techniques, including rheometry, size-exclusion chromatography (SEC), Fourier-transform infrared (FTIR), yellowness index (YI) and tensile properties. It is shown that PS produced via FFF presents a higher level of degradation resulting from the multi-process nature of this fabrication methodology (i.e., Filament fabrication and then FFF), in contrast with PBAM. In addition, the print temperature also plays a role on the degradation extent, and printing PS at a higher temperature induce a higher level of degradation. For ABS, materials produced via FFF and via PBAM show a different degradation mechanism, revealing that the choice of processing type and parameters may influence the irreversible structural changes that the material suffer. PS parts may be produced via PBAM with lower degradation levels and similar properties than their FFF counterparts, while for ABS, further

optimization of the PBAM processing parameters is required to improve the interlayer adhesion.

One possible way to improve the properties of 3D printed material is by the design of new formulations based on mono and hybrid (nano)composites. Here, a complete assessment of formulations based on ABS with graphene nanoplatelets (GNPs), carbon nanotubes (CNTs), and titanium dioxide (TiO_2) is carried out. In the screening phase, rheological analysis points out that formulations containing CNT promote a better dispersion of the other nanoparticles, due to synergistic effects. Printability tests indicated that all the materials were printable, and that GNP and TiO_2 seem to improve the coalescence between deposited filaments. This preliminary analysis helped to define potential compositions for FFF, which were then manufactured into filaments, and 3D printed. The mechanical properties indicate that under tensile loads, the hybrid material containing GNP, CNT and TiO_2 exhibit the best properties, due to the synergy between nanoparticles and confirms the results of the screening phase. In addition, reducing the layer thickness yields higher tensile and flexural properties, whereas the printing temperature has little influence on the mechanical properties. It is highlighted that the combination of the nanoparticles with optimal printing parameters yields better properties for 3D printed ABS, which might increase the range of application of this material. Furthermore, this study outlines a simple yet powerful strategy for the definition of potential compositions for FFF applications and may be employed to assess other formulations.

Finally, a further assessment of the dispersion of nanoparticles in mono- and hybrid ABS based (nano)composites is carried out via transmission electron microscopy (TEM). The results indicate that the composition containing GNP, CNT and TiO_2 present the best dispersion state. In addition, a different filament fabrication route

(twin-screw extrusion) is employed to disperse GNP into ABS. Even though the dispersion of GNP seems to be better (via TEM results), the degradation levels of the polymer due to the high shear yields lower properties of the 3D printed parts.

Overall, this PhD thesis showed how printing parameters, material design and material degradation during processing may affect the final properties of 3D printed styrene-based materials. By establishing relationships between structure, properties and processing, the degradation of polymers during 3D printing was assessed, giving a contribution on the effects of printing technique and parameters on material degradation. In addition, the rheological behavior of polymers undergoing degradation showed a new possible route for the characterization of degraded polymers. Furthermore, a methodology for assessing material formulations in view of extrusion-based additive manufacturing was proposed, giving a contribution to the scientific community in expanding the range of materials available for EAM.

Samenvatting

Een van de grootste uitdagingen van extrusie gebaseerde additive manufacturing (EAM) is het verkrijgen van 3D-geprinte onderdelen waarvan de finale eigenschappen vergelijkbaar zijn met deze van conventionele verwerkingstechnieken zoals spuitgieten. Het EAM-proces is namelijk afhankelijk van een goede inter- en intralaagadhesie van gedeponeerde filamenten en van een afgestemde/specifieke bouwstrategie om onderdelen met goede eigenschappen te maken. Anisotropie en de aanwezigheid van holten in 3D-geprinte onderdelen komen echter vaak voor. De invloed van printparameters en van materiaalformulaties op de uiteindelijke eigenschappen van 3D-geprinte onderdelen is door verschillende onderzoekers onderzocht. Toch is verder onderzoek over dit onderwerp nodig om het potentieel van EAM volledig te benutten. Bovendien is er maar weinig onderzoek uitgevoerd naar de invloed van de printtechniek en de printparameters op de polymeerdegradatie tijdens EAM.

In de literatuurstudie van de doctoraatsthesis wordt besproken hoe de combinatie van experimentele technieken en van modelleringsmethodes nuttig kan zijn om specifieke degradatie van polymeren tijdens het verwerkingsproces verder te onderzoeken. Verder wordt uitgelegd hoe een analyse op moleculair niveau kan bijdragen tot inzicht in het gedrag van materialen die structurele degradatie ondergaan. In het onderzoeksdomien van modellering is de beschrijving van de reologische respons op de onomkeerbare en tijdsafhankelijke veranderingen die de polymeerstructuur ondergaat tijdens de degradatie nog niet grondig uitgevoerd.

Reokinetische analyse is een tool om het reologische gedrag van polymeren onderhevig aan degradatie te beschrijven, voorspellen, analyseren en onderzoeken. In

het eerste experimentele deel van deze doctoraatsthesis wordt een stap gezet naar de validatie van een structureel reokinetisch model door de thermische degradatie van polystyreen (PS) in een reometer te beoordelen. Om de parameter voor de irreversibele progressiefunctie (bv. degradatie) te verkrijgen, werden experimentele analyses via grootte-exclusiechromatografie (SEC) en repeterende reologische testen uitgevoerd. De dimensieloze waarden van het verloop van de opslagmodulus (G'), verliesmodulus (G") en de gemiddelde molaire massa M_m met de verouderingstijd werden geïntegreerd in een eerste-orde kinetische vergelijking. Een tweede reeks parameters van het model werd verkregen door de vloeikrommen van virgin PS en van verouderd PS te integreren in de Carreau-Yasudavergelijking. Het niet-lineaire visco-elastische gedrag van virgin en van gedegradeerde monsters werd beoordeeld via testen uitgevoerd bij constante afschuifsnelheid. Het overshoot en undershoot op de transiënte respons van de viscositeit worden besproken. Terwijl de overschrijding een algemeen verschijnsel is dat wordt waargenomen bij polymeer in de smeltfase, wijst de onderschrijding op het "tuimeleffect", dat voor het eerst experimenteel is waargenomen bij een gedegradeerd polymeer in de smeltfase.

Na evaluatie van het reologische gedrag van PS dat thermische degradatie ondergaat, werd de degradatie tijdens EAM beoordeeld, voor polystyreen (PS) en acrylonitril-butadieen-styreen (ABS). Hiervoor maakte me gebruik van Fused filament fabrication (FFF) en pellet-gebaseerde additieve vervaardigingtechnieken (PBAM). De degradatie werd beoordeeld via een combinatie van experimentele technieken, waaronder reometrie, grootte-exclusiechromatografie (SEC), Fourier-transform infrarood spectrofotometrie (FTIR), geelheidsindex (YI) en trekeigenschappen. Er werd aangetoond dat PS geproduceerd via FFF een hogere degradatie vertoont als gevolg van de meervoudige processing in deze fabricagemethode (d.w.z. filamentvorming, gevolgd door FFF), in tegenstelling tot bij PBAM. Bovendien speelt

ook de printtemperatuur een rol bij de degradatie; het printen van PS bij een hogere temperatuur leidt tot meer degradatie. Voor ABS vertonen de via FFF en via PBAM geproduceerde materialen een verschillend afbraakmechanisme, waaruit blijkt dat de keuze van het verwerkingstype en de parameters van invloed kan zijn op de onomkeerbare structurele veranderingen die het materiaal ondergaat. PS-onderdelen kunnen via PBAM worden geproduceerd met lagere degradatieniveaus en vergelijkbare eigenschappen dan hun FFF-tegenhangers, terwijl voor ABS verdere optimalisatie van de PBAM-procesparameters nodig is om de hechting tussen de lagen te verbeteren.

Een mogelijke manier om de eigenschappen van 3D-geprint materiaal te verbeteren is het ontwerp van nieuwe formuleringen op basis van mono- en hybride (nano)composieten. Binnen het onderzoek wordt een volledige beoordeling uitgevoerd van formuleringen op basis van ABS met grafeennanoplaatjes (GNP's), koolstofnanobuizen (CNT's) en titaandioxide (TiO2). In de screeningfase wees reologische analyse uit dat formuleringen met CNT een betere dispersie van de andere nanodeeltjes bevorderen, als gevolg van synergetische effecten. 3D-printing testen wezen uit dat alle onderzochte materialen printbaar zijn, en dat GNP en TiO_2 de coalescentie tussen gedeponeerde filamenten lijken te verbeteren. Deze voorlopige analyse hielp om potentiële samenstellingen voor FFF te definiëren, die vervolgens werden vervaardigd tot filamenten waarmee er stukken 3D-geprint zijn. De mechanische eigenschappen hiervan gaven aan dat onder trekbelasting het hybride materiaal met GNP, CNT en TiO2 de beste eigenschappen vertoont, dit dankzij de synergie tussen de nanodeeltjes. Dit bevestigt de resultaten van de screeningfase. Bovendien levert het verminderen van de laagdikte hogere trek- en buigeigenschappen op, terwijl de druktemperatuur weinig invloed heeft op de mechanische eigenschappen. Er is ook gebleken dat een combinatie van het gebruik

van nanodeeltjes met een optimalisatie van printparameters betere eigenschappen oplevert voor 3D-geprint ABS, wat het toepassingsgebied van dit materiaal zou kunnen vergroten. Deze studie definieert een eenvoudige maar krachtige strategie voor het bepalen van potentiële samenstellingen voor FFF-toepassingen en kan worden gebruikt om andere formuleringen te beoordelen.

Ten slotte werd de dispersie van nanodeeltjes in mono- en hybride (nano)composieten op basis van ABS verder beoordeeld via transmissie-elektronenmicroscopie (TEM). De resultaten bevestigen dat de samenstelling met GNP, CNT en TiO2 de beste dispersietoestand vertoont. Bovendien wordt een andere wijze van filamentproductie (dubbelschroefextrusie) toegepast om GNP in ABS te dispergeren. Hoewel de dispersie van GNP beter lijkt te zijn (via TEM-resultaten), leidt de degradatie van het polymeer door de hoge afschuifkrachten tot lagere eigenschappen van de 3D-geprinte onderdelen.

In het algemeen toonde deze doctoraatsthesis aan hoe printparameters, materiaalontwerp en materiaaldegradatie tijdens de verwerking de uiteindelijke eigenschappen van 3D-geprinte styreengebaseerde materialen kunnen beïnvloeden. Door relaties te leggen tussen structuur, eigenschappen en verwerking, werd de degradatie van polymeren tijdens 3D printen beoordeeld, wat een inzicht verschaft in de effecten van printtechniek en van printparameters op materiaaldegradatie. Bovendien toont het reologische gedrag van polymeren die degradatie ondergaan een nieuwe mogelijke route voor de karakterisering van gedegradeerde polymeren. Verder werd een methode voorgesteld voor de beoordeling van materiaalformules met het oog op extrusiegebaseerde additieve productie, wat een bijdrage levert aan de wetenschappelijke gemeenschap door het uitbreiden van de reeks materialen die beschikbaar zijn voor EAM.

List of Symbols and Abbreviations

Roman symbols

a	Yasuda Parameter
a_0	Initial radius (μm)
c_p	Specific heat capacity (J kg^{-1} K^{-1})
$Đ$	Dispersity
D_a	Degree of anisotropy (%)
E_a	Apparent activation energy (kJ/mol)
$f(\alpha)$	Reaction model
G'	Storage modulus (Pa)
G''	Loss modulus (Pa)
G_s	Shear modulus, structural rheokinetic model (Pa)
K_{app}	Apparent rate constant (min^{-1})
L/D	Length over diameter ratio
M_m	Mass average molar mass (kg mol^{-1})
M_n	Number average molar mass (kg mol^{-1})
M_z	Z-average molar mass (kg mol^{-1})
n	Power law index
R	Universal gas constant (J K^{-1} mol^{-1})

R1	Absorption ratio (1,2-butadiene/nitrile)
R2	Absorption ratio (1,4-butadiene/nitrile)
T	Temperature (°C)
t	Time (s)
$T_{1\%}$	Temperature of 1% mass loss (°C)
$T_{3\%}$	Temperature of 3% mass loss (°C)
T_c	Crystallization temperature (°C)
T_g	Glass transition temperature (°C)
T_m	Melt temperature (°C)
T_{Nozzle}	Nozzle temperature (°C)
t_{eq}	Characteristic time for equilibrium, structural rheokinetic model (s)
UTS_{XYZ}	Ultimate tensile strength of XYZ printed parts (MPa)
UTS_{ZXY}	Ultimate tensile strength of ZXY printed parts (MPa)
x	Neck radius (μm)

Greek Symbols

α	Extent of conversion
β	Heat rate (°C min^{-1})
δ	Phase angle (°)
tan δ	Loss factor (Pa)

ΔH_m	Enthalpy of fusion (J g^{-1})
η^*	Complex viscosity (Pa.s)
η_0	Zero-shear viscosity (Pa.s)
η_∞	Infinite shear viscosity (Pa.s)
$[\eta]$	Intrinsic viscosity (dL/g)
η_υ	Purely viscous part of viscosity, structural rheokinetic model (Pa.s)
θ	Glancing angle (°)
θ_1	Relaxation time, structural rheokinetic model (s)
θ_2	Retardation time, structural rheokinetic model (s)
λ	Relaxation time (s)
λ_s	Structural parameter, structural rheokinetic model
σ_0	Melt yield stress (Pa)
σ	Stress (Pa)
τ	Shear stress (Pa)
χ_c	Degree of crystallinity (%)
ω	Angular frequency (rad/s)
$\dot{\gamma}$	Shear rate (s^{-1})
$\dot{\gamma}_0$	Characteristic shear rate (s^{-1})
ζ	Irreversible progress function, structural rheokinetic model

Abbreviations

ABS	Acrylonitrile butadiene styrene
AFM	Atomic force microscopy
AM	Additive manufacturing
ANOVA	Analysis of variance
ASTM	American Society for Testing and Materials
BDE	Bond dissociation energy
CEM	Circular economy model
CNT's	Carbon nanotubes
DOE	Design of experiment
DSC	Differential scanning calorimetry
EAM	Extrusion-based additive manufacturing
FEM	Finite element method
FFF	Fused filament fabrication
FLG	Few-layer graphene
FRP	Free radical polymerization
FTIR	Fourier-transform infrared
GNP's	Graphene nanoplatelets
HDPE	High density polyethylene
HIPS	High-impact polystyrene

HNC's	Hybrid nanocomposites
IR	Infrared
ISO	International Organization for Standardization
IV	Intrinsic viscosity
LDPE	Low density polyethylene
LT	Layer thickness
ME	Micro-extrusion
MFI	Melt flow index
MHS	Mark-Houwink-Sakurada equation
MMD	Molar mass distribution
MVR	Melt volumetric ratio
MWCNT	Multi-walled carbon nanotubes
NMR	Nuclear magnetic resonance
OM	Optical microscopy
PA	Polyamide
PB	Polybutadiene
PBAM	Pellet-based additive manufacturing
PB-g-SAN	SAN-grafted-polybutadiene
PCL	Poly(ε-caprolactone)
PCLA	Poly (ε-caprolactone-co-L-lactide)

PE	Polyethylene
PEEK	Polyether ether ketone
PET	Poly(ethylene terephthalate)
PETG	Polyethylene terephthalate glycol
PLA	Poly (lactic acid)
PLATMC	Poly(L-lactide-co-trimethylene carbonate)
PLGA	Poly(L-lactide-co-glycolide)
PLLA	Poly (L-lactic acid)
PMMA	Poly(methyl methacrylate)
PNC's	Polymer nanocomposites
PP	Polypropylene
PS	Polystyrene
SAN	Styrene-Acrylonitrile
SAOS	Small amplitude oscillatory shear tests
SBR	Styrene-butadiene rubber
SEBS	Styrene–ethylene–butylene–styrene
SEC	Size exclusion chromatography
SEM	Scanning electron microscopy
SSE	Single screw extrusion
TEM	Transmission electron microscopy

TGA	Thermogravimetry
THF	Tetrahydrofuran
TiO_2	Titanium dioxide
TPC	Thermoplastic copolyester elastomer
TPU	Thermoplastic polyurethane
TRMS	Time-resolved mechanical spectroscopy
TSE	Twin-screw extrusion
TTS	Time-temperature superposition
UV	Ultraviolet
UV-Vis	Ultraviolet-visible spectrophotometry
VOCs	Volatile organic compounds
WAXS	Wide angle X-ray scattering
XRD	X-ray diffraction
YI	Yellowness index

TABLE OF CONTENTS

List of publications i
Expression of gratitude iv
English abstract viii
Dutch abstract xii
List of symbols and abbreviations xvi

CHAPTER 1. SCOPE AND AIMS 1

CHAPTER 2. MOLECULAR PATHWAYS FOR POLYMER DEGRADATION DURING CONVENTIONAL PROCESSING, ADDITIVE MANUFACTURING, AND MECHANICAL RECYCLING 4

2. 1. ABSTRACT 4
2. 2. INTRODUCTION 5
2. 3. OVERVIEW OF COMMON DEGRADATION REACTIONS 10
2. 4. DOMINANT DEGRADATION REACTIONS ILLUSTRATED FOR EXTRUSION-BASED ADDITIVE MANUFACTURING 16
2. 5. EXPERIMENTAL AND MODELING TECHNIQUES TO ASSESS AND QUANTIFY POLYMER DEGRADATION 26
2. 6. MANUFACTURING CASE STUDIES TO ASSESS DEGRADABILITY 33
2. 7. CONCLUSIONS 44
REFERENCES 46

CHAPTER 3. RHEOLOGY OF POLYSTYRENE MELTS UNDERGOING THERMAL DEGRADATION: A STEP TOWARDS STRUCTURAL KINETIC MODELING 60

3. 1. ABSTRACT 60
3. 2. INTRODUCTION 61
3. 3. MATERIALS AND METHODS 68
3. 3. 1. Materials 68
3. 3. 2. Characterization 68
3. 4 RESULTS AND DISCUSSION 70
3. 4. 1. Identification of optimal temperature for rheological analysis via TGA 70
3. 4. 2. Linking size exclusion chromatography with rheological behavior at 250 °C 74
3. 4. 3. Linear viscoelastic characterization and flow curves at 0 and 240 min of degradation 77

3. 4. 4. Nonlinear viscoelastic behavior of polystyrene melts after 0 and 240 min of degradation 80
3. 5. CONCLUSIONS 84
REFERENCES 86

CHAPTER 4. THERMAL AND THERMAL-OXIDATIVE MOLECULAR DEGRADATION OF POLYSTYRENE AND ACRYLONITRILE BUTADIENE STYRENE DURING 3D PRINTING STARTING FROM FILAMENTS AND PELLETS 90
4. 1. ABSTRACT 90
4. 2. INTRODUCTION 91
4. 3. MATERIALS AND METHODS 95
4. 3. 1. Materials 95
4. 3. 2. Sample preparation 95
4. 3. 3. Characterization 98
4. 4. RESULTS AND DISCUSSION 102
4. 4. 1. Conventional thermal stability of feedstock materials 102
4. 4. 2. Detailed rheological, size-exclusion chromatography and Fourier-Transform infrared spectroscopy analysis for stability under processing conditions 106
4. 4. 3. Analysis of variation in color, mechanical properties and morphology 122
4. 5. CONCLUSIONS 129
REFERENCES 130

CHAPTER 5. EXPLOITING MONO- AND HYBRID NANOCOMPOSITE MATERIALS FOR FUSED FILAMENT FABRICATION WITH ABS AS POLYMER MATRIX 136
5. 1. ABSTRACT 136
5. 2. INTRODUCTION 137
5. 3. MATERIALS AND METHODS 141
5. 3. 1. Materials 141
5. 3. 2. Characterization 141
5. 4. RESULTS AND DISCUSSION 148
5. 4. 1. Testing compositions in view of FFF 148
5. 4. 2. Analysis of selected filaments 165
5. 4. 3. Analysis of FFF printed parts considering the selected filament compositions 174
5. 5. CONCLUSIONS 188
REFERENCES 190

CHAPTER 6. INSIGHTS ON THE DISPERSION OF NANOFILLERS IN ABS AND THE INFLUENCE OF FILAMENT PRODUCTION TECHNIQUE ON THE PROPERTIES OF FILAMENTS AND 3D PRINTED PARTS 196
6. 1. ABSTRACT 196
6. 2. INTRODUCTION 197
6. 3. MATERIALS AND METHODS 200
6. 3. 1. Materials 200
6. 3. 2. Characterization 201
6. 4. RESULTS AND DISCUSSION 202
6. 4. 1. Dispersion of nanofillers 202
6. 4. 2. Influence of filament processing technique on the rheological behavior of filaments and on the properties of 3D printed parts 206
6. 5. CONCLUSIONS 211
REFERENCES 213

CHAPTER 7. CONCLUSIONS AND OUTLOOK 216

APPENDIX A. SUPPORTING INFORMATION FOR CHAPTER 3 222

APPENDIX B. SUPPORTING INFORMATION FOR CHAPTER 4 226

APPENDIX C. SUPPORTING INFORMATION FOR CHAPTER 5 235

Chapter 1

Scope and aims

The subject of this doctoral research lays at the interface between polymer degradation during processing (e.g. conventional extrusion), the rheological behavior of polymers and 3D printing via small-scale extrusion-based additive manufacturing (EAM). This is done aiming at the understanding on how process parameters, processing techniques and material formulations can be chosen and tuned for improved final properties for styrene-based 3D printed parts.

The main goals of this research are: i.) to estimate a group of parameters for further structural rheokinetic model validation considering the rheological behavior of polystyrene (PS) melts undergoing thermal degradation; ii.) to examine the influence of printing parameters and printing technique on the degradation of styrene-based polymers during EAM; iii.) to propose a methodology to assess possible compositions for 3D printing applications based on acrylonitrile butadiene styrene (ABS) and several nanoparticles and iv.) to assess the effect of nanoparticles and printing parameters on the final properties of the 3D printed materials.

This thesis is divided into 7 Chapters, which are briefly described here, in Chapter 1.

The molecular pathways for polymer degradation during conventional processing, mechanical recycling and extrusion-based additive manufacturing are discussed in Chapter 2. This chapter comprises a literature review on the topic and gives an overview of common degradation reactions, followed by the degradation pathways of materials commonly used for EAM applications. The most important experimental

techniques to study polymer degradation during processing are summarized and it is discussed how they can be connected with modeling tools. In addition, case studies of degradation during processing are discussed. This review was published in the journal "*Molecules*".

Following the review, Chapter 3 explores the estimation of parameters for a structural rheokinetic model validation to describe the rheological behavior of polystyrene (PS) melts undergoing thermal degradation. It is discussed how the experimental protocol is defined to track rheological changes without affecting the measurements. Details on the parameter's estimation are given and a discussion on the nonlinear viscoelastic behavior of virgin and aged samples are provided. A publication is in preparation.

The rationalization and assessment of the influence of EAM printing technique and printing parameters on the degradation during processing is discussed in Chapter 4. Fused filament fabrication (FFF) and pellet-based additive manufacturing (PBAM) are used to produce PS and ABS parts. The microscopic and macroscopic properties changes of the virgin materials (pellets) due to processing are assessed for both filaments used in FFF (after single screw extrusion) and for the final 3D printed parts. This chapter was published in the journal "Sustainability".

In Chapter 5, the focus is shifted towards new formulations for improved 3D parts' properties. In this chapter ABS is blended with several nanoparticles, namely graphene nanoplatelets (GNPs), multi-walled carbon nanotubes (CNTs) and titanium dioxide (TiO_2) to generate several possible compositions for EAM applications. A systematic methodology based on rheological measurements and printability tests is proposed to assess the most promising compositions, which are then manufactured into filaments for FFF. Sintering analysis of the filaments is carried out to simulate the adhesion between deposited filaments. This step is followed by the actual printing

of the compositions and the assessment of tensile, flexural and impact properties. This chapter was published in the "*Journal of Applied Polymer Science*".

Chapter 6 encompasses further dispersion analysis of the (nano)composites produced in Chapter 5. In addition, this chapter give extra insights on the influence of filament fabrication technique on the properties of 3D printed parts. The results of this Chapter were published as extended abstracts on the 2nd International Conference on Polymer Process Innovation.

Finally, Chapter 7 summarizes the main findings of this doctoral research and gives an outlook on future research.

Chapter 2

Molecular pathways for polymer degradation during conventional processing, additive manufacturing, and mechanical recycling: state-of-the-art

2. 1. Abstract

The assessment of the extent of degradation of polymer molecules during processing via conventional (e.g. extrusion and injection molding) and emerging (e.g. additive manufacturing; AM) techniques is important for both the final polymer material performance with respect to technical specifications and the material circularity. In this contribution, the most relevant (thermal, thermo-mechanical, thermal-oxidative, hydrolysis) degradation mechanisms of polymer materials during processing are discussed, addressing conventional extrusion-based manufacturing, including mechanical recycling, and AM. An overview is given of the most important experimental characterization techniques, and it is explained how these can be connected with modeling tools. Case studies are incorporated, dealing with polyesters, styrene-based materials, and polyolefins as well as the typical AM polymers. Guidelines are formulated in view of a better molecular scale driven degradation control.

2. 2. Introduction

During their first life cycle polymer goods are exposed to several physical, chemical and/or biological factors that may cause their degradation, as shown in the top right part of Figure 1. These factors for instance include heat, moisture, UV-radiation, mechanical stress, chemicals, oxygen (O_2), and micro-organisms [1–5]. In case the materials are reprocessed in the context of a mechanical recycling process, e.g. reshaping via conversional extrusion, they are again exposed to some of these factors (smallest green arrow in Figure 1), which may induce a more severe degradation [6]. In the limit, one can apply chemical recycling in which the degradation is desired, and one aims at monomer (or oligomer) recovery (largest green arrow in Figure 1).

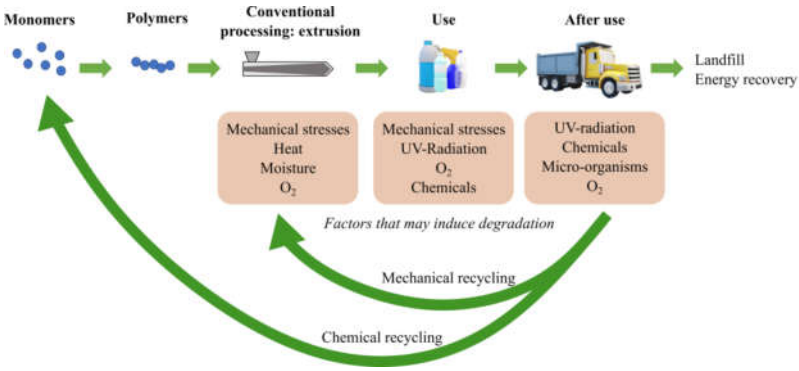

Figure 1: Summary of the most common factors which cause degradation of polymers during the life cycle of polymer goods, also including mechanical recycling in view of circularity. Chemical recycling is added for completeness and in that case, it is a desired degradation.

In general multiple-step processing techniques are more prone to induce polymer degradation, a more recent example being additive manufacturing (AM) or 3D printing via fused filament fabrication (FFF). This AM technique first requires the

filament fabrication via conventional extrusion and then the actual 3D printing, leading to a higher level of polymer degradation than single-step 3D printing [7–9]. AM is defined by ISO/ASTM as a process of joining materials to make parts from 3D model data, usually layer by layer [10]. The main advantages of AM include the near-zero waste for processing, the access to produce very complex tailored parts for specific applications, the minimum need for post-processing, and the possibility of creating products in low amounts in an economically viable way [11]. Note that not only polymers but also ceramics, metals, and composites are suited for AM.

Polymer degradation mechanisms are ideally classified according to the factor or combination of factors that induce it, as summarized in Table 1. Certain factors are common to processing, such as heat, mechanical stresses, oxygen, and moisture, leading to specific types of degradation mechanisms, which are part of the scope of this review. In the present work, emphasis is on thermal, thermo-mechanical and thermal-oxidative degradation, and hydrolysis. Other mechanisms commonly related to the use and disposal of polymer goods (e.g. biodegradation) are also listed in Table 1 for completeness.

Table 1: Most important degradation mechanisms during the life cycle of polymer goods.

Main factor(s)	**Degradation mechanism**
Temperature	Thermal degradation
Temperature and mechanical stresses	Thermo-mechanical degradation
Temperature and oxygen	Thermal-oxidative degradation
Water and temperature	Hydrolysis
UV radiation and oxygen	Photo-oxidative degradation
Chemicals	Chemical degradation
Micro-organisms	Biodegradation

If a polymer undergoes degradation, usually irreversible structural changes take place at the molecular scale so that a good knowledge on polymer chemistry is of added

value to define degradation mechanisms. As exemplified in Figure 2, the degradation changes are related to molecular variations in e.g. chain length, dispersity, presence of certain functional groups, degree of branching, and crosslinking. These changes happening on a microscopic level are responsible for variations of the polymeric material properties such as mechanical [12,13], thermal [13], and optical properties [13,14]. One can also aim at molecular improvement or chain repair by tailoring compounds which protect polymer chains against degradation [15]. These compounds, which are known as stabilizers, are usually incorporated into the material during processing as additives to reduce the degradation rate [16]. A broad range of stabilizers are available on the market and the needed stabilizer type depends on the type of environment against which the polymer must be protected as well as the function of the final polymeric material [17]. Hence, the properties of polymer goods have been improving constantly, through the design of new additives and formulations [18–21].

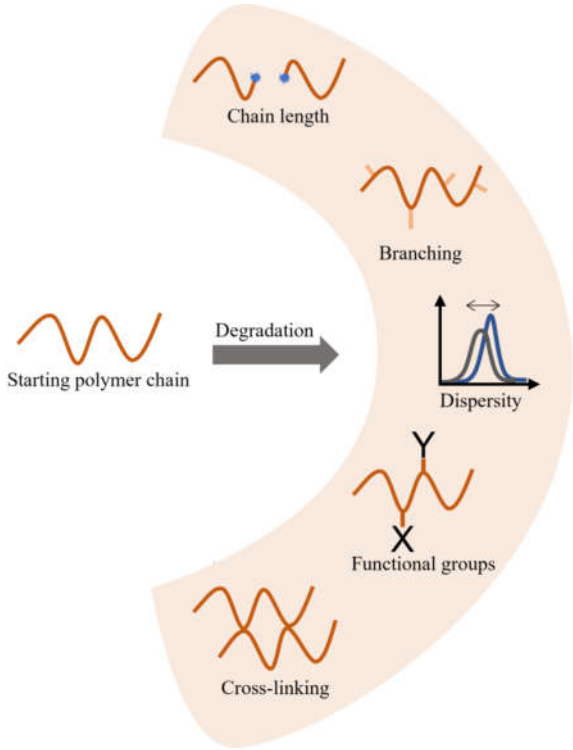

Figure 2: Typical molecular changes due to polymer degradation. Stabilizers can be added to avoid or minimize certain reactions.

Extra research efforts are although still needed, as the current challenges of our society move us towards a circular economy model (CEM). According to CEM, solid wastes should not only be minimized but also efficiently and effectively recycled to keep their value in the economy as long as possible [22,23]. In order to do so, a deeper understanding of polymer degradation mechanisms is needed to produce polymer goods with higher levels of stability. These materials will present longer life-cycles, reducing the amount of waste generated. After use, lower levels of degradation, and lower amounts of active radicals in materials undergoing recycling process may be beneficial in obtaining second generation products with improved properties. In

addition, the knowledge obtained in the first processing cycle may also be transferred to the recycling process, to minimize polymer degradation. For the case of mechanical recycling understanding the degradation during processing is crucial, including both conventional processing and the newer AM techniques. Most interesting is extrusion-based AM (EAM) in which the material is selectively dispensed through a nozzle or orifice [10]. In EAM, the material is heated up above its melt temperature (T_m) for semi-crystalline polymers or above its glass transition temperature (T_g) for amorphous polymers. The material melts or softens, and it is pushed through the nozzle onto a build platform. A sliced 3D model is used to give the commands to the printer, which will create the part in a layer-by-layer fashion [24–27]. The feedstock or bulk raw material for EAM may be filaments, pellets or solutions depending on the nature of the AM. FFF is the most common EAM technique, followed by pellet-based additive manufacturing (PBAM) and syringe based additive manufacturing of which the main principles are highlighted in Figure 3.

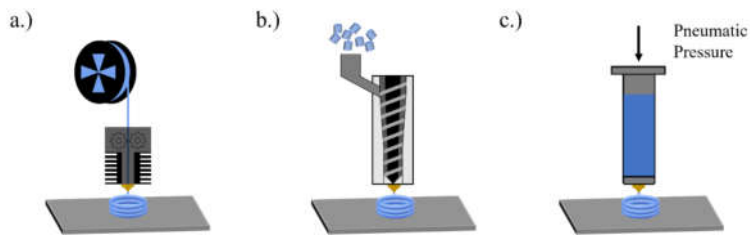

Figure 3: Methods for extrusion-based additive manufacturing (EAM) with in a.) fused filament fabrication, b.) pellet-based additive manufacturing and c.) syringe-based additive manufacturing.

As EAM resembles conventional processing via melt extrusion, it is mostly used to process thermoplastics and composites to, for instance, produce prototypes and

functional components for medical applications, or components for construction, aerospace, architecture and automotive industries [28–32]. Complementary, formulations of highly-filled polymers with metals or ceramics have been printed [33], and polymer solutions and hydrogels using a syringe-based 3D printer [34,35].

The aim of the current review is to summarize the advances in the study of polymer degradation during conventional processing, including mechanical recycling, and EAM. We initially focus on the common degradation pathways involved in polymer processing and zoom in on the degradation shared mechanisms of selected polymers as widely used under EAM conditions. This first part is followed by a second part, summarizing the most employed experimental and modeling techniques to characterize polymer degradation. In a third part, case studies of degradation during processing are dealt for polyester, styrene-based, and polyolefin materials, both under conventional and AM processing conditions.

2. 3. Overview of common degradation reactions

Processing techniques, such as extrusion, injection molding and EAM, usually deal with relatively high temperatures and shear rates, with a certain (limited) amount of oxygen solubilized in the polymer [36]. Temperature, mechanical stress, and oxygen are therefore the most important factors inducing polymer degradation during polymer processing and mechanical recycling promoting thermal, thermo-mechanical and thermal-oxidative degradation, as described in Table 1. Furthermore, hydrolysis may take place, due to the combination of moisture and temperature, especially for polymers prepared via step-growth polymerization or polycondensation [37].

Thermal (radically induced) degradation occurs if the polymer bonds break due to heat, either supplied externally or generated by shearing via heat dissipation [38–42].

Table 2 lists representative bond dissociation energies (BDEs) between common atomic constituents of a polymer. The polymer thermal stability increases if the BDEs are higher. The BDE is although not an exclusive discriminator as also the reactivity of the depropagating radical and the availability of hydrogen atoms for chain transfer matter [43–46].

Table 2: Bond dissociation energy values in kJ mol^{-1} relevant for many polymers [43].

Bond	Aromatic or heterocyclic	Aliphatic
C-C	410	284-368
C=C	-	615
C-H	427-435	381-410
C-Cl	-	326
C-F	-	452
C-O	448	350-389
C-N	460	293-343
C=N	-	615

The major pathways for thermal degradation are chain fission (formally scission; no radicals at the reactant side, consistent with e.g. the work of the Broadbelt group [47]), end-chain β-scission (so-called depolymerization), side-group elimination, and hydrogen abstraction or chain transfer [15,38]. Thermal chain fission is an event in which the polymer chain is randomly broken into large macroradicals (Figure 4a), leading to a fast decrease in average molar mass, with almost no monomer formed in the early stages [15]. End-chain β-scission takes place at chain ends to split off monomer sequentially (Figure 4b), leading to a very small decrease in the average molar mass in the early degradation stages [15]. The contribution of chain fission versus end-chain β-scission depends on the polymer structure and is closely related to the amount of substituents on the alpha carbon, with a more stabilized case leading to more end-chain β-scission [15]. Side-group elimination refers to elimination of side groups attached to a backbone of the polymer. This likely results in an unstable

molecule that undergoes further reaction, leading to the formation of aromatic molecules, fission into smaller fragments, or the formation of char [38].

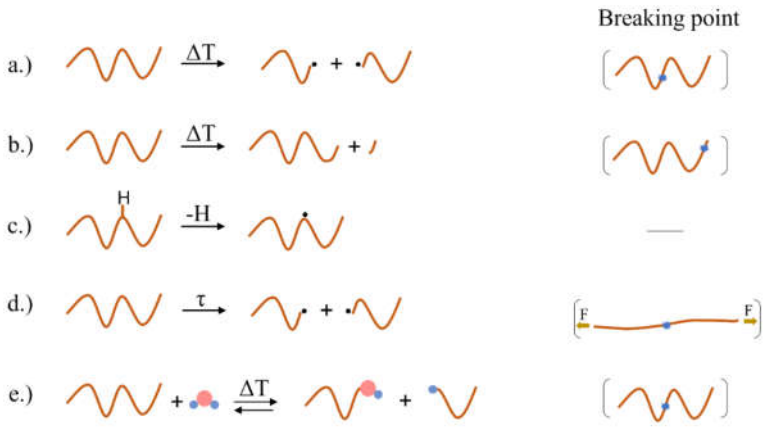

Figure 4: Examples of major pathways in polymer degradation, according to a variation in temperature T and mechanical stress τ or due the presence of water. a.) thermal chain fission, b.) end-chain β-scission, c.) hydrogen abstraction, d) mechanical-stress-induced chain fission and e) hydrolysis.

As shown in Figure 4c, hydrogen abstraction generates a mid-chain radical (MCR), which is prone to further degradation reactions. Mechanical stresses may additionally favor degradation by breaking the chains and generating radicals via a mechanochemical mechanism [47] (Figure 4d), lowering the average molar mass. The formed radical will be available for other reactions as illustrated in the left part of Figure 5, for illustration purposes starting from a MCR. The right part of this figure also puts forward the extra reactions in case oxygen is present for a high temperature modification, defining thermal-oxidative degradation, starting from the same MCR. In general, the radicals are formed due to heat, trace impurities, catalysts, inhibitors, solvents, and other agents used for the synthesis [48]. Notably during processing,

thermal-oxidative and thermo-mechanical degradation may be stimulated by one another. For instance, radicals produced via thermo-mechanical degradation may readily react with oxygen and increase the initiation rate of the thermal-oxidation pathway, as highlighted by the dashed arrows in Figure 5 [17,49].

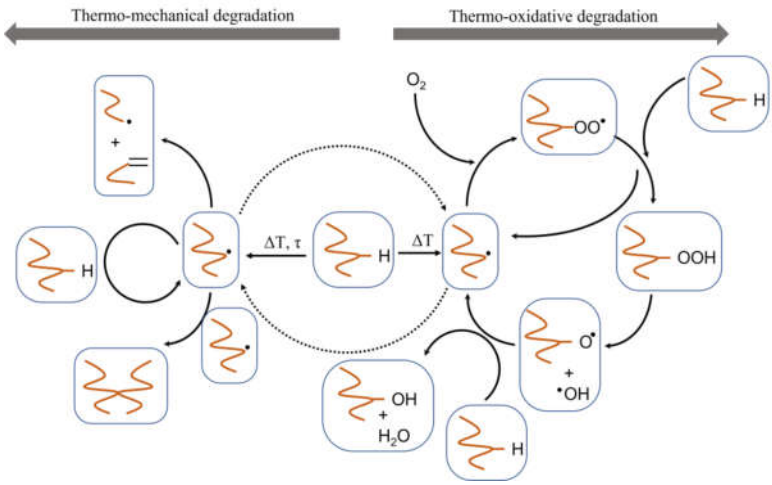

Figure 5: General scheme of thermo-mechanical and thermal-oxidative degradation of polymers, as based on Edeleva et al. [50] starting for illustration purposes from mid-chain radical formation.

As shown in the right part of Figure 5, polymer radicals formed due to thermal degradation react with molecular oxygen, delivering oxidation products based on a autoxidation cycle [51]. The thermal-oxidation mechanism proceeds autocatalytically, as shown by Bolland and Gee [52–54] upon studying the oxidation of rubber and lipids thus unsaturated chains. These authors indicated that the radicals propagate with oxygen to form a peroxyl radical (ROO•), which in turn abstracts a hydrogen from another macromolecule. This transfer leads to a new chain, in which

the newly formed radical center is stabilized by the conjugation with the adjacent double bonds, as shown in Figure 6 [55].

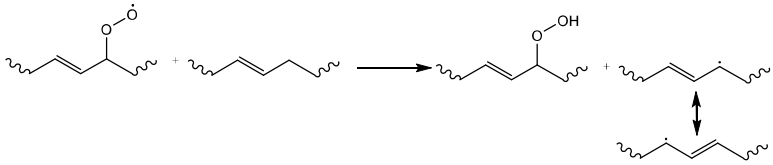

Figure 6: Hydrogen abstraction by a peroxyl radical from an unsaturated polymer chain, forming a hydroperoxide and a stable polymeric radical, as based on [55].

In many cases, the reactions in Figure 6 have also been seen as very likely for several polymers with a saturated carbon chain backbone. However, Gryn'ova et al. [55] put forward that the hydrogen abstraction by the peroxy radical should be (except for unsaturated hydrocarbons) thermodynamically disfavored, as the formed product is less stable than the peroxyl radical. They suggested that structural defects in polymers are responsible for the propagation in the autoxidative cycle, mostly starting from terminal and internal double bonds, which may be formed during the original polymerization procedure and/or the degradation process itself [55]. Hydroperoxide species are assumed as key intermediates in Figure 5 to further reactions, as they quickly decompose to form alkoxy (RO•) and hydroxy (•OH) radicals, leading to the backbone degradation followed by β-scission, as shown in Figure 7 [56].

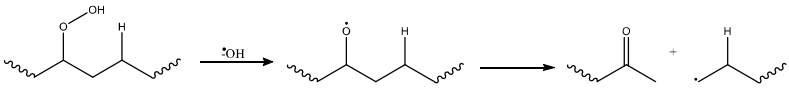

Figure 7: Example of β-scission reaction, starting by the presence of hydroperoxide molecules as formed in the presence of oxygen, as based on [56].

The termination step for Figure 5 depends on the type of atmosphere in which the degradation is occurring. If oxygen is sufficiently available, recombination of peroxy radicals has been put forward as the most probable termination mechanism [51]. During processing, due to the deficient oxygen atmosphere, the concentration of alkyl radicals is however higher than the peroxy radicals and the possibilities for termination are likely conventional termination by recombination and disproportionation of C-centered radicals, as shown in Figure 8.

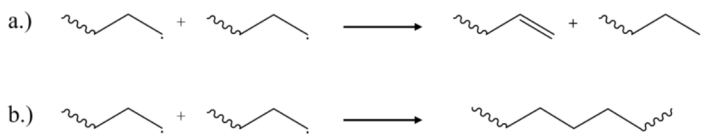

Figure 8: Example of most important termination pathways with less oxygen present: a.) disproportionation and b.) combination.

As a result of thermal-oxidative degradation during polymer processing, new oxygenated functional groups are formed, including peroxides, alcohols, ketones, aldehydes, acids, and esters [51]. Ketones and aldehydes formed by β-scission may react further with hydroperoxides to form other oxidation products. For instance, the formation of peracids proceeds via a multi-step oxidation of aldehydes [57]. Oxygenated functional groups can be formed even in carbon main chain polymers, such as polyolefins [58,59] or styrene-based materials [60].

Finally, Figure 4e highlights the mechanism of hydrolysis, which can occur if moisture is present in a high temperature environment. Certain polymers, especially those containing heteroatoms in the backbone are prone to this degradation mechanism and must be properly dried before processing [37]. Polyesters, polyamides and polycarbonates are among the important commercial polymers that could be

degraded by hydrolysis [15]. This degradation pathway leads to the cleavage of chemical bonds by reaction with water, reducing the average molar mass of the polymer [61].

2. 4. Dominant degradation reactions illustrated for extrusion-based additive manufacturing

The most used polymeric materials for EAM are acrylonitrile butadiene styrene polymer (ABS) [62,63] and poly(lactic acid) (PLA) [62,64,65]. Other polymeric materials which have been employed for EAM applications are polyethylene terephthalate glycol (PETG) [62,64,66,67], polyether ether ketone (PEEK) [62,68–73], high density polyethylene (HDPE) [74], polypropylene [75–77], polyamide (PA) [78,79], and high impact polystyrene (HIPS). The main chemical structure of these polymeric materials and their most relevant degradation routes during EAM, starting from the discussion in Section 2.3, are summarized in Table 3.

Table 3: Main degradation types of common polymers used for extrusion-based additive manufacturing (EAM); chain length must be read as average chain length.

Group	Name and main chemical structure	Degradation mechanism	Main outcome of degradation
Styrene-based materials (Rubber-modified)	Acrylonitrile butadiene styrene (ABS) 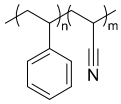 Styrene-Acrylonitrile (SAN) 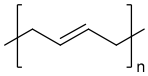 (*trans*-1,4) Polybutadiene (PB)	Thermal-oxidation of butadiene units and Thermo-mechanical	- Decrease of chain length due to chain fission [80] - Increase of chain length due to crosslinking [80,81]
	High-impact polystyrene (HIPS) 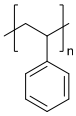 Polystyrene (PS) 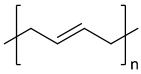 (*trans*-1,4) Polybutadiene (PB)		

Polyesters	Polylactic acid (PLA) 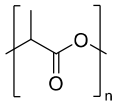 Polyethylene terephthalate glycol (PETG) 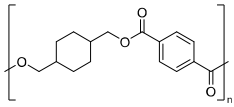	Hydrolysis of ester groups and Thermo-mechanical	- Decrease of chain length due to hydrolysis or due to chain fission [82,83]
Polyolefins	Polypropylene (PP) 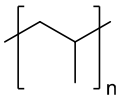 High-density polyethylene (linear) Low-density polyethylene (branched) 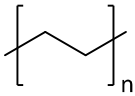	Thermal-oxidation and Thermo-mechanical	- Decrease of chain length due to chain fission [84,85]. - Decrease of chain length due to chain fission [86,87] - Increase of chain length due to branching and crosslinking [86,87]
Polyaryletherketones	Polyether ether ketone (PEEK) 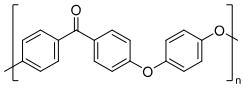	Thermal-oxidation and Thermo-mechanical	- Increase of chain length due to branching and crosslinking [88,89]

Polyamides	Polyamide 12 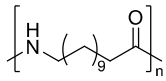	Thermal-oxidation of C-H bonds adjacent to N-H groups and Thermo-mechanical	- Decrease of chain length due to chain fission [90]
	Polyamide 6,6 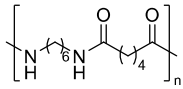		- Increase of chain length due to post-polycondenstion and crosslinking [91]

ABS (entry 1 in Table 3) polymer consists of a matrix based on styrene-acrylonitrile (SAN) copolymer with polybutadiene (PB) rubber dispersed in it, supported by SAN-grafted-polybutadiene (PB-g-SAN) connections. The ABS degradation mechanism is closely related to the degradation paths of its individual components [92]. However, the rubber phase is more susceptible to degradation because of its lower glass transition temperature T_g and higher oxygen permeability [93–95].

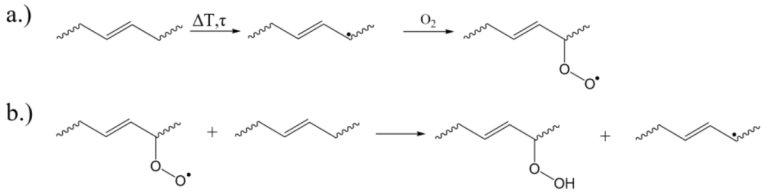

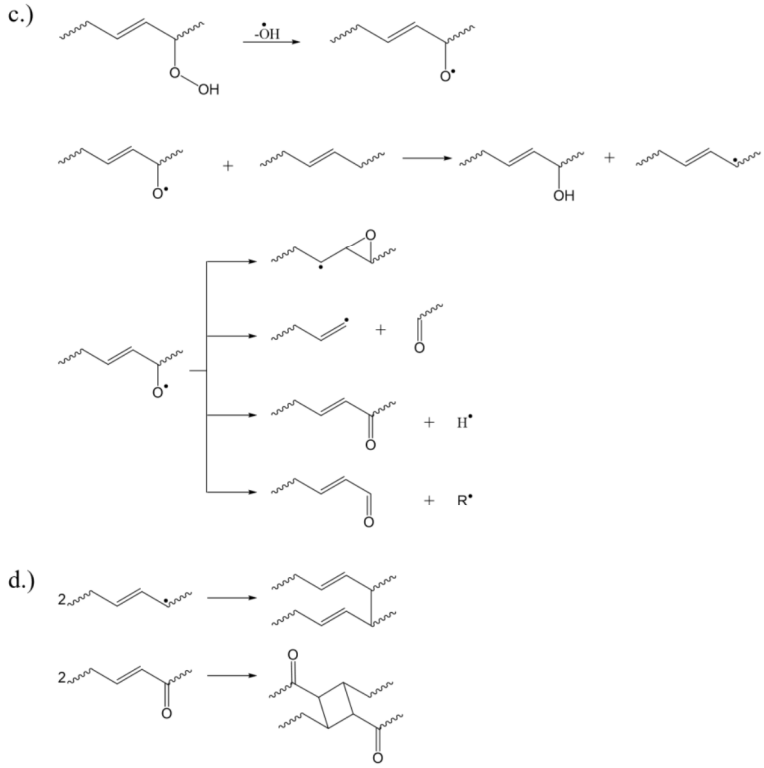

Figure 9: Key steps in thermal-oxidative degradation mechanism of ABS: a.) degradation initiation, b.) hydrogen abstraction leading to the formation of hydroperoxides, c.) possible products following the hydroperoxide decomposition, d.) termination considering the formation of crosslinked structures.

During (additive) manufacturing, the most common degradation route for ABS is proposed to be thermal-oxidation [96–98]. An interesting off-line study has been performed by Shimada and Kabuki [99], mentioning the three stages of initiation, propagation and termination, as included in the auto-oxidative cycle in Figure 5. The first stage involves the production of free radicals which react with oxygen (Figure 9a) and form hydroperoxides via hydrogen abstraction (Figure 9b). Because of the

presence of ethylene functionalities in the PB phase of ABS, the C-H bond in the α-carbon position can be easily oxidized [99]. The hydroperoxides decompose and in following reactions various oxygenated products and groups, particularly hydroxyl and carbonyl, are produced (Figure 9c). In the third stage, termination reactions occur, in which more stable crosslinked structures may be formed, with one example shown in (Figure 9d) [100]. The butadiene grafting sites containing tertiary carbons can be oxidized during a more severe degradation, leading to extensive damage in the polymeric chains by β-scission, as well as breaking of butadiene/SAN grafts [101,102].

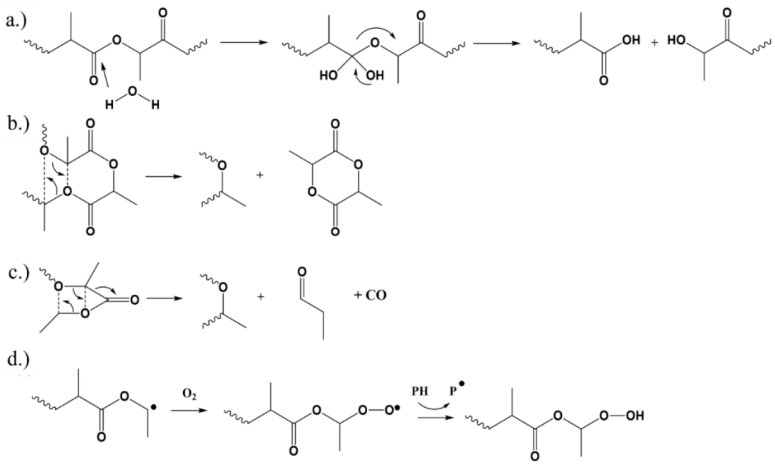

Figure 10: a.) Hydrolysis of PLA [103]. *b.), c.) Nonradical reactions of PLA degradation* [104], *(d.) Hydroperoxide formation and decomposition during the thermal-oxidation of PLA* [105].

PLA (entry 2 in Table 3) is a linear, aliphatic thermoplastic polyester with high rigidity and transparency. PLA is also a biodegradable polymer but with low thermal stability. Due to its hygroscopic nature, hydrolysis is one of the main degradation mechanisms for this polymer (see Figure 10a) [103]. Therefore, the material must be properly dried

prior to processing [106], a common procedure in many EAM studies [107–109]. In addition, McNeill and Leiper [104] discussed that radical reactions for PLA undergoing thermal degradation only occur above 270 °C. They proposed that non-radical degradation mechanisms occur up to 230 °C, as shown in Figure 10b and c. These reactions and hydrolysis end up reducing the average molar mass of the PLA material. Nevertheless, radical reactions could occur, even below this threshold temperature of 270 °C, due to the combination of shear and oxygen [105,110]. Figure 10d for instance shows the reaction mechanism for the development of hydroperoxides during the thermal-oxidative degradation of PLA.

Another interesting polymer material to discuss are polyolefins (entry 3 in Table 3), comprising of materials such as polypropylene (PP), high-density polyethylene (HDPE), and low-density polyethylene (LDPE). These materials are composed of carbon and hydrogen atoms and during degradation chain fission, chain branching (e.g. via macropropagation) and crosslinking are possible. It has been claimed that more branched structures such as LDPE are more susceptible to crosslinking or chain branching reactions during extrusion compared to more linear polymers [87,111].

The degradation mechanisms of PE, in the presence of a low amount of oxygen, has been for instance studied by Holmström and Sörvik [112–114] and typical reactions are summarized in Figure 11. Initiation degradation reactions are shown in Figure 11a. The quick formation of peroxide radicals is followed by hydrogen abstraction with hydroperoxide formation (Figure 11b). Subsequent reactions (Figure 11c) result in the formation of aldehydes, ketones, or hydroxyl compounds and other alkyl radicals. The reaction of a polymer chain with formed radicals leads to an auto-oxidation (Figure 11d), for which R• may be an alkyl radical, RO•, ROO• or HO•. Important termination reactions involving alkoxy radicals are shown in Figure 11e. Other termination

pathways leading to an increase of the average molar mass, including chain branching, are reported in Figure 11f.

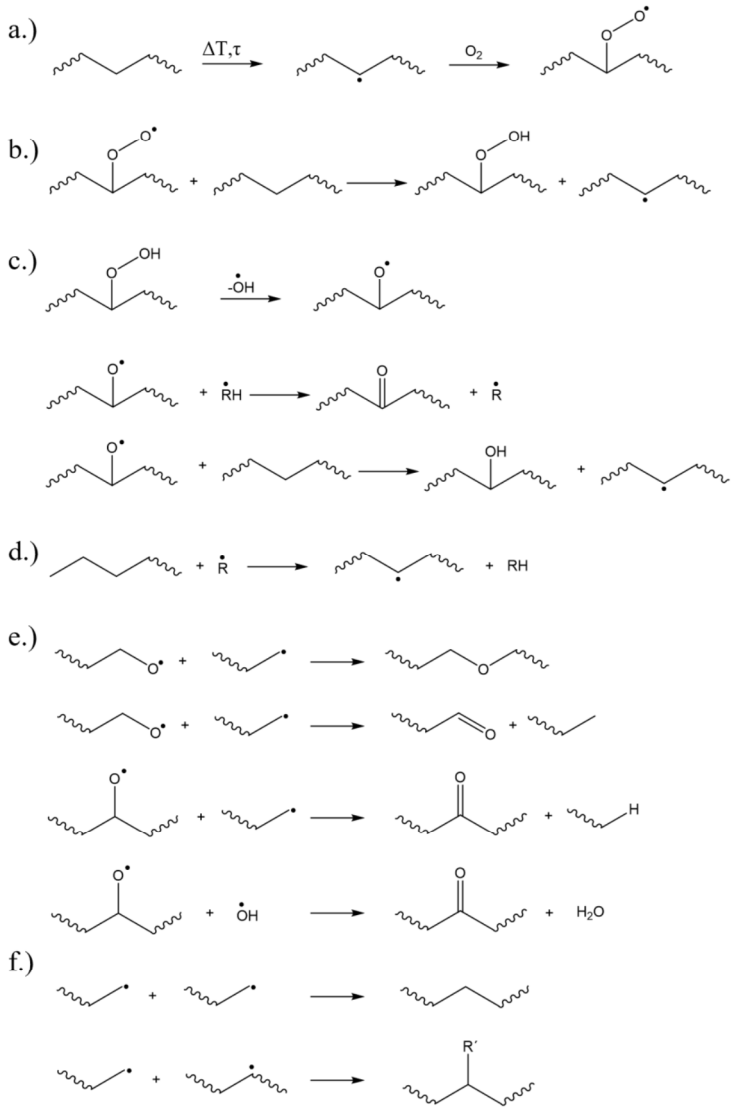

Figure 11: Examples of thermal-oxidative degradation reactions for polyethylene including a.) degradation initiation via a general chain transfer, b.) hydrogen abstraction leading to the

formation of hydroperoxides, c.) possible products following the hydroperoxide decomposition, d.) auto-oxidation of PE, e.) possible termination with alkoxy radicals and f.) termination of alkyl radicals [114]. *R• being an alkyl radical, RO•, ROO• or HO•.*

Due to the presence of tertiary carbons in the backbone of PP (see Table 3) in contrast with PE, its degradation mechanism is chain fission driven [115,116], decreasing the average molar mass. Figure 12 gives an overview of typical reactions for PP degradation, again in the presence of oxygen. Figure 12a displays a degradation initiation with the radical formed reacting with oxygen in Figure 12b. Hydroperoxide is formed by abstracting a hydrogen from a tertiary carbon, which has a lower activation energy than an abstraction reaction on a secondary carbon [57]. This preferred abstraction can be intermolecular (Figure 12c) or intramolecular (Figure 12d). Furthermore, the radicals may decompose via β-scission, yielding for instance ketones, aldehydes and other alkyl radicals (Figure 12e), with termination reactions for low-oxygen containing atmosphere shown in Figure 12f.

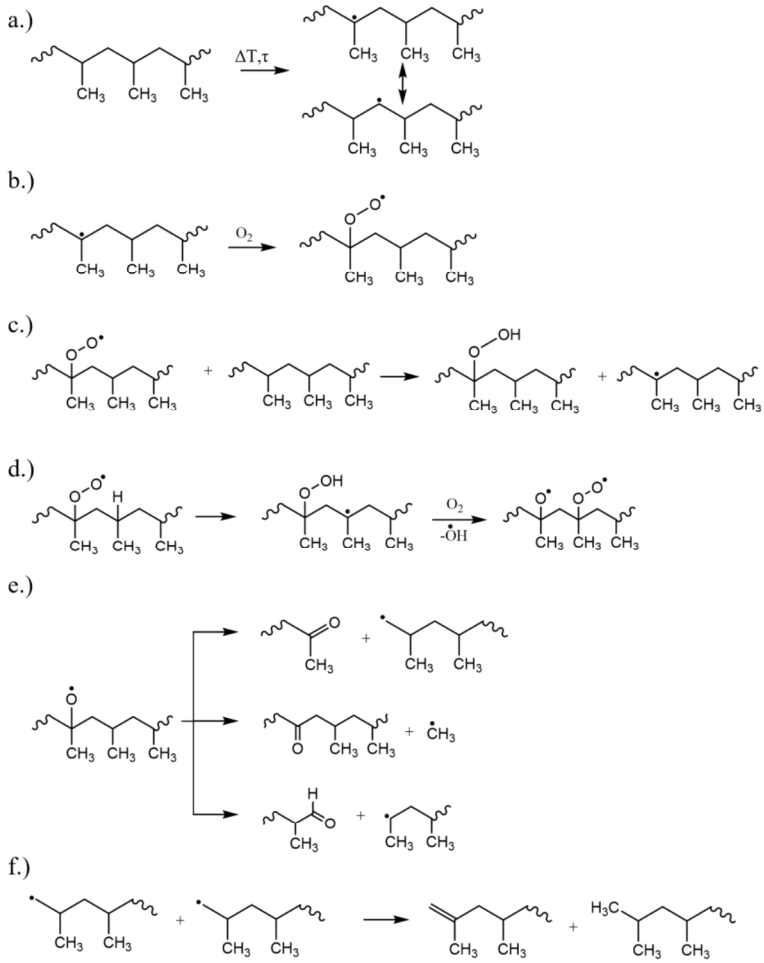

Figure 12: Examples of thermal-oxidative degradation reactions for polypropylene. a.) degradation initiation, b.) reaction of radical with oxygen, c.) intermolecular and d.) intramolecular hydroperoxide formation, e.) formation of oxygenated functional groups and f.) termination.

2. 5. Experimental and modeling techniques to assess and quantify polymer degradation

Irreversible structural changes of polymers are typically investigated by a set of experimental characterization techniques which provide information on the type of degradation mechanism by tracking the molecular properties (e.g. chemical composition, average chain length, chain length distribution, and branching and crosslinking level), the material properties (e.g. thermal, tensile and flexural) and the morphology variations (e.g. single vs. multiphase). These experimental characterization techniques include chromatography, rheometry, viscometry, spectroscopy, thermal analysis, microscopy, and mechanical testing, with a summary provided in Figure 13a.

Complementary (kinetic) modeling can be applied in which typically average properties are compared to experimental data [117,118,127–129,119–126] and subsequently the model is employed to provided additional information hard to access experimentally. A differentiation can be made between deterministic and stochastic modeling tools. With increasing computer capacity specifically in the recent decades Monte Carlo methods have become specifically very interesting. For example, as shown in Figure 13b, coupled matrix based Monte Carlo simulations [117,118] allow to track the functional groups, branches and monomer sequences of individual chains as they come out of a processing unit, allowing a more detailed understanding of the specific molecules that are being degraded, e.g. one can determine if the attack is happening in the lower or higher chain length region and if the mixing pattern in the processing equipment is altering this division. Moreover, a broad range of processing conditions can be scanned a priori to assess the degradation potential of a given

polymeric material either under conventional or AM processing conditions, including also conditions leaning toward full degradation thus chemical recycling.

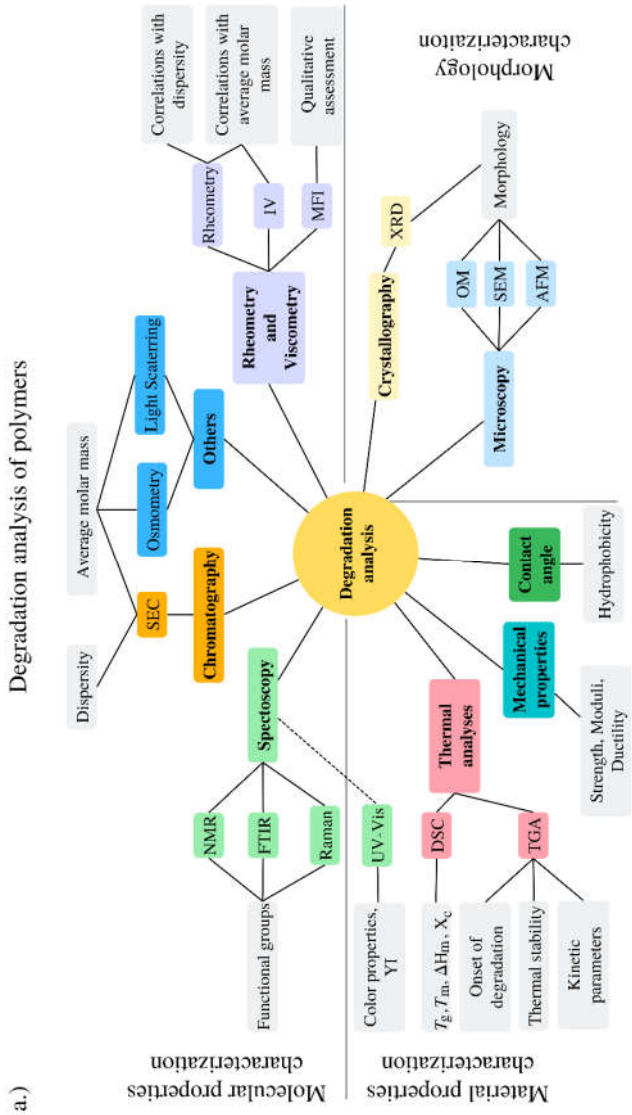

Figure 13: (a) Experimental characterization techniques to assess polymer degradation during processing, either on the molecular, morphological, or material level. Full caption in next page.

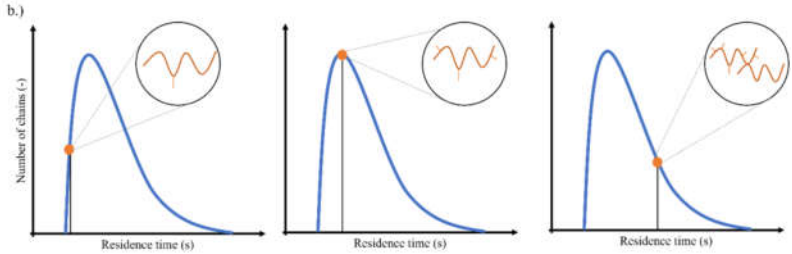

Figure 13: (a) Experimental characterization techniques to assess polymer degradation during processing, either on the molecular, morphological or material level; SEC: size exclusion chromatography; NMR: nuclear magnetic resonance; FTIR: Fourier-transform infrared; IV: intrinsic viscosity; MFI: melt flow index; UV-Vis: ultraviolet-visible spectrophotometry; DSC: differential scanning calorimetry; TGA: thermogravimetric analysis; YI: Yellowness index; T_g*: glass transition temperature;* T_m*: melt temperature;* T_c*: crystallization temperature;* ΔH_m*: enthalpy of fusion;* X_c*: degree of crystallinity; XRD: X-ray diffraction; OM: optical microscopy; SEM: scanning electron microscopy, and AFM: atomic force microscopy. (b) Complementary strength of modeling tools focusing on coupled matrix-based Monte Carlo simulations* [117,118,130]*, delivering the molecular structure of individual molecules (here only on shown) according to their residence time during extrusion-based mechanical recycling.*

In what follows, a concise description is given of the three experimental characterization groups in Figure 13a, making a link to available theoretical tools.

Molecular properties characterization

Chromatography, rheometry and viscometry are the most important characterization techniques employed in the assessment of degradation during processing, as they are very sensitive to (average) molar mass variations [131]. Size exclusion chromatography (SEC), which is a liquid chromatography technique, provides the dispersity ($Đ$), the average molar masses of the polymer such as the number average molar mass (M_n), the mass average molar mass (M_m) and the z-average molar mass

(M_z) as well as the molar mass distribution. Nevertheless, static light scattering and osmometry may also be used to determine M_m and M_n, respectively [132]. These techniques are especially useful in case the polymer has an insoluble fraction in its structure, caused by crosslinking or branching reactions during degradation, leading to the formation of a microgel.

Furthermore, linear viscoelastic measurements in a parallel plate rheometer or capillary rheometer allow to obtain flow curves, which via extrapolation allow the determination of the zero-shear melt viscosity (η_0). This viscosity parameter may be correlated with M_m, for linear polymers often expressed by an empirical power law ($\eta_0 = KM_m^{\alpha}$; K: proportionality factor; a = 3.5 ± 0.2) [133]. A similar expression named the Mark-Houwink(-Sakurada) (MH(S)) equation is used to estimate the average molar mass from intrinsic viscosity measurements in solution ($[\eta] = K_m M_m^{a}$) [133]. In general, more complex relations can be obtained via rheokinetic analysis, which associates the reaction kinetics (e.g. degradation) with rheological constitutive models [134–136].

Other parameter of importance for degradation analysis obtained via rheometry is the relaxation time (λ), which is related to the molecular structure of the material [137]. The dispersity of polymers may also be assessed via rheological analysis either via the storage modulus (G') or via correlations with viscosity [133]. This may be especially useful to estimate the dispersity of polymers which are difficult to analyze via SEC [138,139]. Another technique commonly applied to give a qualitative insight on the degradation of the materials is the melt flow index (MFI). The MFI value indicates the easiness that the material flows. If there is a decrease in the average molar mass of the material, the tendency is that it will flow easily, increasing the MFI.

Spectroscopic techniques measure the behavior of a material in response to electromagnetic irradiation. The most common tool is Fourier-transform infrared (FTIR) spectroscopy, which is a vibrational spectroscopic technique. The different types of interatomic bond vibrations existing in organic molecules, polymers, and composites have been investigated [140] so that it is possible to identify and track changes regarding functional groups present in the polymer e.g. because of degradation. Specifically, carbonyl (>C=O) and hydroxyl (-O-H) vibrational regions are of interest upon analyzing the FTIR spectra of polymers which underwent degradation, located around 1600-1800 cm^{-1} and 3200-3600 cm^{-1}, respectively [57]. For instance, the rate of carbonyl formation can be used to follow oxidative degradation in some polymers [15,141]. In any case, a dedicated computational analysis of spectra is needed [142].

As FTIR, Raman spectroscopy is classified as a vibrational spectroscopic technique, which may be used to monitor chemical species. In this case, the inelastic scattering of light is used to analyze vibrational and rotational modes of molecules [140]. Raman spectroscopy has also been employed to in-line monitor the degradation of PP during processing [143]. In-line characterization methods allow to determine degradation quickly without destroying the material. Another interesting spectroscopic technique is nuclear magnetic resonance (NMR), which is one of the most important tools for the analysis of substances, specifically in the polymer synthesis field. NMR may resolve the structure of the polymer and has therefore been used to probe the chemical variations during their degradation. For instance, the crosslinking degree in polymers undergoing degradation has been assessed [80,144,145]. Likewise, the detection of new functional groups formed due to degradation can be evaluated [146,147]. NMR can provide exact oxidation levels in a material but is more limited in case solid samples (or very high molar mass samples) need to be analyzed or the oxidation levels

are low [148]. In addition, dynamic NMR may be used to probe specimens which undergo physical or chemical changes with time [38]. More information on NMR techniques can be found elsewhere [149,150].

It is important to point out that some (spectroscopic) techniques do not necessarily identify changes in the molecular structure of degraded samples in the early stages of degradation. For instance, FTIR and NMR are popular methods for degradation characterization, however, they can be ineffective at defining small structural changes [131]. Furthermore, sometimes the oxygen content inside the extruder is low enough to avoid the formation of measurable carbonyl quantities by the FTIR technique [151]. Therefore, upon studying low extents of degradation as in the context of mechanical recycling, rheometry and chromatography may be the most sensitive tools in identifying the molecular changes. In any case, the complementary information obtained by modeling tools is highly relevant.

Morphology Characterization

Variations on the morphology of polymers because of degradation can be detected with microscopic techniques such as optical microscopy (OM), scanning electron microscopy (SEM) and atomic force microscopy (AFM) [13,152]. Furthermore, X-ray diffraction techniques may be used to resolve morphological features such as size, distribution and orientation of crystallites and lamellae of polymers, contributing to the study of their degradation [153]. The modeling field is less developed here compared to the molecular/micro-scale, which is understandable as in general regarding chemical/material processes, our knowledge is still more basic on the so-called meso-scale. Interesting modeling approaches have although been developed, for instance the work of Vonka and Kosek [154] puts forward that the morphology evolution of hetero-phase polymers that undergo phase separation and inversion

during their formation can be captured. These authors studied the phase separation occurring in high impact polystyrene (HIPS) during mixing, indicating the phase inversion settling as a function of the frequency of mixing.

Material properties characterization

Thermal analyses are broadly applied for the study of polymer degradation. For instance, thermogravimetric analysis (TGA) allows to track variations on the thermal stability of polymers and the onset of degradation either in the absence or in the presence of oxygen [15,155,156]. It is also possible to study the degradation kinetics of polymers subjected to different heating programs with this technique [157].

Furthermore, differential scanning calorimetry (DSC) is commonly used to monitor variations of T_g, T_m and crystallization temperature (T_c). In addition, for semi-crystalline polymers, the enthalpy of fusion (ΔH_m) is used to calculate their degree of crystallinity (X_c). However, the same lack of sensitivity reported for NMR and FTIR to track early stages of degradation, may be evident for thermal analysis techniques, such as DSC and TGA [131].

Ultraviolet-visible (UV-Vis) spectrophotometry is additionally a technique commonly employed to measure color variations of polymers which underwent degradation. For instance, so-called yellowing is an usual degradation outcome for manufactured polymer parts [158] and the color properties obtained via UV-Vis may be translated into a Yellowness Index (YI), which supports the assessment of degradation of the material. These techniques have also been used in-line to track color changes of for instance poly(L-lactic acid) (PLLA) undergoing extrusion [159].

Degradation has a strong influence on the mechanical properties of polymers as well. For example, predominance of crosslinking over chain fission increases the tensile

strength while decreasing the elongation at break [57]. The reverse effects are observed for dominant chain fission. The influence of degradation on the mechanical properties is usually assessed via impact and tensile tests, tracking the impact resistance, tensile strength, tensile modulus, and elongation at break of the polymer [160–162].

In addition, a water contact angle measurement is a valuable tool to assess polymer degradation, by providing an indication on the hydrophobicity/hydrophilicity of the polymer (surface). Higher contact angles indicate that the material has a higher hydrophobic character. Oxygenated functional groups formed due to degradation may alter this character and the material becomes more hydrophilic, exhibiting smaller contact angles [163]. Furthermore, changes of the surface morphology of the material due to degradation may also change its hydrophobic character [164].

2. 6. Manufacturing case studies to assess degradability

The influence of single extrusion, multiple extrusion, AM, and injection molding on polymeric degradation has been broadly studied in the past decades. For instance, degradation has been assessed for PLA and PLLA [159,165–168], poly(ethylene terephthalate) (PET) [169,170], PS [42,171–173], ABS [174–176], HIPS [177–179], PP [85,143,151,180–183], HDPE [131,180,184], LDPE [132], and poly(methyl methacrylate) (PMMA) [42]. To highlight the advances made, in this section, an overview of the most important findings is given in case study format, differentiating between polyesters, styrene-based materials and polyolefins. A special subsection is also devoted to additive manufacturing.

Taubner et al. [165] investigated the influence of moisture, processing temperature and screw speed on the degradation of PLLA during melt extrusion. The authors identified a higher level of degradation if high temperatures and low screw speeds were employed. This was attributed to the increased residence time of the material in the extruder and the activated nature of degradation reactions. Wang et al. [159] also showed that by increasing the residence time of PLLA in the extruder, the degradation becomes more pronounced. Furthermore, they highlighted that the decrease of the average molar mass of the material could be mainly attributed to thermal degradation for a dried material. In case the material is not dried, hydrolysis also plays a role for the degradation, further decreasing its average molar mass.

Furthermore, Mysiukiewicz et al. [166] investigated the effects of extrusion temperature and screw speed of a co-rotating twin-screw extruder on the properties of different grades of PLA. The materials underwent thermo-mechanical and thermal-oxidative degradation for high processing temperatures and low screw speeds, again due to the increased residence time condition. Structural changes were monitored via rheological measurements, perceived by the significant decrease in the zero-shear viscosity under these conditions. Aldhafeeri et al. [167] discussed that the processing parameters which increase the residence time, i.e. lower screw rate, lower feed rates, a quad screw extruder and kneading blocks, result in a more pronounced degradation of PLA, confirmed by the reduction in the zero-shear viscosity. Additionally, the PLA grades with a low starting viscosity were less susceptible to degradation than the ones with a high starting viscosity at higher screw speeds [166]. In addition, Oliveira et al. [168] studied the effect of temperature, shear and oxygen on the degradation of PLA.

The authors found out that thermo-mechanical degradation induced a higher degree of irreversible structural changes for the material than thermal-oxidative degradation.

Alongside PLA emphasis has also been on the processing of PET. For example, Spinacé and de Paoli [169] studied the effects of multiple extrusion cycles on PET properties. They observed a dramatic change of the mechanical properties after few extrusion cycles. The MFI, carboxylic end group content and color properties changed right after the first processing cycle, while no changes in thermal properties could be recorded. Al-AbdulRazzak and Jabarin [170] in turn assessed the effects of moisture, temperature and type of resin on the degradation of PET processed via injection molding. The authors concluded that the contribution of the different types of degradation to the overall (average) molar mass decrease depends on the processing conditions. For a high moisture content, the most important degradation mechanism is hydrolysis. In contrast, for low moisture contents, thermal and thermal-oxidative degradation become the most important degradation mechanisms. Additionally, material grades with a higher initial carboxyl content led to higher levels of carboxyl end-group generation because of hydrolysis. In turn, the rate of hydrolysis increased due to an autocatalytic mechanism promoted by these newly formed groups.

Manufacturing of styrene-based materials

Whitlock and Porter [171] studied the source of degradation of PS during its extrusion in a capillary rheometer. The role of the temperature, initial average molar mass and type of atmosphere were evaluated. At higher processing temperatures, the decrease in the average molar mass is more pronounced, indicating a more severe degradation. The measurement of the average molar mass at different concentric sections of extrudates indicated the existence of an (average) molar mass gradient throughout the specimen, with a reduced molar mass close to barrel, in comparison to the middle of

the extrudate, which exemplifies the effect of shear on the degradation process. The authors also put forward that differences between the initial molar mass affect the rate of degradation, as the highest molar mass species were most subjected to shear-induced degradation. In addition, processing the materials in air led to a higher level of degradation, compared to processing under nitrogen, highlighting that air present in any conventional processing scheme may play a prominent role in degradation of PS.

La Mantia et al. [172] processed PS at different screw speeds, temperatures and processing times, evidencing that by increasing the shear rate, the degradation of the material was also increased. They also corroborate the work of Whitlock and Porter [171], stating that processing in air caused a more severe degradation, due to a combined action of oxygen, temperature and mechanical stresses.

Capone et al. [42] in turn explored the degradation of PS (and PMMA) during processing at different temperatures and using different screw speeds. They also evaluated the thermal stability of the polymer in the capillary rheometer, showing that in the absence of mechanical stresses and limited contact to oxygen, thermal-oxidative degradation is insignificant at temperatures below than 210–230 °C. The authors pointed out that a low screw speed may induce the degradation of PS partially due to longer residence times. Finite element method (FEM) simulations suggested that at the highest rates, wall slippage phenomena may occur, which reduce the actual mechanical stress in the extruded polymers and may be a reason why the degradation level is smaller at high shear rates than first expected. In addition, the increase in temperature led to a reduction in the viscosity of the materials, confirming that combined effects of temperature and mechanical stresses can accelerate degradation in a synergistic mode. Furthermore, an estimation of the temperature, along the barrel

and in the channel sections via simulation showed a continuous temperature increase up to the extruder head, corresponding to output temperatures 20 to 60 °C higher than the set temperature.

Upon assessing ultrahigh speed extrusion of PS, Farahanchi et al. [173] also measured an overshoot in the processing temperature. In their case, it was as high as 33 °C at the highest rotation speed employed (4000 rpm). Because of the high screw speeds used in their study, the mechanical stresses were the most important factor causing to decrease the viscosity and average molar mass of PS.

Other styrenic polymers that have been investigated in terms of degradation during processing are ABS and HIPS, which are rubber-modified polymers, as described before. For instance, Karahaliou and Tarantili [174] investigated the effect of multiple extrusion cycles on ABS degradation. Even though the material exhibited yellowing and variations for FTIR spectra due to oxidation, no strong variations for its mechanical properties and MFI were witnessed. Similarly, Boldizar and Möller [175] reported minor degradation for ABS after multiple extrusion cycles, with only an increase for the elongation at break of the material. On the contrary, Salari and Ranjbar [176] reported degradation of the polybutadiene (PB-g-SAN) phase of ABS as the most important aspect to influence the properties of the material after multiple processing cycles, leading to yellowing, reduced elongation at break, lower impact strength and an increased MFI. In addition, Kalfoglou and Chaffey [177] investigated the relevance of the processing temperature and the use of successive processing on the degradation of HIPS. During regular processing the properties of HIPS changed only to a small extent. A decrease in elongation at break and impact resistance for HIPS after several processing cycles, or at high processing temperatures, was reported and attributed to the variations of the morphology of the material. A decrease at the

interface quality between both PB and SAN phases was highlighted because of shearing leading to agglomeration of particles, directly influencing the properties. Furthermore, the PS matrix, also underwent degradation, presenting a reduced average molar mass.

Vilaplana et al. [178] also assessed the influence of multiple extrusion cycles on the degradation of HIPS. They reported that (multiple) processing do not strongly affect the material properties, suggesting a low degree of degradation. Nevertheless, a slight increase in the MFI, with a reduction for the elongation at break and an increase in tensile strength were reported after few extrusion cycles. Furthermore, it was discussed how changes in the chemical structure of HIPS were induced because of processing, with the formation of oxidative moieties and the consumption of part of the unsaturations. Parres and Crespo [179] also indicated that the extrusion process of HIPS slightly affects its mechanical and thermal properties. The authors highlighted the design of new materials less prone to degradation, with the addition of styrene-butadiene rubber (SBR) and styrene–ethylene–butylene–styrene (SEBS).

Manufacturing of polyolefins

Hinsken et al. [180] studied the thermal-oxidative and thermo-mechanical degradation of PP and HDPE during multiple extrusions. For PP, it was found that the average molar mass decreases after every extrusion pass via chain fission, resulting from the β-scission of alkoxy radicals, the breakdown of peroxy radicals and shear. The first extrusion pass promoted the most significant decrease in the average molar mass, and this may be influenced by the increased shear (due to the high molar mass), as previously discussed for PS.

A similar study was conducted by Da Costa et al. [181], although with a deeper focus on the rheological property changes of PP undergoing multiple extrusion cycles. The rheological properties of PP changes after multiple cycles of extrusion, not only by a viscosity decrease but also by the reduction of the elasticity of the polymer melt. The authors pointed out that the factors which are important in determining the rate of degradation are the average residence time and residence time distribution. The effect of the screw element types on the degradation of PP was also assessed. Complementary, Canevarolo and Babetto [182] reported that use of kneading blocks at 90° caused a higher degree of degradation to the material compared to left-handed conveying elements. This was attributed to a lower oxidation level, because of the lower amount of oxygen available inside the barrel.

More recently, the degradation of PP has been monitored in-line via Raman Spectroscopy [143]. The results show a good relationship with SEC measurements, MFI and tensile properties, indicating that free radicals terminated with oxygen-containing functional groups instead of methyl groups and that long chains were more easily damaged in the extrusion.

Gonzáles-Gonzáles et al. [85] assessed the effects of extrusion temperature and extrusion cycles on the degradation of PP as well. While not evidencing oxidation during extrusion of PP, as seen via FTIR, the authors observed a big drop of the average molar masses and a lowering of the dispersity after each extrusion cycle. This effect was more pronounced at higher temperatures. da Costa et al. [183] carried out a similar study and they reported that degradation is more pronounced at high shear levels than at high temperatures, with a strong influence on the thermal properties and break properties due to the degradation of the material via chain fission.

Upon studying HDPE, Hinsken et al. [180] showed that chain branching and crosslinking reactions resulted in an increase of the average molar mass of the polymer. These reactions were favored compared to chain fission which is happening simultaneously, in contrast with what was observed for PP. Moss and Zweifel [184] also studied the effects of multiple extrusion in HDPE and discussed that depending on the type of HDPE used, the degradation could be either via chain fission or crosslinking, resulting in a decreased or increased average molar mass, respectively. Their study reveals that vinyl group reactions are primarily responsible for the average molar mass increase, as the increase correlates with a higher content of vinyl groups originally present.

The increase in viscosity of HDPE due to processing has also been reported in injection molding by Rex et al. [131] and was also attributed to degradation via crosslinking, branching, or chain extension. The authors put forward several important factors for the occurrence of fission, namely a low terminal vinyl group content, the presence of oxygen in the environment, and a high average chain length. Consistently, they highlighted that branching and crosslinking are favored over fission due to the oxygen deficient conditions of the injection molding process, limiting the transformation of alkyl radicals into peroxy radicals, as well as due to the relatively short average polymer chain lengths used.

The degradation of LDPE has also been subject of research. For example, Zatloukal et al. [132] observed that the average molar mass of LDPE gradually increased after different processing cycles. The authors discussed that chain fission, branching, crosslinking and gel formation occur simultaneously, with chain fission prevailing in processing for one or two cycles and microgel formation after this. The authors

indicated that the prevailing degradation mechanism of LDPE is the formation of more supramolecular structures via crosslinking and ultimately microgel particles.

Hence, depending on the type of polymer being manufactured, the material and processing parameters may promote chain fission, branching or crosslinking during processing. Overall, it can be stated that processing parameters which increase the residence time of the material will lead to degradation (cf. Figure 14), that processing temperatures must be carefully chosen, and that the materials must be properly dried to reduce degradation. In addition, the combination of these parameters may act synergistically, leading to a more severe degradation.

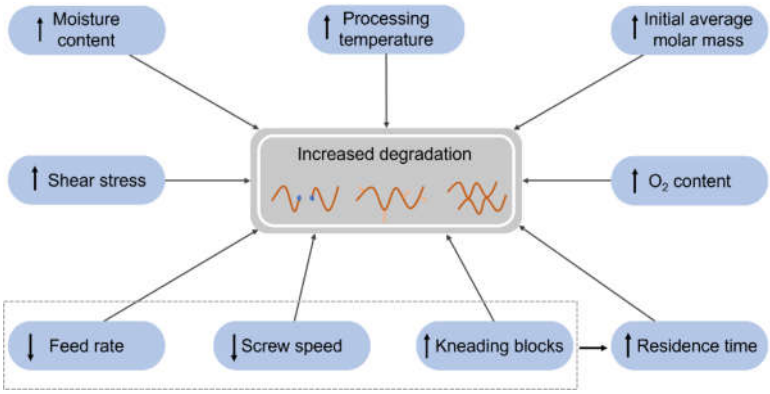

Figure 14: Summary on the influence of processing parameters on the degradation of polymers.

Additive manufacturing

Jagenteufel et al. [185] studied the degradation of ABS and PP during FFF and they concluded that the printing process resulted in negligible degradation in both materials, because of the short exposure time to high temperatures. Nevertheless, Wojtyła et al. [186] put forward that materials commonly used for 3D printing may emit both volatile organic compounds (VOC's) and ultrafine particles during

processing. The authors state that ABS in particular can be a source of potentially harmful VOC in the temperature range of FFF process.

Fernandez et. al [187] assessed the influence of the filament production, the printing temperature and the printing velocity on the degradation of copolyesters. It was observed that printing at lower velocities and at higher temperatures led to an increased degradation of one of the material grades assessed. The temperature was the most important factor in the degradation, as seen by the dramatic decrease in complex viscosity and relaxation time for this material, implying a decrease in its average molar mass. Nevertheless, the mechanical properties of the printed parts were not reduced as an effect of degradation as the coalescence between deposited layers was slightly improved at higher temperatures. Yet, the printing temperature parameter can only be tuned to a certain extent, as a further increase in printing temperature may result in polymer degradation, in case the onset temperature for degradation is reached [26,188–190].

Other materials used in EAM often exhibit low thermal stability and are prone to degradation, limiting their processing parameters and recyclability. Spoerk et al. [191] for example assessed the thermal stability of commercial filaments for FFF by means of rheological time sweep tests. They showed that PETG, thermoplastic copolyester elastomer (TPC) and PLA exhibit a decrease in viscosity after few seconds of testing, indicating a low thermal stability, whereas ABS exhibited an increase in the viscosity with time, probably due to the degradation of polybutadiene phase via crosslinking. Furthermore, Ahlinder et al. [192] evaluated the process induced degradation for aliphatic polyesters, PLLA, poly(ε-caprolactone) (PCL) and copolymers for tissue engineering applications, i.e. poly (ε-caprolactone-co-L-lactide) (PCLA) and poly(L-lactide-co-trimethylene carbonate) (PLATMC), that commonly undergo degradation

during processing. Due to the low shear rate in the extruder (2 s^{-1}), their process was mostly controlled by temperature. The degradation was monitored via SEC, evaluating the M_n variation of the materials before and after each processing step. PLLA showed a reduction in M_n of approximately 12 and 17% from pellet to filament and from pellet to 3D printed scaffold, respectively. The change in M_n from pellets to 3D printed scaffold utilizing PCL, PCLA and PLATMC was 3, 6 and 4%, respectively, indicating low levels of degradation for these materials. The authors concluded that by tailoring the extrusion and FFF processing parameters, it is possible to use FFF for scaffold fabrication of the materials investigated.

Gradwohl et al. [193] evaluated the type of EAM process on the degradation of poly(L-lactide-co-glycolide) (PLGA) copolymer. In the first process, the polymer was extruded into a filament which was further used to manufacture 3D printed parts in a commercial printer via FFF. In the second process, the pellets were directly fed into a pellet-based 3D printer (PBAM) to obtain 3D printed parts. These authors observed a decrease in M_n and M_m on the specimens fabricated via both processes. The M_n of the pellets was reduced by 19 and 26% for FFF and PBAM, respectively. The more pronounced degradation via PBAM was attributed to the longer residence time of the material in the micro-extruder, related to the lower printing speed employed. Furthermore, successive prints exhibited even more lowered M_n and M_m values for the PBAM process, indicating that the PBAM settings should be further optimized. This was also observed for syringe based 3D printing of PLGA based scaffolds, which induced more severe degradation than scaffolds produced via FFF, in case printed with too long melting times [194].

La Gala et al. [195] recently compared the properties of ABS and PLA produced via FFF and PBAM. Via FTIR, a higher degree of degradation of ABS manufactured via

FFF compared to PBAM has been reported. No significant differences regarding degradation were found for PLA processed via both techniques. In a follow-up study, the effects of printing parameters and technique on the degradation and macroscopic properties have been studied for PS and ABS [7]. The FFF process generated for ABS more fission as the mechanical loading in the filament production step is high, whereas in the PBAM process more crosslinking is evident thus a higher thermal loading took place. With PS always fission occurred with for FFF more because of the two processing steps instead of one, specifically for higher printing temperatures.

2. 7. Conclusions

We have reviewed the most important degradation pathways for polymers during processing, including both the virgin production, the mechanical recycling and the additive manufacturing, mainly differentiating between thermal, thermo-mechanical, thermal-oxidative degradation, and hydrolysis. Even though several reaction pathways are already established, the understanding of specific degradation mechanisms for a given polymer system is still lacking. In this context, it is relevant to further combine experimental techniques commonly used to characterize polymer degradation as well as to further combine these techniques with modeling. Special attention should be paid to further improving chromatography and rheometry, as they can be seen as sensitive techniques to capture molecular changes, even at early stages of degradation.

Case studies on the degradation of polyesters, styrene-based polymers and polyolefins using conventional processing have been addressed. They aimed at assessing the effects of processing parameters on the degradation during processing. Among these parameters, the most important are the processing temperature, processing speed, feed

rate, screw type, and screw elements. Molecular properties have been also explored, especially the initial average molar mass of the polymer, and in some situations, the grade of material. Other important insights have been provided by recyclability studies that assess the effects of multiple extrusion on the properties of the polymer materials. Overall, it can be stated that parameters which increase the residence time will induce a higher degree of degradation of the material. Furthermore, the processing temperature must be carefully chosen, as at too high temperatures the polymer materials are becoming too prone to degradation.

The volume of literature concerning polymer degradation during extrusion-based additive manufacturing (EAM) is remarkably smaller than during conventional processing, which can be partially understood by their more recent development. However, research covering degradation during conventional processing in the past decades may also be incorporated, at least to certain extent, for these newer manufacturing techniques. Note that FFF includes two processing steps, which may further contribute to the degradation of the printed polymeric materials, as they are subjected to factors which induce degradation twice prior to their use.

REFERENCES

1. IUPAC. *Compendium of Polymer Terminology and Nomenclature*; Jones, R.G., Wilks, E.S., Metanomski, W.V., Kahovec, J., Hess, M., Stepto, R., Kitayama, T., Eds.; Royal Society of Chemistry: Cambridge, 2009; Vol. 0; ISBN 978-0-85404-491-7.
2. Moens, E.; De Smit, K.; Marien, Y.; Trigilio, A.; Van Steenberge, P.; Van Geem, K.; Dubois, J.-L.; D'hooge, D. Progress in Reaction Mechanisms and Reactor Technologies for Thermochemical Recycling of Poly(methyl methacrylate). *Polymers (Basel).* **2020**, *12*, 1667, doi:10.3390/polym12081667.
3. De Smit, K.; Wieme, T.; Marien, Y.W.; Van Steenberge, P.H.M.; D'hooge, D.R.; Edeleva, M. Multi-scale reactive extrusion modelling approaches to design polymer synthesis, modification and mechanical recycling. *React. Chem. Eng.* **2022**, *7*, 245–263, doi:10.1039/D1RE00556A.
4. Scaffaro, R.; Maio, A.; Sutera, F.; Gulino, E.; Morreale, M. Degradation and Recycling of Films Based on Biodegradable Polymers: A Short Review. *Polymers (Basel).* **2019**, *11*, 651, doi:10.3390/polym11040651.
5. Ito, M.; Nagai, K. Degradation issues of polymer materials used in railway field. *Polym. Degrad. Stab.* **2008**, *93*, 1723–1735, doi:10.1016/j.polymdegradstab.2008.07.011.
6. Ragaert, K.; Delva, L.; Van Geem, K. Mechanical and chemical recycling of solid plastic waste. *Waste Manag.* **2017**, *69*, 24–58, doi:10.1016/j.wasman.2017.07.044.
7. Ceretti, D.V.A.; Marien, Y.W.; Edeleva, M.; La Gala, A.; Cardon, L.; D'hooge, D.R. Thermal and Thermal-Oxidative Molecular Degradation of Polystyrene and Acrylonitrile Butadiene Styrene during 3D Printing Starting from Filaments and Pellets. *Sustainability* **2022**, *14*, 15488, doi:10.3390/su142315488.
8. Vilaplana, F.; Karlsson, S.; Ribes-Greus, A. Changes in the microstructure and morphology of high-impact polystyrene subjected to multiple processing and thermo-oxidative degradation. *Eur. Polym. J.* **2007**, *43*, 4371–4381, doi:10.1016/j.eurpolymj.2007.07.017.
9. Cosate de Andrade, M.F.; Fonseca, G.; Morales, A.R.; Mei, L.H.I. Mechanical recycling simulation of polylactide using a chain extender. *Adv. Polym. Technol.* **2018**, *37*, 2053–2060, doi:10.1002/adv.21863.
10. ISO/ASTM52900-15 Standard Terminology for Additive Manufacturing – General Principles – Terminology (ASTM52900). *Int. Organ. Stand. Geneva, Switz.* **2015**, *i*, 1–9, doi:1.
11. Bikas, H.; Stavropoulos, P.; Chryssolouris, G. Additive manufacturing methods and modeling approaches: A critical review. *Int. J. Adv. Manuf. Technol.* **2016**, *83*, 389–405, doi:10.1007/s00170-015-7576-2.
12. Tiganis, B.E.; Burn, L.S.; Davis, P.; Hill, A.J. Thermal degradation of acrylonitrile-butadiene-styrene (ABS) blends. *Polym. Degrad. Stab.* **2002**, *76*, 425–434, doi:10.1016/S0141-3910(02)00045-9.
13. Konarzewski, M.; Durejko, T.; Łazińska, M.; Czerwińska, M.; Prasuła, P.; Panowicz, R. Thermo-oxidative aging of the polyoxymethylene (POM), acrylonitrile–butadiene–styrene (ABS) and polycarbonate (PC) polymers – a

comparative study. *J. Polym. Res.* **2022**, *29*, doi:10.1007/s10965-022-03065-8.
14. Scott, G. Mechano-chemical degradation and stabilization of polymers. *Polym. Eng. Sci.* **1984**, *24*, 1007–1020, doi:10.1002/pen.760241302.
15. Hawkins, W.L. *Polymer Degradation and Stabilization*; Polymers Properties and Applications; Springer: Berlin, 1984; ISBN 978-3-642-69378-6.
16. Gensler, R.; Plummer, C.J.G.; Kausch, H.H.; Kramer, E.; Pauquet, J.R.; Zweifel, H. Thermo-oxidative degradation of isotactic polypropylene at high temperatures: Phenolic antioxidants versus HAS. *Polym. Degrad. Stab.* **2000**, *67*, 195–208, doi:10.1016/S0141-3910(99)00113-5.
17. Gijsman, P. Polymer Stabilization. In *Applied Plastics Engineering Handbook*; Elsevier, 2017; pp. 395–421 ISBN 9780323390408.
18. Kumar, A.P.; Depan, D.; Singh Tomer, N.; Singh, R.P. Nanoscale particles for polymer degradation and stabilization-Trends and future perspectives. *Prog. Polym. Sci.* **2009**, *34*, 479–515, doi:10.1016/j.progpolymsci.2009.01.002.
19. Chen, J.; Xia, L.; Kong, M.; He, Y.; Lv, Y.; Huang, Y.; Li, G. Optimized design of environmentally-friendly polydopamine nanoparticles for the stabilization of both thermo- and photo-oxidation of polypropylene: Size effects. *Polym. Test.* **2022**, *116*, 107795, doi:10.1016/j.polymertesting.2022.107795.
20. Takacs, K.; Tatraaljai, D.; Pregi, E.; Huszthy, P.; Pukanszky, B. Synthesis and evaluation of a novel natural-based phosphine antioxidant for the thermal stabilization of polyethylene. *J. Therm. Anal. Calorim.* **2022**, *147*, 12513–12522, doi:10.1007/s10973-022-11421-5.
21. Dintcheva, N.T.; Al-Malaika, S.; Arrigo, R.; Morici, E. Novel strategic approach for the thermo- and photo- oxidative stabilization of polyolefin/clay nanocomposites. *Polym. Degrad. Stab.* **2017**, *145*, 41–51, doi:10.1016/j.polymdegradstab.2017.04.014.
22. Shamsuyeva, M.; Endres, H.J. Plastics in the context of the circular economy and sustainable plastics recycling: Comprehensive review on research development, standardization and market. *Compos. Part C Open Access* **2021**, *6*, 100168, doi:10.1016/j.jcomc.2021.100168.
23. Ghosh, S.K. *Circular Economy: Global Perspective*; Ghosh, S.K., Ed.; Springer Singapore: Singapore, 2020; ISBN 978-981-15-1051-9.
24. Van Waeleghem, T.; Marchesini, F.H.; Cardon, L.; D'hooge, D.R. Melt exit flow modelling and experimental validation for fused filament fabrication: From Newtonian to non-Newtonian effects. *J. Manuf. Process.* **2022**, *77*, 138–150, doi:10.1016/j.jmapro.2022.03.002.
25. Penumakala, P.K.; Santo, J.; Thomas, A. A critical review on the fused deposition modeling of thermoplastic polymer composites. *Compos. Part B Eng.* **2020**, *201*, 108336, doi:10.1016/j.compositesb.2020.108336.
26. Turner, B.N.; Strong, R.; Gold, S.A. A review of melt extrusion additive manufacturing processes: I. Process design and modeling. *Rapid Prototyp. J.* **2014**, *20*, 192–204, doi:10.1108/RPJ-01-2013-0012.
27. Vyavahare, S.; Teraiya, S.; Panghal, D.; Kumar, S. Fused deposition modelling: a review. *Rapid Prototyp. J.* **2020**, *26*, 176–201, doi:10.1108/RPJ-04-2019-0106.
28. Lalegani Dezaki, M.; Mohd Ariffin, M.K.A.; Hatami, S. An overview of fused deposition modelling (FDM): research, development and process

optimisation. *Rapid Prototyp. J.* **2021**, *27*, 562–582, doi:10.1108/RPJ-08-2019-0230.
29. Salifu, S.; Desai, D.; Ogunbiyi, O.; Mwale, K. Recent development in the additive manufacturing of polymer-based composites for automotive structures—a review. *Int. J. Adv. Manuf. Technol.* **2022**, *119*, 6877–6891, doi:10.1007/s00170-021-08569-z.
30. Najmon, J.C.; Raeisi, S.; Tovar, A. Review of additive manufacturing technologies and applications in the aerospace industry. In *Additive Manufacturing for the Aerospace Industry*; Elsevier, 2019; pp. 7–31 ISBN 9780128140635.
31. Salmi, M. Additive manufacturing processes in medical applications. *Materials (Basel).* **2021**, *14*, 1–16, doi:10.3390/ma14010191.
32. Paolini, A.; Kollmannsberger, S.; Rank, E. Additive manufacturing in construction: A review on processes, applications, and digital planning methods. *Addit. Manuf.* **2019**, *30*, 100894, doi:10.1016/j.addma.2019.100894.
33. Gonzalez-Gutierrez, J.; Cano, S.; Schuschnigg, S.; Kukla, C.; Sapkota, J.; Holzer, C. Additive manufacturing of metallic and ceramic components by the material extrusion of highly-filled polymers: A review and future perspectives. *Materials (Basel).* **2018**, *11*, doi:10.3390/ma11050840.
34. Song, D.; Xu, Y.; Liu, S.; Wen, L.; Wang, X. Progress of 3D Bioprinting in Organ Manufacturing. *Polymers (Basel).* **2021**, *13*, 3178, doi:10.3390/polym13183178.
35. Janarthanan, G.; Thavasyappan, T.; Hong, S.; Noh, I. Chapter 2. Introduction to Hydrogel Synthesis and Crosslinking Methods for Developing Bioinks for 3D Bioprinting. In *Injectable Hydrogels for 3D Bioprinting*; Royal Society of Chemistry, 2021; pp. 21–47.
36. Gijsman, P. Review on the thermo-oxidative degradation of polymers during processing and in service. *E-Polymers* **2008**, 1–34, doi:10.1515/epoly.2008.8.1.727.
37. Pickett, J.E.; Coyle, D.J. Hydrolysis kinetics of condensation polymers under humidity aging conditions. *Polym. Degrad. Stab.* **2013**, *98*, 1311–1320, doi:10.1016/j.polymdegradstab.2013.04.001.
38. Pielichowski, K.; Njuguna, J. *Thermal Degradation of Polymeric Materials*; Smithers Rapra: Shawbury, 2005; ISBN 9781859574980.
39. De Smit, K.; Marien, Y.W.; Van Geem, K.M.; Van Steenberge, P.H.M.; D'hooge, D.R. Connecting polymer synthesis and chemical recycling on a chain-by-chain basis: a unified matrix-based kinetic Monte Carlo strategy. *React. Chem. Eng.* **2020**, *5*, 1909–1928, doi:10.1039/D0RE00266F.
40. Gaitanelis, D.; Worrall, C.; Kazilas, M. Detecting, characterising and assessing PEEK's and CF-PEEK's thermal degradation in rapid high-temperature processing. *Polym. Degrad. Stab.* **2022**, *204*, 110096, doi:10.1016/j.polymdegradstab.2022.110096.
41. Carrasco, F.; Santana, O.; Cailloux, J.; Maspoch, M.L. Kinetics of the thermal degradation of poly(lactic acid) obtained by reactive extrusion: Influence of the addition of montmorillonite nanoparticles. *Polym. Test.* **2015**, *48*, 69–81, doi:10.1016/j.polymertesting.2015.09.014.
42. Capone, C.; Di Landro, L.; Inzoli, F.; Penco, M.; Sartore, L. Thermal and mechanical degradation during polymer extrusion processing. *Polym. Eng. Sci.* **2007**, *47*, 1813–1819, doi:10.1002/pen.20882.

43. Kholodovych, V.; Welsh, W.J. Thermal-Oxidative Stability and Degradation of Polymers. In *Physical Properties of Polymers Handbook*; Mark, J.E., Ed.; Springer New York: New York, NY, 2007; pp. 927–938 ISBN 978-0-387-31235-4.
44. Van Steenberge, P.H.M.; Vandenbergh, J.; Reyniers, M.-F.; Junkers, T.; D'hooge, D.R.; Marin, G.B. Kinetic Monte Carlo Generation of Complete Electron Spray Ionization Mass Spectra for Acrylate Macromonomer Synthesis. *Macromolecules* **2017**, *50*, 2625–2636, doi:10.1021/acs.macromol.7b00333.
45. Huang, J.B.; Zeng, G.S.; Li, X.S.; Cheng, X.C.; Tong, H. Theoretical studies on bond dissociation enthalpies for model compounds of typical plastic polymers. *IOP Conf. Ser. Earth Environ. Sci.* **2018**, *167*, doi:10.1088/1755-1315/167/1/012029.
46. Grunenberg, J. Ill-defined chemical concepts: The problem of quantification. *Int. J. Quantum Chem.* **2017**, *117*, 1–11, doi:10.1002/qua.25359.
47. Sohma, J. Mechano-radical formation in polypropylene by an extruder action and its after-effects. *Colloid Polym. Sci.* **1992**, *270*, 1060–1065, doi:10.1007/BF00652868.
48. *Chemical kinetics: Polymer degradation*; Bamford, C.H., Tipper, C.F.H., Eds.; Elsevier: Amsterdam, 1975; Vol. 14; ISBN 3904144987.
49. Gol'dberg, V.M.; Zaikov, G.E. Kinetics of mechanical degradation in melts under model conditions and during processing of polymers-A review. *Polym. Degrad. Stab.* **1987**, *19*, 221–250, doi:10.1016/0141-3910(87)90057-7.
50. Edeleva, M.; Zafeiris, K.; Fiorio, R.; D'hooge, D.R.; Chariditis, C.A.; Cardon, L. Increasing sustainability of additive manufacturing techniques: minimization of degradation and optimization of the printing parameters, Accepted. In *Springer Handbook of Circular Plastics Economy*; Buettner, A., Weidner, E., Eds.
51. Zweifel, H. *Stabilization of Polymeric Materials*; Springer Berlin Heidelberg: Berlin, Heidelberg, 1998; Vol. 33; ISBN 978-3-642-80307-9.
52. Bolland, J.L.; A, P.R.S.L. Kinetic studies in the chemistry of rubber and related materials. I. The thermal oxidation of ethyl linoleate. *Proc. R. Soc. London. Ser. A. Math. Phys. Sci.* **1946**, *186*, 218–236, doi:10.1098/rspa.1946.0040.
53. Bolland, J.L.; Gee, G. Kinetic studies in the chemistry of rubber and related materials. III. Thermochemistry and mechanisms of olefin oxidation. *Trans. Faraday Soc.* **1946**, *42*, 244, doi:10.1039/tf9464200244.
54. Bolland, J.L. Kinetic studies in the chemistry of rubber and related materials. VI. The benzoyl peroxide-catalysed oxidation of ethyl linoleate. *Trans. Faraday Soc.* **1948**, *44*, 669–677, doi:10.1039/tf9484400669.
55. Gryn'ova, G.; Hodgson, J.L.; Coote, M.L. Revising the mechanism of polymer autooxidation. *Org. Biomol. Chem.* **2011**, *9*, 480–490, doi:10.1039/c0ob00596g.
56. Singh, B.; Sharma, N. Mechanistic implications of plastic degradation. *Polym. Degrad. Stab.* **2008**, *93*, 561–584, doi:10.1016/j.polymdegradstab.2007.11.008.
57. Nguyen, T.Q. Polymer Degradation and Stabilization. In *Handbook of Polymer Reaction Engineering*; Wiley-VCH Verlag GmbH: Weinheim, Germany, 2008; pp. 757–831 ISBN 9783527310142.
58. Bracco, P.; Costa, L.; Luda, M.P.; Billingham, N. A review of experimental

studies of the role of free-radicals in polyethylene oxidation. *Polym. Degrad. Stab.* **2018**, *155*, 67–83, doi:10.1016/j.polymdegradstab.2018.07.011.

59. Homstrom, A.; Sorvik, E.M. Thermooxidative Degradation of Polyethylene - 1 and 2. Structural Changes Occurring in Low-Density Polyethylene, High-Density Polyethylene, and Tetratetracontane Heated in Air. *J Polym Sci Polym Chem Ed* **1978**, *16*, 2555–2586, doi:10.1002/pol.1978.170161012.
60. Adeniyi, J.B.; Kolawole, E.G. Thermal and photo-degradation of unstabilized ABS. *Eur. Polym. J.* **1984**, *20*, 43–47, doi:10.1016/0014-3057(84)90220-9.
61. Vert, M.; Li, S.; Garreau, H.; Mauduit, J.; Boustta, M.; Schwach, G.; Engel, R.; Coudane, J. Complexity of the hydrolytic degradation of aliphatic polyesters. *Angew. Makromol. Chemie* **1997**, *247*, 239–253, doi:10.1002/apmc.1997.052470116.
62. Algarni, M.; Ghazali, S. Comparative Study of the Sensitivity of PLA, ABS, PEEK, and PETG's Mechanical Properties to FDM Printing Process Parameters. *Crystals* **2021**, *11*, 995, doi:10.3390/cryst11080995.
63. Peterson, A.M. Review of acrylonitrile butadiene styrene in fused filament fabrication: A plastics engineering-focused perspective. *Addit. Manuf.* **2019**, *27*, 363–371, doi:10.1016/j.addma.2019.03.030.
64. Hsueh, M.-H.; Lai, C.-J.; Wang, S.-H.; Zeng, Y.-S.; Hsieh, C.-H.; Pan, C.-Y.; Huang, W.-C. Effect of Printing Parameters on the Thermal and Mechanical Properties of 3D-Printed PLA and PETG, Using Fused Deposition Modeling. *Polymers (Basel).* **2021**, *13*, 1758, doi:10.3390/polym13111758.
65. Cojocaru, V.; Frunzaverde, D.; Miclosina, C.O.; Marginean, G. The Influence of the Process Parameters on the Mechanical Properties of PLA Specimens Produced by Fused Filament Fabrication—A Review. *Polymers (Basel).* **2022**, *14*, doi:10.3390/polym14050886.
66. Guessasma, S.; Belhabib, S.; Nouri, H. Printability and tensile performance of 3D printed polyethylene terephthalate glycol using fused deposition modelling. *Polymers (Basel).* **2019**, *11*, doi:10.3390/polym11071220.
67. Özen, A.; Auhl, D.; Völlmecke, C.; Kiendl, J.; Abali, B.E. Optimization of Manufacturing Parameters and Tensile Specimen Geometry for Fused Deposition Modeling (FDM) 3D-Printed PETG. *Materials (Basel).* **2021**, *14*, 2556, doi:10.3390/ma14102556.
68. Zanjanijam, A.R.; Major, I.; Lyons, J.G.; Lafont, U.; Devine, D.M. Fused Filament Fabrication of PEEK: A Review of Process-Structure-Property Relationships. *Polymers (Basel).* **2020**, *12*, 1665, doi:10.3390/polym12081665.
69. Rinaldi, M.; Ghidini, T.; Cecchini, F.; Brandao, A.; Nanni, F. Additive layer manufacturing of poly (ether ether ketone) via FDM. *Compos. Part B* **2018**, *145*, 162–172, doi:10.1016/j.compositesb.2018.03.029.
70. Yang, C.; Tian, X.; Li, D.; Cao, Y.; Zhao, F.; Shi, C. Influence of thermal processing conditions in 3D printing on the crystallinity and mechanical properties of PEEK material. *J. Mater. Process. Technol.* **2017**, *248*, 1–7, doi:10.1016/j.jmatprotec.2017.04.027.
71. Arif, M.F.; Kumar, S.; Varadarajan, K.M.; Cantwell, W.J. Performance of biocompatible PEEK processed by fused deposition additive manufacturing. *Mater. Des.* **2018**, *146*, 249–259, doi:10.1016/j.matdes.2018.03.015.
72. Deng, X.; Zeng, Z.; Peng, B.; Yan, S.; Ke, W. Mechanical properties optimization of poly-ether-ether-ketone via fused deposition modeling. *Materials (Basel).* **2018**, *11*, doi:10.3390/ma11020216.

73. Geng, P.; Zhao, J.; Wu, W.; Ye, W.; Wang, Y.; Wang, S.; Zhang, S. Effects of extrusion speed and printing speed on the 3D printing stability of extruded PEEK filament. *J. Manuf. Process.* **2019**, *37*, 266–273, doi:S1526612518301981.
74. Schirmeister, C.G.; Hees, T.; Licht, E.H.; Mülhaupt, R. 3D printing of high density polyethylene by fused filament fabrication. *Addit. Manuf.* **2019**, *28*, 152–159, doi:10.1016/j.addma.2019.05.003.
75. Carneiro, O.S.; Silva, A.F.; Gomes, R. Fused deposition modeling with polypropylene. *Mater. Des.* **2015**, *83*, 768–776, doi:10.1016/j.matdes.2015.06.053.
76. Charlon, S.; Le Boterff, J.; Soulestin, J. Fused filament fabrication of polypropylene: Influence of the bead temperature on adhesion and porosity. *Addit. Manuf.* **2021**, *38*, 4–11, doi:10.1016/j.addma.2021.101838.
77. Spoerk, M.; Gonzalez-Gutierrez, J.; Lichal, C.; Cajner, H.; Berger, G.R.; Schuschnigg, S.; Cardon, L.; Holzer, C. Optimisation of the adhesion of polypropylene-based materials during extrusion-based additive manufacturing. *Polymers (Basel).* **2018**, *10*, doi:10.3390/polym10050490.
78. Liao, G.; Li, Z.; Luan, C.; Wang, Z.; Yao, X.; Fu, J. Additive Manufacturing of Polyamide 66: Effect of Process Parameters on Crystallinity and Mechanical Properties. *J. Mater. Eng. Perform.* **2022**, *31*, 191–200, doi:10.1007/s11665-021-06149-6.
79. Qi, S.; Gao, X.; Su, Y.; Dong, X.; Cavallo, D.; Wang, D. Correlation between welding behavior and mechanical anisotropy of long chain polyamide 12 manufactured with fused filament fabrication. *Polymer (Guildf).* **2021**, *213*, 123318, doi:10.1016/j.polymer.2020.123318.
80. Vilaplana, F.; Karlsson, S.; Ribes-Greus, A.; Schade, C.; Nestle, N. NMR relaxation reveals modifications in rubber phase dynamics during long-term degradation of high-impact polystyrene (HIPS). *Polymer (Guildf).* **2011**, *52*, 1410–1416, doi:10.1016/j.polymer.2011.02.005.
81. Bai, X.; Liang, P.; Zhang, M.; Gong, S.; Zhao, L. Effects of Reprocessing on Acrylonitrile–Butadiene–Styrene and Additives. *J. Polym. Environ.* **2022**, *30*, 1803–1819, doi:10.1007/s10924-021-02314-z.
82. Garcia Gonçalves, L.M.; Rigolin, T.R.; Frenhe, B.M.; Prado Bettini, S.H. On the recycling of a biodegradable polymer: Multiple extrusion of poly (Lactic acid). *Mater. Res.* **2020**, *23*, doi:10.1590/1980-5373-MR-2020-0274.
83. Hosseini, S.S.; Taheri, S.; Zadhoush, A.; Mehrabani-Zeinabad, A. Hydrolytic degradation of poly(ethylene terephthalate). *J. Appl. Polym. Sci.* **2007**, *103*, 2304–2309, doi:10.1002/app.24142.
84. Saikrishnan, S.; Jubinville, D.; Tzoganakis, C.; Mekonnen, T.H. Thermo-mechanical degradation of polypropylene (PP) and low-density polyethylene (LDPE) blends exposed to simulated recycling. *Polym. Degrad. Stab.* **2020**, *182*, 109390, doi:10.1016/j.polymdegradstab.2020.109390.
85. González-González, V.A.; Neira-Velázquez, G.; Angulo-Sánchez, J.L. Polypropylene chain scissions and molecular weight changes in multiple extrusion. *Polym. Degrad. Stab.* **1998**, *60*, 33–42, doi:10.1016/S0141-3910(96)00233-9.
86. Andersson, T.; Stålbom, B.; Wesslén, B. Degradation of polyethylene during extrusion. II. Degradation of low-density polyethylene, linear low-density polyethylene, and high-density polyethylene in film extrusion. *J. Appl. Polym. Sci.* **2004**, *91*, 1525–1537, doi:10.1002/app.13024.

87. Jin, H.; Gonzalez-Gutierrez, J.; Oblak, P.; Zupančič, B.; Emri, I. The effect of extensive mechanical recycling on the properties of low density polyethylene. *Polym. Degrad. Stab.* **2012**, *97*, 2262–2272, doi:10.1016/j.polymdegradstab.2012.07.039.
88. Phillips, R.; Glauser, T.; Månson, J.A.E. Thermal stability of PEEK/carbon fiber in air and its influence on consolidation. *Polym. Compos.* **1997**, *18*, 500–508, doi:10.1002/pc.10302.
89. Pascual, A.; Toma, M.; Tsotra, P.; Grob, M.C. On the stability of PEEK for short processing cycles at high temperatures and oxygen-containing atmosphere. *Polym. Degrad. Stab.* **2019**, *165*, 161–169, doi:10.1016/j.polymdegradstab.2019.04.025.
90. Su, K.H.; Lin, J.H.; Lin, C.C. Influence of reprocessing on the mechanical properties and structure of polyamide 6. *J. Mater. Process. Technol.* **2007**, *192–193*, 532–538, doi:10.1016/j.jmatprotec.2007.04.056.
91. Filippone, G.; Carroccio, S.C.; Mendichi, R.; Gioiella, L.; Dintcheva, N.T.; Gambarotti, C. Time-resolved rheology as a tool to monitor the progress of polymer degradation in the melt state - Part I: Thermal and thermo-oxidative degradation of polyamide 11. *Polymer (Guildf).* **2015**, *72*, 134–141, doi:10.1016/j.polymer.2015.06.059.
92. Suzuki, M.; Wilkie, C.A. The thermal degradation of acrylonitrile-butadiene-styrene terpolymei as studied by TGA/FTIR. *Polym. Degrad. Stab.* **1995**, *47*, 217–221, doi:10.1016/0141-3910(94)00122-O.
93. Allen, N.S.; Edge, M.; Wilkinson, A.; Liauw, C.M.; Mourelatou, D.; Barrio, J.; Martínez-Zaporta, M.A. Degradation and stabilization of styrene-ethylene-butadiene-styrene (SEBS) block copolymer. *Polym. Degrad. Stab.* **2000**, *71*, 113–122, doi:10.1016/S0141-3910(00)00162-2.
94. Boyle, D.J.; Gesner, B.D. Aging of polyblends. *J. Appl. Polym. Sci.* **1968**, *12*, 1193–1197, doi:10.1002/app.1968.070120517.
95. Fiorio, R.; D'hooge, D.R.; Ragaert, K.; Cardon, L. A statistical analysis on the effect of antioxidants on the thermal-oxidative stability of commercial massand emulsion-polymerized ABS. *Polymers (Basel).* **2018**, *11*, doi:10.3390/polym11010025.
96. Casale, A.; Salvatore, O.; Pizzigoni, G. Measurement of aging effects of ABS polymers. *Polym. Eng. Sci.* **1975**, *15*, 286–293, doi:10.1002/pen.760150410.
97. Vadori, R.; Misra, M.; Mohanty, A.K. Studies on the reaction of acrylonitrile butadiene styrene to melt processing conditions. *Macromol. Mater. Eng.* **2015**, *300*, 750–757, doi:10.1002/mame.201400415.
98. Blom, H.; Yeh, R.; Wojnarowski, R.; Ling, M. Detection of degradation of ABS materials via DSC. *Thermochim. Acta* **2006**, *442*, 64–66, doi:10.1016/j.tca.2006.01.015.
99. Shimada, J.; Kabuki, K. The mechanism of oxidative degradation of ABS resin. Part I. The mechanism of thermooxidative degradation. *J. Appl. Polym. Sci.* **1968**, *12*, 655–669, doi:10.1002/app.1968.070120405.
100. Adeniyi, J.B. Clarification and discussion of chemical transformations involved in thermal and photo-oxidative degradation of ABS. *Eur. Polym. J.* **1984**, *20*, 291–299, doi:10.1016/0014-3057(84)90050-8.
101. Scaffaro, R.; Botta, L.; Di Benedetto, G. Physical properties of virgin-recycled ABS blends: Effect of post-consumer content and of reprocessing cycles. *Eur. Polym. J.* **2012**, *48*, 637–648, doi:10.1016/j.eurpolymj.2011.12.018.

102. Charles, A.; Bassan, P.M.; Mueller, T.; Elkaseer, A.; Scholz, S.G. On the Assessment of Thermo-mechanical Degradability of Multi-recycled ABS Polymer for 3D Printing Applications. In *Smart Innovation, Systems and Technologies*; Springer Singapore, 2019; Vol. 155, pp. 363–373 ISBN 9789811392702.
103. Al-Itry, R.; Lamnawar, K.; Maazouz, A. Improvement of thermal stability, rheological and mechanical properties of PLA, PBAT and their blends by reactive extrusion with functionalized epoxy. *Polym. Degrad. Stab.* **2012**, *97*, 1898–1914, doi:10.1016/j.polymdegradstab.2012.06.028.
104. McNeill, I.C.; Leiper, H.A. Degradation studies of some polyesters and polycarbonates-2. Polylactide: Degradation under isothermal conditions, thermal degradation mechanism and photolysis of the polymer. *Polym. Degrad. Stab.* **1985**, *11*, 309–326, doi:10.1016/0141-3910(85)90035-7.
105. Amorin, N.S.Q.S.; Rosa, G.; Alves, J.F.; Gonçalves, S.P.C.; Franchetti, S.M.M.; Fechine, G.J.M. Study of thermodegradation and thermostabilization of poly(lactide acid) using subsequent extrusion cycles. *J. Appl. Polym. Sci.* **2014**, *131*, 1–8, doi:10.1002/app.40023.
106. Speranza, V.; De Meo, A.; Pantani, R. Thermal and hydrolytic degradation kinetics of PLA in the molten state. *Polym. Degrad. Stab.* **2014**, *100*, 37–41, doi:10.1016/j.polymdegradstab.2013.12.031.
107. Bakrani Balani, S.; Chabert, F.; Nassiet, V.; Cantarel, A. Influence of printing parameters on the stability of deposited beads in fused filament fabrication of poly(lactic) acid. *Addit. Manuf.* **2019**, *25*, 112–121, doi:10.1016/j.addma.2018.10.012.
108. Wang, S.; Daelemans, L.; D'hooge, D.R.; Couck, L.; Van Den Broeck, W.; Cornillie, P.; Gou, M.; De Clerck, K.; Cardon, L. Lifting the quality of fused filament fabrication of polylactic acid based composites. *Compos. Part B Eng.* **2021**, *210*, 108613, doi:10.1016/j.compositesb.2021.108613.
109. Zhao, P.; Rao, C.; Gu, F.; Sharmin, N.; Fu, J. Close-looped recycling of polylactic acid used in 3D printing: An experimental investigation and life cycle assessment. *J. Clean. Prod.* **2018**, *197*, 1046–1055, doi:10.1016/j.jclepro.2018.06.275.
110. Kopinke, F.D.; Remmler, M.; Mackenzie, K.; Möder, M.; Wachsen, O. Thermal decomposition of biodegradable polyesters - II. Poly(lactic acid). *Polym. Degrad. Stab.* **1996**, *53*, 329–342, doi:10.1016/0141-3910(96)00102-4.
111. Schyns, Z.O.G.; Shaver, M.P. Mechanical Recycling of Packaging Plastics: A Review. *Macromol. Rapid Commun.* **2021**, *42*, 1–27, doi:10.1002/marc.202000415.
112. Holmström, A.; Sörvik, E. Thermal degradation of polyethylene in a nitrogen atmosphere of low oxygen content. I. Changes in molecular weight distribution. *J. Chromatogr. A* **1970**, *53*, 95–108, doi:10.1016/S0021-9673(00)86708-4.
113. Holmström, A.; Sörvik, E.M. Thermal degradation of polyethylene in a nitrogen atmosphere of low oxygen content. II. Structural changes occuring in low-density polyethylene at an oxygen content less than 0.0005%. *J. Appl. Polym. Sci.* **1974**, *18*, 761–778, doi:10.1002/app.1974.070180314.
114. Holmström, A.; Sörvik, E.M. Thermal degradation of polyethylene in a nitrogen atmosphere of low oxygen content. III. Structural changes occuring in low-density polyethylene at oxygen contents below 1.2%. *J. Appl. Polym.*

Sci. **1974**, *18*, 779–804, doi:10.1002/app.1974.070180315.
115. Adams, J.H. Analysis of the nonvolatile oxidation products of polypropylene I. Thermal oxidation. *J. Polym. Sci. Part A-1 Polym. Chem.* **1970**, *8*, 1077–1090, doi:10.1002/pol.1970.150080505.
116. Adams, J.H.; Goodrich, J.E. Analysis of nonvolatile oxidation products of polypropylene. II. Process degradation. *J. Polym. Sci. Part A-1 Polym. Chem.* **1970**, *8*, 1269–1277, doi:10.1002/pol.1970.150080519.
117. De Keer, L.; Kilic, K.I.; Van Steenberge, P.H.M.; Daelemans, L.; Kodura, D.; Frisch, H.; De Clerck, K.; Reyniers, M.-F.; Barner-Kowollik, C.; Dauskardt, R.H.; et al. Computational prediction of the molecular configuration of three-dimensional network polymers. *Nat. Mater.* **2021**, *20*, 1422–1430, doi:10.1038/s41563-021-01040-0.
118. Figueira, F.L.; Wu, Y.-Y.; Zhou, Y.-N.; Luo, Z.-H.; Van Steenberge, P.H.M.; D'hooge, D.R. Coupled matrix kinetic Monte Carlo simulations applied for advanced understanding of polymer grafting kinetics. *React. Chem. Eng.* **2021**, *6*, 640–661, doi:10.1039/D0RE00407C.
119. Wang, L.; Broadbelt, L.J. Kinetics of segment formation in nitroxide-mediated controlled radical polymerization: comparison with classic theory. *Macromolecules* **2010**, *43*, 2228–2235, doi:10.1021/ma9019703.
120. Ali Parsa, M.; Kozhan, I.; Wulkow, M.; Hutchinson, R.A. Modeling of functional group distribution in copolymerization: A comparison of deterministic and stochastic approaches. *Macromol. Theory Simulations* **2014**, *23*, 207–217, doi:10.1002/mats.201300156.
121. Zhou, Y.N.; Luo, Z.H. State-of-the-Art and Progress in Method of Moments for the Model-Based Reversible-Deactivation Radical Polymerization. *Macromol. React. Eng.* **2016**, *10*, 516–534, doi:10.1002/mren.201500080.
122. Mastan, E.; Li, X.; Zhu, S. Modeling and theoretical development in controlled radical polymerization. *Prog. Polym. Sci.* **2015**, *45*, 71–101, doi:10.1016/j.progpolymsci.2014.12.003.
123. Van Steenberge, P.H.M.; Sedlacek, O.; Hernández-Ortiz, J.C.; Verbraeken, B.; Reyniers, M.F.; Hoogenboom, R.; D'hooge, D.R. Visualization and design of the functional group distribution during statistical copolymerization. *Nat. Commun.* **2019**, *10*, 1–14, doi:10.1038/s41467-019-11368-6.
124. Al-Harthi, M.A.; Masihullah, J.K.; Abbasi, S.H.; Soares, J.B.P. Dynamic Monte Carlo simulation of ATRP in a batch reactor. *Macromol. Theory Simulations* **2009**, *18*, 307–316, doi:10.1002/mats.200900001.
125. Ballard, N.; Hamzehlou, S.; Ruipérez, F.; Asua, J.M. On the Termination Mechanism in the Radical Polymerization of Acrylates. *Macromol. Rapid Commun.* **2016**, *37*, 1364–1368, doi:10.1002/marc.201600278.
126. Van Steenberge, P.H.M.; Hutchinson, R.A. Design of 2-hydroxyethyl methacrylate-functional macromonomer dispersants by semi-batch cobalt chain transfer polymerization. *AIChE J.* **2019**, *65*, doi:10.1002/aic.16723.
127. D'hooge, D.R. In Silico Tracking of Individual Species Accelerating Progress in Macromolecular Engineering and Design. *Macromol. Rapid Commun.* **2018**, *39*, 1–5, doi:10.1002/marc.201800057.
128. Pladis, P.; Baltsas, A.; Kiparissides, C. A Comprehensive Model for the Simulation of Ethylene Decomposition in High-Pressure LDPE Autoclaves. In *Computer Aided Chemical Engineering*; Elsevier Masson SAS, 2017; Vol. 40, pp. 337–342 ISBN 9780444639653.
129. Edeleva, M.; Van Steenberge, P.H.M.; Sabbe, M.K.; D'hooge, D.R.

Connecting gas-phase computational chemistry to condensed phase kinetic modeling: The state-of-the-art. *Polymers (Basel).* **2021**, *13*, 1–39, doi:10.3390/polym13183027.

130. De Smit, K.; Edeleva, M.; Trigilio, A.D.; Marien, Y.W.; Van Steenberge, P.H.M.; D'hooge, D.R. Kinetic Monte Carlo residence time distributions and kinetics in view of extrusion-based polymer modification and recycling. *React. Chem. Eng.* **2023**, doi:10.1039/D2RE00387B.
131. Rex, I.; Graham, B.A.; Thompson, M.R. Studying single-pass degradation of a high-density polyethylene in an injection molding process. *Polym. Degrad. Stab.* **2005**, *90*, 136–146, doi:10.1016/j.polymdegradstab.2005.03.002.
132. Zatloukal, M.; Muras, J.; Šimek, L. Influence of the repeated extrusion on the degradation of polyethylene . Structural changes in low density polyethylene. **2008**, *44*, 2652–2658, doi:10.1016/j.eurpolymj.2008.05.028.
133. Dealy, J.M.; Larson, R.G. *Structure and Rheology of Molten Polymers*; Carl Hanser Verlag GmbH & Co. KG: München, 2006; ISBN 978-3-446-21771-3.
134. Malkin, A.Y.; Kulichikhin, S.G. Rheokinetics of free-radical polymerization. *Polymer (Guildf).* **1984**, *25*, 778–784, doi:10.1016/0032-3861(84)90006-5.
135. Malkin, A.Y. Rheology in polymerization processes. *Polym. Eng. Sci.* **1980**, *20*, 1035–1044, doi:10.1002/pen.760201509.
136. Aulagner, P.; Ainser, A.; Carrot, C.; Guillet, J. Free radical degradation of polypropylene in the bulk: Coupling of kinetic and rheological models. *J. Polym. Eng.* **2000**, *20*, 381–401, doi:10.1515/POLYENG.2000.20.5.381.
137. Berzin, F.; Vergnes, B.; Delamare, L. Rheological behavior of controlled-rheology polypropylenes obtained by peroxide-promoted degradation during extrusion: Comparison between homopolymer and copolymer. *J. Appl. Polym. Sci.* **2001**, *80*, 1243–1252, doi:10.1002/app.1210.
138. Tuminello, W.H.; Treat, T.A.; English, A.D. Poly(tetrafluoroethylene): Molecular Weight Distributions and Chain Stiffness. *Macromolecules* **1988**, *21*, 2606–2610, doi:10.1021/ma00186a050.
139. Tuminello, W.H. Molecular weight distributions of tetrafluoroethylene-hexafluoropropylene copolymers. *Polym. Eng. Sci.* **1989**, *29*, 645–653, doi:10.1002/pen.760291006.
140. Ponnamma, D.; Rouxel, D.; Thomas, S. Spectroscopy—introducing the advantages and application areas in polymer nanocomposites. In *Spectroscopy of Polymer Nanocomposites*; Elsevier, 2016; pp. 1–14 ISBN 9780323401838.
141. Mylläri, V.; Ruoko, T.P.; Syrjälä, S. A comparison of rheology and FTIR in the study of polypropylene and polystyrene photodegradation. *J. Appl. Polym. Sci.* **2015**, *132*, 1–6, doi:10.1002/app.42246.
142. Scheirs, J. *Compositional and Failure Analysis of Polymers: A Practical Approach*; John Wiley & Sons: Chichester, UK, 2000;
143. Guo, X.; Lin, Z.; Wang, Y.; He, Z.; Wang, M.; Jin, G. In-line monitoring the degradation of polypropylene under multiple extrusions based on Raman spectroscopy. *Polymers (Basel).* **2019**, *11*, 1–11, doi:10.3390/polym11101698.
144. Zhao, J.; Yang, R.; Iervolino, R.; Barbera, S. Changes of chemical structure and mechanical property levels during thermo-oxidative aging of NBR. *Rubber Chem. Technol.* **2013**, *86*, 591–603, doi:10.5254/RCT.13.87969.
145. Harris, D.J.; Assink, R.A.; Gillen, K.T. 1H T2-NMR monitoring of

crosslinked polyolefin aging. *J. Appl. Polym. Sci.* **2003**, *90*, 2578–2582, doi:10.1002/app.12872.

146. Hoshino, A.; Tsuji, M.; Fukuda, K.; Nonagase, M.; Sawada, H.; Kimura, M. Changes in molecular structure of biodegradable plastics during degradation in soils estimated by FT-IR and NMR. *Soil Sci. Plant Nutr.* **2002**, *48*, 469–473, doi:10.1080/00380768.2002.10409228.
147. Vaillant, D.; Lacoste, J.; Dauphin, G. The oxidation mechanism of polypropylene: contribution of 13C-NMR spectroscopy. *Polym. Degrad. Stab.* **1994**, *45*, 355–360, doi:10.1016/0141-3910(94)90205-4.
148. Celina, M.C.; Linde, E.; Martinez, E. Carbonyl Identification and Quantification Uncertainties for Oxidative Polymer Degradation. *Polym. Degrad. Stab.* **2021**, *188*, 109550, doi:10.1016/j.polymdegradstab.2021.109550.
149. Cheng, H.N.; English, A.D. Advances in the NMR Spectroscopy of Polymers: An Overview. In *ACS Symposium Series*; 2002; Vol. 834, pp. 3–20.
150. Miyoshi, T. Characterization of polymers by NMR. In *Molecular Characterization of Polymers*; Elsevier, 2021; pp. 409–440 ISBN 9780128197684.
151. Cáceres, C.A.; Zborowski, L.; Canevarolo, S.V. Thermo-mechanical degradation and VOC emission of unstabilized and stabilized polypropylene copolymer during multiple extrusions. *Mater. Res.* **2011**, *14*, 569–575, doi:10.1590/S1516-14392011005000081.
152. Bai, X.; Isaac, D.H.; Smith, K. Reprocessing acrylonitrile–butadiene–styrene plastics: Structure–property relationships. *Polym. Eng. Sci.* **2007**, *47*, 120–130, doi:10.1002/pen.20681.
153. Chatterjee, N.; Basu, S.; Palit, S.K.; Maiti, M.M. An XRD characterization of the thermal degradation of polyacrylonitrile. *J. Polym. Sci. Part B Polym. Phys.* **1995**, *33*, 1705–1712, doi:10.1002/polb.1995.090331201.
154. Vonka, M.; Kosek, J. Modelling the morphology evolution of polymer materials undergoing phase separation. *Chem. Eng. J.* **2012**, *207–208*, 895–905, doi:10.1016/j.cej.2012.06.091.
155. Rimez, B.; Rahier, H.; Assche, G. Van; Artoos, T.; Biesemans, M.; Mele, B. Van The thermal degradation of poly (vinyl acetate) and poly (ethylene- co -vinyl acetate), Part I : Experimental study of the degradation mechanism. *Polym. Degrad. Stab.* **2008**, *93*, 800–810, doi:10.1016/j.polymdegradstab.2008.01.010.
156. Thébault, M.; Pizzi, A.; Essawy, H.A.; Barhoum, A.; Van Assche, G. Isocyanate free condensed tannin-based polyurethanes. *Eur. Polym. J.* **2015**, *67*, 513–526, doi:10.1016/j.eurpolymj.2014.10.022.
157. Howell, B.A.; Cui, Y.; Priddy, D.B. Assessment of the thermal degradation characteristics of isomeric poly(styrene)s using TG, TG/MS and TG/GC/MS. *Thermochim. Acta* **2003**, *396*, 167–177, doi:10.1016/S0040-6031(02)00522-1.
158. Jouan, X.; Gardette, J.L. Photo-oxidation of ABS: Part 2-Origin of the photodiscoloration on irradiation at long wavelengths. *Polym. Degrad. Stab.* **1992**, *36*, 91–96, doi:10.1016/0141-3910(92)90054-9.
159. Wang, Y.; Steinhoff, B.; Brinkmann, C.; Alig, I. In-line monitoring of the thermal degradation of poly(l-lactic acid) during melt extrusion by UV-vis spectroscopy. *Polymer (Guildf).* **2008**, *49*, 1257–1265, doi:10.1016/j.polymer.2008.01.010.

160. Fiorio, R.; Díez, S.V.; Sánchez, A.; D'hooge, D.R.; Cardon, L. Influence of different stabilization systems and multiple ultraviolet a (UVA) aging/recycling steps on physicochemical, mechanical, colorimetric, and thermal-oxidative properties of ABS. *Materials (Basel).* **2020**, *13*, doi:10.3390/ma13010212.
161. Diaz, C.M.; Gao, X.; Robisson, A.; Amarante, M.; Zhu, S.S. Effect of hydrolytic degradation on the mechanical property of a thermoplastic polyether ester elastomer. *Polym. Degrad. Stab.* **2018**, *155*, 35–42, doi:10.1016/j.polymdegradstab.2018.07.002.
162. Maïza, S.; Lefebvre, X.; Brusselle-Dupend, N.; Klopffer, M.H.; Cangémi, L.; Castagnet, S.; Grandidier, J.C. Physicochemical and mechanical degradation of polyamide 11 induced by hydrolysis and thermal aging. *J. Appl. Polym. Sci.* **2019**, *136*, 1–10, doi:10.1002/app.47628.
163. Hurley, C.R.; Leggett, G.J. Quantitative investigation of the photodegradation of polyethylene terephthalate film by friction force microscopy, contact-angle goniometry, and X-ray photoelectron spectroscopy. *ACS Appl. Mater. Interfaces* **2009**, *1*, 1688–1697, doi:10.1021/am900250q.
164. Hernández-Fernández, J.; Rayón, E.; López, J.; Arrieta, M.P. Enhancing the Thermal Stability of Polypropylene by Blending with Low Amounts of Natural Antioxidants. *Macromol. Mater. Eng.* **2019**, *304*, 1–13, doi:10.1002/mame.201900379.
165. Taubner, V.; Shishoo, R. Influence of processing parameters on the degradation of poly(L-lactide) during extrusion. *J. Appl. Polym. Sci.* **2001**, *79*, 2128–2135, doi:10.1002/1097-4628(20010321)79:12<2128::AID-APP1020>3.0.CO;2-%23.
166. Mysiukiewicz, O.; Barczewski, M.; Skórczewska, K.; Matykiewicz, D. Correlation between processing parameters and degradation of different polylactide grades during twin-screw extrusion. *Polymers (Basel).* **2020**, *12*, doi:10.3390/POLYM12061333.
167. Aldhafeeri, T.; Alotaibi, M.; Barry, C.F. Impact of Melt Processing Conditions on the Degradation of Polylactic Acid. **2022**.
168. Oliveira, M.; Santos, E.; Araújo, A.; Fechine, G.J.M.; Machado, A. V.; Botelho, G. The role of shear and stabilizer on PLA degradation. *Polym. Test.* **2016**, *51*, 109–116, doi:10.1016/j.polymertesting.2016.03.005.
169. Silva Spinacé, M.A.; De Paoli, M.A. Characterization of poly(ethylene terephthalate) after multiple processing cycles. *J. Appl. Polym. Sci.* **2001**, *80*, 20–25, doi:10.1002/1097-4628(20010404)80:1<20::AID-APP1069>3.0.CO;2-S.
170. Al-AbdulRazzak, S.; Jabarin, S.A. Processing characteristics of poly(ethylene terephthalate): Hydrolytic and thermal degradation. *Polym. Int.* **2002**, *51*, 164–173, doi:10.1002/pi.813.
171. Whitlock, L.R.; Porter, R.S. The source of degradation during extrusion of polystyrene. *J. Appl. Polym. Sci.* **1973**, *17*, 2761–2770, doi:10.1002/app.1973.070170913.
172. La Mantia, F.P.; Valenza, A. Long-term thermomechanical degradation of molten polystyrene. *Polym. Degrad. Stab.* **1985**, *13*, 105–111, doi:10.1016/0141-3910(85)90059-X.
173. Farahanchi, A.; Malloy, R.; Sobkowicz, M.J. Effects of ultrahigh speed twin screw extrusion on the thermal and mechanical degradation of polystyrene. *Polym. Eng. Sci.* **2016**, *56*, 743–751, doi:10.1002/pen.24301.

174. Karahaliou, E.-K.; Tarantili, P.A. Stability of ABS compounds subjected to repeated cycles of extrusion processing. *Polym. Eng. Sci.* **2009**, *49*, 2269–2275, doi:10.1002/pen.21480.
175. Boldizar, A.; Möller, K. Degradation of ABS during repeated processing and accelerated ageing. *Polym. Degrad. Stab.* **2003**, *81*, 359–366, doi:10.1016/S0141-3910(03)00107-1.
176. Salari, D.; Ranjbar, H. Study on the Recycling of ABS Resins: Simulation of Reprocessing and Thermo-oxidation. *Iran. Polym. J.* **2008**, *17*, 599–610.
177. Kalfoglou, N.K.; Chaffey, C.E. Effects of extrusion on the structure and properties of high-impact polystyrene. *Polym. Eng. Sci.* **1979**, *19*, 552–557, doi:10.1002/pen.760190805.
178. Vilaplana, F.; Ribes-Greus, A.; Karlsson, S. Degradation of recycled high-impact polystyrene. Simulation by reprocessing and thermo-oxidation. *Polym. Degrad. Stab.* **2006**, *91*, 2163–2170, doi:10.1016/j.polymdegradstab.2006.01.007.
179. Parres, F.; Crespo, J.E. Degradation of high-impact polystyrene with processing and its recovery via the addition of styrene-butadiene rubber and styrene-ethylene-butylene-styrene block copolymer. *J. Appl. Polym. Sci.* **2011**, *121*, 574–581, doi:10.1002/app.33625.
180. Hinsken, H.; Moss, S.; Pauquet, J.; Zweifela, H. Degradation of Polyolefins during Melt Processing. **1991**, *34*, 279–293.
181. Da Costa, H.M.; Ramos, V.D.; Rocha, M.C.G. Rheological properties of polypropylene during multiple extrusion. *Polym. Test.* **2005**, *24*, 86–93, doi:10.1016/j.polymertesting.2004.06.006.
182. Canevarolo, S. V.; Babetto, A.C. Effect of screw element type in degradation of polypropylene upon multiple extrusions. *Adv. Polym. Technol.* **2002**, *21*, 243–249, doi:10.1002/adv.10028.
183. da Costa, H.M.; Ramos, V.D.; de Oliveira, M.G. Degradation of polypropylene (PP) during multiple extrusions: Thermal analysis, mechanical properties and analysis of variance. *Polym. Test.* **2007**, *26*, 676–684, doi:10.1016/j.polymertesting.2007.04.003.
184. Moss, S.; Zweifel, H. Degradation and stabilization of high density polyethylene during multiple extrusions. *Polym. Degrad. Stab.* **1989**, *25*, 217–245, doi:10.1016/S0141-3910(89)81009-2.
185. Jagenteufel, R.; Hofstaetter, T.; Kamleitner, F.; B. Pedersen, D.; Tosello, G.; N. Hansen, H. Rheology of high melt strength polypropylene for additive manufacturing. *Adv. Mater. Lett.* **2017**, *8*, 712–716, doi:10.5185/amlett.2017.1450.
186. Wojtyła, S.; Klama, P.; Baran, T. Is 3D printing safe? Analysis of the thermal treatment of thermoplastics: ABS, PLA, PET, and nylon. *J. Occup. Environ. Hyg.* **2017**, *14*, D80–D85, doi:10.1080/15459624.2017.1285489.
187. Fernandez, E.; Ceretti, D.A.; Wang, S.; Jiang, Y.; Zhang, J.; D'hooge, D.R.; Cardon, L. Fused filament fabrication of copolyesters by understanding the balance of inter- and intra-layer welding. *Plast. Rubber Compos.* **2020**, *0*, 1–7, doi:10.1080/14658011.2020.1855386.
188. Gao, X.; Qi, S.; Kuang, X.; Su, Y.; Li, J.; Wang, D. Fused filament fabrication of polymer materials: A review of interlayer bond. *Addit. Manuf.* **2021**, *37*, 101658, doi:10.1016/j.addma.2020.101658.
189. Bakrani Balani, S.; Chabert, F.; Nassiet, V.; Cantarel, A. Influence of printing parameters on the stability of deposited beads in fused filament fabrication of

poly(lactic) acid. *Addit. Manuf.* **2019**, *25*, 112–121, doi:10.1016/j.addma.2018.10.012.

190. Costa, A.E.; Ferreira da Silva, A.; Sousa Carneiro, O. A study on extruded filament bonding in fused filament fabrication. *Rapid Prototyp. J.* **2019**, *25*, 555–565, doi:10.1108/RPJ-03-2018-0062.
191. Spoerk, M.; Arbeiter, F.; Raguž, I.; Holzer, C.; Gonzalez-Gutierrez, J. Mechanical recyclability of polypropylene composites produced by material extrusion-based additive manufacturing. *Polymers (Basel).* **2019**, *11*, doi:10.3390/polym11081318.
192. Ahlinder, A.; Fuoco, T.; Morales-López, Á.; Yassin, M.A.; Mustafa, K.; Finne-Wistrand, A. Nondegradative additive manufacturing of medical grade copolyesters of high molecular weight and with varied elastic response. *J. Appl. Polym. Sci.* **2020**, *137*, 18–20, doi:10.1002/app.48550.
193. Gradwohl, M.; Chai, F.; Payen, J.; Guerreschi, P.; Marchetti, P.; Blanchemain, N. Effects of two melt extrusion based additive manufacturing technologies and common sterilization methods on the properties of a medical grade PLGA copolymer. *Polymers (Basel).* **2021**, *13*, 1–15, doi:10.3390/polym13040572.
194. Lee, H.; Yoo, J.J.; Kang, H.W.; Cho, D.W. Investigation of thermal degradation with extrusion-based dispensing modules for 3D bioprinting technology. *Biofabrication* **2016**, *8*, doi:10.1088/1758-5090/8/1/015011.
195. La Gala, A.; Ceretti, D.V.A.; Fiorio, R.; Cardon, L.; D'hooge, D.R. Comparing pellet- and filament-based additive manufacturing with conventional processing for ABS and PLA parts. *J. Appl. Polym. Sci.* **2022**, *139*, 1–14, doi:10.1002/app.53089.

Chapter 3

Rheology of polystyrene melts undergoing thermal degradation: a step towards structural rheokinetic modeling

3. 1. Abstract

An important aspect of polymer degradation during processing is the understanding and description of the rheological behavior of polymer melts undergoing degradation. In this chapter, we give a step towards a structural rheokinetic modeling approach to model this process by assessing the thermal degradation of commercial polystyrene (PS) melts. To do so, appropriate conditions for the rheological testing of virgin and aged polystyrene are first defined. This is followed by the estimation of a group of parameters for the model validation. Specifically, based on time sweep measurements and size-exclusion chromatography (SEC), the parameter regarding the irreversible progress function is determined. A second set of parameters are estimated by fitting the flow curves of virgin and aged samples to the Carreau-Yasuda equation. In addition, the nonlinear viscoelastic behavior of the samples is measured, indicating the common overshoot in the transient response of viscosity during constant shear rate tests. Furthermore, following the overshoot, the aged sample presents also an undershoot on the curves. This is attributed to the *tumbling* effect, and it is for the first time reported for aged polymer melts. The estimation of model parameters based on the nonlinear viscoelastic behavior of the samples are currently in progress. The

modeling part of this chapter is performed in collaboration with Professor Flávio H. Marchesini.

3. 2. Introduction

The degradation of thermoplastic polymers such as polyolefins, polyesters, and polystyrene (PS) results in irreversible changes of the macromolecular building blocks, described by the breakage or formation of covalent bonds, due to chain fission or chain branching and crosslinking reactions, respectively. In many cases, this relates to a negative deviation from the desired macroscopic properties, *e.g.* loss of mechanical strength, dielectric quality and aesthetic appearance [1,2]. The understanding and description of the rheological behavior of polymer melts undergoing degradation is crucial, since most processing pathways occur in the melt state with high temperatures at large deformation rates [3,4], with certain polymers characterized by a relatively low stability [5,6].

Rheometry has been widely used to experimentally study polymer degradation. One simple way to do so, is by comparing flow curves of virgin and degraded materials [7–10]. The obtained flow curves may be fitted to empirical equations such as the Carreau-Yasuda [11,12] or Cross equations [13]. Then, parameters including the power-law index (n) and the zero-shear viscosity η_0 may be obtained. By doing so, one can for instance, establish correlations between η_0 and the mass average molar mass (M_m), as discussed in Chapter 1. Frequency sweep tests have additionally been used to evaluate polymer degradation by associating the relaxation time to average molar masses [10,14,15]. Furthermore, time-resolved mechanical spectroscopy (TRMS) allowed the characterization of the dynamic properties of polymers undergoing structural changes [16]. In TRMS the material is probed repeatedly at a

single frequency for a defined number of scans and the viscoelastic properties are monitored as a function of time [16]. If a sufficiently larger set of single frequency data are tested, the rheological behavior of the material can be obtained for the whole frequency spectrum for a specific time. For instance, the degradation of polyamide (PA) 11 [17] and polyethylene terephthalate (PET) [18] under nitrogen and air have been studied through TRMS. The results reveal that different degradation mechanisms take place depending on the atmosphere employed in the test. Under N_2, an increase in the zero-frequency viscosity was tracked over ageing time, suggesting an increase in the molar mass due to post-condensation. Under air, the appearance of an apparent yield stress indicated that cross-linking happened. Furthermore, chain fission may take place, perceived by the decreased values of zero-frequency viscosity.

The polymer dynamics behavior has been described by rheological constitutive models [19], based either on the tube model, proposed by Doi and Edwards [20], or on continuum mechanics models [21]. Nevertheless, there is a lack of detailed rheological models that can properly predict the rheological behavior of polymers undergoing degradation, especially due to the complexity of this process. Such models should capture and predict all irreversible changes that the polymers may be subjected to at a given moment, which is related to the kinetics of the process. Irreversible changes, as relevant in the present work, are usually attributed to the formal formation or breakage of covalent bonds.

To specifically highlight the temporal variation of rheological macroscopic properties due to chemical reaction(s), in the modeling field, the term rheokinetics is utilized [22]. In its most basic format rheokinetics is only considered to establish correlations between the degree of overall conversion and (average) molar mass characteristics and then of the latter characteristics and rheological data (*e.g.* viscoelastic changes)

[23]. An example is provided in Figure 1a, in which time dependent polymerization conversion data for free radical polymerization (FRP) [22] are first used to determine kinetic parameters, based on a simplified kinetic scheme (initiator dissociation, chain initiation/propagation, and termination) and basic kinetic formulas (e.g. average kinetics). Then the model conversion predictions are linked to viscosity measurements through a second set of formulas (see η(α) and η(t) in Figure 1a). If Arrhenius equations are considered for the chemical kinetics, it is possible to predict temperature dependent rheokinetic curves, typically based on overall apparent activation energies, as shown at the bottom of Figure 1a.

In a more advanced rheokinetic modeling, a so-called constitutive model is considered that is linked with the (reaction) kinetics and ideally combined with mass, momentum and energy balance equations. This combination is done to fundamentally describe the variations in stresses and velocities for a polymer flow undergoing deformation in a given environment with certain temperature boundaries. Depending on the complexity of these constitutive equations one focuses either more on macroscopic or molecular rheological properties.

For example, Garcia-Sandoval *et al*. [24] have studied the inhomogeneous flow of micellar solutions using a kinetic theory based on transient network models. As shown in the top part of Figure 1b, four kinetics steps have been considered: (i) the formation (k_1^+) of (wormlike) chains (fraction *y*) out of small building blocks, which can be seen as "monomers" (fraction *x*), (ii) the reverse flow induced degradation (k_1^-), (iii) the formation of entanglements (k_2^+) and (iv) the flow induced breakage into unentangled chains (k_2^-). The reaction kinetics have been coupled to an upper-convected Maxwell constitutive model by acknowledging the dependences of modulus and relaxation time

on the concentration of each species type, which in turns is influenced by other parameters such as chemical potential, affinities, and viscous dissipation.

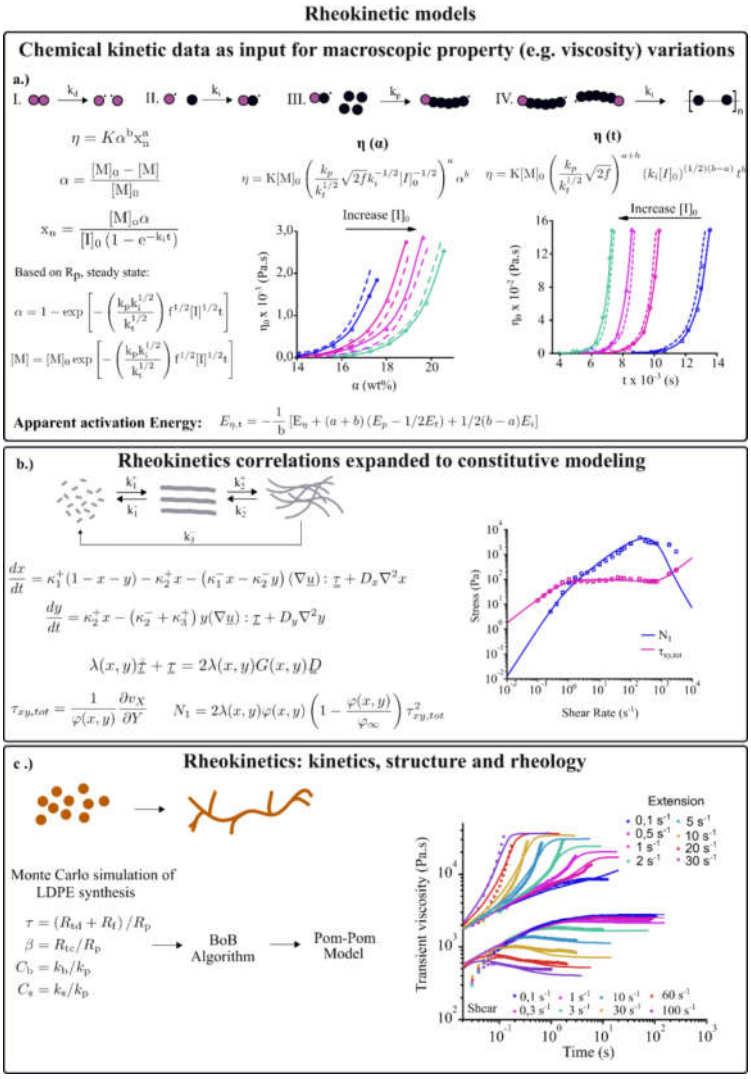

Figure 1: Three common approaches for rheokinetic modeling of polymers. Where: η: viscosity; K: constant; C: concentration of polymer being formed; N: number-average degree

of polymerization; a and b: constants that characterize the viscous properties of solutions; α: conversion; [M]: monomer concentration; $[M]_0$: initial monomer concentration; k_i, k_p, and k_t: rate constants of initiation, propagation and termination of the polymerization process; f: initiator efficiency; [I]: initiator concentration; t: time; $[I]_0$: initial concentration of initiator; $E_{\eta,t}$: apparent activation energy, fixed viscosity; E_η: activation energy of the viscous flow; E_i, E_p and E_t: activation energy of elementary reaction of initiation, propagation and termination; R_p: rate of propagation; x: fraction of short rod-like micelles that compose free wormlike chains; y: fraction of short rod-like micelles that compose entangled wormlike chains; λ: characteristic relaxation time as a function of x, y; G: moduli as a function of x,y; τ: contribution of free and entangled wormlike micelles to the stress tensor; D: deformation tensor; φ: fluidity (inverse of viscosity) as a function of x,y; φ_∞: fluidity of solvent and the short rod-like micelles; ∇u: gradient of velocity; u: velocity vector; D_x, D_y: mass diffusion coefficients; dx/dt, dy/dt : time evolutions of free and entangled wormlike chains, respectively; $\partial V_x/\partial Y$: shear rate; N_1: first normal stress difference; $\tau_{xy,tot}$: total shear stress; $\overset{\nabla}{\tau}$: upper-convected time derivative of stress tensor; κ_1^+, κ_2^+: kinetic constants related to the formation of chains and nodes; $\kappa_1^-, \kappa_2^-, \kappa_3^+$: kinetic constants related to structural modification by flow.

The constitutive model parameters have been obtained from SAOS and simple shear tests at steady state. These authors predicted the shear stress and first normal stress difference as a function of shear rate under banded flow conditions, as shown at the right side of Figure 1b. These simulation results have been accompanied by the prediction of other properties of the system, including fluidity, microstates fraction, birefringence and orientation angle as function of shear rate.

It should be stressed that Maxwell-like models do not fully grasp the true behavior of polymer material flows, as they are only able to describe certain nonlinear viscoelastic phenomena in a qualitative manner [19]. Such models can for instance not represent yield stress, neither separate thixotropic and fundamental viscoelastic behavior [25].

To avoid this one can *e.g.* consider the deterministic modeling of the (molecular) structure of the polymer, utilizing constitutive equations based on the tube model to predict both linear and nonlinear molecular scale driven rheological behavior throughout the polymerization process. For instance, Read *et al.* [26] have focused on the relationships between the structure and dynamics of highly branched PE (thus low density polyethylene; LDPE) as a function of the chemical kinetics of the polymerization process. More in detail, the polymerization kinetics and modeling structure was assessed using (conditional) Monte Carlo simulation, followed by the simulation of reptation and arm-retractions for the polymer ensemble. The full linear response was obtained using so-called "pom-pom" modes, which is based on tube physics. By doing so, the authors could describe the transient viscosity response to shear and extension at a constant rate, as shown in Figure 1c.

Another constitutive modeling approach is the so-called structural rheokinetic modeling. In structural rheokinetic models, the time effects are based on a constitutive equation in which the rheological parameters are a function of a single (average) structural parameter, λ_s [25]. This parameter characterizes the instantaneous structure of the materials. This type of approach has been used to model the rheological behavior of structured fluids, such as emulsions and suspensions, which present time-dependent rheological effects (e.g. thixotropy) and yield stress [25,27]. Under this framework, Marchesini *et al*. [28] proposed a structural rheokinetic model, which accounts for the prediction of both reversible and irreversible changes that materials may undergo, either related to build-up or breakdown of the material's structure. The irreversible processes are covered by irreversible progress functions ($\zeta(t)$), which describe the evolution of the irreversible processes (reactions) in place, being incorporated in the calculus of the structural parameter. These irreversible progress functions provide values between 0 and 1, indicating that the irreversible process has

not yet begun and that it has finished, respectively. In addition, the constitutive equation of the model is based on a modified Jeffreys mechanical analog. The model parameters are obtained by i.) describing the evolution of the irreversible process and fitting experimental data to the irreversible progress function, ii.) fitting the flow curves of samples at the initial and intermediate/final states of the irreversible process to the Carreau-Yasuda equation and iii.) fitting the transient response of viscosity in constant shear rate tests of samples at initial and intermediate/final states of the irreversible process to the model equations. Details on the model are given in Section A1 of Appendix A.

The model of Marchesini *et al.* [28] has already been successfully applied for the study of the flow of cement-based materials accounting for hydration reactions with a switch from a paste-like to a full solid material [28,29]. The relevance of this model is evidenced by the broadness of its possible applications, as it can be adjusted for different classes of materials, and it is able to predict thixotropy and structure build-up or breakage, with the latter being of the most importance in polymer degradation processes. Furthermore, in case of polymer melts undergoing degradation, by characterizing the initial (virgin) and final (aged) rheological response of the polymer, it would be possible to retrieve the rheological behavior of the material at intermediate states. Moreover, this modeling approach can be applied for polymers with different molecular properties, including different molar masses, dispersity, and architectures, as well as to detect other types of irreversible processes such as polymerization and branching.

In this chapter, we focus on the first stages of PS thermal degradation in the lower shear rates regime. A commercial PS prepared via free-radical polymerization (FRP) was chosen because it is the most produced type of PS industrially, as well as due to

its high importance in terms of application. The experimental protocol is designed to obtain the irreversible progress function and flow curve parameters. These parameters will be used for further validation of the structural rheokinetic model proposed by Marchesini *et al.* [28] for polymer melts undergoing thermal degradation. The experimental protocol is deliberately chosen to evaluate the rheokinetic model for which the conversion of degradation is not too high, but the irreversible breakdown of the material's structure due to the reduction of M_m and via chain fission is still sufficiently developed. In addition, constant shear rate tests are performed and the overshoot and undershoot effects are discussed.

3. 3. Materials and methods

3. 3. 1. Materials

A commercial polystyrene (PS) prepared via free radical polymerization was purchased from Sigma Aldrich in the shape of pellets, with a mass average molar mass (M_m) of 232 kg mol^{-1} and a dispersity of 1.8, as measured by size exclusion chromatography (SEC) analysis. In general, PS-x means the PS sample has been aged *x* minutes vs. the virgin sample (PS-0).

3. 3. 2. Characterization

Thermogravimetry (TGA)

The degradation of PS under nitrogen atmosphere was investigated in a Netzsch Simultaneous thermal analysis (STA 449 F3 Jupiter) equipment in the TGA mode. Isothermal runs were performed at 220, 250, 280, and 310 °C for 240 min. The mass loss curves were used to choose the conditions in which the rheological tests should

be carried out to enable reliable rheological data recording. As will be explained in the Results and Discussion, a maximal temperature of 250 °C is recommended in the scope of the present study.

Overall/apparent activation energy values for the degradation process were obtained by means of the Ozawa/Flynn/Wall isoconversional method, as described in ASTM 1641 [30]. Dynamic tests were performed from 30 to 600 °C, with heating rates of 5, 10, 15 and 20 °C min^{-1} for virgin and aged samples.

Parallel plate rheometry

A rheometer (MCR 702, Anton-Paar) was used with the parallel plate configuration with 25 mm of diameter and 1 mm gap to carry out the rheological measurements. The experiments were designed to study the behavior of the material after 0 and 240 min of exposure to 250 °C. Flow curves were obtained from constant shear rate measurements, in a shear rate range from 0,01 to 10 s^{-1}. The Cox-Merz rule [31] was used to expand the range of shear rate by means of frequency sweep tests from 10 to 6.10^2 rad s^{-1}, with 1% of strain amplitude. Changes of storage modulus (G'), loss modulus (G'') and complex viscosity (η^*) were also monitored as a function of time for 240 min at 250 °C via time sweep measurements. Furthermore, frequency sweep tests from 0.1 to 6.10^2 rad s^{-1} were carried out at 190, 200, 220 and 250 °C, after ageing times of 0 and 240 min for each temperature. Time-temperature superposition was carried out to obtain master curves at a reference temperature of 250 °C for both ageing conditions.

The samples were prepared in a disk-like shape with 1 mm thickness and 25 mm diameter via compression molding at 200 °C, using a hot press. The pellets were pre-heated for 5 min and then compression molded for 5 min. They were cooled under

environmental conditions. A fresh specimen was used for each measurement. The tests were carried out under nitrogen atmosphere. Each measurement was performed at least three times and the results are represented by the mean values with standard deviation.

Size exclusion chromatography

Absolute average molar masses and the molar mass distribution (MMD) of PS degraded under nitrogen atmosphere for different times (0, 30, 60, 120 and 240 min) were determined at 40 °C with a PL GPC50Plus, equipped with three mixed PL gel columns. PS samples were solubilized in tetrahydrofuran (THF), which was used as an eluent at a flow rate of 1.0 mL min^{-1}.

3. 4. Results and discussion

3. 4. 1. Identification of optimal temperature for rheological analysis via TGA

Accurately monitoring the isothermal degradation process of polymers via parallel plate rheometry presents experimental challenges. First of all, the specimen should not be subjected to any change of state (*i.e.* liquid to gas) and if there is a reduction of the sample thickness the gap must be adjusted, otherwise the measurement is no longer accurate. Also, the specimen cannot undergo dripping out of the plates and no bubbles should be present inside the specimen.

Bearing these experimental constraints in mind, TGA has been employed to assist on the determination of the degradation temperature and time for the rheological testing. The mass losses over time plots under isothermal conditions at 220, 250, 280, and 310

°C are shown in Figure 2a. The degradation behavior of PS at 220 and 250 °C proceeds in a very similar fashion, both exhibiting a low degradation rate, with after 240 min only reaching a mass loss decrease of 0,4 and 1% respectively. This contrasts with the behavior at higher temperatures of 280 and 310 °C, which reached already 1% of mass loss after 73 and 35 min, respectively.

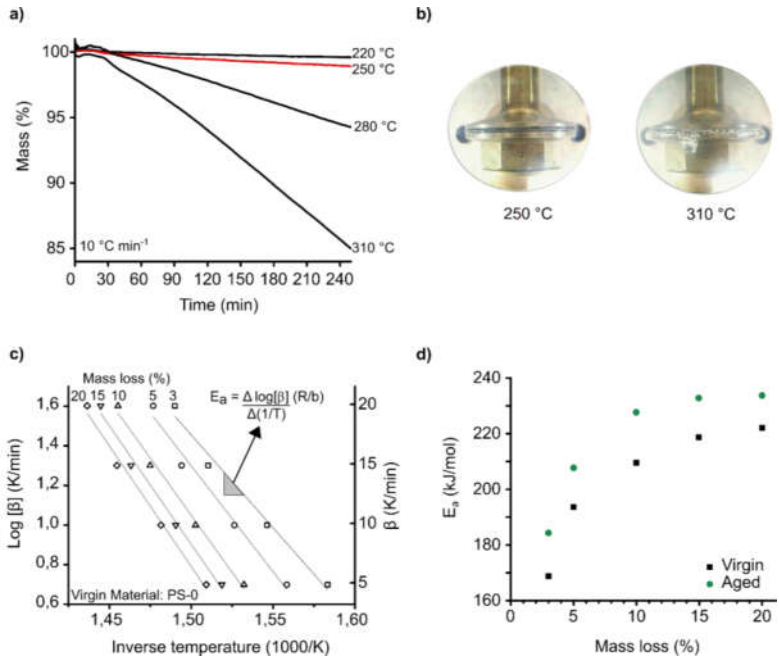

Figure 2: Isothermal degradation behavior of polystyrene (PS) toward identification of optimal rheological analysis temperature. a) isothermal mass loss curves at different temperatures (optimal temperature in red), b) parallel plate rheometry specimen at two temperatures (the optimal one and a non-suited one), c) isoconversional approach for calculating apparent activation energies (PS-0), d) apparent activation energy of PS-0 and PS-240.

To interpret these results properly, we must recall that in this research a free radical polymerized PS was used. The main chemical principles behind its synthesis and thermal degradation have been extensively studied [32–35]. PS prepared via FRP has a relatively lower thermal stability than anionic polymerized PS, specially due to the presence of weaker bonds that lead to earlier molar mass reduction [36]. Therefore, already at lower degradation temperatures (e.g. 220 °C), one can expect a decrease of the average molar mass without significant formation of volatiles. Under such conditions the main degradation mechanism is related to weak links formed during the radical polymerization process, such as head-to-head linkages [37]. At higher degradation temperatures (e.g. 280 °C), there is still a negligible formation of volatiles but there are also more regular degradation initiation pathways (like for the anionic product). In contrast, McNeil *et al.* [33] put forward that above 300 °C PS quickly degrades (or unzips) to monomers, dimers, trimers and other compounds, such as toluene. In other words, there is likely a transition temperature window from more polymer degradation to full depolymerization.

It is thus likely that a too high temperature is not suited for rheological analysis. The general state of the specimen in the rheometer at 250 and 310 °C has thus been compared, as highlighted in Figure 2b. At 310 °C, the specimen drips out of the plates and exhibits a high contribution of bubbles, indicating that at this temperature appropriate rheological testing cannot be performed, whereas at 250 °C the specimen meets all the criteria for the rheological testing. In addition, a too decreased viscosity hinders conventional rheometry testing of PS at higher temperatures for long times, as the specimen conditions must be kept (rather) constant throughout the measurements. With this in mind, it has been decided to track in what follows only the isothermal degradation of PS by means of rheometry (and other techniques) at the

temperature of 250 °C, for times ranging from 0 min to 240 min so that PS experiences around 1% of (TGA) mass loss.

In addition, we calculate the apparent activation energy for the degradation of the samples studied, according to the Osawa/Flynn/Wall method. This method is a model-free (isoconversional) method of kinetic analysis calculating dependence of activation energy E_a on degree of conversion (α) for dynamic experiments with different constant heating rates β. Practically, isoconversional methods can be used to determine E_a variations accurately in a simple way [38–42]. The overall conversion derivative (dα/dt) in the solid/molten state can be formally described by Equation (1) [38]:

$$d\alpha/dt = k(T)\, f(\alpha), \qquad (1)$$

in which f(α) is a function of conversion and depends on the mechanism and k is an apparent (overall/apparent) kinetic coefficient assumed to follow the Arrhenius equation (Equation (2)):

$$k(T) = A.\exp(-E_a/RT), \qquad (2)$$

in which A corresponds to the overall pre-exponential factor and, E_a is the overall activation energy, R is the gas constant, and T is the absolute temperature. Isoconversional methods assume that the conversion function f(α) does not change with the variation of the heating rate (β) for all values of conversion (α). Therefore, by carrying out experiments at different heating rates, the temperatures at fixed values of conversion can be measured, and the apparent activation energies obtained. Figure 2c shows the raw data for the application of the Ozawa/Flynn/Wall method considering PS-0. The values of the associated apparent activation energies are plotted in Figure 2d, with for comparison also the data for PS-240 (with the raw data shown in Figure A1 of Appendix A). For both cases an increase in activation energy is

monitored with mass loss. A closer inspection reveals that there is a slight difference between the activation energies of PS-0 and PS-240, with the PS-240 (apparent) activation energies higher than those for PS-0. This confirms that aging leads already to degradation. Notably for PS-0 the behavior and range of activation energies is in agreement with literature data [43].

3. 4. 2. Linking size exclusion chromatography with rheological behavior at 250 °C

An important aspect of the model being validated is that the degradation parameters for the irreversible progress function are obtained from experiments. To properly describe these irreversible processes under certain flow conditions it is crucial to at least obtain information regarding the evolution of the irreversible process. As shown by de Miranda et al. [29] when studying hydration of cements, this can be done for instance by means of calorimetric study, in which the dimensionless cumulative heat is used to obtain parameters of the irreversible processes. In addition, this can be carried out by means of a chemical kinetic study using any technique suitable to monitor the reaction progress. For thermoplastics, a combination of chromatography and rheological experiments can be employed to obtain the required information.

Therefore, after determining the stable isothermal conditions for the rheological study of PS degradation, time sweep tests were carried out at 250 °C to investigate the behavior of G' and G'' over time (frequency of 1 Hz or 6.28 rad s^{-1}). As shown in Figure 3a, both G' and G'' decrease over time. After 240 min, G' reduces by 22% and G'' by 15%. SEC traces for samples degraded up to different times indicate a similar trend for the MMD, as shown in Figure 3b. Specifically, a reduction of 21% in M_m of PS after 240 min of degradation is registered. The results obtained via SEC thus

suggest that the recorded behavior of G' and G'' during time sweep tests is closely related to the structural breakdown of the material, induced by thermal degradation.

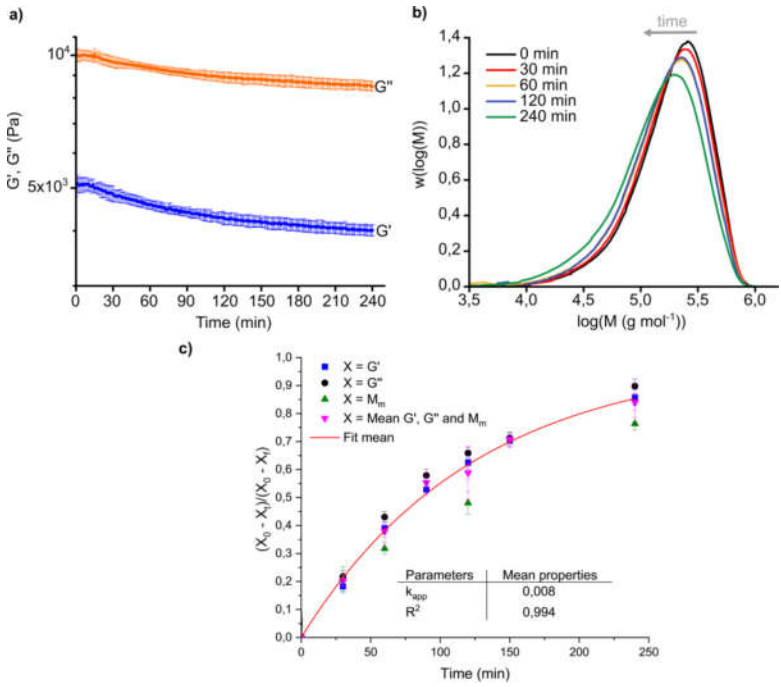

Figure 3: a) Storage and loss modulus (G' and G'') obtained via time sweep tests at 250 °C up to 240 min (frequency of 1 Hz), b) size exclusion chromatography (SEC) traces of polystyrene (PS) degraded for 0, 30, 60, 120 and 240 min at 250 °C. c) Correlation of G', G'' and M_m, all in dimensionless format (the red line represents the average curve fitting to Equation 3).

For the thermal degradation of polystyrene, we assume a first-order kinetic process, as already broadly reported for PS degradation [44–48]. A first-order kinetic process reflects intramolecular transfer and random chain fission of the main chain [49], which is the case in this work, due to the conditions chosen (i.e. range of conversion at the selected time and temperature and material selection). Following this assumption, ,

the thermal degradation process can be described by the irreversible progress function (Equation 3):

$$\zeta(t) = 1 - e^{(-K_{app}.t)}, \quad (3)$$

in which ζ(t) is the irreversible progress function, K_{app} is the apparent rate constant and t is the time.

To obtain the parameter of the irreversible progress function (Equation (3)), dimensionless G', G'' and M_m values have been calculated, according to Equation (4):

$$Y = \frac{X_0 - X_t}{X_0 - X_{final}}, \quad (4)$$

in which Y is the property being put in the dimensionless format (G', G'' or M_m), X_0 represents their value at initial time, X_t represents their value at time t and X_{final} represents their value when the irreversible process is concluded. Considering that the maximum ageing time studied here is 240 min, by using X_{final} it is possible to define the intermediate values of the conversion at 240 min. The values of X_{final} for each property was defined by fitting the dimensional data for each one of the properties to Equation 3.

After calculating the dimensionless values for *G'*, *G''* and M_m, (blue, black and green points, respectively, in Figure 3c) they were averaged (pink points in Figure 3c) and fitted to Equation 3. The fitting curve of the averaged dimensionless G', G'' and M_m is also shown in Figure 3c.

It is interesting to note that the average fitting curve describes reasonably well the three properties assessed. This indicates that a proper link between rheological properties and the mass average molar mass evolution may be established. As

previously mentioned, this is of enormous importance for the structural rheokinetic modelling approach used here, which relies on the experimental description of the evolution of the irreversible process. As an output of the fitting procedure, the parameter K_{app}, which describes the apparent constant rate of degradation reaction has been estimated to be 8 x 10^{-3} min^{-1}.

3. 4. 3. Linear viscoelastic characterization and flow curves at 0 and 240 min of degradation

The characterization of the linear viscoelastic behavior of both PS-0 and P-240 was made by means of frequency sweep tests as well, covering frequencies between 10^{-1} and 6.10^{2} rad s^{-1}. Figure 4a displays G' and G'' as a function of the angular frequency for PS-0 and PS-240. It follows that G' and G'' values for PS-0 are higher than those for PS-240 throughout the entire range of frequencies, as expected due to a higher M_m. Even though the variation is not big, it is important to recall that in this study very low conversion values of degradation (i.e. ~1%) are being assessed. The relaxation time calculated as the inverse of the crossover frequency ($G' = G''$) is 0.1 and 0.08 s, for PS-0 and PS-240, respectively. The relaxation time is proportional to the average molar mass of the material so that it is again confirmed that PS-240 exhibits a reduced average molar mass. Figure 4b shows the master curves for the virgin and aged PS reduced to 250 °C, while Figure 4c shows the dependence of the shift factors with the temperature. It is possible to see that the effects of degradation become only apparent in the master curves at lower reduced frequencies (high temperatures) as at higher reduced frequencies (lower temperatures) the degradation is less pronounced.

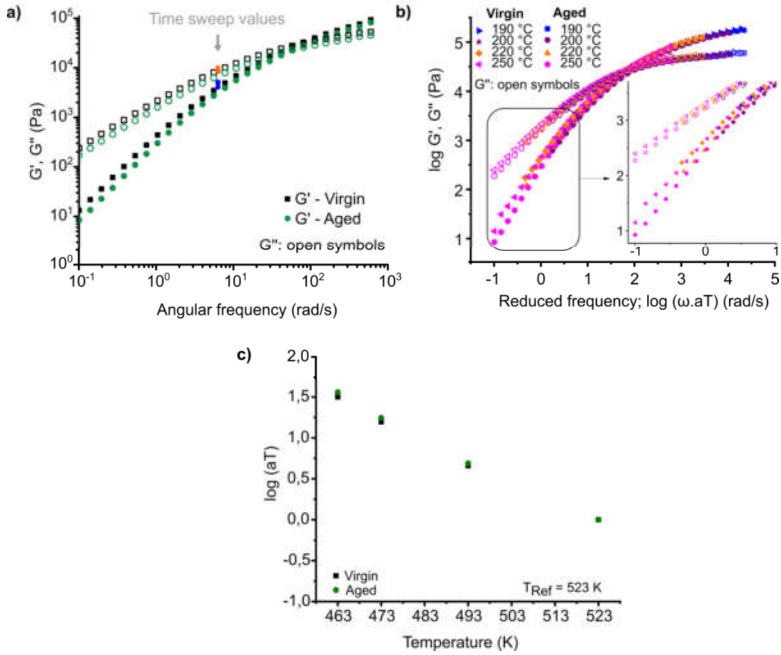

Figure 4: a) Loss and storage modulus (G' and G'') as a function of the angular frequency for PS-0 and PS-240; b) Master curve for virgin and aged PS at temperature reference of 250 °C; c) Temperature dependence of the shift factors used to build the master curve.

As described in Section 3.2, the flow curves for PS-0 and PS-240 (depicted in Figure 5) are obtained by means of constant shear rate tests and by validating the Cox-Merz rule, to expand the (shear rate) range of the graph. The Cox-Merz rule has been employed as this rule is valid for both samples and consistent with reports for PS elsewhere [50]. The points in Figure 5 present the average between at least three measurements of steady state viscosity and complex viscosity, with the error bars representing the standard deviation. The experimental points were fitted to the Carreau-Yasuda equation (Equation (5)):

$$\eta(\dot{\gamma}) = [\eta_0 - \eta_\infty]\left[1 + \left(\frac{\dot{\gamma}}{\dot{\gamma}_0}\right)^a\right]^{\frac{n-1}{a}} + \eta_\infty, \qquad (5)$$

in which, η_0 is the zero-shear rate viscosity, η_∞ is the infinite shear viscosity of the second Newtonian plateau, $\dot{\gamma}_0$ is the characteristic shear rate that marks the transition from the zero-shear viscosity to the power-law region, a is the Yasuda parameter and n is the power law index. The results of the fitting procedure are represented by the red lines in Figure 5. The equation selected promotes a good fitting of the experimental data, assuming η_∞ to be 0.1 Pa.s.

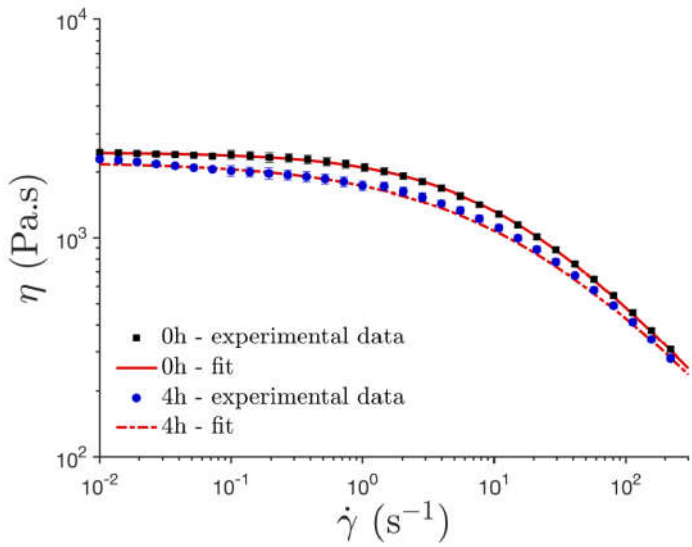

Figure 5: Flow curve for polystyrene (PS) with 0 min (virgin) and 240 min degradation/aging time at 250 °C using the Cox-Merz rule. The red lines represent the fitting of the experimental data to the Carreau-Yasuda equation (Equation 5).

From Figure 5 it is possible to see that the degradation led to a reduction on the viscosity of polystyrene. A closer inspection on the Carreau-Yasuda equation parameters obtained from the fitting (see Table 1) indicate a reduction of 10% on the zero-shear rate viscosity of the aged material, in comparison with the virgin one,

confirming the decrease in the average molar mass of polystyrene tracked via SEC analysis and time sweep measurements. The characteristic shear rate ($\dot{\gamma}_0$) increases with ageing. The power law index (n) was not affected by the degradation process, whereas the Yasuda parameter (a) decreases with the ageing.

Table 1: Parameters from fitting the data to Carreau-Yasuda equation (Equation 5).

Parameter	Virgin Material (PS-0)	Aged Material (PS-240)
η_0 (Pa.s)	2457 ± 27	2219 ± 19
$\dot{\gamma}_0$ (s^{-1})	11.25 ± 1	15.20 ± 2
n (-)	0.33 ± 0.01	0.33 ± 0.01
a (-)	0.70 ± 0.01	0.55 ± 0.01

3. 4. 4. Nonlinear viscoelastic behavior of polystyrene melts after 0 and 240 min of degradation

The transient viscosity response to constant shear rate tests for PS-0 and PS-240 are exhibited in Figure 6a and Figure 6b. The viscosity decrease with an increase in shear rate is expected in both cases. As from shear rates of 1 and 0.464 s^{-1} for samples PS-0 and PS-240, respectively, an overshoot is seen in the curves. The overshoot is a typical nonlinear viscoelastic behavior of polymer melts and polymer solutions [51]. At small shear rates, (i.e. $\dot{\gamma} < 1$ and 0.464 s^{-1} for PS-0 and PS-240, respectively) the material is under the linear viscoelastic regime and this effect is not observed. Above this values, the flow enters the nonlinear viscoelastic regime [19]. This phenomenon is related to the resistance of the polymer to deformation due to entanglements. At a certain point, the molecules start to disentangle, reducing the resistance to the flow, and then reducing monotonically the viscosity up to a steady state value, which is where the value for steady state viscosity should be defined, in case an undershoot is

not observed. The time to reach the steady state decreases with increasing shear rate. This equilibration period ranges from 1 to 10 s, which is in agreement with the literature [52–54]. The fact that the overshoot is seen for the aged samples at smaller shear rates indicate that the resistance to flow due to entanglements is lower for this sample. In other words, lower shear rates are needed for the onset of the disentanglement process. This is related to the reduced average molar mass of this sample.

A closer inspection of Figure 6b shows that the overshoot is followed by an undershoot for the aged samples. In this case, the steady state viscosity values are obtained after the undershoot. For the virgin material (Figure 6a), this is only seen for the sample tested at the shear rate of 2.15 s^{-1}. The undershoot has been recently attributed to the *tumbling* effect [52,55], even though it has also observed previously [56]. The tumbling effect is an unexpected molecular mechanism, which was first observed via video fluorescence microscopy of dilute solutions of DNA [57]. It has been shown via molecular dynamics simulations [58] that entangled polymers may also experience it. The molecular process behind this effect is described by a "tumbling" rotational motion of polymer chains when submitted to strong flows [19], usually at higher shear rates than the ones used here. Sefiddashti et al. [58] put forward that this effect is closely related to disentanglements. At high shear rates, the number of entanglements dramatically decrease, until they become negligible. In this case, the chains that are stretched and aligned in the direction of the flow, may recoil and rotate. One implication of the tumbling effect is that it may give rise to additional relaxation mechanisms which are not incorporated in most tube models [19]. This effect is usually perceived at high shear flows. Rheological measurements at high shear rates are challenging, due to flow instabilities, including wall slip, shear banding, and edge fracture. Costanzo et al. [52] have, for instance, employed a cone-partioned-plate

geometry to reduce this effects and measure the transient response of polystyrene melts up to 100 s^{-1} during constant shear rate tests.

In this work, the tumbling effect, as perceived by the undershoot that follows the overshoot in constant shear rate tests is mostly happening for the aged sample. This is likely related to the decrease of the average molar mass of the polymer and of its relaxation time. Important to note is that this effect has not yet been reported for degraded samples and may implicate on a novel characterization pathway for polymer degradation via rheometry. The potential of this effect to assess the level of polymer degradation will be subject of a future study. This effect is, however, not exclusive for polymers undergoing degradation, and polymer melts presenting different molecular properties or at different test conditions may also show this effect. Also, this would probably not be seen for molecules with long chain branches or partially cross linked, due to the hindering of this relaxation mechanism.

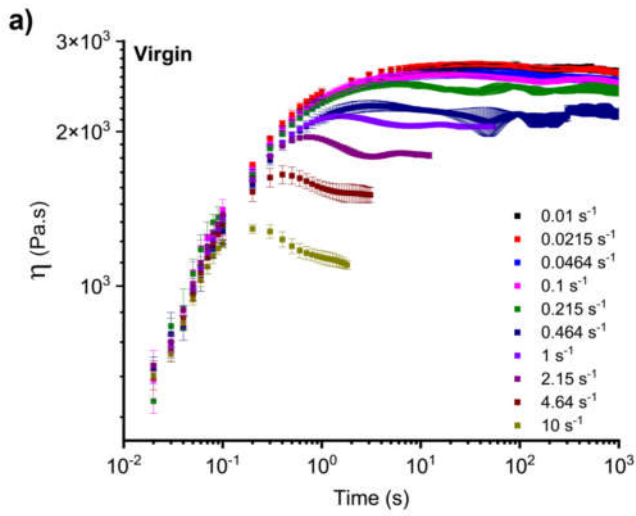

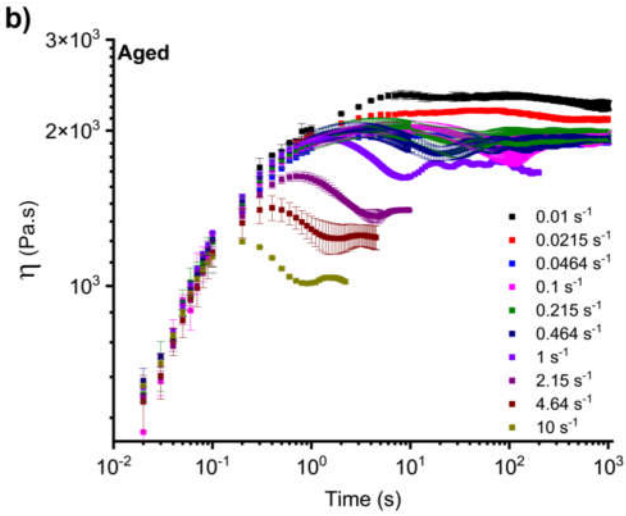

Figure 6: Transient shear viscosity at different shear rates for a) virgin and b) aged materials.

A first attempt to fit the transient viscosity data obtained from constant shear rate tests to the model equations was carried out for virgin polystyrene at specific shear rates (Figure 7).

A close inspection on the results indicate that the model must be further adjusted to properly describe the nonlinear viscoelastic behavior of polystyrene melts. Specifically, adjustments on the structural parameter evolution equation are in progress, possibly yielding better fitting of the results. Another possibility would be an adjustment on the constitutive equation of the model.

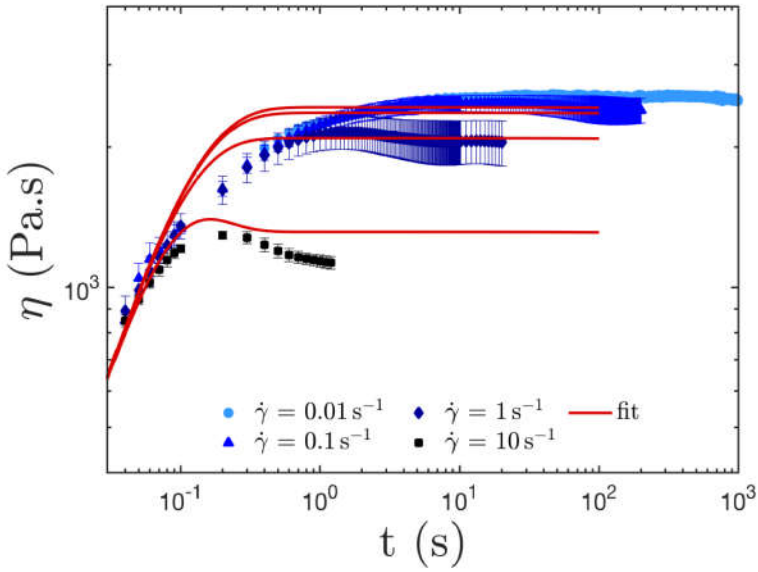

Figure 7: Fitting of structural rheokinetic model equation to the transient viscosity data obtained via constant shear rate tests of virgin polystyrene melts.

3. 5. Conclusions

In this chapter, the rheological behavior of polystyrene (PS) melts undergoing degradation was assessed to obtain a group of parameters for a further structural rheokinetic model validation. In the first step, a rigorous experimental analysis was carried out to define the appropriate conditions to perform the thermal degradation of PS in the rheometer, considering the specimen requirements for such test. It was shown that ageing times up to 240 minutes at 250 °C under N_2 atmosphere induce a sufficient irreversible breakdown of the material's structure without disrupting the state of the specimen in the rheometer.

Once the conditions for the rheological tests were defined, the evolution of *G'*, *G''*, and M_m, obtained via time sweep tests and size-exclusion chromatography (SEC) were

used to estimate the parameter K_{app}, related to the irreversible progress function of the model. To do so, the experimental (dimensionless) data was fitted to the irreversible progress function, which is assumed to be a first-order kinetics equation. The fitting curve describes well the experimental results and indicate a good correlation between the properties measured by the different techniques.

Then, flow curves for the virgin and aged polystyrene were obtained by means of frequency sweep tests and constant shear rate tests, considering the Cox-Merz rule. The flow curves were fitted to the Carreau-Yasuda equation to estimate a second set of parameters for the model validation.

The nonlinear viscoelastic behavior of virgin and aged samples measured via constant shear rate tests exhibited the common overshoot on the transient response of viscosity for both virgin and aged samples. However, fort the aged sample, the onset of disentanglement occurs at lower shear rates, due to its reduced average molar mass. Furthermore, following the overshoot, an undershoot was observed on the curves of aged samples. This experimental observation was attributed to the *tumbling* effect which is for the first time reported for aged polymer melts, indicating future perspectives on the characterization of polymer degradation via rheometry. Furthermore, a first attempt to fit the transient viscosity to the structural rheokinetic model equations indicate that further adjustments in the model are needed.

REFERENCES

1. Real, L.P.; Gardette, J.L.; Pereira Rocha, A. Artificial simulated and natural weathering of poly(vinyl chloride) for outdoor applications: The influence of water in the changes of properties. *Polym. Degrad. Stab.* **2005**, *88*, 357–362, doi:10.1016/j.polymdegradstab.2004.11.012.
2. Fabiyi, J.S.; McDonald, A.G.; Wolcott, M.P.; Griffiths, P.R. Wood plastic composites weathering: Visual appearance and chemical changes. *Polym. Degrad. Stab.* **2008**, *93*, 1405–1414, doi:10.1016/j.polymdegradstab.2008.05.024.
3. Hawkins, W.L. *Polymer Degradation and Stabilization*; Polymers Properties and Applications; Springer: Berlin, 1984; ISBN 978-3-642-69378-6.
4. Ph, R.O. *Degradable Polymers*; Scott, G., Ed.; Springer Netherlands: Dordrecht, 2002; ISBN 978-90-481-6091-4.
5. Choong, G.Y.H.; Focatiis, D.S.A. De A method for the determination and correction of the effect of thermal degradation on the viscoelastic properties of degradable polymers. *Polym. Degrad. Stab.* **2016**, *130*, 182–188.
6. Harrison, G.M.; Melik, D.H. Application of degradation kinetics to the rheology of poly(hydroxyalkanoates). *J. Appl. Polym. Sci.* **2006**, *102*, 1794–1802, doi:10.1002/app.24473.
7. Mysiukiewicz, O.; Barczewski, M.; Skórczewska, K.; Matykiewicz, D. Correlation between processing parameters and degradation of different polylactide grades during twin-screw extrusion. *Polymers (Basel).* **2020**, *12*, doi:10.3390/POLYM12061333.
8. Andersson, T.; Stålbom, B.; Wesslén, B. Degradation of polyethylene during extrusion. II. Degradation of low-density polyethylene, linear low-density polyethylene, and high-density polyethylene in film extrusion. *J. Appl. Polym. Sci.* **2004**, *91*, 1525–1537, doi:10.1002/app.13024.
9. Saikrishnan, S.; Jubinville, D.; Tzoganakis, C.; Mekonnen, T.H. Thermo-mechanical degradation of polypropylene (PP) and low-density polyethylene (LDPE) blends exposed to simulated recycling. *Polym. Degrad. Stab.* **2020**, *182*, 109390, doi:10.1016/j.polymdegradstab.2020.109390.
10. Amintowlieh, Y.; Tzoganakis, C.; Hatzikiriakos, S.G.; Penlidis, A. Effects of processing variables on polypropylene degradation and long chain branching with UV irradiation. *Polym. Degrad. Stab.* **2014**, *104*, 1–10, doi:10.1016/j.polymdegradstab.2014.03.016.
11. Carreau, P.J. Rheological Equations from Molecular Network Theories. *Trans. Soc. Rheol.* **1972**, *16*, 99–127, doi:10.1122/1.549276.
12. Yasuda, K.; Armstrong, R.C.; Cohen, R.E. Shear flow properties of concentrated solutions of linear and star branched polystyrenes. *Rheol. Acta* **1981**, *20*, 163–178, doi:10.1007/BF01513059.
13. Cross, M.M. No Title. In *Polymer Systems: Deformation and Flow*; 1968.
14. Kealy, T. Rheological Analysis of the Degradation of HDPE During Consecutive Processing Steps and for Different Processing Conditions. *J. Appl. Polym. Sci.* **2009**, *112*, 639–648, doi:10.1002/app.29418.
15. Carrot, C.; Revenu, P.; Guillet, J. Rheological behavior of degraded polypropylene melts: From MWD to dynamic moduli. *J. Appl. Polym. Sci.* **1996**, *61*, 1887–1897, doi:10.1002/(SICI)1097-4628(19960912)61:11<1887::AID-APP4>3.0.CO;2-F.
16. Mours, M.; Winter, H.H. Time-resolved rheometry. *Rheol. Acta* **1994**, *33*, 385–397, doi:10.1007/BF00366581.

17. Filippone, G.; Carroccio, S.C.; Mendichi, R.; Gioiella, L.; Dintcheva, N.T.; Gambarotti, C. Time-resolved rheology as a tool to monitor the progress of polymer degradation in the melt state - Part I: Thermal and thermo-oxidative degradation of polyamide 11. *Polymer (Guildf).* **2015**, *72*, 134–141, doi:10.1016/j.polymer.2015.06.059.
18. Kruse, M.; Wagner, M.H. Time-resolved rheometry of poly(ethylene terephthalate) during thermal and thermo-oxidative degradation. *Rheol. Acta* **2016**, *55*, 789–800, doi:10.1007/s00397-016-0955-2.
19. Dealy, J.M.; Larson, R.G. *Structure and Rheology of Molten Polymers*; Carl Hanser Verlag GmbH & Co. KG: München, 2006; ISBN 978-3-446-21771-3.
20. Doi, M.; Edwards, S.F. *The theory of polymer dynamics*; New York, 1986;
21. Larson *Constitutive equations for polymer melts and solutions*; 1989; Vol. 33; ISBN 0409901199.
22. Kulichikhin, S.G.; Malkin, A.Y.; Polushkina, O.M.; Kulichikhin, V.G. Rheokinetics of free-radical polymerization of acrylamide in an aqueous solution. *Polym. Eng. Sci.* **1997**, *37*, 1331–1338, doi:10.1002/pen.11779.
23. Malkin, A.Y.; Kulichikhin, S.G. Rheokinetics of free-radical polymerization. *Polymer (Guildf).* **1984**, *25*, 778–784, doi:10.1016/0032-3861(84)90006-5.
24. García-Sandoval, J.P.; del Campo, A.M.; Bautista, F.; Manero, O.; Puig, J.E. Nonhomogeneous Flow of Micellar Solutions : A Kinetic — Network Theory Approach. *AIChE J.* **2018**, *64*, 2277–2292, doi:DOI 10.1002/aic.16079.
25. Mewis, J.; Wagner, N.J. Thixotropy. *Adv. Colloid Interface Sci.* **2009**, *147–148*, 214–227, doi:10.1016/j.cis.2008.09.005.
26. Read, D.J.; Auhl, D.; Das, C.; Den Doelder, J.; Kapnistos, M.; Vittorias, I.; McLeish, T.C.B. Linking models of polymerization and dynamics to predict branched polymer structure and flow. *Science (80-.).* **2011**, *333*, 1871–1874, doi:10.1126/science.1207060.
27. de Souza Mendes, P.R. Modeling the thixotropic behavior of structured fluids. *J. Nonnewton. Fluid Mech.* **2009**, *164*, 66–75, doi:10.1016/j.jnnfm.2009.08.005.
28. Marchesini, F.H.; Oliveira, R.M.; Althoff, H.; de Souza Mendes, P.R. Irreversible time-dependent rheological behavior of cement slurries: Constitutive model and experiments. *J. Rheol. (N. Y. N. Y).* **2019**, *63*, 247–262, doi:10.1122/1.5054879.
29. Miranda, L.R.M. De; Marchesini, F.H.; Lesage, K.; De Schutter, G. The evolution of the rheological behavior of hydrating cement systems: Combining constitutive modeling with rheometry, calorimetry and mechanical analyses. *Cem. Concr. Res.* **2023**, *164*, 107046, doi:10.1016/j.cemconres.2022.107046.
30. ASTM E1641-16 Standard Test Method for Decomposition Kinetics by Thermogravimetry Using the Ozawa / Flynn / Wall Method 1. *ASTM Stand. Test Method Decompos. Kinet. by Thermogravim. Using Ozawa / Flynn / Wall Method 1* **2013**, 1–7, doi:10.1520/E1641-13.2.
31. Cox, W.P.; Merz, E.H. Correlation of dynamic and steady flow viscosities. *J. Polym. Sci.* **1958**, *28*, 619–622, doi:10.1002/pol.1958.1202811812.
32. Faravelli, T.; Pinciroli, M.; Pisano, F.; Bozzano, G.; Dente, M.; Ranzi, E. Thermal degradation of polystyrene. *J. Anal. Appl. Pyrolysis* **2001**, *60*, 103–121, doi:10.1016/S0165-2370(00)00159-5.
33. McNeill, I.C.; Zulfiqar, M.; Kousar, T. A detailed investigation of the products of the thermal degradation of polystyrene. *Polym. Degrad. Stab.* **1990**, *28*, 131–151, doi:10.1016/0141-3910(90)90002-O.

34. Guaita, M.; Chiantore, O.; Costa, L. Changes in degree of polymerization in the thermal degradation of polystyrene. *Polym. Degrad. Stab.* **1985**, *12*, 315–332, doi:10.1016/0141-3910(85)90123-5.
35. Woloszyn, J.D.; Hesse, P.; Hungenberg, K.D.; Mcauley, K.B. Parameter selection and estimation techniques in a styrene polymerization model. *Macromol. React. Eng.* **2013**, *7*, 293–310, doi:10.1002/mren.201200074.
36. Cameron, G.G.; Kerr, G.P. Thermal degradation of polystyrene-I. Chain scission at low temperatures. *Eur. Polym. J.* **1968**, *4*, 709–717, doi:10.1016/0014-3057(68)90052-9.
37. Chiantore, O.; Camino, G.; Costa, L.; Grassie, N. "Weak links" in polystyrene. *Polym. Degrad. Stab.* **1981**, *3*, 209–219, doi:10.1016/0141-3910(81)90034-3.
38. Chrissafis, K. Kinetics of thermal degradation of polymers : CComplementary use of isoconversional and model-fitting methods. *J. Therm. Anal. Calorim.* **2009**, *95*, 273–283, doi:10.1007/s10973-008-9041-z.
39. Vyazovkin, S.; Sbirrazzuoli, N. Isoconversional kinetic analysis of thermally stimulated processes in polymers. *Macromol. Rapid Commun.* **2006**, *27*, 1515–1532, doi:10.1002/marc.200600404.
40. Nahid, M.; Antonakou, E. V; Hamid, H.; Achilias, D.S. Thermochimica Acta Kinetic analysis of thermal and catalytic degradation of polymers found in waste electric and electronic equipment. *Thermochim. Acta* **2019**, *675*, 69–76, doi:10.1016/j.tca.2019.03.001.
41. Vrandec, N.S.; Erceg, M. Thermal degradation of poly (3-hydroxybutyrate)/ poly (ethylene oxide) blends : Thermogravimetric and kinetic analysis. *Eur. Polym. J.* **2016**, *81*, 376–385, doi:10.1016/j.eurpolymj.2016.06.024.
42. Balart, R.; Garcia-sanoguera, D.; Quiles-carrillo, L.; Montanes, N.; Torres-giner, S. Kinetic Analysis of the Thermal Degradation of Recycled Acrylonitrile-Butadiene-Styrene by non-Isothermal Thermogravimetry. *Polymers (Basel).* **2019**, doi:10.3390/polym11020281.
43. D., P.J.; Sergey, V.; A., W.C. Kinetics of the Thermal and Thermo-Oxidative Degradation of Polystyrene, Polyethylene and Poly(propylene). *Macromol. Chem. Phys.* **2001**, *202*, 775–784, doi:10.1002/1521-3935(20010301)202:6<775::AID-MACP775>3.0.CO;2-G.
44. Camiti, P.; Beltrame, P.L.; Armada, M.; Gervasini, A.; Audisio, G. Polystyrene Thermodegradation. 2. Kinetics of Formation of Volatile Products. *Ind. Eng. Chem. Res.* **1991**, *30*, 1624–1629, doi:10.1021/ie00055a032.
45. Ali, G.; Nisar, J.; Iqbal, M.; Shah, A.; Abbas, M.; Shah, M.R.; Rashid, U.; Bhatti, I.A.; Khan, R.A.; Shah, F. Thermo-catalytic decomposition of polystyrene waste: Comparative analysis using different kinetic models. *Waste Manag. Res.* **2020**, *38*, 202–212, doi:10.1177/0734242X19865339.
46. Ding, L.; Zhao, J.; Pan, Y.; Guan, J.; Jiang, J.; Wang, Q. Insights into Pyrolysis of Nano-Polystyrene Particles: Thermochemical Behaviors and Kinetics Analysis. *J. Therm. Sci.* **2019**, *28*, 763–771, doi:10.1007/s11630-019-1123-7.
47. Aguado, R.; Olazar, M.; Gaisán, B.; Prieto, R.; Bilbao, J. Kinetics of polystyrene pyrolysis in a conical spouted bed reactor. *Chem. Eng. J.* **2003**, *92*, 91–99, doi:10.1016/S1385-8947(02)00119-5.
48. Şenocak, A.; Alkan, C.; Karadağ, A. Thermal Decomposition and a Kinetic Study of Poly(Para-Substituted Styrene)s. *Am. J. Anal. Chem.* **2016**, *07*, 246–253, doi:10.4236/ajac.2016.73021.
49. Denq, B.-L.; Chiu, W.-Y.; Lin, K.-F. Kinetic model of thermal degradation of

polymers for nonisothermal process. *J. Appl. Polym. Sci.* **1997**, *66*, 1855–1868, doi:10.1002/(SICI)1097-4628(19971205)66:10<1855::AID-APP3>3.0.CO;2-M.

50. Hieber, C.A.; Chiang, H.H. Some correlations involving the shear viscosity of polystyrene melts. *Rheol. Acta* **1989**, *28*, 321–332, doi:10.1007/BF01329342.
51. Tseng, H.C. A constitutive analysis of stress overshoot for polymer melts under startup shear flow. *Phys. Fluids* **2021**, *33*, doi:10.1063/5.0054379.
52. Costanzo, S.; Huang, Q.; Ianniruberto, G.; Marrucci, G.; Hassager, O.; Vlassopoulos, D. Shear and Extensional Rheology of Polystyrene Melts and Solutions with the Same Number of Entanglements. *Macromolecules* **2016**, *49*, 3925–3935, doi:10.1021/acs.macromol.6b00409.
53. Schweizer, T. Comparing cone-partitioned plate and cone-standard plate shear rheometry of a polystyrene melt Measurement of the Elongational Properties of Polymer Melts by Gravity Spinning Comparing cone-partitioned plate and cone-standard plate shear rheometry of a po. **2013**, *1071*, doi:10.1122/1.1584428.
54. Schweizer, T.; Meerveld, J. Van; Öttinger, H.C. Nonlinear shear rheology of polystyrene melt with narrow molecular weight distribution — Experiment and theory narrow molecular weight distribution — Experiment. **2004**, *1345*, doi:10.1122/1.1803577.
55. Masubuchi, Y.; Ianniruberto, G.; Marrucci, G. Stress undershoot of entangled polymers under fast startup shear flows in primitive chain network simulations. *Nihon Reoroji Gakkaishi* **2018**, *46*, 23–28, doi:10.1678/rheology.46.23.
56. Auhl, D.; Ramirez, J.; Likhtman, A.E.; Chambon, P.; Fernyhough, C. Linear and nonlinear shear flow behavior of monodisperse polyisoprene melts with a large range of molecular weights. *J. Rheol. (N. Y. N. Y).* **2008**, *52*, 801–835, doi:10.1122/1.2890780.
57. Smith, D.E.; Babcock, H.P.; Chu, S. Single-Polymer Dynamics in Steady Shear Flow. *Science (80-.).* **1999**, *283*, 1724–1727, doi:10.1126/science.283.5408.1724.
58. Nafar Sefiddashti, M.H.; Edwards, B.J.; Khomami, B. Individual chain dynamics of a polyethylene melt undergoing steady shear flow. *J. Rheol. (N. Y. N. Y).* **2015**, *59*, 119–153, doi:10.1122/1.4903498.

Chapter 4

Thermal and thermal-oxidative molecular degradation of polystyrene and acrylonitrile butadiene styrene during 3D printing starting from filaments and pellets

4. 1. Abstract

An important polymer processing technique is additive manufacturing (AM), which enables shape-free design of complex final parts with limited waste during the development change, at least if the impact of molecular degradation reactions is minimized. In the present work, polystyrene (PS) and acrylonitrile butadiene styrene (ABS) polymer have been processed via: (i) fused filament fabrication (FFF), separately accounting for the prior single screw extrusion (SSE) filament production; and (ii) pellet-based additive manufacturing (PBAM), which are two important AM techniques. The influence of printing temperature, layer thickness, printing velocity, and printing technique on the degradation of both polymeric materials is studied by means of thermogravimetric analysis (TGA), size exclusion chromatography (SEC), small amplitude oscillatory shearing tests (SAOS), Fourier-transform infrared spectroscopy (FTIR), and yellowness index (YI) measurements. For ABS, SSE-FFF leads to more fission (higher mechanical loading) whereas PBAM results in more cross-linking (more thermal loading). For PS, fission is always dominant and this more evident under FFF conditions. ABS also exhibits yellowing upon processing,

indicating thermo-oxidative degradation although below the FTIR sensitivity limit. The selected PBAM conditions with PS are already delivering printed specimens with good mechanical properties and lower degradation. For ABS, a further PBAM optimization is still desired compared to the FFF counter case, taking into account layer-by-layer adhesion.

4. 2. Introduction

Extrusion-based additive manufacturing (EAM) is one of the most employed techniques for 3D printing of thermoplastics due to its low cost and versatility (e.g., shape-freedom), with as advantage less waste material and thus higher sustainability during the research and design phase [1,2]. EAM includes the broadly used fused filament fabrication (FFF) technique and the more recently developed pellet-based additive manufacturing (PBAM) technique [3–9]. FFF is a manufacturing technique in which a filament must be produced in advance to be used as feedstock for the actual additive manufacturing (AM) process. The filament is typically produced via conventional (single screw) extrusion and gives the possibility of tailoring the composition of the feedstock by introducing additives such as fillers and antioxidants. In contrast, PBAM allows direct usage of pellets, reducing the processing steps required to obtain the final 3D printed part. Furthermore, it allows a wider range of materials to be additively manufactured at a lower cost than FFF, with faster processing speeds and less processing-induced degradation of the material [10].

An important group of polymers to consider for AM are polystyrenics, which are used in several applications such as packaging, automotive components, and electronic equipment [11,12]. Specifically, acrylonitrile butadiene styrene (ABS) polymer is already broadly applied for FFF [13]. ABS is a multi-phase rubber-modified polymer,

based on styrene-acrylonitrile (SAN) random copolymer and polybutadiene (PB) rubber, including graft connections similar to its simplified form high impact polystyrene (HIPS) [12,14]. It has a great toughness, and a good impact, abrasion and chemical resistance [15], making it superior compared to polystyrene (PS), being a brittle, rigid and transparent thermoplastic. So far, PS filaments or pellets have not been thoroughly investigated for EAM purposes. Notably, Akintola et al. [16] produced 3D printed PS-based boron nitride nanotube nanocomposites for thermal management and electronic packaging applications. Sevastaki et al. [17], in turn, produced 3D printed parts for photocatalytic applications based on recycled PS/TiO_2 composites. However, the authors indicated that further investigation is still needed to obtain 3D printed parts with a higher quality.

A significant AM research angle is the understanding of the degree of degradation the polymer experiences during processing. The extent of thermoplastic degradation is usually analyzed by a combined group of characterization techniques that assess changes in the chemical structure of the material. These changes in the chemical structure of the polymer may be reflected in the material properties, influencing the application potential, shelf life and recyclability. Notably, polymer degradation during conventional processing has already been broadly studied [18–23], and also several investigations exist for polymer recycling toward EAM applications [24–28]. These studies have revealed that a polymer (composite) can undergo thermal, thermo-mechanical, thermo-oxidative, photo-oxidative and hydrolytic degradation, leading to irreversible structural changes [29]. Hence, the most important factors for degradation during processing are the temperature, humidity, oxygen content, mechanical stress loadings, and residence time [30]. Thermal degradation essentially leads to (average) molar mass changes [19] caused by chemical reactions promoting chain scission, branching or cross-linking. Although the impact of oxygen may be less evident, as

most processing tools limit the entrance path to the molten polymer, it may be still present in small amounts, due to its given solubility in polymers [31].

The degradation is more pronounced in case the materials undergo multiple processing cycles, such as in mechanical recycling of thermoplastics or 3D printing via FFF. Limiting the number of processing steps provides, therefore, a solution for less degradation. As PBAM involves only one processing step after the pellet production stage, it may inherently cause less structural changes to the material during processing as it will be exposed to less thermal and mechanical stresses. When it comes to recycled materials, depending on the processing conditions, the differences between FFF and PBAM would be minimized, as the post-consumer and post-industrial waste would unavoidably undergo at least one processing step.

Nevertheless, a comparison of FFF and PBAM for a wide material pallet is interesting. Recently La Gala et al. [32] put forward a comparison for ABS and poly(lactic acid) (PLA), highlighting the need to optimize PBAM conditions. This can explain the differences between the results of Gradwohl et al. [33], reporting for poly(lactic-co-glycolic) (PLGA) a stronger degradation with PBAM attributed to a longer residence time, and the results of La Gala et al. [32] reporting a more pronounced degradation of ABS manufactured via FFF in comparison with PBAM.

It should be stressed that the few EAM degradation studies mostly deal with FFF only. For example, Fernandez et al. [34] assessed the influence of printing parameters on the performance of different copolyesters. The authors explained how the combination of a high printing temperature and a low printing velocity can lead to degradation if the chemical structure is prone to chemical modifications. However, the extent of degradation did not result in a reduction in the macroscopic properties, as the coalescence between deposited layers was slightly improved at higher temperatures.

Similarly, the study of Jagenteufel et al. [35] put forward that the printing process of ABS, PLA and polypropylene (PP) via FFF led to negligible degradation. However, no reports on the very systematic variation in FFF and PBAM parameters and the degradation degree of the material exist. A non-trivial optimization is also expected as increasing the printing speed could lead to less degradation, but detrimental effects on the quality of the 3D printed part are likely caused above a threshold printing speed. In addition, the best operating window is likely material dependent, and different for FFF and PBAM. A more detailed focus on degradation mechanisms and degrees is thus relevant, bearing in the mind the rather new nature of FFF and PBAM and their potential use for recycling purposes [36–38]. Defining and developing processing pathways which induce less degradation in the material is important to propitiate a more sustainable approach to polymer production [39,40].

In the present work, we investigate the effect of the most relevant EAM parameters on the degradation of both PS and ABS. The influence of the FFF printing temperature, layer thickness and printing velocity on the degradation of PS and ABS is assessed via rheological analysis, size exclusion chromatography (SEC) analysis and Fourier Transform infrared spectroscopy (FTIR), to indicate the changes of the molecular properties. Under defined conditions, the same analysis is then carried out for PBAM samples, and the results are compared. The degradation during manufacturing is correlated with macroscopic properties as well. It is highlighted that the molecular degradation mechanism is different under PBAM and FFF conditions for PS and ABS.

4. 3. Materials and methods

4. 3. 1. Materials

Two amorphous styrene-based commercially available polymers were used: (i) general purpose ABS (Terluran GP-22, INEOS, London, UK) with a density of 1040 kg m^{-3}, as obtained by emulsion polymerization, with a glass transition temperature (T_g) of 100 °C; and (ii) a conventional polystyrene (PS) (441147, Sigma Aldrich, St. Louis, MO, USA) with a density of 1040 kg m^{-3} and T_g of 100 °C. Furthermore, tetrahydrofuran (THF; CL00.2027, Chem-Lab, Zedelgem, Belgium) was used in the SEC analysis.

4. 3. 2. Sample preparation

Filament Fabrication

ABS and PS filaments for FFF were produced using a single screw extruder (SSE) (Brabender 19, 19 mm screw diameter, length over diameter ratio (L/D) of 25, Brabender, Duisburg, Germany). A rolling system and spooling device developed in-house were used to pool the extrudate into a filament with a controlled (average) diameter of 1.75 mm, and to wind it for further FFF application. The processing parameters used are described in Table 1.

Table 1. Extrusion parameters used for producing ABS and PS filaments.

Material	Temperature Profile (°C)				Screw Speed (rpm)	Spooling Speed (m min^{-1})
	Zone 1	Zone 2	Zone 3	Zone 4		
ABS	145	185	205	210	27	5.0
PS	215	220	225	230	13	2.2

Fused Filament Fabrication

Prusa printers (Prusa i3 MK3S+, Prusa, Prague, Czech Republic) were employed to manufacture a set of tensile specimens for examination of the influence of the nozzle temperature, layer thickness and printing velocity and their combination on the degradation and tensile properties of PS and ABS specimens. The samples were named as follows: "Material_Nozzle Temperature_Layer Thickness_Printing Velocity_Processing Route" and are described for the FFF case in Table 2. The nozzle temperatures were 220 and 270 °C for ABS; and 240 and 270 °C for PS; the layer thicknesses were 0.15 and 0.25 mm; and the print velocities were 40 and 120 mm s^{-1}. Fixed printing parameters used to produce the specimens were 100% infill, with a rectilinear pattern and 45° infill angle, a nozzle with 0.4 mm diameter, a bed temperature of 110 °C, and an XYZ build pattern (parallel to the bed). To prevent warpage of PS parts, a 2 mm brim was initially printed and removed later.

Table 2. Samples produced via FFF.

Material	Run	Sample	Nozzle Temperature (°C)	Layer thickness (mm)	Print velocity (mm s^{-1})
ABS	1	ABS_220_0.15_40_FFF	220	0.15	40
	2	ABS_270_0.15_40_FFF	270	0.15	40
	3	ABS_220_0.25_40_FFF	220	0.25	40
	4	ABS_270_0.25_40_FFF	270	0.25	40
	5	ABS_220_0.15_120_FFF	220	0.15	120
	6	ABS_270_0.15_120_FFF	270	0.15	120
	7	ABS_220_0.25_120_FFF	220	0.25	120
	8	ABS_270_0.25_120_FFF	270	0.25	120
PS	9	PS_240_0.15_40_FFF	240	0.15	40
	10	PS_270_0.15_40_FFF	270	0.15	40
	11	PS_240_0.25_40_FFF	240	0.25	40
	12	PS_270_0.25_40_FFF	270	0.25	40
	13	PS_240_0.15_120_FFF	240	0.15	120
	14	PS_270_0.15_120_FFF	270	0.15	120
	15	PS_240_0.25_120_FFF	240	0.25	120
	16	PS_270_0.25_120_FFF	270	0.25	120

Pellet-based additive manufacturing

Tensile specimens of both ABS and PS were also produced via pellet-based additive manufacturing (PBAM). Pellets of ABS and PS were directly fed into a PBAM system developed in-house [10], with the printing parameters shown in Table 3. Furthermore, the bed temperature was set to 110 °C, the layer thickness to 0.25 mm, the nozzle diameter to 0.4 mm, and the printing velocity to 40 mm s^{-1}. An overview of the samples produced via PBAM is provided in Table 3.

Table 3. Samples and printing parameters used in PBAM system.

Material	Sample	Temperature Profile (°C)			Screw Speed (rpm)
		Zone 1	Zone 2	Zone 3	
ABS	ABS_220_0.25_40_PBAM	220	220	220	0.8
	ABS_270_0.25_40_PBAM	220	270	270	0.8
PS	PS_240_0.25_40_PBAM	220	240	240	0.1
	PS_270_0.25_40_PBAM	220	270	270	0.1

Compression molding

Pellets, filaments and a part of the tested tensile specimens of ABS and PS were chopped and compression molded for further characterization via rheological testing, size-exclusion chromatography (SEC), and Fourier-transform infrared (FTIR) spectroscopy. The samples were prepared in a disk-like shape with 1 mm thickness and 25 mm diameter at 220 °C, using a hot press. The materials were pre-heated for 5 min and then compression molded for 5 min. They were cooled under environmental conditions.

4. 3. 3. Characterization

Thermal stability of raw materials

The thermal stability was assessed by thermogravimetric analysis (TGA) in a Netzsch (Selb, Germany) Simultaneous thermal analysis (STA 449 F3 Jupiter) equipment in the TGA mode, under nitrogen atmosphere. Dynamic runs were carried out from 30 to 600 °C with a heating rate of 10 °C min^{-1}. Isothermal runs were performed for 2000 s at 220 and 270 °C for ABS, and at 240 and 270 °C for PS, which reflects the processing temperatures used to 3D print the materials (see Table 2 and Table 3).

To further assess the thermal stability, rheological time sweep tests were carried out in a rheometer (MCR 702, Anton Paar, Graz, Austria) for 2000 s at 220 and 270 °C for ABS, and at 240 and 270 °C for PS. The parallel plate configuration was used (25 mm in diameter and 1 mm in gap), with a frequency of 1 rad s^{-1} and a strain amplitude of 1%, under nitrogen atmosphere.

Degradation analysis

The influence of processing steps on the degradation of the materials employed in the present work was done by means of linear viscoelastic characterization of the pellets, filaments and specimens produced via additive manufacturing (FFF and PBAM), SEC and FTIR.

Linear viscoelastic properties

The linear viscoelastic characterization of the materials was performed in a rheometer (MCR 702, Anton Paar, Graz, Austria) by means of small amplitude oscillatory shearing tests (SAOS), using the parallel plate configuration (25 mm in diameter and

1 mm in gap). Frequency sweep tests of pellets, filaments and tested tensile specimens (sample preparation as described in Section 2.2—Compression molding) were carried out at 220 °C, with a strain amplitude of 1%, from 600 to 0.1 rad s^{-1}, under nitrogen atmosphere.

Size-exclusion chromatography

A PL-GPC 50 Plus instrument with an autosampler and a refractive index (RI) detector was used to perform SEC analysis. The set-up is equipped with a 50 × 7.5 mm Resipore guard column followed by two Resipore 300 × 7.5 mm columns in series (Agilent Technologies, Santa Clara, CA, USA). Tetrahydrofuran (THF; flow rate of 1 mol min^{-1}) was used as eluent. The temperature of the column compartment was maintained at 30 °C. Calibration was performed using narrow polystyrene standards (Medium EasiVials kit, Agilent Technologies, Santa Clara, CA, USA) in the 1.62×10^2 to 4.83×10^5 g mol^{-1} range.

Fourier-Transform infrared spectroscopy

FTIR analysis was carried out in a spectrometer (Tensor 27, Bruker, Billerica, MA, USA) in the attenuated total reflection mode (ATR). The investigated spectral range was from 4000 to 600 cm^{-1}, with a resolution of 4 cm^{-1}. Values of absorbance were determined using the baseline method. For ABS, attention is paid to the absorbance peaks of C=C bonds with different configurations, specifically, the 1,2-butadiene monomer unit at 911 cm^{-1} and the 1,4 butadiene monomer unit at 966 cm^{-1}, as they may decrease gradually because of the PB phase degradation. These peaks were compared with the absorbance peaks of (unmodified) nitrile entities, which are not expected to change, at 2237 cm^{-1} using the absorption ratios R1 to R2, as defined by Equation (1) and Equation (2) [41–43].

$$R1 = \frac{\text{Absorbance at } 911\ \text{cm}^{-1}}{\text{Absorbance at } 2237\ \text{cm}^{-1}} \quad (1)$$

$$R2 = \frac{\text{Absorbance at } 966\ \text{cm}^{-1}}{\text{Absorbance at } 2237\ \text{cm}^{-1}} \quad (2)$$

For PS, all the spectra were normalized to the peak at 1606 cm^{-1}, which corresponds to the in-plane stretch of the C=C bonds in the aromatic ring or other conjugated double bonds [44].

Color variations, mechanical properties, specific mechanical energy and morphology

Yellowness index

The color measurements were performed with a spectrophotometer (UltraScan VIS, HunterLab, Reston, VA, USA) using a D65 light source and 10° viewing angle. All color measurements were obtained from compression molded specimens. The yellowness index (YI) was obtained by the International Commission on illumination (CIE) tristimulus values X, Y and Z according to the CIELAB color system, and determined according to Equation (3) [45].

$$YI = \frac{100.(1.3013X - 1.1498Z)}{Y} \quad (3)$$

Specific mechanical energy (SME)

The specific mechanical energy (SME) related to the processing of ABS and PS via SSE and PBAM was calculated according to Equation (4) [46]:

$$SME = 2\frac{2\pi}{60}.\frac{C.N}{Q}, \quad (4)$$

in which C is the torque (Nm), N is the screw speed (rpm) and Q is output (kg/h). SME is defined as the mechanical energy applied to a system per unit mass of processed material [47] and is commonly used to assess and compare extrusion processes. It may give an interesting insight on the influence of the processing technique on polymer degradation.

Tensile tests

Tensile tests were carried out using a universal testing machine (5565, Instron, Norwood, MA, USA) with a 10 kN load cell, following ISO 527 with 1BA specimens. The tests were conducted in a controlled environment under an atmosphere of 23 °C and 50% relative humidity.

Morphological analysis

The fracture morphology of a mechanically tested specimen was assessed via scanning electron microscopy (SEM) via a Phenom Pro Desktop (ThermoFischer Scientific, Waltham, MA, USA). The specimens were sputtered with a 7 nm thin layer of gold prior to imaging.

Statistical analysis

A factorial design 2^3 (three factors, two levels of each factor) was conducted to evaluate the influence of each factor and their interactions on the complex viscosity (η^*) of ABS and PS, and on the melt yield stress of ABS (σ_0) produced via FFF, employing analysis of variance (ANOVA). Factor A represents the printing temperature (levels: 220 or 270 °C for ABS and 240 or 270 °C for PS), Factor B

represents the layer thickness (levels: 0.15 or 0.25 mm), and Factor C represents the print velocity (levels: 40 or 120 mm s^{-1}). The values of the factors were codified according to the level of each factor, i.e., −1 for the lower level and +1 for the higher level. Two replications of each experiment were done, reflecting the sources of variability both between runs and within runs [48]. The order of the mixtures within each replication was randomized. The results obtained were compared using the Tukey's test, which indicates if there is a significant difference between the average results of two populations [48]. A conventional significance level (α) of 0.05 was considered.

4. 4. Results and discussion

First emphasis is the thermal stability of ABS and FFF feedstock (raw) materials in view of their 3D printing, considering TGA and basic rheological analysis. This more conventional analysis up to longer times is further supported by dedicated rheological, SEC and FTIR analysis to obtain more molecular scale driven insights under actual processing conditions, e.g., shorter analysis times. In a final stage, attention is paid to color, mechanical and morphological changes, always comparing FFF and PBAM. Specific emphasis is on the assessment of the impact of mechanical and thermal contributions to the degradation pattern.

4. 4. 1. Conventional thermal stability of feedstock materials

The thermal stability of the feedstock materials for EAM must be assessed to assure that the printing temperature is sufficiently below their degradation temperature. The dynamic and isothermal TGA variations for raw PS and ABS material are shown in Figure 1. According to the curves obtained in the dynamic mode (Figure 1a), the degradation of the tested materials has an onset temperature of 404 and 397 °C for

ABS and PS, respectively. The temperature of 1% mass loss ($T_{1\%}$) further indicates the thermal stability of the materials and is as high as 310 and 336 °C for ABS and PS, respectively. The degradation onset temperature and $T_{1\%}$ for ABS and PS are indicated by the vertical dashed lines in Figure 1a, in black and red, respectively. These results mean that no major degradation should be seen under the chosen processing temperatures used in the present work (Table 1).

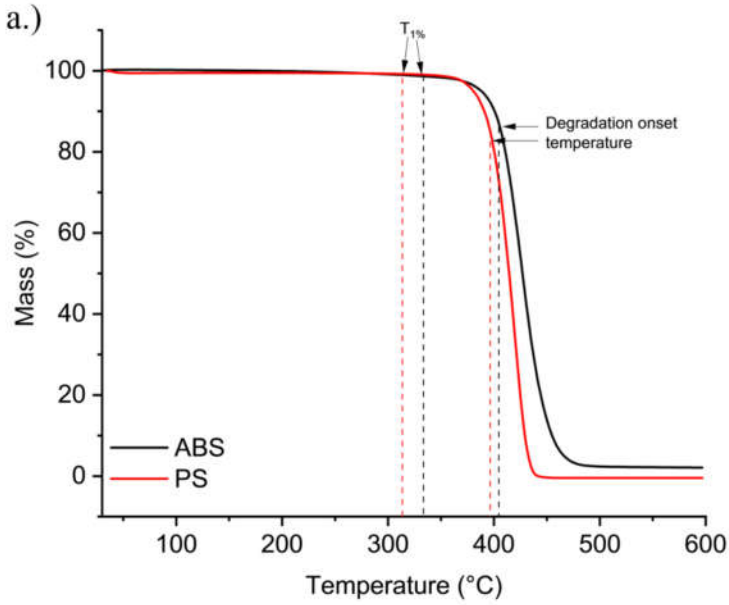

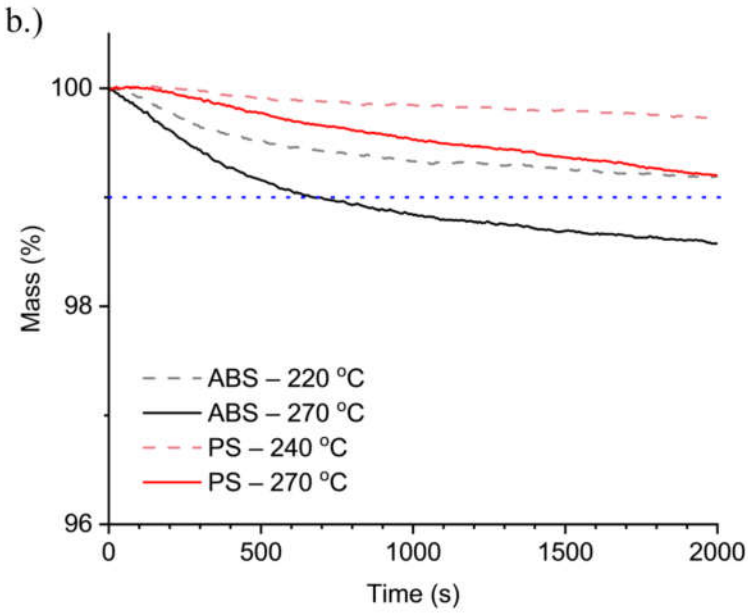

Figure 1. Thermogravimetric analysis of PS and ABS in: (a) dynamic; and (b) isothermal mode.

The isothermal TGA results in Figure 1b indicate that at the final time of 2000 s ABS experienced a mass decrease of 0.82 and 1.43% at 220 and 270 °C, respectively. For PS, at the same testing time, both test conditions promoted a mass decrease under 1% (indicated by the blue dashed line in Figure 1b) so that care should be taken for translation of non-isothermal findings in isothermal results, with the former showing more degradation. Notably, at the lowest time in Figure 1b (300 s) the changes in the mass are always minor and the chosen processing parameters (Table 1; below 300 s) should be suitable for both materials. The mass variation with time under the test conditions is also shown in table format in Appendix B (Table B1).

Supplementary to the thermal tests, low frequency rheological time sweep tests allow us to assess the stability of the feedstock materials. Specifically, monitoring the

complex viscosity (η*) over time can give insights on irreversible structural changes in the polymers [49], e.g., caused by chemical reactions that promote cross-linking, branching, or chain fission. The complex viscosity was obtained as a function of time and normalized by the first measured value after 15 s of testing (η^*_{15}). The normalized complex viscosity (η^*_t/η^*_{15})) is shown in Figure 2.

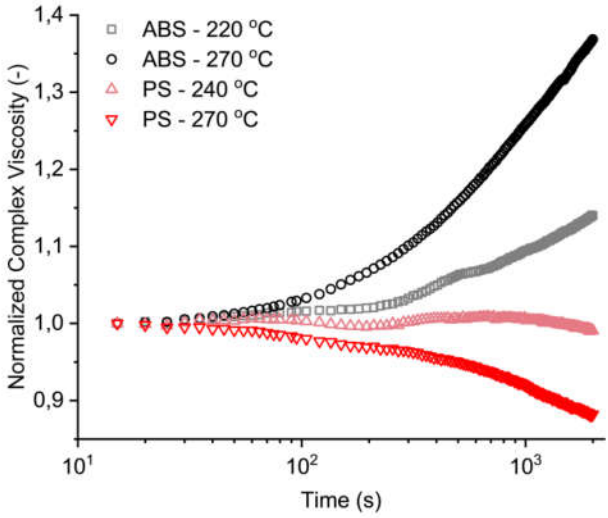

Figure 2. Time sweep plots complementary to Figure 1; normalized with the first recorded value.

Figure 2 shows that ABS exhibits at both 240 and 270 °C an increase in the normalized complex viscosity at both test temperatures, but more pronouncedly at 270 °C. This is attributed to the degradation of the PB phase, leading to cross-linking. In the initial stages of ABS degradation it has been indicated that the PB phase is attacked and unsaturated groups are consumed forming hydroperoxides, which in turn decompose and promote the formation of cross-linked structures [50]. Some level of oxygen is

thus assumed to be present in the samples under this premise, giving rise to thermo-oxidation of the PB phase. In contrast, PS is stable at 240 °C with a constant normalized viscosity throughout the test, indicating that no structural changes are happening at this temperature, which agrees with the TGA data of Figure 1b. At 270 °C, PS exhibits even a decrease in the normalized complex viscosity, as a result of degradation via chain fission [51]. As the isothermal TGA (Figure 1b) results indicate negligible mass loss, we can assume a limited contribution of random chain fission [52] and only a small fraction of low molar mass compound formation.

Overall, Figure 2 indicates that PS and ABS are likely very stable at the processing temperatures selected, especially for at least 40 s upon considering the higher processing temperatures. Due to the short residence times in AM, the actual printing processing step should not induce dedicated material degradation so that the materials should be suitable for printing. Still, it must be kept in mind that these tests only account for the thermal stability of the materials, e.g., not mechanical stresses. Furthermore, in the case of FFF the filament already underwent a processing step, which may have already caused changes in its chemical structure. Therefore, further degradation analysis is needed to fully assess the effects of each step along the manufacturing chain.

4. 4. 2. Detailed rheological, size-exclusion chromatography and Fourier-Transform infrared spectroscopy analysis for stability under processing conditions

The effect of the filament manufacturing via single screw extrusion (SSE), the 3D printing via FFF, and the FFF processing parameters (printing temperature, layer thickness and printing velocity) on the complex viscosity of ABS and PS are shown

as a function of the angular frequency in Figure 3. The results for the raw materials are added in all graphs for comparison. In the case of ABS printed at 220 °C (Figure 3a) and at 270 °C (Figure 3b), no major differences can be seen. This indicates a limited amount of structural changes as a result of processing, including the filament fabrication, consistent with the work of Jagenteufel et al. [35]. Even though the time sweep tests (Figure 2) show an increase in the complex viscosity of ABS with time, the materials have now been subjected to thermal and mechanical stresses. The latter stresses may have caused a certain level of chain fission, which decreases the viscosity and average molar mass of the material, compensating cross-linking increases. In contrast, in the case of PS (Figure 3c,d), it is clear that the processing leads to structural changes (with lower chain lengths) because of degradation. The filament fabrication reduces the complex viscosity of PS, which is further decreased after the FFF process, especially if the material is processed at 270 °C.

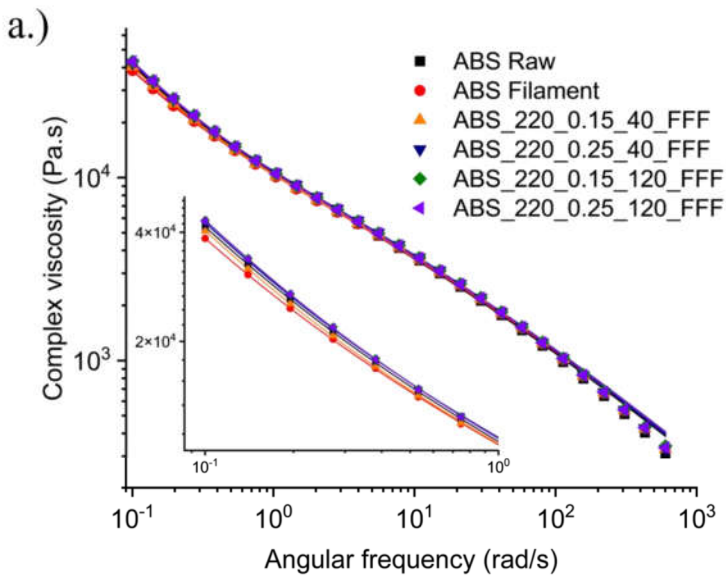

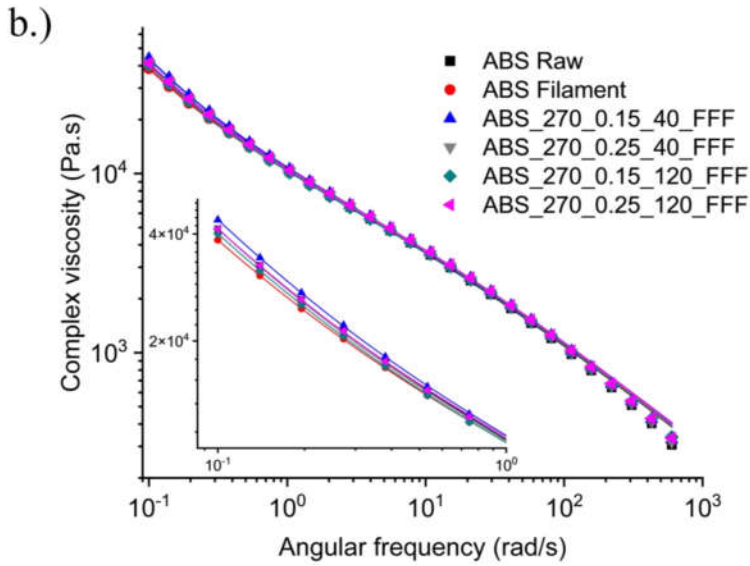
b.)
ABS Raw
ABS Filament
ABS_270_0.15_40_FFF
ABS_270_0.25_40_FFF
ABS_270_0.15_120_FFF
ABS_270_0.25_120_FFF
Complex viscosity (Pa.s)
Angular frequency (rad/s)

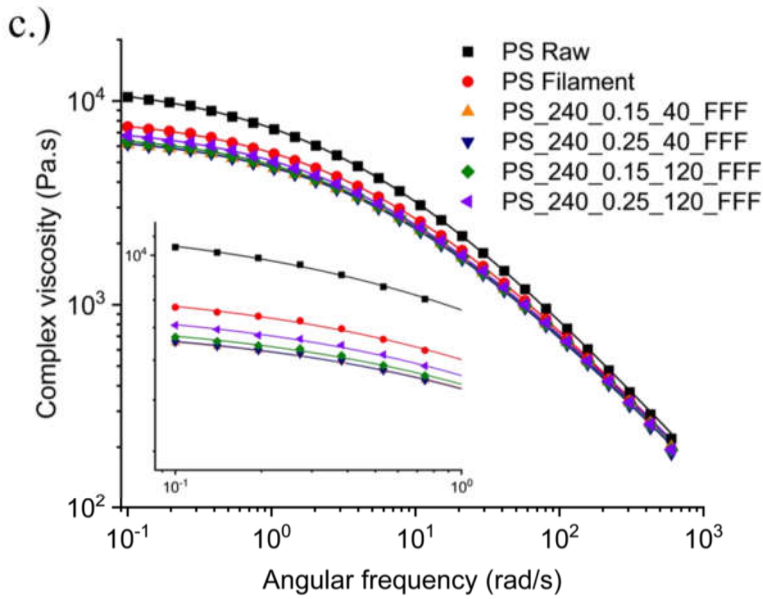
c.)
PS Raw
PS Filament
PS_240_0.15_40_FFF
PS_240_0.25_40_FFF
PS_240_0.15_120_FFF
PS_240_0.25_120_FFF
Complex viscosity (Pa.s)
Angular frequency (rad/s)

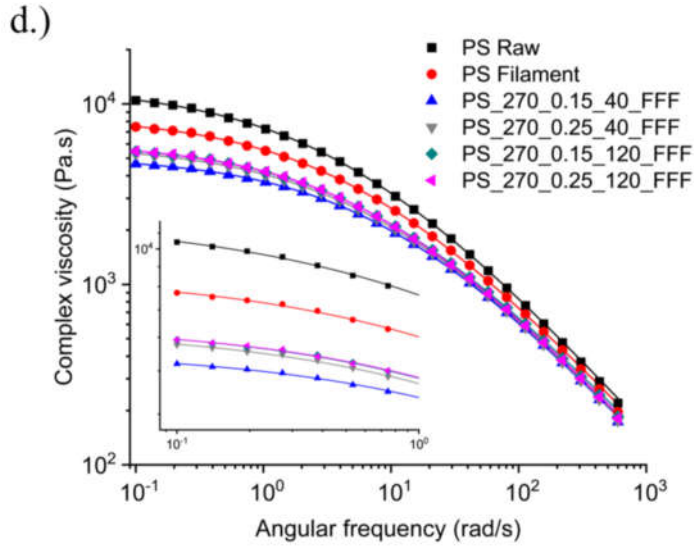

Figure 3. Effect of processing steps and processing parameters on the complex viscosity of ABS printed at (a) 220 °C and (b) 270 °C and of PS printed at (c) 240 °C and (d) 270 °C. Symbols: experimental data points, lines: modified Carreau–Yasuda fitting.

As discussed elsewhere [53–56], ABS may exhibit a plateau for its storage modulus (*G*') in the low-frequency regime, indicating a non-terminal behavior and an apparent yield stress, which is consistent with the increase in the complex viscosity in this regime (see also different curvature in Figure 3 top row (ABS) compared to bottom row (PS)). This non-terminal behavior is related to the contribution of the interfacial interactions involving the (grafted) rubber phase (PB-g-SAN) to the overall elastic response of the material. Due to this non-terminal behavior, the traditional models for fitting the polymer viscosity curve are unsuitable and instead the complex viscosity data in the present work (Figure 3 top row; ABS) have been described by a modified Carreau–Yasuda model (lines in Figure 3) [57]:

$$\eta * (\omega) = \frac{\sigma_0}{\omega} + \eta_0[1 + (\lambda\omega)^a]^{(n-1)/a} \quad (5)$$

where σ_0 is the melt yield stress, η_0 the zero-shear viscosity, λ the relaxation time, n the power law index, and a the Yasuda parameter. As PS (lines in bottom Figure 3) does not exhibit an apparent yield stress, Equation (5) then becomes the regular Carreau–Yasuda model. The fitting parameters for ABS and PS are presented in Table 4.

Table 4. Parameters of complex viscosity fitting to the modified Carreau–Yasuda model for ABS Equation (5) and PS samples (Equation (5) with no σ_0); Results for both fused filament fabrication (FFF-) and pellet-based additive manufacturing (PBAM); before FFF a conventional single screw extrusion (SSE) is performed.

Processing Technique	Entry	Sample	σ_0 (Pa)	η_0 (Pa·s)	λ (s)	*a* (-)	*n* (-)
-	1	ABS Raw	2797	24,073	0.55	0.35	0.32
SSE	2	ABS Filament	2516	22,452	0.63	0.37	0.35
SSE + FFF	3	ABS_220_0.15_40_FFF	2824	17,983	0.43	0.41	0.34
	4	ABS_270_0.15_40_FFF	3130	19,369	0.45	0.40	0.34
	5	ABS_220_0.25_40_FFF	2979	18,654	0.46	0.42	0.34
	6	ABS_270_0.25_40_FFF	2905	18,817	0.44	0.40	0.33
	7	ABS_220_0.15_120_FFF	3073	18,826	0.49	0.41	0.35
	8	ABS_270_0.15_120_FFF	2758	19,793	0.55	0.39	0.36
	9	ABS_220_0.25_120_FFF	3046	19,356	0.49	0.40	0.34
	10	ABS_270_0.25_120_FFF	2836	20,397	0.51	0.39	0.34
PBAM	11	ABS_220_0.25_40_PBAM	2139	32,862	0.78	0.34	0.33
	12	ABS_270_0.25_40_PBAM	2369	43,684	1.45	0.32	0.34
-	13	PS Raw	-	12,423	0.23	0.56	0.21
SSE	14	PS Filament	-	8530	0.18	0.57	0.24
SSE + FFF	15	PS_240_0.15_40_FFF	-	6833	0.14	0.58	0.24
	16	PS_270_0.15_40_FFF	-	5093	0.11	0.59	0.24
	17	PS_240_0.25_40_FFF	-	6885	0.15	0.58	0.24
	18	PS_270_0.25_40_FFF	-	5953	0.13	0.56	0.23
	19	PS_240_0.15_120_FFF	-	7094	0.16	0.58	0.25
	20	PS_270_0.15_120_FFF	-	6105	0.14	0.57	0.25
	21	PS_240_0.25_120_FFF	-	7628	0.19	0.58	0.26
	22	PS_270_0.25_120_FFF	-	6064	0.15	0.60	0.25
PBAM	23	PS_240_0.25_40_PBAM	-	8671	0.21	0.58	0.26
	24	PS_270_0.25_40_PBAM	-	6773	0.26	0.65	0.31

An inspection of the fitting parameters in Table 4 allows a better understanding of the structural changes that occurred in both materials due to processing. In the case of ABS, the experimental complex viscosity data in Figure 3a,b seem at first sight not to change much after the different processing steps. However, the fitting results depict a decrease in the zero-shear viscosity in the steps of both filament production and 3D printing. The zero-shear viscosity decreases around 7% after the filament fabrication and from 15 to 25% after FFF, compared to the raw material. The melt yield stress in turn first decreases in the filament fabrication step, but after FFF the materials exhibit an increase as high as 12% with respect to the raw material. The reduction in the viscosity of ABS can be related to chain fission of the main chains [58] so that the contribution of the PB-g-SAN phase becomes more pronounced, increasing the melt yield stress. Moreover, the oxidation of the grafted PB can lead to a de-grafting of SAN, which can be one of the reasons for the decrease in the zero-shear viscosity [58].

For PS, the filament fabrication rather strongly reduces the zero-shear viscosity of the raw material by 31% (see entries 13 and 14 in Table 4). If the printing processing has been carried out at 240 °C, the decrease in the viscosity ranges from −39 to −45% compared to the raw material and from −10 to −20% compared to the filament (see entries 15, 17, 19 and 21 in Table 4). Even more pronounced degradation occurs if PS is printed at 270 °C, with viscosity values −50 to −59% lower than the raw material and −28 to −40% lower than the filament (see entries 16, 18, 20 and 22 in Table 4). This indicates that at 240 °C, the most critical step in the degradation of PS is the filament fabrication, whereas at 270 °C both the SSE and FFF step lead to major changes in the structure.

For all FFF data in Table 4, λ decreases with processing steps, and a and n slightly increase with the processing steps. The same has been reported by Berzin et al. [59]

upon studying the controlled degradation of PP during extrusion. The relaxation time λ is directly related to the average molar mass of the polymer [60] so it is logical that it follows the same trend of the complex viscosity, for ABS and PS processed via FFF. An increase in *n* indicates that the material linear viscoelastic behavior is closer to the conventional Newtonian behavior, with the shear-thinning effect being less pronounced. This has been attributed to the decrease in the average molar mass and narrowing of dispersity of the polymer [59,61].

The ANOVA results for the zero-shear viscosity of FFF specimens allow us to conclude that the only significant factors are the printing velocity for ABS (p-value < 0.05) and the printing temperature for PS (p-value < 0.002); the other p-values can be seen in Table B2 of Appendix B. Lower printing velocities result in a lower zero-shear viscosity in the case of ABS, and high printing temperatures result in a lower zero-shear viscosity for PS. The (ABS) melt yield stress was, although not significantly affected by any of the ANOVA factors, showing that the changes for this property are quite limited and consistent with the very similar data points at low frequencies.

The measured complex viscosity variations for ABS and PS printed via the second AM technique PBAM are shown in Figure 4 (open symbols). The plots of the raw materials, filaments and specimens printed via FFF under similar conditions are included for comparison. The fitting parameters of the complex viscosity (lines in Figure 4) are again shown in Table 4. For the PBAM printed ABS, the complex viscosity variations in Figure 4a show that these samples exhibit somewhat higher values than the raw material and filaments. An analysis of the fitting parameters in Table 4 indicates a completely different trend than the one observed for the FFF printed specimens.

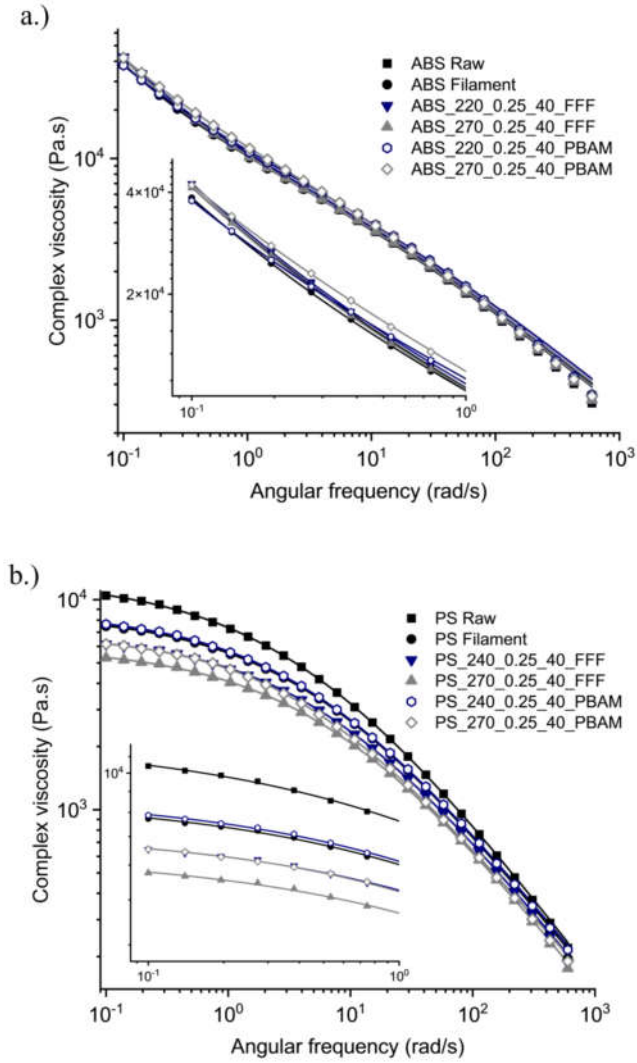

Figure 4. Effect of type of printing technique on the complex viscosity of: (a) ABS; and (b) PS. The lines represent the (modified) Carreau–Yasuda fitting.

Compared to the raw material, the melt yield stress decreases by 23 and 15%, and the viscosity increases by 35 and 81% in case the material has been printed at 220 and

270 °C, respectively. This suggests that the printing conditions such as shear rate, residence time and presence of residual oxygen, have resulted under PBAM conditions in a completely different structural changes for ABS. The increase in viscosity may be related to the cross-linking formation in the PB-g-SAN phase of ABS. As the screw speed used to produce specimens via PBAM is 0.8 rpm, which is significantly lower than the one used to process the feedstock (raw material) for FFF (27 rpm), the mechanical stresses related to PBAM are lower than the ones used to manufacture the feedstock. Hence, cross-linking in the PB-g-SAN phase is predominant over chain fission under PBAM conditions.

In the case of PS, as shown in Figure 4b, the PBAM process leads to less structural variations than the FFF process. If processed at 240 °C via PBAM, the complex viscosity plot overlaps the curve for the filament manufactured via SSE. If processed at 270 °C via PBAM, the complex viscosity plot still overlaps the one for the FFF printed specimen at 240 °C. The reduction in the zero-shear viscosity in Table 4 is 30% and 45% for the materials printed via PBAM, compared to the raw material. Even though structural changes still happened, their effect is thus less pronounced in PBAM compared to FFF.

To further establish correlations between the processing conditions and the polymer structure, SEC traces have been obtained for all the materials (raw, filament, and after FFF and PBAM). The corresponding values of the mass average molar mass (M_m) and dispersity ($Đ$) are shown in Table 5. ABS specimens show a decrease in M_m, from the raw material to the filament, with a further decrease after FFF processing. The dispersity is increased from the raw material after the first processing step (from 1.36 to 2.16), and after FFF it ranges from 2.04 to 2.12. The ABS samples produced via PBAM presented fractions that could not be dissolved, indicating cross-linking. The

M_m results for these ABS samples in Table 5 therefore only account for the soluble fraction and cannot be directly correlated with the rheological tests. However, the already discussed increase in the zero-shear viscosity for PBAM samples is compatible with the cross-linking formation assumption, again indicating that this processing route leads to a different degradation mechanism of the material compared to FFF.

Table 5. Mass average molar mass (M_m) and dispersity (Đ) for ABS and PS raw material, their filaments and after printing via FFF and PBAM; only soluble fraction for ABS.

Sample—ABS	M_m (kg mol^{-1})	Đ	Sample—PS	M_m (kg mol^{-1})	Đ
ABS Raw	121.5	1.36	PS Raw	301.6	2.19
ABS Filament	120.0	2.16	PS Filament	278.1	2.26
ABS_220_0.15_40_FFF	116.3	2.04	PS_240_0.15_40_FFF	270.3	2.16
ABS_270_0.15_40_FFF	119.2	2.00	PS_270_0.15_40_FFF	256.1	2.35
ABS_220_0.25_40_FFF	116.4	2.07	PS_240_0.25_40_FFF	274.2	2.06
ABS_270_0.25_40_FFF	118.4	2.06	PS_270_0.25_40_FFF	267.5	2.72
ABS_220_0.15_120_FFF	117.8	2.05	PS_240_0.15_120_FFF	274.6	2.22
ABS_270_0.15_120_FFF	117.7	1.98	PS_270_0.15_120_FFF	268.1	2.21
ABS_220_0.25_120_FFF	115.9	2.12	PS_240_0.25_120_FFF	270.7	2.19
ABS_270_0.25_120_FFF	115.8	2.12	PS_270_0.25_120_FFF	265.8	2.14
ABS_220_0.25_40_PBAM	116.5	2.04	PS_240_0.25_40_PBAM	285.9	2.22
ABS_270_0.25_40_PBAM	117.3	2.68	PS_270_0.25_40_PBAM	267.0	2.23

Regarding PS, the trends for M_m in Table 5 confirm the rheological testing results. M_m decreases 8% from the raw material to the filament and a further decrease is observed after the FFF process, especially at 270 °C, with decreases ranging from -9 to 15%. For the PBAM processed specimens, the decrease in M_m is only 5 and 11% for the specimens processed at 240 and 270 °C, respectively. This again puts forward the reduced structural changes in PS if processed via this route. For completeness it is mentioned here that no major trends are noticed for the dispersity in Table 5, so it is likely the variations in n are related to M_m variations only.

The scaling of η_0 with M_m for ABS and PS is shown in Figure 5, and is based on the well-known equation for linear polymers: $\eta_0 = KM_m^{\alpha}$ [62], in which K is a proportionality factor and α = 3.4. For ABS (Figure 5a), the values for the PBAM samples are not included to increase the correlation potential; however, a rather weak correlation between both properties is still observed as evident from a low coefficient of determination R^2. It should although be admitted that the M_m variation range is rather small compared to a standard range to identify a 3.4 type of power. The data for the ABS FFF samples are also rather scattered, revealing that the FFF process does not lead to very clear systematic variations, even though both properties are decreased after this processing step. In contrast, as shown in Figure 5b, PS samples exhibit a stronger correlation between both properties, indicating that the processing parameters strongly influenced the degradation. This is also obvious from the larger M_m range in Figure 5b compared to Figure 5a.

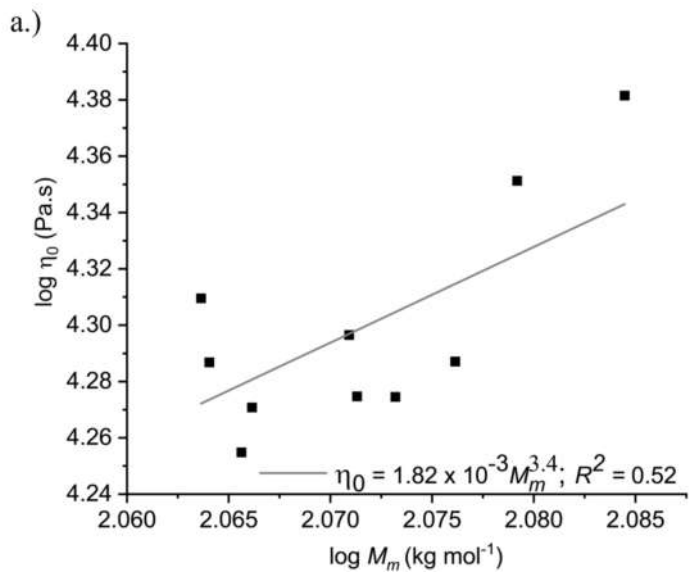

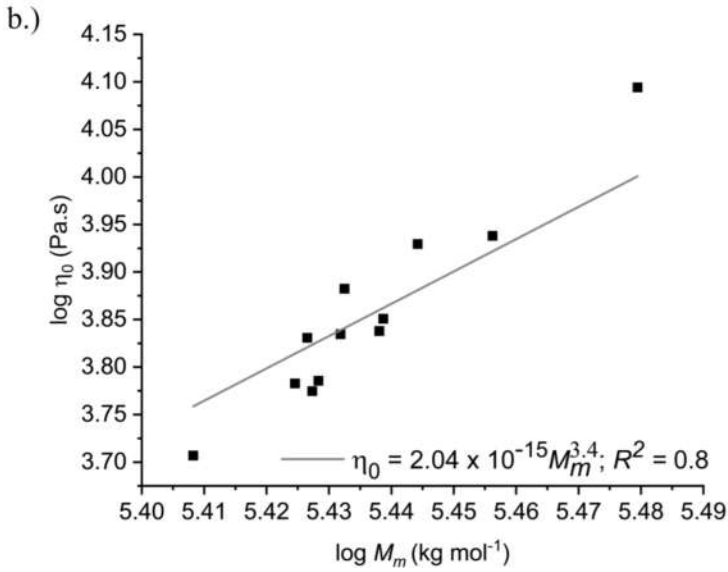

Figure 5. Scaling of zero-shear viscosity with mass average molar mass for: (a) ABS; and (b) PS. Squares are the data from Table 4 and Table 5. Line is the fit.

Further analysis is possible via the consideration of FTIR results. Consistent with literature data [63], important peaks can be assigned for raw PS and ABS, as shown in Figure 6. For the other samples, the spectra are included in Appendix B (Figure B1). Because styrene is present in both PS and ABS, several peaks are shared between these materials including two aliphatic CH stretching signals at around 2920 and 2850 cm^{-1}, 3 to 5 aromatic CH stretching signals between 3000 and 3100 cm^{-1} and two aromatic CH wagging signals at approximately 700 and 750 cm^{-1}, with the second one at one third of the height of the first one. ABS presents extra peaks, which are attributed to triple CN bond of the acrylonitrile group at 2237 cm^{-1} and two peaks that refer to the PB phase. They are centered at 965 and 910 cm^{-1}, and represent stretches regarding CH in *trans* butadiene and CH_2 in vinyl butadiene [64].

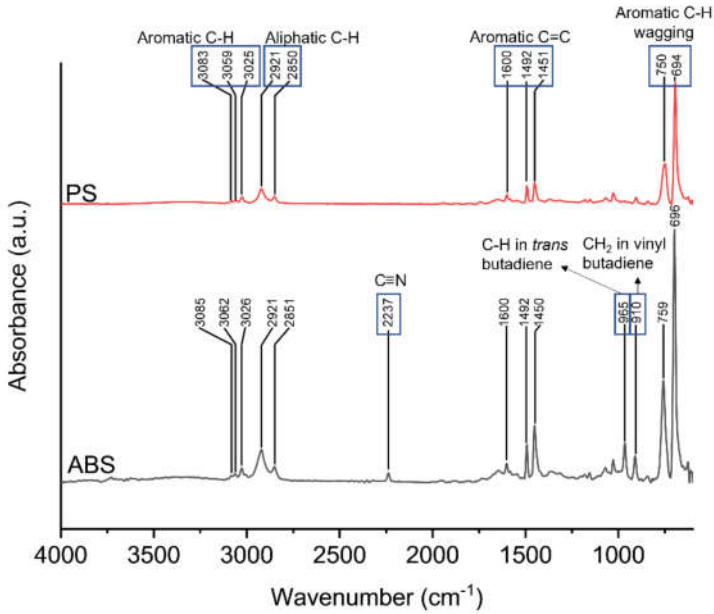

Figure 6. Most important peak assignments for raw PS and ABS material in the Fourier Transform infrared spectra.

To assess the degradation of the PB phase in ABS it has been recommended to mainly inspect the variation in the ratios R1 and R2 (Equation (1) and Equation (2)) [41], with the results in the present work shown in Figure 7. Upon comparing the results for the filament and samples prepared via FFF and PBAM with the raw material, no (clearly) statistically significant differences are seen for both R1 and R2, highlighting that FTIR can be less sensitive than rheological analysis.

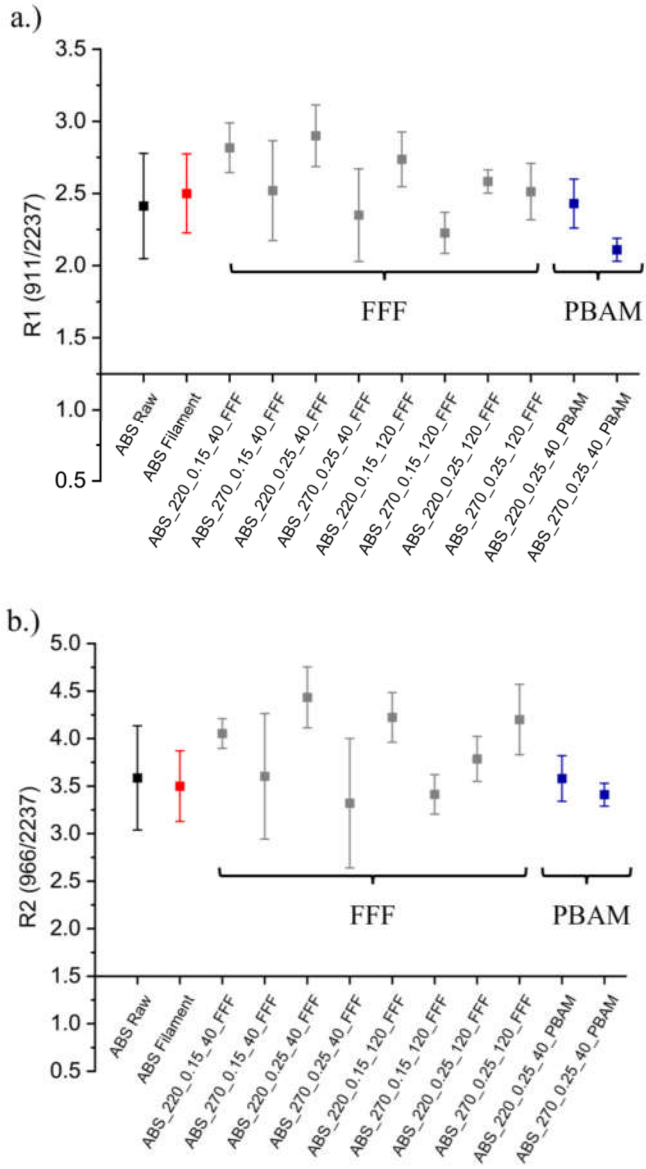

Figure 7. Measured Fourier Transform Infrared (FTIR) ratios for the ABS raw material, filament, samples manufactured via FFF and via PBAM. (a): Equation (1) and (b) Equation (2); colors as guide of the eye to identify raw materials from processed materials.

It is interesting to evaluate oxygen-related FTIR peaks [65] as well, noting that such moieties may also be due to the presence of additives [66,67]. Originally, ABS and PS have no hydroxyl (~3296 cm^{-1}) or carbonyl groups (~1723 cm^{-1}), nor peaks in the region of C-O stretching vibrations (~1000–1300 cm^{-1}). Nevertheless, it has been indicated that thermo-mechanical degradation may induce several reactions that can be responsible for the appearance of a wide range of oxidative moieties [65,68]. Due to the limited amount of oxygen in the polymer melt, it is at first sight unlikely that radicals are easily converted in peroxy radicals [69], so that the FTIR spectra may present no (significant) changes regarding the peaks of hydroxyl, carbonyl or other C-O stretches. Indeed, in the present work, no major changes are found for ABS, as shown in Figure 8a for the carbonyl region and in Appendix B for the hydroxyl and C-O stretches regions (Figure B2). However, in previous work [32], FTIR spectra of mass polymerized ABS samples manufactured via FFF and PBAM have been compared and samples prepared via FFF displayed larger peaks around 1250 and 1750 cm^{-1}, which regards C=O and C-O stretches in ester moieties, indicating the more pronounced degradation of ABS via FFF. This can be related to the different processing conditions in that work or to the different type of ABS (mass polymerized vs. emulsion polymerized).

For PS, no major differences in the hydroxyl groups band have been detected (see Figure B3 of Appendix B). The carbonyl group region, however, exhibited differences between the specimens, as is clear from the zoomed wavenumber range in Figure 8b. A clear increase is observed for the carbonyl absorption band at 1743 cm^{-1}. Upon studying thermal and mechanical degradation of PS via FTIR in air, D'Esposito et al. [70] also found a prominent peak around 1730 cm^{-1} attributed to an aldehydic compound. Between 1656 and 1644 cm^{-1} an increase in the absorption peak can also emerge because of a disproportionation reaction leading to double bond formation

[70]. Furthermore, the sample PS_270_0.15_40, showing the biggest drop in the mass average molar mass and viscosity, exhibits the highest peak among FFF samples. This indicates a higher level of degradation for the highest temperature and longer residence time.

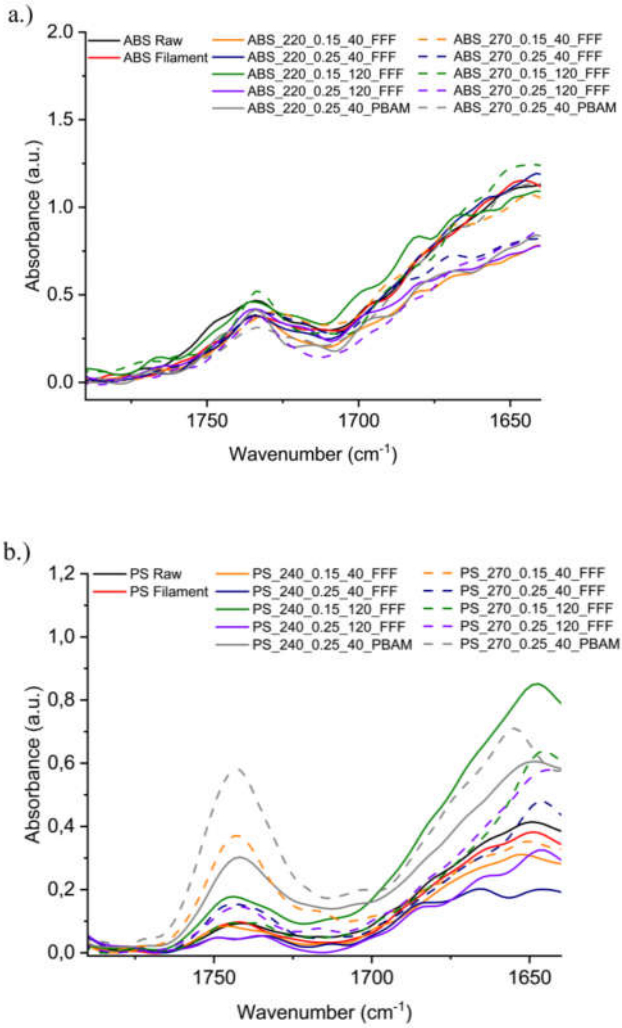

Figure 8. Carbonyl stretches region on FTIR spectra of: (a) ABS; and (b) PS samples.

4. 4. 3. Analysis of variations in color, specific mechanical energy, mechanical properties and morphology

One of the possible outcomes of degradation due to processing is yellowing [58,65,71]. Such discoloration is attributed for the formation of carbonyl substituents during thermo-oxidative degradation, although as in the present work a yellowing is not automatically captured FTIR sensitivity wise specifically for low oxygen contents (cf. Figure 7 and Figure 8). It should be realized that a color change is likely undesirable and may limit the range of applications of the materials, especially in case aesthetics are important. A visual inspection of the ABS specimens produced via FFF and PBAM, as incorporated in Figure 9, confirms the yellowing due to processing. This feature is more pronounced for the specimens produced via FFF at 270 °C, whereas PS samples did not show any visual color changes, as can be seen in Appendix B (Figure B4).

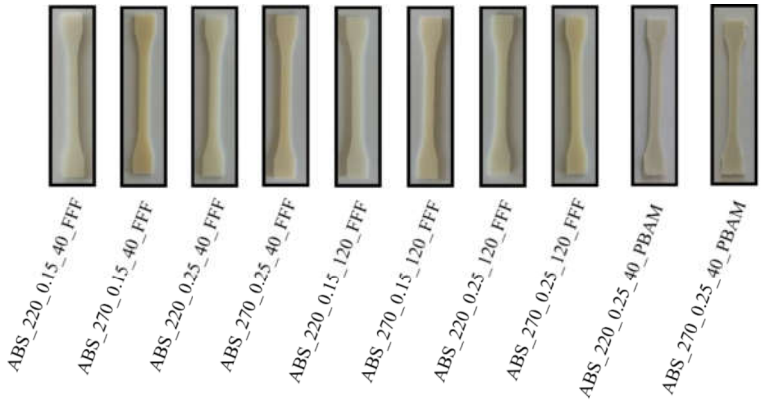

Figure 9. Variation in the color of ABS specimens produced via FFF and PBAM.

The ABS yellowing has been quantified by means of the yellowness index (YI), as shown in Figure 10. Every processing step (SSE, SSE + FFF or PBAM) leads to an increase in the YI of the ABS specimens. After filament production (SSE), the YI value increased by 33%. For FFF an increase in YI ranging from 60 to 90% and from 132 to 260% is measured for samples processed at 220 and 270 °C, respectively, putting forward that a two-step processing enables more opportunity for thermo-oxidation. This is somewhat supported only by specimens produced via PBAM at 220 °C exhibiting an increase in the YI like the FFF samples, whereas at 270 °C the YI of a specimen printed via PBAM is 20% lower than its counterpart produced via FFF, being in the range of samples processed at 220 °C. Under PBAM conditions, more thermal degradation likely takes place and thus less thermo-oxidative degradation.

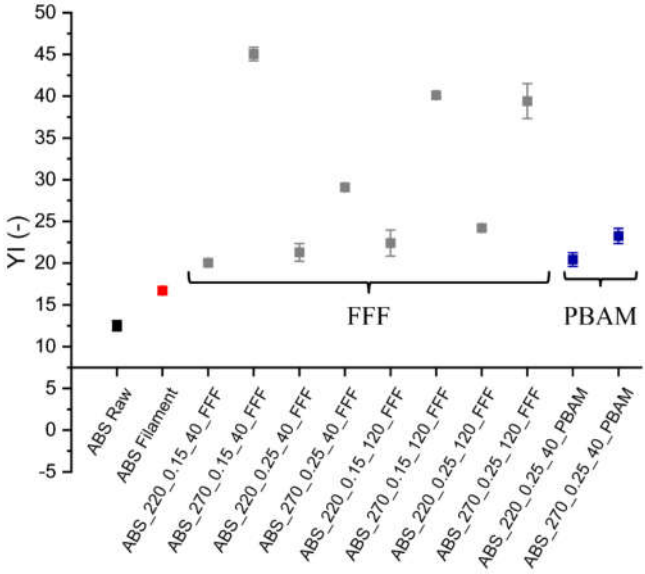

Figure 10. Yellowing index (YI) for ABS raw material, filament, specimens manufactured via FFF and via PBAM: colors as guide of the eye to identify raw materials from processed materials.

One of the factors causing yellowing in ABS samples during processing is the oxidation of the PB phase [58]. As an example, mass polymerized ABS usually shows a lower YI than emulsion polymerized ABS due to its lower PB content [41]. The FFF sample ABS_270_0.15_40 shows the highest increase in the YI, which might be due to a combination of a high temperature and longer residence time (lower printing velocity and layer thickness), indicating a higher level of degradation for this specimen. Even though no major changes are seen in the FTIR spectra of ABS, the yellowing indicates that some level of degradation occurred.

The specific mechanical energy related to the processing of ABS and PS via SSE and PBAM was calculated according to Equation (4) and are reported in Table 6. From the results, it is possible to observe that SSE has a higher SME for both ABS and PS, corroborating the degradation analysis of these materials which indicated a higher level of degradation on the preparation of filaments via SSE.

Table 6. SME related to single-screw extrusion (SSE) process and pellet-based additive manufacturing (PBAM).

	ABS		**PS**	
	SSE	PBAM	SSE	PBAM
Torque (Nm)	75	27	90	32
Screw speed (rpm)	27	0,8	13	0,1
Output (kg/h)	1,5	0,04	1	0,02
SME (kJ/h)	17	6	15	2

The tensile strength results for additively manufactured ABS and PS are shown in Figure 11 (raw data in Table B3 of Appendix B). The tensile strength of ABS produced via FFF is mostly affected by the layer thickness. Printing with a small layer thickness yields the highest values of tensile strength. This is probably due to the increase in the exit contact pressure [72], which forces the layers into a more intimate

contact, improving the bond strength between the deposited filaments. Printing at higher temperatures lead to similar or slightly lower results for tensile strength, while the printing velocity did not show specific trends.

The latter trend is not captured for PS samples. If both techniques (FFF and PBAM) are compared, at 240 °C, the results for tensile properties are similar, while a decrease in the tensile strength is seen for the PS printed via PBAM at 270 °C. This suggests that the best (FFF) printing parameters for PS are printing with a low layer thickness, lower temperature, and a high printing velocity. Furthermore, printing PS with PBAM under such conditions may be an alternative to further reduce degradation.

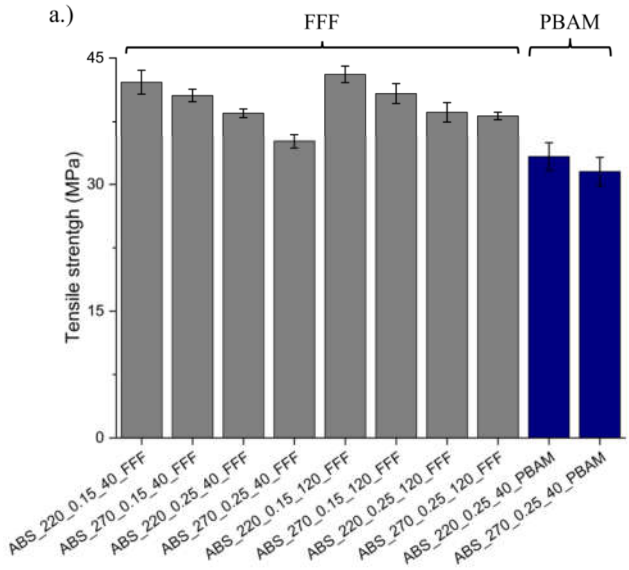

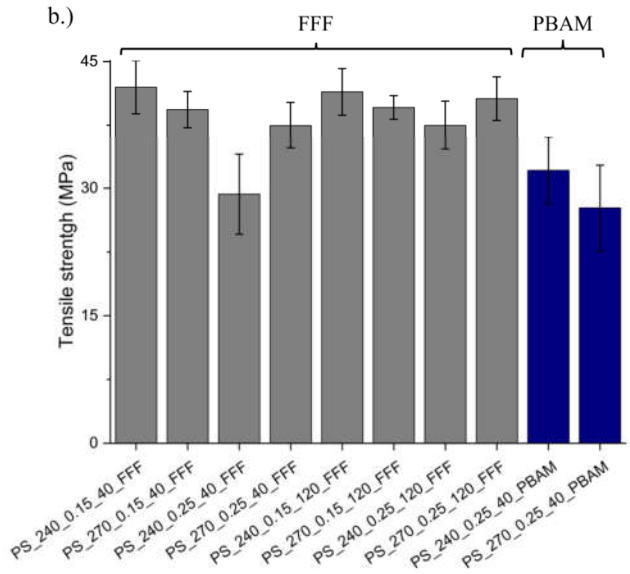

Figure 11. Comparison of tensile strength of: (a) ABS; and (b) PS specimens printed via FFF and PBAM.

The results for the tensile modulus and strain at break are, for completeness, included in Appendix B (Table B3), together with the stress–strain curves for ABS and PS samples (Figures B5 and B6, respectively). The tensile modulus of ABS and PS are not influenced by the printing parameters and printing technique, as no statistically significant differences are seen between the samples. The same is observed for the strain at break of samples produced via FFF. Nevertheless, samples produced via PBAM usually exhibit lower strain at break than FFF samples. For instance, ABS samples manufactured via PBAM exhibit a decrease in this property of 50 and 52%, if printed at 220 and 270 °C, respectively. A similar trend in strain at break for ABS has been reported by La Gala et al. [32]. A reduction in the strain at break in ABS specimens has been attributed to the degradation of the PB phase [65]. However, since no major changes in FTIR and YI data are perceived between FFF and PBAM ABS

in the present work, it is likely that this is due to a lower bond strength between the deposited filaments, leading to premature failure of the specimens. Furthermore, for PS, a decrease of 46% of strain at break is seen for the sample printed at 270 °C via PBAM compared to FFF. Hence, it is worthwhile improving the actual PBAM process from a deposition point of view.

Fracture surfaces of tensile tested ABS and PS produced via FFF and PBAM are included in Figure 12, to better interpret the variations in mechanical results obtained via both techniques. For ABS printed at 220 °C, the interface between layers is more noticeable and the coalescence level is lower, supporting the hypothesis of a lower bond strength for these specimens, specifically for the PBAM technique. For PS printed at 240 °C, both morphologies are similar and both techniques yield similar mechanical results. For the materials printed at 270 °C, the specimens produced via PBAM present a rougher structure, highlighting the relevance of PBAM optimization in future work, concerning machine design to improve the melt efficiency and to reduce the thermal degradation. In addition, few possibilities to improve the results may be performed based on processing parameters, namely layer thickness (LT) and nozzle diameter (ND). It has been reported that an increase the ratio of ND to LT, leads to an increase on the final properties of the 3D printed parts, due to an increased contact surface between layers [73–75]. For instance, a reduced layer thickness may be employed, to increase the exit contact pressure of the deposited polymer filament onto the previous one, improving the interlayer bonding [72]. In addition, by employing a larger nozzle diameter, the force to spread the deposited filament onto the previous one is higher, which increases the contact surface between them [76]. For PS, it can be stated that PBAM, as conducted in the present work, is already a suitable alternative to produce parts with less undesired structural changes and similar properties than FFF in case the printing temperature is 240 °C.

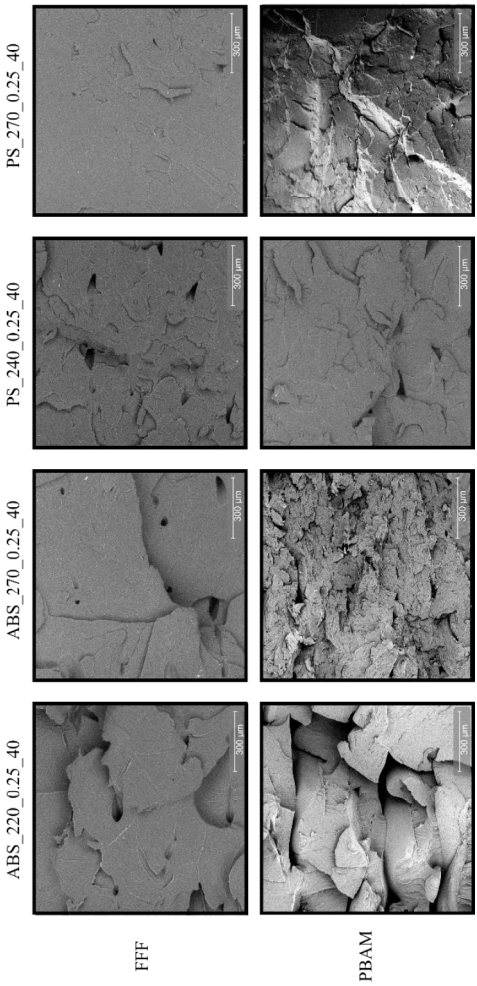

Figure 12. Scanning electron microscopy (SEM) micrographs of tensile fractured ABS and PS specimens produced via FFF and PBAM.

4. 5. Conclusions

The influence of printing temperature, layer thickness, printing velocity and printing technique on the degradation of ABS and PS has been assessed and compared for FFF and PBAM. For ABS, manufacturing samples via FFF with prior filament production (SSE) are characterized by a different degradation mechanism (more fission) than manufactured samples via PBAM (more cross-linking). This has been deduced by different variations in the zero-shear viscosity, melt yield stress and molar mass, due to the lower mechanical stresses employed in PBAM and thus a more thermally driven degradation. Even though no clear differences in the FTIR spectra have been noticed, the YI measurements show that samples produced via FFF at higher temperatures present a higher level of degradation. Hence, care should be taken upon using (ABS) FTIR data ignoring potential sensitivity issues.

For PS, FFF with prior SSE promotes a higher level of degradation according to the same mechanism compared to PBAM, as is clear from more significant zero-shear viscosity and average molar mass decreases. PBAM can even be preferred over FFF, as the mechanical layer-by-layer properties are also acceptable under the selected printing conditions. For ABS, further optimization of such PBAM conditions is still needed as likely too much cross-linking is still active under the currently selected conditions.

In addition to the optimization of the PBAM process, other materials of interest for extrusion-based additive manufacturing could be tested to obtain more insights on the degradation during 3D printing via both techniques.

REFERENCES

1. Turner, B.N.; Strong, R.; Gold, S.A. A review of melt extrusion additive manufacturing processes: I. Process design and modeling. *Rapid Prototyp. J.* **2014**, *20*, 192–204, doi:10.1108/RPJ-01-2013-0012.
2. Penumakala, P.K.; Santo, J.; Thomas, A. A critical review on the fused deposition modeling of thermoplastic polymer composites. *Compos. Part B Eng.* **2020**, *201*, 108336, doi:10.1016/j.compositesb.2020.108336.
3. Volpato, N.; Kretschek, D.; Foggiatto, J.A.; Gomez da Silva Cruz, C.M. Experimental analysis of an extrusion system for additive manufacturing based on polymer pellets. *Int. J. Adv. Manuf. Technol.* **2015**, *81*, 1519–1531, doi:10.1007/s00170-015-7300-2.
4. La Gala, A.; Fiorio, R.; Erkoç, M.; Cardon, L.; D'hooge, D.R. Theoretical evaluation of the melting efficiency for the single-screw micro-extrusion process: The case of 3D printing of abs. *Processes* **2020**, *8*, 1–22, doi:10.3390/pr8111522.
5. Moreno Nieto, D.; Casal López, V.; Molina, S.I. Large-format polymeric pellet-based additive manufacturing for the naval industry. *Addit. Manuf.* **2018**, *23*, 79–85, doi:10.1016/j.addma.2018.07.012.
6. Wang, S.; Daelemans, L.; D'hooge, D.R.; Couck, L.; Van Den Broeck, W.; Cornillie, P.; Gou, M.; De Clerck, K.; Cardon, L. Lifting the quality of fused filament fabrication of polylactic acid based composites. *Compos. Part B Eng.* **2021**, *210*, 108613, doi:10.1016/j.compositesb.2021.108613.
7. Mohamed, O.A.; Masood, S.H.; Bhowmik, J.L. Optimization of fused deposition modeling process parameters: a review of current research and future prospects. *Adv. Manuf.* **2015**, *3*, 42–53, doi:10.1007/s40436-014-0097-7.
8. Ngo, T.D.; Kashani, A.; Imbalzano, G.; Nguyen, K.T.Q.; Hui, D. Additive manufacturing (3D printing): A review of materials, methods, applications and challenges. *Compos. Part B Eng.* **2018**, *143*, 172–196, doi:10.1016/j.compositesb.2018.02.012.
9. Van Waeleghem, T.; Marchesini, F.H.; Cardon, L.; D'hooge, D.R. Melt exit flow modelling and experimental validation for fused filament fabrication: From Newtonian to non-Newtonian effects. *J. Manuf. Process.* **2022**, *77*, 138–150, doi:10.1016/j.jmapro.2022.03.002.
10. La Gala, A.; Fiorio, R.; Ceretti, D.V.A.; Erkoç, M.; Cardon, L.; D'hooge, D.R. A Combined Experimental and Modeling Study for Pellet-Fed Extrusion-Based Additive Manufacturing to Evaluate the Impact of the Melting Efficiency. *Materials (Basel).* **2021**, *14*, 5566, doi:10.3390/ma14195566.
11. Vilaplana, F.; Karlsson, S.; Ribes-Greus, A. Changes in the microstructure and morphology of high-impact polystyrene subjected to multiple processing and thermo-oxidative degradation. *Eur. Polym. J.* **2007**, *43*, 4371–4381, doi:10.1016/j.eurpolymj.2007.07.017.
12. De Keer, L.; Van Steenberge, P.H.M.; Reyniers, M.; Marin, G.B.; Hungenberg, K.; Seda, L.; D'hooge, D.R. A complete understanding of the reaction kinetics for the industrial production process of expandable polystyrene. *AIChE J.* **2017**, *63*, 2043–2059, doi:10.1002/aic.15587.
13. Peterson, A.M. Review of acrylonitrile butadiene styrene in fused filament fabrication: A plastics engineering-focused perspective. *Addit. Manuf.* **2019**, *27*, 363–371, doi:10.1016/j.addma.2019.03.030.

14. Moore, J.D. Acrylonitrile-butadiene-styrene (ABS) - a review. *Composites* **1973**, *4*, 118–130, doi:10.1016/0010-4361(73)90585-5.
15. Dey, A.; Eagle, I.N.R.; Yodo, N. A review on filament materials for fused filament fabrication. *J. Manuf. Mater. Process.* **2021**, *5*, doi:10.3390/jmmp5030069.
16. Akintola, T.M.; Tran, P.; Sweat, R.D.; Dickens, T. Thermomechanical multifunctionality in 3d-printed polystyrene-boron nitride nanotubes (Bnnt) composites. *J. Compos. Sci.* **2021**, *5*, doi:10.3390/jcs5020061.
17. Sevastaki, M.; Suchea, M.P.; Kenanakis, G. 3D Printed Fully Recycled Tio2-Polystyrene Nanocomposite Photocatalysts for Use Against Drug Residues. *Nanomaterials* **2020**, *10*, 1–11, doi:10.3390/nano10112144.
18. Hinsken, H.; Moss, S.; Pauquet, J.; Zweifela, H. Degradation of Polyolefins during Melt Processing. **1991**, *34*, 279–293.
19. Colin, X.; Verdu, J. Polymer degradation during processing. *Comptes Rendus Chim.* **2006**, *9*, 1380–1395, doi:10.1016/j.crci.2006.06.004.
20. Capone, C.; Di Landro, L.; Inzoli, F.; Penco, M.; Sartore, L. Thermal and mechanical degradation during polymer extrusion processing. *Polym. Eng. Sci.* **2007**, *47*, 1813–1819, doi:10.1002/pen.20882.
21. Gol'dberg, V.M.; Zaikov, G.E. Kinetics of mechanical degradation in melts under model conditions and during processing of polymers-A review. *Polym. Degrad. Stab.* **1987**, *19*, 221–250, doi:10.1016/0141-3910(87)90057-7.
22. Whitlock, L.R.; Porter, R.S. The source of degradation during extrusion of polystyrene. *J. Appl. Polym. Sci.* **1973**, *17*, 2761–2770, doi:10.1002/app.1973.070170913.
23. Abbas-Abadi, M.S. The effect of process and structural parameters on the stability, thermo-mechanical and thermal degradation of polymers with hydrocarbon skeleton containing PE, PP, PS, PVC, NR, PBR and SBR. *J. Therm. Anal. Calorim.* **2021**, *143*, 2867–2882, doi:10.1007/s10973-020-09344-0.
24. Schyns, Z.O.G.; Shaver, M.P. Mechanical Recycling of Packaging Plastics: A Review. *Macromol. Rapid Commun.* **2021**, *42*, 1–27, doi:10.1002/marc.202000415.
25. Schweighuber, A.; Felgel-Farnholz, A.; Bögl, T.; Fischer, J.; Buchberger, W. Investigations on the influence of multiple extrusion on the degradation of polyolefins. *Polym. Degrad. Stab.* **2021**, *192*, 109689, doi:10.1016/j.polymdegradstab.2021.109689.
26. Zander, N.E.; Gillan, M.; Lambeth, R.H. Recycled polyethylene terephthalate as a new FFF feedstock material. *Addit. Manuf.* **2018**, *21*, 174–182, doi:10.1016/j.addma.2018.03.007.
27. Lee, D.; Lee, Y.; Lee, K.; Ko, Y.; Kim, N. Development and Evaluation of a Distributed Recycling System for Making Filaments Reused in Three-Dimensional Printers. *J. Manuf. Sci. Eng. Trans. ASME* **2019**, *141*, doi:10.1115/1.4041747.
28. Anderson, I. Mechanical Properties of Specimens 3D Printed with Virgin and Recycled Polylactic Acid. *3D Print. Addit. Manuf.* **2017**, *4*, 110–115, doi:10.1089/3dp.2016.0054.
29. Hawkins, W.L. *Polymer Degradation and Stabilization*; Polymers Properties and Applications; Springer: Berlin, 1984; ISBN 978-3-642-69378-6.
30. Badia, J.D.; Gil-Castell, Ó.; Teruel-Juanes, R.; Ribes-Greus, A. Recycling of Polylactide. *Encycl. Renew. Sustain. Mater.* **2020**, 282–295,

doi:10.1016/b978-0-12-803581-8.10569-7.
31. Gijsman, P. Review on the thermo-oxidative degradation of polymers during processing and in service. *E-Polymers* **2008**, 1–34, doi:10.1515/epoly.2008.8.1.727.
32. La Gala, A.; Ceretti, D.V.A.; Fiorio, R.; Cardon, L.; D'hooge, D.R. Comparing pellet- and filament-based additive manufacturing with conventional processing for ABS and PLA parts. *J. Appl. Polym. Sci.* **2022**.
33. Gradwohl, M.; Chai, F.; Payen, J.; Guerreschi, P.; Marchetti, P.; Blanchemain, N. Effects of two melt extrusion based additive manufacturing technologies and common sterilization methods on the properties of a medical grade PLGA copolymer. *Polymers (Basel).* **2021**, *13*, 1–15, doi:10.3390/polym13040572.
34. Fernandez, E.; Ceretti, D.A.; Wang, S.; Jiang, Y.; Zhang, J.; D'hooge, D.R.; Cardon, L. Fused filament fabrication of copolyesters by understanding the balance of inter- and intra-layer welding. *Plast. Rubber Compos.* **2020**, *0*, 1–7, doi:10.1080/14658011.2020.1855386.
35. Jagenteufel, R.; Hofstaetter, T.; Kamleitner, F.; B. Pedersen, D.; Tosello, G.; N. Hansen, H. Rheology of high melt strength polypropylene for additive manufacturing. *Adv. Mater. Lett.* **2017**, *8*, 712–716, doi:10.5185/amlett.2017.1450.
36. Chu, J.S.; Koay, S.C.; Chan, M.Y.; Choo, H.L.; Ong, T.K. Recycled plastic filament made from post-consumer expanded polystyrene and polypropylene for fused filamant fabrication. *Polym. Eng. Sci.* **2022**, 3786–3795, doi:10.1002/pen.26144.
37. Nguyen, H.T.; Crittenden, K.; Weiss, L.; Bardaweel, H. Recycle of waste tire rubber in a 3D printed composite with enhanced damping properties. *J. Clean. Prod.* **2022**, *368*, 133085, doi:10.1016/j.jclepro.2022.133085.
38. Fico, D.; Rizzo, D.; De Carolis, V.; Montagna, F.; Esposito Corcione, C. Sustainable Polymer Composites Manufacturing through 3D Printing Technologies by Using Recycled Polymer and Filler. *Polymers (Basel).* **2022**, *14*, 3756, doi:10.3390/polym14183756.
39. Madhu, N.R.; Erfani, H.; Jadoun, S.; Amir, M.; Thiagarajan, Y.; Chauhan, N.P.S. Fused deposition modelling approach using 3D printing and recycled industrial materials for a sustainable environment: a review. *Int. J. Adv. Manuf. Technol.* **2022**, *122*, 2125–2138, doi:10.1007/s00170-022-10048-y.
40. Gomes, T.E.; Cadete, M.S.; Dias-de-Oliveira, J.; Neto, V. Controlling the properties of parts 3D printed from recycled thermoplastics: A review of current practices. *Polym. Degrad. Stab.* **2022**, *196*, 109850, doi:10.1016/j.polymdegradstab.2022.109850.
41. Fiorio, R.; D'hooge, D.R.; Ragaert, K.; Cardon, L. A statistical analysis on the effect of antioxidants on the thermal-oxidative stability of commercial massand emulsion-polymerized ABS. *Polymers (Basel).* **2018**, *11*, doi:10.3390/polym11010025.
42. Adeniyi, J.B.; Kolawole, E.G. Thermal and photo-degradation of unstabilized ABS. *Eur. Polym. J.* **1984**, *20*, 43–47, doi:10.1016/0014-3057(84)90220-9.
43. Santos, R.M.; Botelho, G.L.; Machado, A. V. Artificial and natural weathering of ABS. *J. Appl. Polym. Sci.* **2010**, *116*, NA-NA, doi:10.1002/app.31663.
44. Zhu, X. Effects of acids on thermal and thermooxidative degradation of polystyrene. *Polym. Degrad. Stab.* **1997**, *57*, 163–173, doi:10.1016/s0141-

3910(96)00182-6.
45. ASTM Standard Practice for Calculating Yellowness and Whiteness Indices from Instrumentally Measured Color Coordinates. *Annu. B. ASTM Stand.* **2015**, *06*, 1–6, doi:10.1520/E0313-20.
46. Pradel, J.L.; David, C.; Quinebèche, S.; Blondel, P. Scale up tools in reactive extrusion and compounding processes. Could 1D-computer modeling be helpful? *AIP Conf. Proc.* **2014**, *1593*, 530–533, doi:10.1063/1.4873837.
47. Thompson, S.A.; Williams, R.O. Specific mechanical energy – An essential parameter in the processing of amorphous solid dispersions. *Adv. Drug Deliv. Rev.* **2021**, *173*, 374–393, doi:10.1016/j.addr.2021.03.006.
48. Montgomery, D.C. *Design and Analysis of Experiments*; 5th ed.; John Wiley & Sons: New York, NY, 2001;
49. Spoerk, M.; Arbeiter, F.; Raguž, I.; Holzer, C.; Gonzalez-Gutierrez, J. Mechanical recyclability of polypropylene composites produced by material extrusion-based additive manufacturing. *Polymers (Basel).* **2019**, *11*, doi:10.3390/polym11081318.
50. Adeniyi, J.B. Clarification and discussion of chemical transformations involved in thermal and photo-oxidative degradation of ABS. *Eur. Polym. J.* **1984**, *20*, 291–299, doi:10.1016/0014-3057(84)90050-8.
51. Cameron, G.G.; Kerr, G.P. Thermal degradation of polystyrene-I. Chain scission at low temperatures. *Eur. Polym. J.* **1968**, *4*, 709–717, doi:10.1016/0014-3057(68)90052-9.
52. Guyot, A. Recent developments in the thermal degradation of polystyrene-A review. *Polym. Degrad. Stab.* **1986**, *15*, 219–235, doi:10.1016/0141-3910(86)90052-2.
53. Münstedt, H. Rheology of rubber-modified polymer melts. *Polym. Eng. Sci.* **1981**, *21*, 259–270, doi:10.1002/pen.760210503.
54. Aoki, Y. Rheological properties of abs polymer melts having a good dispersion of rubber particles. *J. Nonnewton. Fluid Mech.* **1986**, *22*, 91–99, doi:10.1016/0377-0257(86)80005-2.
55. Bertin, M. -P; Marin, G.; Montfort, J. -P Viscoelastic properties of acrylonitrile-butadiene-styrene (ABS) polymers in the molten state. *Polym. Eng. Sci.* **1995**, *35*, 1394–1406, doi:10.1002/pen.760351711.
56. Ceretti, D.V.A.; Fiorio, R.; Van Waeleghem, T.; Desmet, A.; Florizoone, B.; Cardon, L.; D'hooge, D.R. Exploiting mono- and hybrid nanocomposite materials for fused filament fabrication with acrylonitrile butadiene styrene as polymer matrix. *J. Appl. Polym. Sci.* **2022**, *139*, 1–21, doi:10.1002/app.52922.
57. Lertwimolnun, W.; Vergnes, B. Influence of compatibilizer and processing conditions on the dispersion of nanoclay in a polypropylene matrix. *Polymer (Guildf).* **2005**, *46*, 3462–3471, doi:10.1016/j.polymer.2005.02.018.
58. Karahaliou, E.-K.; Tarantili, P.A. Stability of ABS compounds subjected to repeated cycles of extrusion processing. *Polym. Eng. Sci.* **2009**, *49*, 2269–2275, doi:10.1002/pen.21480.
59. Berzin, F.; Vergnes, B.; Delamare, L. Rheological behavior of controlled-rheology polypropylenes obtained by peroxide-promoted degradation during extrusion: Comparison between homopolymer and copolymer. *J. Appl. Polym. Sci.* **2001**, *80*, 1243–1252, doi:10.1002/app.1210.
60. Filippone, G.; Carroccio, S.C.; Mendichi, R.; Gioiella, L.; Dintcheva, N.T.; Gambarotti, C. Time-resolved rheology as a tool to monitor the progress of polymer degradation in the melt state - Part I: Thermal and thermo-oxidative

degradation of polyamide 11. *Polymer (Guildf).* **2015**, *72*, 134–141, doi:10.1016/j.polymer.2015.06.059.
61. Tzoganakis, C.; Hamielec, A.E.; Tang, Y.; Vlachopoulos, J. Controlled degradation of polypropylene: A comprehensive experimental and theoretical investigation. *Polym. Plast. Technol. Eng.* **1989**, *28*, 319–350, doi:10.1080/03602558908048602.
62. Dealy, J.M.; Larson, R.G. *Structure and Rheology of Molten Polymers*; Carl Hanser Verlag GmbH & Co. KG: München, 2006; ISBN 978-3-446-21771-3.
63. Signoret, C.; Caro-Bretelle, A.S.; Lopez-Cuesta, J.M.; Ienny, P.; Perrin, D. MIR spectral characterization of plastic to enable discrimination in an industrial recycling context: I. Specific case of styrenic polymers. *Waste Manag.* **2019**, *95*, 513–525, doi:10.1016/j.wasman.2019.05.050.
64. Saviello, D.; Pouyet, E.; Toniolo, L.; Cotte, M.; Nevin, A. Synchrotron-based FTIR microspectroscopy for the mapping of photo-oxidation and additives in acrylonitrile-butadiene-styrene model samples and historical objects. *Anal. Chim. Acta* **2014**, *843*, 59–72, doi:10.1016/j.aca.2014.07.021.
65. Salari, D.; Ranjbar, H. Study on the Recycling of ABS Resins: Simulation of Reprocessing and Thermo-oxidation. *Iran. Polym. J.* **2008**, *17*, 599–610.
66. Desrousseaux, C.; Cueff, R.; Aumeran, C.; Garrait, G.; Mailhot-Jensen, B.; Traoré, O.; Sautou, V. Fabrication of acrylonitrile-butadiene-styrene nanostructures with anodic alumina oxide templates, characterization and biofilm development test for Staphylococcus epidermidis. *PLoS One* **2015**, *10*, 1–21, doi:10.1371/journal.pone.0135632.
67. Moss, S.; Zweifel, H. Degradation and stabilization of high density polyethylene during multiple extrusions. *Polym. Degrad. Stab.* **1989**, *25*, 217–245, doi:10.1016/S0141-3910(89)81009-2.
68. Samper, M.D.; Garcia-Sanoguera, D.; Parres, F.; López, J. Recycling of expanded polystyrene from packaging. *Prog. Rubber, Plast. Recycl. Technol.* **2010**, *26*, 83–92, doi:10.1177/147776061002600202.
69. McNeill, I.C.; Razumovskii, L.P.; Gol'dberg, V.M.; Zaikov, G.E. The thermo-oxidative degradation of polystyrene. *Polym. Degrad. Stab.* **1994**, *45*, 47–55, doi:10.1016/0141-3910(94)90177-5.
70. D'Esposito, L.; Koenig, J.L. A comparison of the thermal and mechanical degradation of glassy polystyrene by Fourier transform infrared spectroscopy. *Polym. Eng. Sci.* **1979**, *19*, 162–165, doi:10.1002/pen.760190220.
71. Achtioui, T.; Lacoste, C.; Le Baillif, M.; Erre, D. Prediction of the yellowing of styrene-stat-Acrylonitrile and acrylonitrile-butadiene-styrene during processing in an internal mixer. *J. Polym. Eng.* **2018**, *38*, 983–993, doi:10.1515/polyeng-2017-0305.
72. Coogan, T.J.; Kazmer, D.O. Modeling of interlayer contact and contact pressure during fused filament fabrication. *J. Rheol. (N. Y. N. Y).* **2019**, *63*, 655–672, doi:10.1122/1.5093033.
73. Syrlybayev, D.; Zharylkassyn, B.; Seisekulova, A.; Akhmetov, M.; Perveen, A.; Talamona, D. Optimisation of Strength Properties of FDM Printed Parts—A Critical Review. *Polymers (Basel).* **2021**, *13*, 1587, doi:10.3390/polym13101587.
74. Yang, L.; Li, S.; Li, Y.; Yang, M.; Yuan, Q. Experimental Investigations for Optimizing the Extrusion Parameters on FDM PLA Printed Parts. *J. Mater. Eng. Perform.* **2019**, *28*, 169–182, doi:10.1007/s11665-018-3784-x.

75. Triyono, J.; Sukanto, H.; Saputra, R.M.; Smaradhana, D.F. The effect of nozzle hole diameter of 3D printing on porosity and tensile strength parts using polylactic acid material. *Open Eng.* **2020**, *10*, 762–768, doi:10.1515/eng-2020-0083.
76. Vicente, C.M.S.; Martins, T.S.; Leite, M.; Ribeiro, A.; Reis, L. Influence of fused deposition modeling parameters on the mechanical properties of ABS parts. *Polym. Adv. Technol.* **2020**, *31*, 501–507, doi:10.1002/pat.4787.

Chapter 5

Exploiting mono- and hybrid nanocomposite materials for fused filament fabrication with ABS as polymer matrix

5. 1. Abstract

Acrylonitrile butadiene styrene (ABS) based polymeric composites consisting of mono- and hybrid nano-compounds, i.e. graphene nanoplatelets (GNP's), multi-walled carbon nanotubes (CNT's), and titanium dioxide (TiO_2), are studied for fused filament fabrication (FFF). Rheological analysis in a screening step reveals that nanocomposites containing CNT result in a better nano-filler dispersion within the matrix and enhanced matrix interaction. The addition of GNP and TiO_2 leads to a better coalescence between the deposited filaments. For the actual FFF specimens, emphasis is on the tensile, flexural and impact properties as well as the void content. It is shown that the joint addition of GNP, CNT and TiO_2 gives rise to a remarkable synergistic effect, leading to an improved dispersion and an increased tensile modulus and strength of 3D printed ABS by 16 and 20%. Decreasing the layer thickness increases the mechanical properties of the materials, while the printing temperature does not lead to major variations of the mechanical properties, due to a dominant effect of the addition of nanoparticles. It is also shown that for well-designed composites the slower sintering and higher void content is overruled by the reinforcement effect.

5. 2. Introduction

The prospects of extrusion-based additive manufacturing (EAM) have been positively expanding in the past years. This is due to the exponential increase in the academic and technological research on this group of manufacturing techniques, with significant progress for fused filament fabrication (FFF) and pellet-based additive manufacturing (PBAM) [1–6].

FFF is an AM technique in which a polymer feedstock filament is molten and extruded through a nozzle, being deposited onto a heated bed through a layer-by-layer pattern, creating a three-dimensional (3D) structure. Parts manufactured via FFF typically exhibit anisotropic properties and the occurrence of voids is common, due to the nature and complexity of the manufacturing technique [7]. Hence, the final performance of an FFF printed part is not only dependent on the material but also closely related to the processing parameters. Not surprisingly, the macroscopic properties of additively manufactured parts are usually lower than their counterparts produced via conventional processing tools such as large-scale extrusion and injection molding [8]. The application range of FFF has thus still room to grow and further research must be carried out to fully exploit its potential.

An important design aspect is the control of the coalescence degree between FFF deposited filaments as this degree is associated to the final part strength [8–12]. Coalescence can be realized via the surface contact between deposited filaments, followed by neck growth driven by surface tension variation, so-called sintering, and the molecular diffusion and entanglement of polymer chains through/along the interface [13]. It has been specifically reported that the neck growth has a significant effect on the coalescence, but it is quickly hindered in FFF due to the rapid cooling

rates [12]. Furthermore, it has been found that the contact pressure during printing is crucial for establishing the interlayer contact for the polymer chains to diffuse to enable final part strength [14]. In any case, it may be useful to clarify the effect of the material type and properties on the bond quality and the mechanical anisotropy of 3D printed parts [13].

Acrylonitrile-butadiene-styrene polymer (ABS) is one of the most used polymeric materials for EAM/FFF, displaying under well-defined conditions a high toughness, a good dimensional stability, easy processability, and chemical resistance. ABS is a rubber-modified polymer, and its structure consists of polybutadiene (PB) particles dispersed in a styrene-acrylonitrile copolymer (SAN) phase, hence, it is a multiphase structure. The PB particles contain SAN grafts (PB-g-SAN), similar to the related high-impact polystyrene material [15]. ABS can be synthesized via emulsion or bulk polymerization, with for the latter typically a higher amount of grafts [16].

The rheological behavior of ABS has been subject to significant research [16–20]. The linear viscoelastic behavior of this material is a function of its complex multiphase structure thus the rubber phase, the grafting contribution, and the SAN phase itself. Particularly, in the low-frequency region, the so-called terminal region, a plateau is formed in a way that the storage loss modulus G' is no longer dependent on the frequency, indicating a pseudo-solid-like behavior. This behavior is further enhanced with the addition of well-dispersed nano-sized fillers [21]. The rheological properties of nanocomposites give thus indications on the state of the nanoparticle dispersion and the interactions between them and the polymer chains [22].

The addition of nano-sized fillers to a polymer matrix may be valuable in improving or generating several properties of 3D printed parts [23,24]. The potential of these materials is not limited to one single filler type and the fabrication of novel hybrid

nanocomposites may push even further the window of advanced applications. A hybrid nanocomposite consists in a combination of two or more nano-sized fillers dispersed in a polymer matrix, exhibiting improved properties than its *mono-nanocomposite* (with only one nanofiller) counterpart due to synergistic effects [25]. The synergism occurs if the interaction between the different nanoparticles creates a better response than the sum of the responses of the individual components, at the same concentration [25]. Ideally, only very low loading levels (< 5 m%) are needed to generate improvements in the properties, which largely depends on the characteristics of the fillers, their interaction with each other and with the matrix [26–28]. Hybrid nanocomposites showing advanced properties have been reported for different polymer matrixes, including ABS [29], cured epoxy resins [30–32], polypropylene (PP) [33,34], and thermoplastic polyurethane (TPU) [35,36], employing a variety of carbon-based and inorganic nano-sized fillers.

It should be stressed that in several cases the hybrid synergy could not be (fully) exploited, highlighting the need for further research. For example, poly(lactic acid) (PLA) based hybrid composites have been manufactured containing graphene nanoplatelets (GNP's) and carbon nanotubes (CNT's), or a combination of them in different proportions [37] to then evaluate the electrical and mechanical properties for the filaments, and the hot pressed and 3D printed parts. No synergistic interactions between the fillers could although be evidenced for the tensile properties and a decrease in the properties from filament to 3D printed parts could be observed. Similarly, Dul *et al.* [38] reported the fabrication of filaments and 3D printing of ABS-based hybrid nanocomposites with GNP's and CNT's in varying proportions to then evaluate the electrical, mechanical, and shielding properties, also considering the effect of the printing direction. Also here no synergistic effects between the different

particles could be identified and the authors attributed this to the high mass concentration of particles used.

In this work, the FFF potential of ABS-based mono and hybrid (nano)composite compositions containing GNP's, multi-walled CNT's, and titanium dioxide (TiO_2) nano powder was assessed. ABS was chosen as a matrix because it is already broadly applied for FFF and, therefore, basic conditions for 3D printing are known. GNP and CNT were chosen based on the fact that carbon nanofillers with different geometries (lamellar and fiber-like, respectively) may yield significant hybrid effects, based on an improved dispersion and the creation of co-supporting networks that facilitates thermal, mechanical and electric load transfers [39–42]. Furthermore, TiO_2 was chosen as it may improve the dispersion of CNT and vice-versa, by mutually hindering their reagglomeration [43,44]. With this approach, a good dispersion of fillers is expected, and therefore, a synergetic effect as well.

In a first phase, compositions are assessed via rheological analysis, printability tests and design of experiment (DOE) analysis The most interesting compositions are fully characterized via differential scanning calorimetry (DSC), thermogravimetric analysis (TGA), X-ray diffraction (XRD), and microscopy, and submitted to sintering analysis. Finally, 3D printed specimens have been fabricated to evaluate the effect of the printing orientation, layer thickness (LT), nozzle temperature, and composition on the tensile, flexural and impact properties of the ABS-based composites. It is shown that a smart design of the FFF composition increases the properties of the matrix by improved dispersion of the nanoparticles and their synergistic effect.

5. 3. Materials and methods

5. 3. 1. Materials

A general-purpose ABS (Terluran GP-22, INEOS) was used in this research, with a melt volumetric ratio (MVR) of 19 cm^3/10 min and a (room temperature) density of 1040 kg/m^3. Three nano-sized materials were used as fillers. The first filler type were multi-walled carbon nanotubes (MWCNT's, NC7000TM, Nanocyl) with an average tube diameter of 9.5 nm, 1.5 µm length, and 250 – 300 m^2/g surface area. The second filler type were graphene nanoplatelets (GNP's) (C-750-900407, Sigma Aldrich) with a thickness of a few nm, an average particle size of less than 2 µm, 750 m^2/g surface area, and a bulk density of 0.2 to 0.4 g/cm^3. The third filler type was titanium (IV) oxide (TiO_2) nano powder (634662, Sigma Aldrich), with a particle size smaller than 100 nm.

5. 3. 2. Characterization

Testing phase: from blending to printing

In the first (testing) phase of this research, 7 ABS-based hybrid nanocomposite compositions for FFF were assessed, with their compositions shown in entry 2-8 in Table 1, and taking as reference case unmodified ABS (entry 1 in Table 1). These compositions were realized by blending in a micro-extruder with a co-rotating, conical twin-screw configuration (Haake Minilab II, ThermoFisher Scientific). The extrusion was performed at 220 ºC, with a rotation speed of 150 rpm. To improve the dispersion of the nanoparticles in the matrix, each composition was cycled via the backflow channel for 30 seconds prior to flushing. The extrudate was pulled via a rolling system, aiming to keep the extrudate diameter constant. These extrudates were further used

for rheological analysis and printability testing. Prior to processing and characterization, ABS and ABS-based composites were dried in the oven for 4 hours at 80 ºC.

Table 1: Compositions of samples investigated in this research

Experiment	Sample	Composition (m.%)			
		ABS	GNP	CNT	TiO_2
1	ABS	100	0	0	0
2	ABS_CNT	99	0	1	0
3	ABS_GNP	99.5	0.5	0	0
4	ABS_GNP_CNT	98.5	0.5	1	0
5	ABS_TiO_2	99	0	0	1
6	ABS_CNT_TiO_2	98	0	1	1
7	ABS_GNP_TiO_2	98.5	0.5	0	1
8	ABS_GNP_CNT_TiO_2	97.5	0.5	1	1

The linear viscoelastic behavior of the samples was measured in a rheometer (MCR 702, Anton-Paar) operating with the parallel plate configuration (25 mm in diameter and 1 mm gap), under N_2 atmosphere. The storage modulus (G'), loss modulus (G''), and complex viscosity (η*) at 220 and 270 °C of each specimen were monitored as a function of the (angular) frequency with an amplitude of strain of 1%, assuring the material was in the linear viscoelastic domain. For pure ABS, an extra run at 250 °C was performed. Pelletized extrudates were used to prepare the specimen for rheological tests in a disk-like shape with 1 mm thickness and 25 mm diameter via compression molding at 220 °C, using a hot press.

A factorial design 2^3 (three factors, two levels of each factor) was conducted to evaluate the influence of each factor and their interactions on the rheological properties, employing analysis of variance (ANOVA). Factor A represents the CNT

content (levels: 0 or 1 m.%), factor B represents the GNP content (levels: 0 or 0.5 m.%), and factor C represents the TiO_2 content (levels: 0 or 1 m.%). The values of the factors were codified according to the level of each factor, i.e. −1 for the lower level and +1 for the higher level. Two replications of each experiment were done, reflecting the sources of variability both between runs and within runs [45]. The order of the mixtures within each replication was randomized. The results obtained were compared using the Tukey's test, which indicates if there is a significant difference between the average results of populations [45]. A conventional significance level (α) of 0.05 was considered.

Table 2: FFF printing parameters used for the initial printability testing (1 cm³ cubes).

Printing parameters	
Infill	15%
Infill pattern	rectilinear
Infill angle	45°
Layer thickness	0.25 mm
Nozzle diameter	0.4 mm
Bed temperature	110 °C
Nozzle Temperature	255 °C

Printability tests of the extrudates were performed by printing 1 cm^3 cubes of each composition via an FFF 3D printer (Prusa i3 MK3S+), using the printing parameters shown in Table 2.

From the testing phase to promising FFF filaments

FFF filaments of selected compositions (entries 3, 4, 7, and 8 in Table 1) were produced in a dedicated two-step route. In the first step, masterbatches with a higher concentration of each component with respect to ABS were produced in a micro-

extruder (Haake Minilab II, ThermoFisher Scientific) at 220 ºC, with a rotation speed of 150 rpm. This step was carried out to induce a high level of nanoparticle dispersion in the matrix. In the second step, the masterbatches were pelletized and diluted into ABS to reach the desired content composition (cf. Table 1) using a single screw extruder (Brabender 19, 19 mm screw diameter; length over diameter ratio L/D of 25). The temperature profile of the extruder was set to 145-185-205-210 °C, with a screw speed of 27 rpm. A rolling system and spooling device were used to pool the extrudate into a filament with a controlled (average) diameter of 1,75 mm and wind it into a spool for further FFF application. The spooling speed was approximately 5 m/min.

The thermal stability of the filaments was evaluated by means of thermogravimetric analysis (TGA). The measurements were performed in a TGA (STA 449 F3 Jupiter, Netzsch) from 30 to 700 ºC under N_2 atmosphere using a heating rate of 10 ºC/min. The glass transition temperature (T_g) and the specific heat capacity (c_p) of the filaments were determined by means of differential scanning calorimetry (DSC). A DSC 214 Polyma (Netzsch) was used to perform the measurements. The glass transition temperature was obtained from the second heating cycle considering a temperature program from 30 to 300 ºC, with a heating rate of 10 ºC/min under N_2 atmosphere. The specific heat capacity of the filaments was determined based on ASTM E1269-11, from 220 to 270 °C with a 5 °C/min heating rate. An isothermal step of 5 minutes was performed at 220 °C before the heating ramp and after the heating ramp at 270 °C.

The dispersion of nanoparticles and the morphology of the filaments were assessed via scanning electron microscopy (SEM) in a Phenom Pro Desktop (ThermoFischer Scientific). The filaments were cryogenically fractured and gold sputtered specimen (7 nm thickness) prior to analysis.

Wide angle X-ray scattering (WAXS) was performed in a Xeuss 3.0 Compact Q-Xoom SAXS/WAXS/USAXS system (Xeuss 3.0, Xenocs, France) with X-ray wavelength of 0.154 nm, and an operating voltage and current of 50 kV and 0.6 mA. A Eiger2 R1M detector was used with a sample to detector distance of 0.055 m. The filaments were grinded before analysis and powder samples were transferred into a hollow aluminum ring (h = 1 mm, d = 20 mm) with one side sealed with Kapton tape (h = 0.18mm).

The sintering process of the filaments was assessed via hot stage optical microscopy, utilizing a VXH500 microscope (Keyence) with thermal treatment (MicrOptik, MDTC-600) under N_2 atmosphere. Two types of tests were performed, i.e. "dynamic" and "isothermal" sintering. In the dynamic measurements, as shown in Figure 1b, two sliced cross sections of filaments were placed in contact with each other on the hot stage. These were submitted to an isotherm of 5 minutes at 110 ºC and then heated up to 280 ºC with a heating rate of 2.5 ºC/min, as shown in Figure 1a. The initial time for sintering was considered the time in which the neck between the disks was first created. For the isothermal measurements, four disks were placed in contact with each other on the hot stage, as depicted in Figure 1b. This configuration was chosen to better simulate the 3D printing process, with restrictions imposed by neighboring deposited strands of polymer. As shown in Figure 1a, the specimen was heated up from 80 °C to either 220 or 270 °C at a heating rate of 50 °C/min and maintained at the final temperature for 15 minutes. The initial time for sintering was considered the time in which the hot stage reached the test temperature. Micrographs were obtained every 15 seconds. The neck diameter was measured with the aid of ImageJ software (definition of x in Figure 1b).

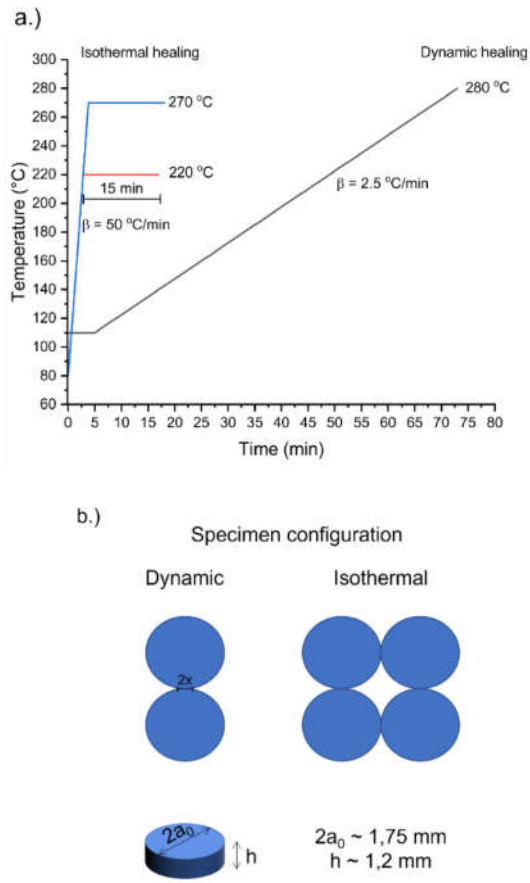

Figure 1: Sintering analysis. a.) Temperature programs and b.) specimen configuration; x related to definition neck growth.

The variation of the linear viscoelastic properties of the FFF samples with the temperature was assessed in a rheometer (MCR 702, Anton-Paar), considering a parallel plate configuration with 25 mm of diameter and 1 mm gap under N_2 atmosphere. The complex viscosity (η*) of each specimen was monitored as a function of temperature with an angular frequency of 1 rad/s and an amplitude of strain

of 1%, assuring that the material was in the linear viscoelastic domain. Pelletized filaments were used to prepare the specimen for rheological testing in a disk-like shape with 1 mm thickness and 25 mm diameter via compression molding at 220 °C, using a hot press.

FFF of filaments and characterization of 3D printed parts

Prusa printers (Prusa i3 MK3S+) with a 0.4 mm nozzle were used to 3D print specimens for tensile, flexural and impact tests. Here, the influence of the nozzle temperature (T_{Nozzle}) and LT on the final mechanical properties of the materials was assessed. Furthermore, the influence of the build orientation on the tensile properties was evaluated. The main processing parameters are shown in Table 3.

Table 3: FFF printing parameters for tensile specimens

Fixed settings	
Infill	100%
Infill pattern	rectilinear
Infill angle	45°
Perimeter velocity	100 mm/s
Infill velocity	200 mm/s
Nozzle diameter	0.4 mm
Bed temperature (°C)	110
Varying settings	
Nozzle Temperature (°C)	220 - 240 - 255 -270
Layer thickness (mm)	0,15 - 0,25 - 0,35
Build orientation	

Mechanical tests were conducted in a controlled environment under an atmosphere of 23°C and 50% relative humidity. Tensile testes were carried out in an Instron 5565

following ISO 527 with 1BA specimens. The flexural tests were performed in an Instron 4464, following ISO 178 on rectangular shaped bars with a length of 80 mm, a width of 10 mm, and a thickness of 4 mm. Charpy impact tests were performed in a Tinius Olsen IT503, according to ISO 179. The specimen had a rectangular shape with a length of 100 mm, a width of 10 mm and a thickness of 4 mm, utilizing a V-shaped notch with a depth of 2 mm in the mid-length of the bar. The stored energy in the pendulum amounts to 2.78 J.

The quality of the prints was evaluated by means of optical microscopy in a VXH500 microscope (Keyence) on the impact fractured surfaces. The void content in each specimen was evaluated from the micrographs of impact fractured surfaces. With the aid of ImageJ software, the voids in a pre-defined area were screened by brightness/contrast offsets. Then they were counted as percentage of this pre-defined area.

5. 4. Results and discussion

In this section first a range of nanocomposites is tested/screened in view of their use in FFF applications. Both rheological analysis and printability tests are conducted. Then the most interesting compositions are selected and their filament material properties are further tested. Finally, an advanced analysis of the mechanical properties of 3D printed specimens is carried out.

5. 4. 1. Testing compositions in view of FFF

Rheological analysis

Figure 2 shows the (angular) frequency dependence of the storage and loss modulus (G' and G"), and the complex viscosity (η*) of unmodified ABS (entry 1 in Table 1)

at different temperatures. As shown in Figure 2a (closed symbols), in the low-frequency regime, a plateau for G' is established that broadens and increases in magnitude with a rise in temperature.

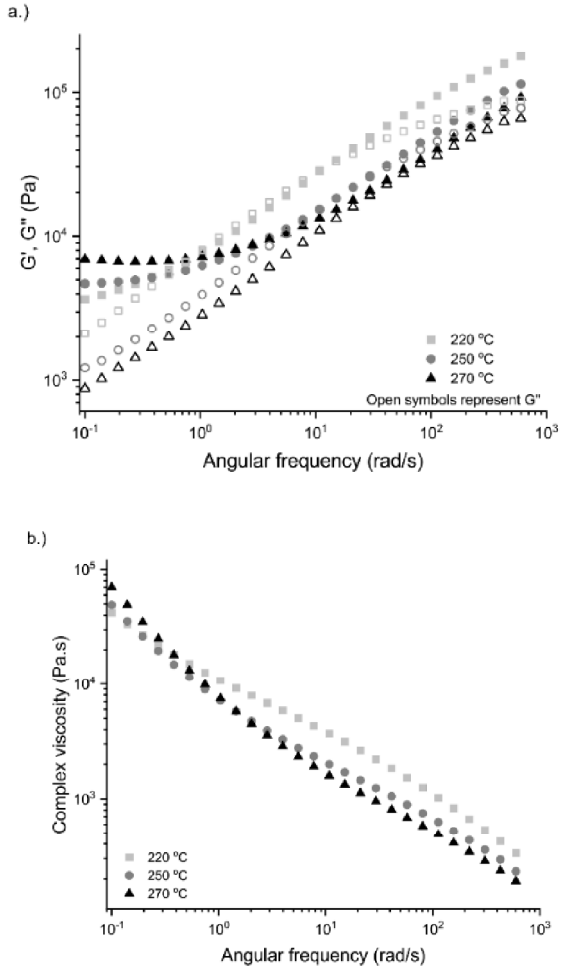

Figure 2: Storage modulus (G') and loss modulus (G") (a.) and complex viscosity (b.) of ABS (entry 1 in Table 1) at three temperatures.

This plateau formation is a typical non-terminal behavior, as reported for some ABS types [46]. The deviation from the terminal behavior in the low-frequency regime indicates an apparent yield stress [47]. The apparent yield stress is also consistent with the increasing values of the complex viscosity in the low-frequency region in Figure 2b. The non-terminal behavior means that the molecular motion is hindered, resulting in incomplete relaxation of the polymer chains [48].

The contribution of the interfacial interactions between the (grafted) rubber phase (PB-g-SAN) and the SAN phase to the overall elastic response is more pronounced at higher temperatures (250 and 270 °C), as the difference between *G*' (closed symbols) and *G*'' (open symbols) in Figure 2a is more pronounced at a higher temperature. A closer inspection reveals that *G*' is higher than *G*'' through the entire range of frequencies at the elevated temperatures, while at 220 °C there are two cross-over points between the *G*' and *G*'' curves, indicating that in a specific region *G*'' is higher than *G*' and the overall viscous response of the material is higher. As explained above, ABS is a multiphase material exhibiting a complex rheological behavior. The time-temperature superposition is found invalid for ABS from 220 to 270 °C, as assessed via van Gurp-Palmen plots [49,50] and shown in Figure C1 of Appendix C. The same finding has been previously reported for temperatures above 200 °C [51]. It is hypothesized that with an increase in temperature the 3D network formation of the PB phase is facilitated as a result of the viscosity reduction of the SAN phase. This leads to a pronounced increase in *G*' and a decrease in *G*", preventing the superposition [51].

The storage and loss moduli of ABS and ABS-based composites at 220 ºC are shown in Figure 3. It follows from that the addition of GNP (red symbols) has little influence with respect to the storage and loss modulus of unmodified ABS (black symbols).

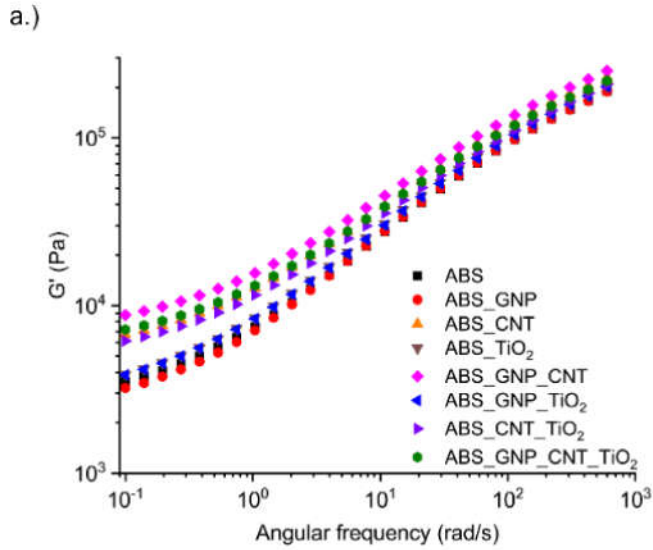

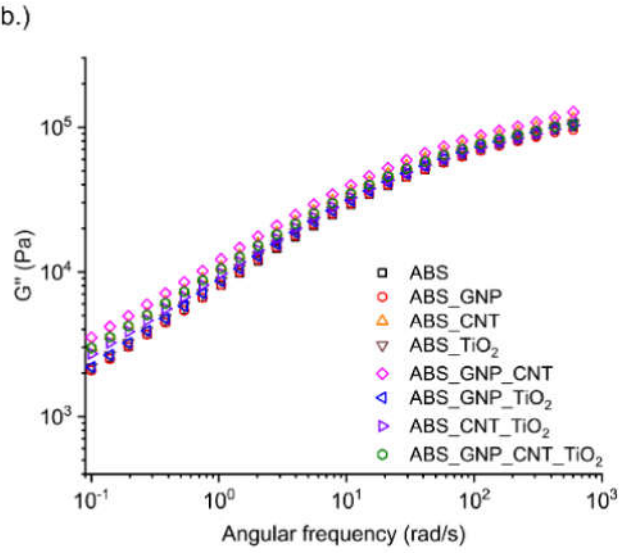

Figure 3: Storage modulus G' (a.) and loss modulus G'' (b.) at 220 °C of extrudate compositions (entry 2-8 in Table 1). Also repeated the 220°C curves for unmodified ABS from Figure 2.

This is in contrast to literature data regarding ABS/graphene oxide composites processed via the coagulation method, with an increased G' and G'' and enhancement of the non-terminal behavior even at very small concentrations (0.048% vol.% or 0.1 m%) [48]. For TPU/graphene nanocomposites prepared via melt-mixing [52], non-terminal behavior has been seen above 1.5 m.% and the rheological percolation threshold has been calculated as 1.2 m.%. This may indicate that the amount of GNP used in this study was not high enough to reach the percolation threshold or that the distribution of GNP within ABS was not satisfactory, and therefore no 3D network was formed. The addition of TiO_2 has also little influence on the rheological properties of ABS (brown vs. black symbols in Figure 3), only slightly increasing its *G*' value but not enhancing the non-terminal behavior. The same has been observed for PP/TiO_2 nanocomposites [53].

Interestingly, for the mono nanocomposites in Figure 3, CNT's have the largest influence on the rheological properties of ABS (orange vs black symbols). The magnitude of *G*' is doubled with respect to ABS in the low frequency region and the dependence of *G*' on the frequency is reduced. *G*' is now also higher than *G*'' throughout the entire range of frequencies studied. The higher the concentration of CNT added to the matrix, the more dramatic the increase in *G*', as reported for ABS/CNT [54], PMMA/CNT [55] and PS/CNT [56] mono nanocomposites. However, deviations of the linear viscoelastic behavior have been seen at concentrations of CNT as low as 1 m.% [56]. Here the concentration of CNT was not increased, as the final material would be very brittle, making its application in 3D printing unviable.

For the hybrid nanocomposites (fuchsia, blue, purple and green symbols in Figure 3), the most remarkable compositions are ABS_GNP_CNT (fuchsia symbols) and

ABS_GNP_CNT_TiO_2 (green symbols), who both share a GNP and CNT contribution. The ABS_GNP_CNT composition exhibits a strong synergy between the nanoparticles, as this composition shows the highest *G*' value throughout the entire range of frequencies studied. Upon comparison with mono nanocomposites the combination of GNP and CNT leads to a storage modulus 273% and 135% higher than the one for ABS_GNP and ABS_CNT in the low-frequency region, respectively. The synergetic effect is confirmed at the same nanoparticle concentration (1.5 m.%) as can be seen in Figure 4.

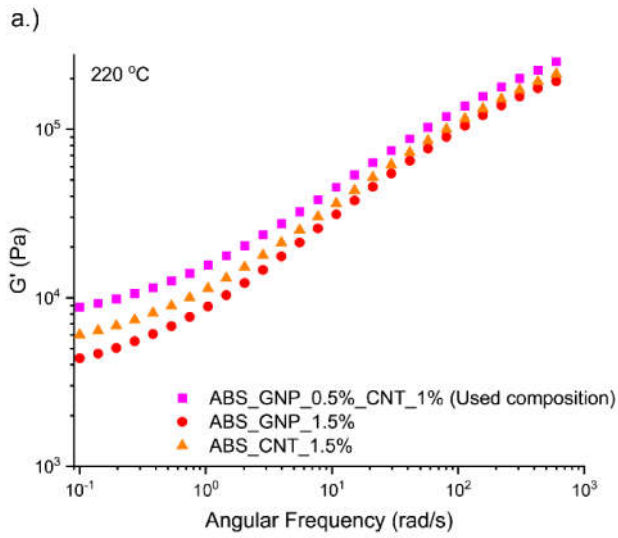

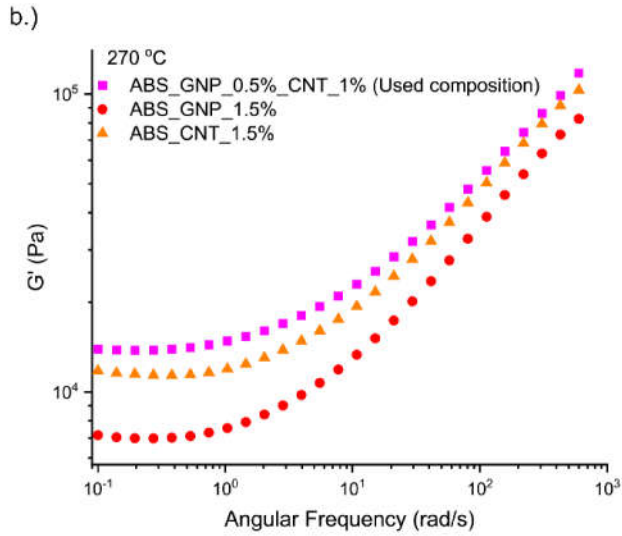

Figure 4: Proof of hybrid effect at the concentration of 1.5 m% in total in the nanocomposite at a.) 220 and b.) 270 °C

In contrast, Jyoti *et al.* [29] reported no synergy effects between graphene oxide and CNT's in an ABS based hybrid nanocomposite with only intermediate *G*' and *G*'' values for the hybrid, highlighting the relevance of the material design in the current work. This intermediate behavior has been also reported for PLA-based hybrid nanocomposites functionalized with GNP and CNT [57].

The ABS_GNP_CNT_TiO_2 hybrid composite in Figure 3 (green symbols) also exhibits synergy between the particles, leading to higher *G*' values than the single nanoparticle compositions. Yet, the effect is less pronounced than that observed for ABS_GNP_CNT (fuchsia symbols), highlighting the material tuning possibility via the extra addition of TiO_2. Furthermore, ABS_GNP_CNT (fuchsia symbols) and ABS_GNP_CNT_TiO_2 (green symbols) do not exhibit a cross-over point between *G*''

and *G*', and *G*' is larger than *G*'' throughout the entire range of frequencies, indicating that the elastic response dominates the response of both composites.

The hybrids ABS_GNP_TiO_2 (blue symbols) and ABS_CNT_TiO_2 (purple symbols) do not exhibit synergy between nanoparticles at 220°C, according to rheological results in Figure 3. However, it has been indicated that the use of TiO_2 for hybrid nanocomposites with CNT can improve the dispersion of CNT in the matrix [43,58], leading to improved mechanical properties as seen for epoxy based hybrid composites [43]. This is a key aspect regarding the fabrication of nanocomposites for 3D printing applications using CNT as core component, as will be investigated further in this contribution.

At the highest temperature of 270 °C, the non-terminal behavior of the compositions is dramatically enhanced, as illustrated in Figure 5. This is consistent with the already discussed temperature effect for the unmodified ABS data in Figure 2, which relates to the increased contribution of the rubbery phase to the overall elastic response of the material. The formation of a 3D network also involving nanoparticles broadens even more the plateau already seen for unmodified ABS. Therefore, under well-chosen compositions there is a cooperation between the PB-g-SAN phase and the nanoparticles, whereas the relaxation of the SAN phase remains mostly hindered. At 270 °C the relative order of the composites remains the same as for 220 °C, except for ABS_GNP (red symbols in Figure 5) that now exhibits a higher value of *G*' and *G*" compared to the hybrids ABS_GNP_TiO_2 (blue symbols in Figure 5) and ABS_TiO_2 (brown symbols in Figure 5).

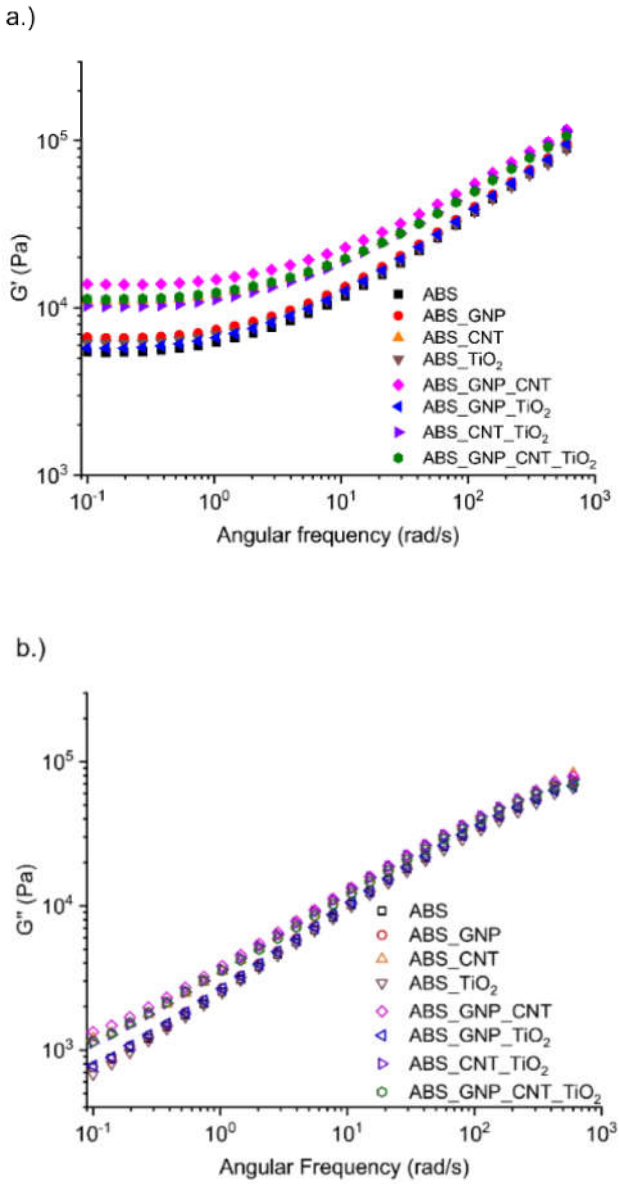

Figure 5: Storage modulus G' (a.) and loss modulus G" (b.) at 270 ºC of extrudate compositions (entry 2-8 in Table 1). Also repeated the 270°C curves for unmodified ABS from Figure 2.

.

Further insights on the influence of nanoparticles on the viscoelastic features can be obtained by inspecting the frequency dependency of the loss factor (tan δ), as shown in Figure 6 for 220 and 270 °C (subplot a and subplot b). The loss factor is the ratio between *G*'' and *G*' with δ being the phase angle, indicating the damping characteristics of the materials or how much energy it dissipates. The curves for all compositions (entries 2-8 in Table 1) exhibit the same shape as the curve for unmodified ABS at a particular temperature. The hybrids ABS_GNP_CNT (fuchsia symbols) and ABS_GNP_CNT_TiO_2 (green symbols) exhibit the lowest values of the loss factor, indicating a more solid-like behavior, with the nanoparticles and their interaction contributing to the hindrance of energy dissipation. Furthermore, at 220 °C (subplot a), the height of the peak decreases and the width of the peak increases for composition containing CNT's. At 270 °C (subplot b), the values of tan δ for all specimens are lower than at 220 °C, showing the relevance of studying temperature effects.

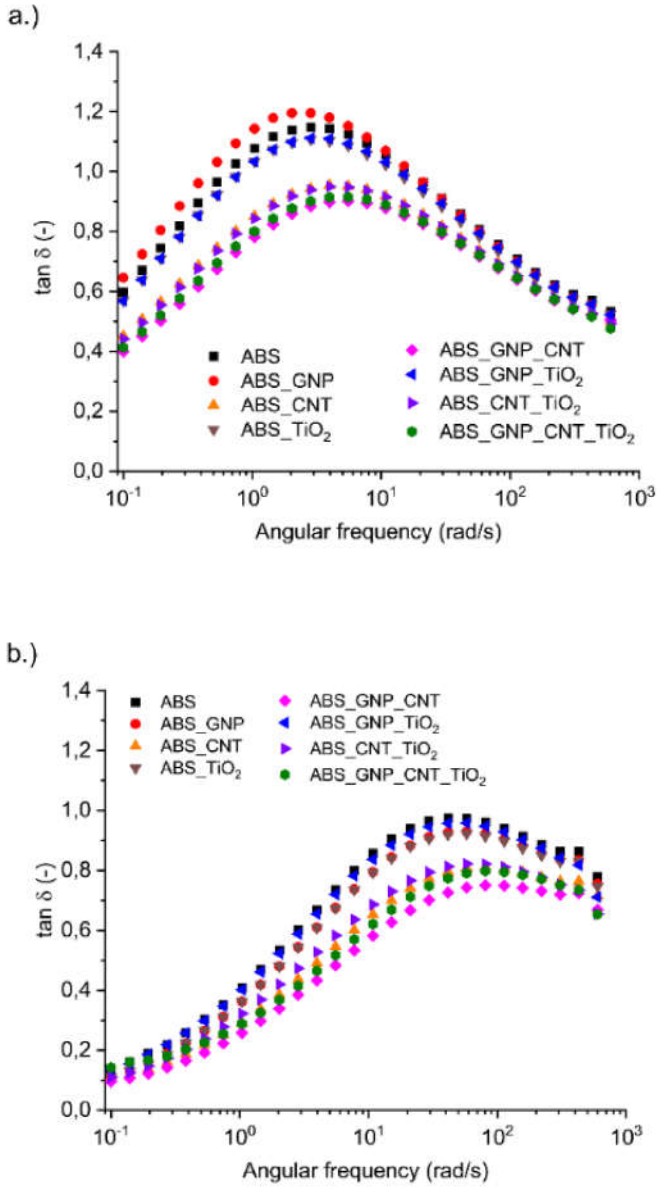

Figure 6: Loss factor (tan δ) of ABS and extrudate compositions (entries 2-8 in Table 1) at (a.) 220 and (b) 270 °C.

Extra insights additionally follow from model predictions. The traditional models for fitting the viscosity curve of polymers are unsuitable for the current polymer-based system, as they do not converge if the material exhibits apparent yield stress. Therefore, a modified Carreau-Yasuda model [59] is used to fit the η^*data:

$$\eta^*(\omega) = \frac{\sigma_0}{\omega} + \eta_0[1 + (\lambda\omega)^a]^{(n-1)/a} \ , \quad (1)$$

in which σ_0 is the melt yield stress, η_0 the zero-shear viscosity, λ the relaxation time, n the power law index, and a the Yasuda parameter. Figure 7 shows the measured η^*data for all compositions (symbols) and the model fitting results (lines) at 220 and 270 °C.

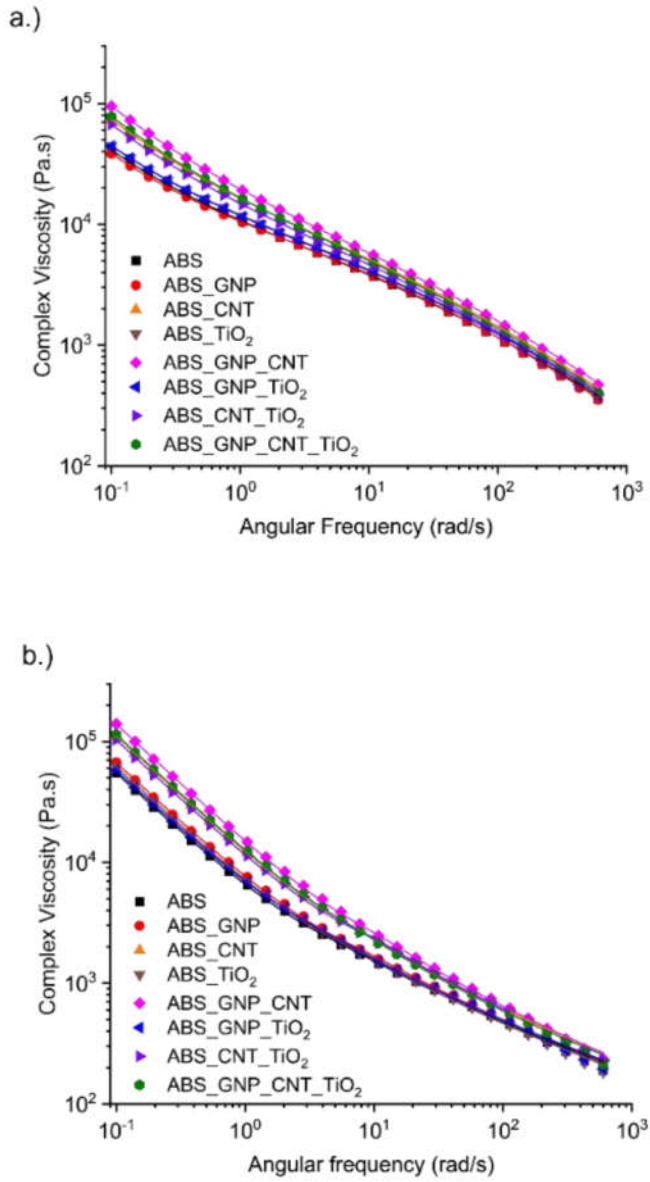

Figure 7: Complex viscosity of ABS composites at 220 (a.) and 270 ºC (b.). Lines represent the modified Carreau-Yasuda fitting (Equation (1)).

The model predictions correspond well to the experimental data. The calculated parameters from the model fitting are reported in Table 4. While λ, *n* and *a* seem to be slightly affected by the addition of nanoparticles, σ_0 and η_0 are strongly affected.

Table 4: Parameters obtained from fitting the data to the modified Carreau-Yasuda model.

Sample	Temperature (°C)	Fitting parameters – Modified Carreau-Yasuda model				
		σ_0 (Pa)	η_0 (Pa.s)	λ (s)	*a* (-)	*n* (-)
ABS	**220**	2743	22397	0.609	0.381	0.355
ABS_GNP		2559	18241	0.459	0.43	0.348
ABS_CNT		5423	33080	0.730	0.384	0.335
ABS_TiO$_2$		2956	24063	0.635	0.399	0.352
ABS_GNP_CNT		7313	38539	0.787	0.378	0.332
ABS_GNP_TiO$_2$		2940	25095	0.655	0.383	0.352
ABS_CNT_TiO$_2$		5025	28386	0.718	0.393	0.339
ABS_GNP_CNT_TiO$_2$		5930	32165	0.713	0.383	0.327
ABS	**270**	5364	1220	0.082	1.54	0.48
ABS_GNP		6574	1114	0.066	2.08	0.48
ABS_CNT		10989	1383	0.068	1.88	0.45
ABS_TiO$_2$		6073	1103	0.071	1.81	0.47
ABS_GNP_CNT		13780	1282	0.054	2.32	0.43
ABS_GNP_TiO$_2$		5645	1345	0.09	1.46	0.47
ABS_CNT_TiO$_2$		10164	1392	0.065	2.12	0.44
ABS_GNP_CNT_TiO$_2$		11261	1366	0.068	1.70	0.43

The model interpretation allows to deduce that the addition of nanoparticles and the creation of hybrid nanocomposites lead to an increase in σ_0, except for ABS_GNP at 220 °C. At 270 °C, σ_0 is approximately doubled the value at 220 °C for every composition, again confirming the solid-like transition at elevated temperature. The hybrids ABS_GNP_CNT and ABS_GNP_CNT_TiO$_2$ show the highest values of σ_0 at 220 and 270 °C, again indicating a synergistic effect between the GNP and CNT particles and probably the formation of a well-defined 3D network. The effect of

nanoparticle addition on $\eta_0$is most noticeable at 220 °C, with ABS_GNP_CNT displaying the highest η_0, 72% higher than unmodified ABS. The addition of TiO_2 reduces the complex viscosity of the hybrids containing CNT, suggesting a beneficial effect in processing, aiding in the dispersion of CNT's. At 270 °C, the effect of the nanoparticle addition on $\eta_0$is however less pronounced.

Interesting in Figure 7 are the frequency variations of the η^*curves at the two temperatures. Because σ_0 is doubled at 270 °C and the values of $\eta^*$are very small, compared to the data at 220 °C, the curves show a region of yield stress, immediately followed by a transition to the shear thinning region. At 220 °C, with higher values of $\eta^*$and lower values of σ_0, it is possible to divide the curves in three regions, being yield stress, a transition from a zero-shear viscosity plateau to shear thinning, and a shear thinning region. Complementary it can be said that the addition of nanoparticles and creation of hybrids affect more η_0 at 220 °C and more σ_0 at 270 °C because of the improved elastic contribution at the latter temperature.

The ANOVA results for the rheological properties *G*', *G*'' and η^*at 0.1 and 113 rad/s measured at 220 and 270 °C are shown in Table 5. At 220 °C, all the factors and their combination (particles and hybrids) are statistically significant for *G*' and η^* at 0.1 rad/s. At the higher frequency, at 220 °C, the influence of the factors and their combination on the properties are not statistically significant, apart from the factor A (CNT). At 270 °C, only the factors A (CNT) and C (TiO_2) are statistically significant. Overall it follows that factor A (CNT) is significant for all the properties at all conditions and the factor C (TiO_2) can be seen statistically significant for all properties other than *G*''. Hence, again the relevance of adding CNT and TiO_2 comes forward.

Table 5: ANOVA result: p-values. Values in bold indicate statistically significant effect on the respective property.

Variation source	Temperature (°C)	At 0.1 rad/s			At 113 rad/s		
		G'	*G"*	*η**	*G'*	*G"*	*η**
CNT	220	0.00	0.00	0.00	0.00	0.00	0.00
GNP		0.01	0.048	0.00	0.18	0.30	0.20
TiO_2		0.01	0.23	0.01	0.66	0.68	0.66
GNP_CNT		0.00	0.31	0.00	0.57	0.55	0.55
CNT_TiO_2		0.00	0.06	0.00	0.17	0.16	0.16
GNP_TiO_2		0.03	0.41	0.03	0.91	0.75	1.00
CNT_GNP_TiO_2		0.02	0.36	0.02	0.61	0.52	0.58
CNT	270	0.00	0.00	0.00	0.00	0.00	0.00
GNP		0.46	0.10	0.46	0.90	0.51	0.74
TiO_2		0.03	0.28	0.03	0.03	0.03	0.02
GNP_CNT		0.37	0.05	0.36	0.93	0.54	0.77
CNT_TiO_2		0.28	0.76	0.29	0.81	0.67	0.98
GNP_TiO_2		0.96	0.26	0.95	0.70	0.69	0.67
CNT_GNP_TiO_2		0.29	0.23	0.29	0.45	0.62	0.48

Cube printability tests

To qualitatively assess the printability of ABS and its nanocomposites 1 cm^3 cubes have been printed for every composition described in Table 1, with the bottom layer of each cube shown in Figure 8. All the compositions could be successfully printed and showed a good adhesion to the bed for the printing conditions selected. Furthermore, the addition of only CNT seems to worsen the coalescence between the different strands of filament compared to ABS. This feature is even more pronounced for the composition containing GNP and CNT. On the contrary, if these compositions also contain TiO_2, the coalescence seems to improve substantially, again confirming the usefulness of this compound.

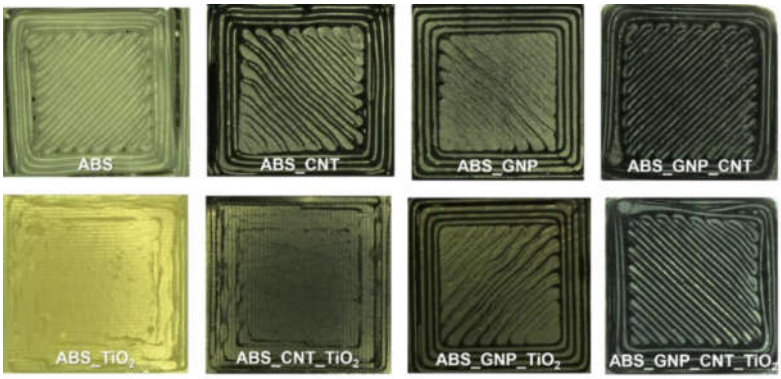

Figure 8: Printability tests of compositions for FFF; extra info in Figure C2 of Appendix C.

It is known that melt viscosity and coalescence are related [60–63]. It follows from Table 4 that CNT leads to an increase in η_0 and that the addition of TiO_2 into CNT-containing compounds decreases η_0, suggesting an improved coalescence. Furthermore, the sole addition of TiO_2 and GNP to ABS seems to have a positive impact on its coalescence, also following the η_0 decrease in Table 4.

Selection of compositions for filament production and use in FFF

Figures 3-7 and Table 4 have demonstrated that the addition of nanoparticles and their hybrid combinations influence the rheological properties, due to the interaction between each other and with the matrix. A first assessment is that the pseudo-solid-like behavior is most enhanced for the compositions with CNT, thus CNT_TiO_2, GNP_CNT, and GNP_CNT_TiO_2. Table 5 further highlights that the addition of CNT and TiO_2 are both statistically relevant. Furthermore, based on basic printing results in Figure 8, the coalescence of the polymer filaments after deposition is positively affected by the addition of GNP and TiO_2. This second assessment thus also highlights the relevance of the use of GNP and TiO_2.

After the combined assessment, a selected number of compositions are chosen to produce filaments for FFF, namely ABS_GNP, ABS_GNP_TiO_2, ABS_GNP_CNT, and ABS_GNP_CNT_TiO_2 (entries 3, 4, 7 and 8 in Table 1). Also, ABS filament is included for comparison.

5. 4. 2. Analysis of selected filaments

The thermal properties of the filaments have been analyzed by means of TGA and DSC and the results are reported in Table 6. The addition of nanoparticles to ABS has only a small influence in the temperature at 3% mass loss ($T_{3\%}$), T_g and c_p. From a processing point of view, these results indicate that the printing may be carried out under the same conditions for the different compositions, especially regarding the upper and lower printing temperatures (220-270 °C).

Table 6: Thermal properties of the filaments.

Sample	$T_{3\%}$ (°C)	T_g (°C)	c_p at 252 °C (J/g.K)
ABS	369.0	104.4	2.21
ABS_GNP	369.6	105.7	2.27
ABS_GNP_TiO_2	369.0	102.9	2.13
ABS_GNP_CNT	367.5	106.3	2.18
ABS_GNP_CNT_TiO_2	372.7	103.4	2.10

X-ray diffraction has been carried out to evaluate the structure of the nanoparticles as such, to confirm their presence in ABS, and to understand their dispersion within the matrix. Figure 9a shows the diffractograms of the nanoparticles used in this study. Pristine GNP exhibit a diffraction peak at 2θ = 26.1°, which corresponds to a *d*-spacing of 0.34 nm in a graphitic layer structure. For (MW)CNT, due to the superficial modification, this peak is shifted towards a slightly lower angle 2θ = 25.4° which

corresponds to an increased *d*-spacing of 0.35 nm [64]. TiO_2 exhibits two diffraction peaks, indicating the presence of two polymorphs: anatase and rutile. Anatase has a diffraction peak related to the diffraction plane (101) at 25° while rutile shows a peak related to the diffraction plane (110) located at 2θ = 27.1°, corresponding to a *d*-spacing of 0.35 and 0.32 nm, respectively [65].

The XRD patterns of unmodified ABS and the FFF selected ABS-based nanocomposites contain a broad peak at 19.4° and a shoulder around 11.3°, as shown in Figure 9b, due to the amorphous structure of ABS [66]. Nanocomposites with GNP and/or CNT (but no TiO_2) do not exhibit the nanoparticle diffraction peak characteristics and no differences in their diffractogram pattern are seen upon comparison to unmodified ABS. Previous work [26,67] has attributed the absence of peaks to a good dispersion of the fillers in the matrix, with only a detectable agglomeration as the content of nanoparticles increases. ABS nanocomposites with CNT's and few layer graphene (FLG) prepared via solution casting, for instance, exhibit the characteristic diffraction peak only above concentrations of 1 and 0.5 m%, respectively [26]. In case of PLA/CNT nanocomposites, the graphitic (002) diffraction peak is invisible at a CNT concentration up to 3 m.% [67]. Considering the specimens with TiO_2, the anatase diffraction peak at 25° is visible in Figure 8b, indicating the presence of TiO_2 in the samples [68]. The rutile diffraction peak has a lower intensity and is invisible in the diffractograms. Hence, the XRD data are only partially useful in view of the scope of the present work, explaining the dedicated consideration of SEM analysis.

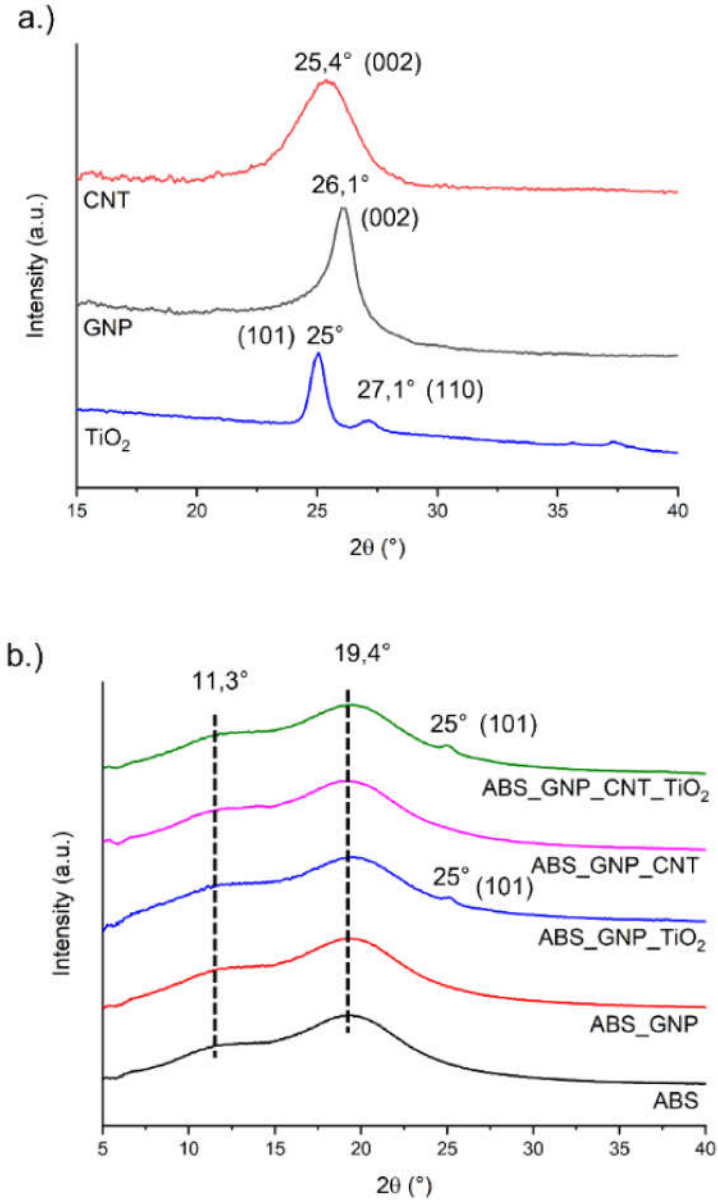

Figure 9: XRD patterns for nanoparticles (a.) and selected FFF nanocomposites (b.) used in this study.

Scanning electron micrographs of the cross section of the filaments are displayed in Figure 10, giving an indication on the distribution and dispersion state of the nanoparticles in the matrix. For the lower magnification (Figure 10a-e), agglomerates are observed for ABS_GNP, ABS_GNP_TiO_2, and ABS_GNP_CNT (indicated by arrows), which confirms that the absence of the characteristic peaks of GNP and CNT in their diffractograms (Figure 9b) is at least partially related to their low concentration and lesser dispersion in the matrix. The higher magnification micrographs (Figure 10g-i) show the enlargement of the regions indicated by the arrows. ABS_GNP displays smaller size agglomerate, whereas ABS_GNP_TiO_2 and ABS_GNP_CNT are characterized by larger agglomerates. GNP and TiO_2 do not exhibit a good interaction, and they agglomerate into distinct regions, corroborating the rheological tests results (Figures 3-7), which indicate poor synergy between particles and lower viscosity for ABS_GNP_TiO_2 compared to the other hybrids, especially at 220 °C. It has been reported that CNT has a preferable dispersion within the SAN phase, due to the difficulty in penetrating the cross-linked PB phase [69,70]. This may also apply for the other particles used in this study and it is also a factor that contributes for their difficult dispersion into the matrix. This indicates that the process employed for the dispersion can still be further improved. Furthermore, ABS_GNP_CNT may undergo re-agglomeration, while still exhibiting a level of mobility and better interaction with the matrix above T_g.

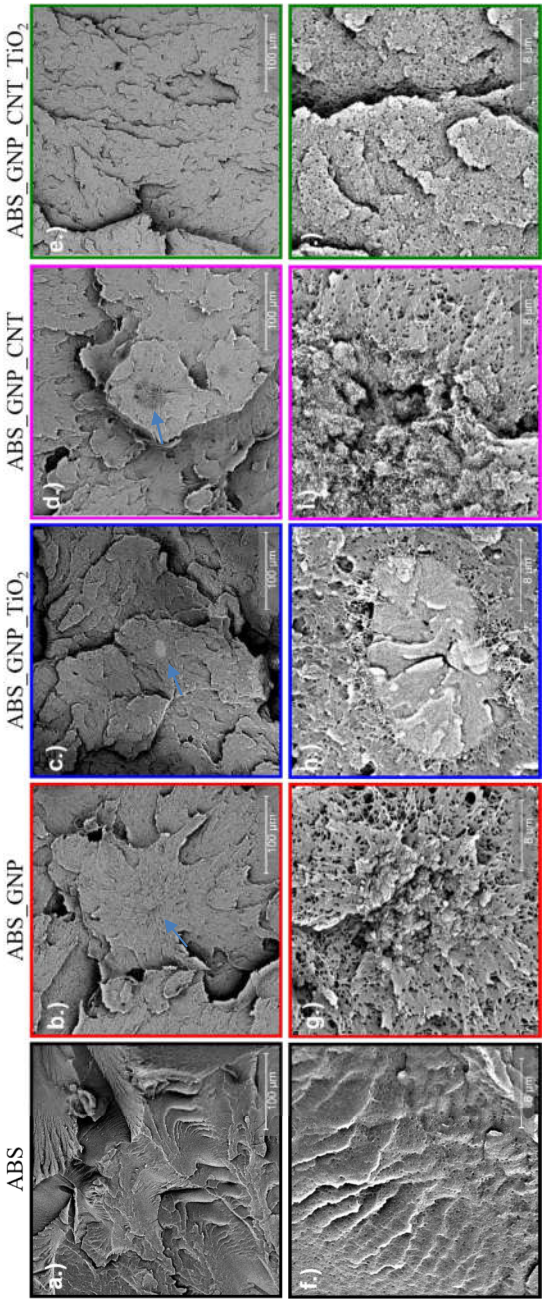

Figure 10: Scanning electron microscopy of filaments at low magnification (x820) (a.)-(e.) and at high magnification (x9400) (f.)-(j.), for ABS, ABS_GNP, ABS_GNP_TiO$_2$, ABS_GNP_CNT, and ABS_GNP_CNT_TiO$_2$. Arrows represent agglomerates.

Nevertheless ABS_GNP_CNT_TiO_2 exhibits a good level of dispersion and distribution throughout the matrix, as shown in Figure 10e and Figure 10j, highlighting an optimal interaction among these nanoparticles generating an improved dispersion under hybrid conditions. It has been previously reported that TiO_2 assists in the dispersion of CNT's, due to a synergistic interaction [58]. This is confirmed in the present work as upon combination with GNP, TiO_2 forms agglomerates. Zhang *et al.* [44] attributed the better dispersion of CNT's in the presence of TiO_2 to the change in the local flow behavior and shear amplification effect, causing CNT to further disperse, which in turn would prevent TiO_2 particles to re-agglomerate. In addition, surface modification of CNT's or even to the geometry of the particles can support the interaction. This further corroborates the prior rheological analysis for ABS_GNP_CNT_TiO_2, displaying that most pronounced increase in *G*', and is also consistent with the dominant role of CNT and TiO_2 based on ANOVA analysis.

Sintering analysis of the filaments has been performed by means of hot stage microscopy with subsequent image analysis to measure the neck growth as function of temperature and/or time. All the samples have been evaluated in the dynamic mode, whereas ABS and ABS_GNT_CNT_TiO_2 have also been evaluated in the isothermal mode at 220 and 270 °C.

With an increase in the temperature in the dynamic mode, as shown in Figure 11a, all the materials exhibit an increase in the neck radius, as normalized by the initial radius of the disks (a_0); the actual evolution of the neck radius at selected times is shown in Figure C3 of Appendix C. This indicates a higher degree of sintering with the temperature increase, which is closely related to the decrease in the complex viscosity in Figure 11c and the increased mobility of the polymer chains. ABS_GNP_CNT (fuchsia symbols) and ABS_GNP_CNT_TiO_2 (green symbols) exhibit the lowest

dimensionless neck radii throughout the entire temperature range, as they have a more pronounced pseudo-solid-like behavior. ABS_GNP and ABS_GNP_TiO_2 in turn show higher dimensionless neck radii, even higher than for unmodified ABS. The complex viscosity of these compositions is in the same range of unmodified ABS with the evolution in temperature, whereas for ABS_GNP_CNT and ABS_GNP_CNT_TiO_2 the complex viscosity values are way higher, as shown in Figure 11c.

In the isothermal sintering measurements at 220 and 270 °C, in Figure 11b, the dimensionless neck radius stabilizes and stops growing approximately after 120 s. The temperature plays an important role as sintering carried out at 270 °C yields higher values of the dimensionless neck radius. This is due to the decrease in η^*(Figure 11c) and a higher free volume [71], allowing the polymer chains to move more easily, enhancing the neck growth. This is linked to the overall coalescence process in 3D printing with parts printed at higher temperatures likely showing less voids in their structure.

Section C.2. of Appendix C shows modeling results for the determination of the overall activation energy for sintering (E_a), further underpinning the dynamic mode results. The overall sintering mechanism could be seen as diffusional, e.g. three dimensional (D3) or spherical geometry (D4). Diffusion mechanisms are related to the melt viscosity, as illustrated in Figure 11d (270 °C), considering the overall activation energy values obtained for mechanisms D3 and D4 and employing the modified Carreau-Yasuda fittings.

a.)

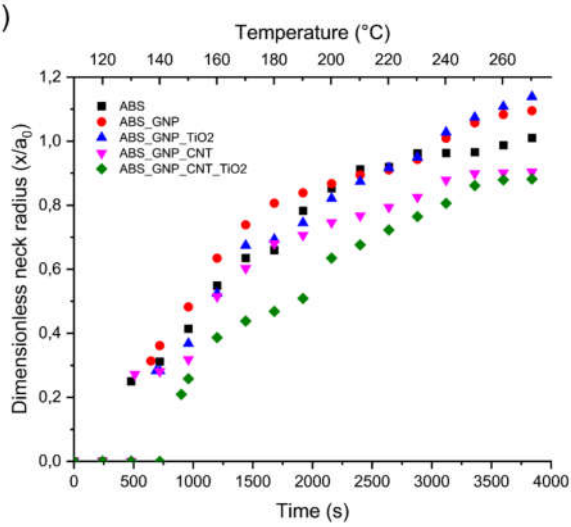
Temperature (°C)
120
140
160
180
200
220
240
260
1,2
1,0
0,8
0,6
0,4
0,2
0,0
Dimensionless neck radius (x/a0)
ABS
ABS_GNP
ABS_GNP_TiO2
ABS_GNP_CNT
ABS_GNP_CNT_TiO2
0
500
1000
1500
2000
2500
3000
3500
4000
Time (s)

b.)

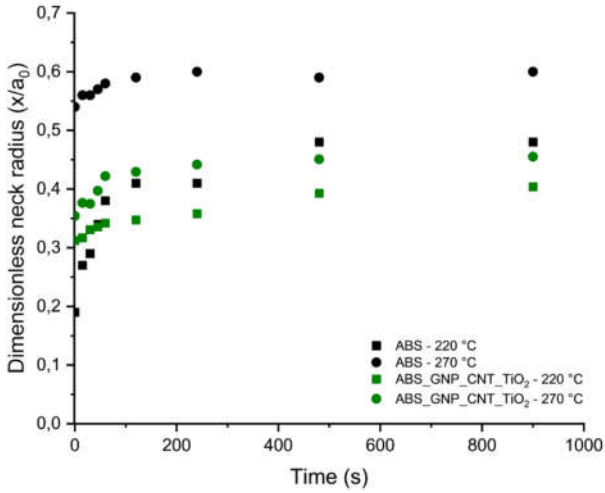
0,7
0,6
0,5
0,4
0,3
0,2
0,1
0,0
Dimensionless neck radius (x/a0)
ABS - 220 °C
ABS - 270 °C
ABS_GNP_CNT_TiO2 - 220 °C
ABS_GNP_CNT_TiO2 - 270 °C
0
200
400
600
800
1000
Time (s)

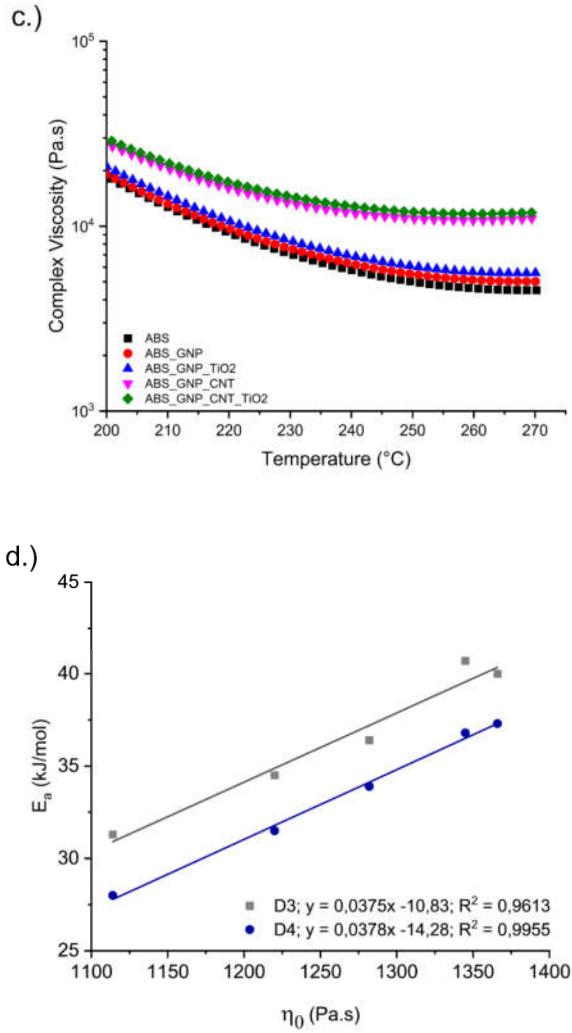

Figure 11: Evolution of dimensionless neck radius with temperature (non-isothermal runs) (a.) and time (isothermal runs) (b.) as well as the evolution of complex viscosity with temperature (at 1 rad/s) (c.). Correlation between zero-shear viscosity at 270 ºC (Table 4) and the overall activation energy (E_a) for the D3 and D4 diffusion mechanisms (cf. Table C2 from Appendix C) (d.).

It is additionally interesting to compare the dynamic and isothermal results. Due to the different heating programs and specimen settings, both results should although be carefully compared. In the isothermal tests, the neck radius obtained is way lower than the one obtained in the non-isothermal tests at the specific temperature, i.e. 220 or 270 °C. This is probably due to the volumetric expansion during heating which may be a source of experimental error during measurements in the dynamic mode, whereas during isothermal analysis the evolution of the neck radius occurs already after expansion. These simple tests give insights on the overall sintering process of the different materials, as it is possible to understand how far the neck can grow in each sample. This can be correlated with void formation due to partial coalescence during printing. However, this testing does not give any information about the bond strength, which is also a function of diffusion and randomization of chains in the polymer, being related to the mobility of chains and re-entanglement at the interface after alignment [72]. Moreover, the coalescence process in actual FFF is an extremely non-isothermal process also involving cooling. Coalescence may be quickly hindered by the fast cooling rates involved in the process and the wetting contact may be purely due to pressure variations [14].

5. 4. 3. Analysis of FFF printed parts considering the selected filament compositions

Influence of the layer thickness (LT)

The influence of LT on the tensile and flexural of (unmodified) ABS and the selected ABS-based nanocomposites at 255 °C is shown on Table 7. Considering the tensile and flexural properties, an increase of LT usually decreases the properties [51] and this has been attributed to porosity variations and an increased inter-layer interface,

which contributes to an overall improved bond strength of the part. Additionally, as reported by Coogan and Kazmer [14], small LT's increase the exit contact pressure, which forces the layers into a more intimate contact. This is a crucial step for the formation and strengthening of the bond via diffusion and entanglement of the polymer chains across the interface. For unmodified ABS, the highest value of tensile strength is indeed recorded at the lowest LT of 0.15 mm. A value of 40.0 MPa is obtained, which is 24% higher than the value obtained for the specimen printed with a LT of 0.35 mm. The highest flexural strength is recorded for the ABS specimen printed with a LT of 0.15 mm as well, namely 57.3 MPa. This value is 10% higher than the flexural strength for the material printed with a LT of 0.35 mm. The same effect can be seen for the flexural modulus. The tensile modulus and tensile strain at break are not influenced by LT but also exhibits higher deviations.

ABS-based nanocomposites show at first sight similar trends in the mechanical properties with changes in LT as for unmodified ABS, which is consistent with data for 3D printed ABS/CNT nanocomposites [73]. No major changes for the tensile modulus and strain at break with a change in the LT are seen in Table 7 for the ABS-based nanocomposites, whereas the tensile strengths are reduced or maintained constant with an increase in LT, depending on the composition. The flexural modulus and flexural strength always decrease with increased LT. The addition of the particles thus reduces the ductility of the matrix. For completeness it is mentioned here that the strain at break of all compositions exhibits high standard deviations, which is likely due to the defects present in the parts.

Table 7: Influence of layer thickness on the mechanical properties of ABS and ABS based nanocomposites (printing temperature is 255°C; XYZ printing).

Composition	Layer thickness (mm)	Tensile Properties		
		Modulus (MPa)	Strength (MPa)	Strain at break (%)
ABS	0.15	2669 ± 129	40.0 ± 2.3	4.6 ± 1.5
	0.25	2789 ± 228	38.1 ± 2.2	5.5 ± 1
	0.35	2441 ± 225	32.2 ± 1.1	5.9 ± 1.4
ABS_GNP	0.15	2589 ± 237	36.7 ± 2.1	4.5 ± 0.6
	0.25	2749 ± 96	39.3 ± 1.1	5.1 ± 1.4
	0.35	2768 ± 127	38.3 ± 1.4	4.6 ± 0.9
ABS_GNP_TiO_2	0.15	2541 ± 173	38.3 ± 1.8	5.9 ± 1.4
	0.25	2598 ± 128	35.2 ± 0.8	5.8 ± 1.3
	0.35	2502 ± 172	32.2 ± 1.5	4.7 ± 0.5
ABS_GNP_CNT	0.15	2834 ± 367	40.3 ± 2.0	4.5 ± 1.1
	0.25	2309 ± 163	30.9 ± 3.7	4.2 ± 0.7
	0.35	2683 ± 188	35.8 ± 0.9	4.1 ± 0.7
ABS_GNP_CNT_TiO_2	0.15	2986 ± 79	45.4 ± 2.1	3.7 ± 0.4
	0.25	2754 ± 102	41.1 ± 1.3	3.6 ± 0.4
	0.35	2886 ± 178	42.4 ± 0.9	3.6 ± 0.4
		Flexural Properties		**Impact Strength** (kJ/m^2)
		Modulus (MPa)	Strength (MPa)	
ABS	0.15	1545 ± 45	57.3 ± 0.9	13.2 ± 1.6
	0.25	1351 ± 28	50.3 ± 0.7	15.1 ± 1.7
	0.35	1395 ± 36	51.9 ± 1.2	16.3 ± 1.2
ABS_GNP	0.15	1488 ± 20	55.5 ± 1	9.3 ± 0.4
	0.25	1372 ± 35	51.3 ± 1.1	11.1 ± 1.3
	0.35	1366 ± 24	50.6 ± 0.7	9.3 ± 0.9
ABS_GNP_TiO_2	0.15	1444 ± 42	54.8 ± 1.2	6.9 ± 0.7
	0.25	1267 ± 37	49.8 ± 1.5	7.6 ± 0.5
	0.35	1301 ± 61	49.1 ± 1.4	7.5 ± 0.2
ABS_GNP_CNT	0.15	1624 ± 43	60.2 ± 0.9	7 ± 0.5
	0.25	1455 ± 66	53.9 ± 3.2	7.9 ± 0.5
	0.35	1394 ± 23	50.8 ± 1.1	7.9 ± 0.5
ABS_GNP_CNT_TiO_2	0.15	1502 ± 127	55.9 ± 3.6	6.5 ± 0.6
	0.25	1478 ± 46	53.1 ± 1	6.6 ± 0.5
	0.35	1444 ± 46	52.1 ± 1.6	6 ± 0.5

A closer inspection of the data in Table 7 reveals that the largest change in properties is found for ABS_GNP_CNT specimens, which experience a drop of 18% for the flexural modulus and 16% for the flexural strength, with the increase in LT from 0.15

to 0.35 mm. For other compositions, the drop for the flexural strength is around 10% and, for the flexural modulus, it ranges from 4% for to 10%. It is also clear that the influence of the nanoparticles on the tensile properties is more noticeable for the specimens printed at higher LT. This means that the addition of nanoparticles counterbalances the reduced performance of ABS due to an increased LT, as mentioned before. For instance, ABS_GNP, ABS_GNP_CNT, and ABS_GNP_CNT_TiO_2 printed with a LT of 0.35 mm exhibit tensile strength values that are 18, 11 and 31% higher than printed ABS, respectively. Likewise, Dul *et al.* [74] reported that certain printing strategies combined with the addition of carbon nanoparticles could improve the ABS properties. The same has been observed by Sezer *et al.* [75] upon printing ABS/CNT nanocomposites with different raster angles. The use of 0°/90° raster angles increased the properties significantly, as the nanoparticles become aligned in the direction of the load due to the printing strategy. Furthermore, the beneficial aspect of nanoparticles at higher LT is also interesting from a processing point of view, as materials printed with a higher LT demand less printing time.

Overall, the hybrid composite with the most altered rheological behavior, i.e. ABS_GNP_CNT_TiO_2 results in the best tensile properties, leading to the highest tensile strength for all LT assessed. This is due to the optimal dispersion of the fillers in the matrix (Figure 10) and synergistic effects among them (Figures 3-7). ABS_GNP_CNT shows the best flexural properties, slightly increasing the flexural modulus and flexural strength of the matrix. The higher drop of the flexural properties with increased LT for ABS_GNP_CNT compared to ABS_GNP_CNT_TiO_2 indicates that interaction between GNP, CNT and TiO_2 favors the bonding between the layers. The use of ABS_GNP_TiO_2 results in a worsening of all the mechanical properties, and this is probably due the lack or very poor interaction between GNP

and TiO_2, leading to a poor dispersion of TiO_2, as also indicated above. The TiO_2 agglomerates may act as stress concentrators, and this worsens the mechanical properties of the matrix. Consistently worsening of properties of 3D printed ABS with both GNP [76] and TiO_2 [68] added to the matrix have been reported. Furthermore, the use of GNP does not lead to any important improvement of the ABS properties other than an increased tensile strength upon printing at higher LT.

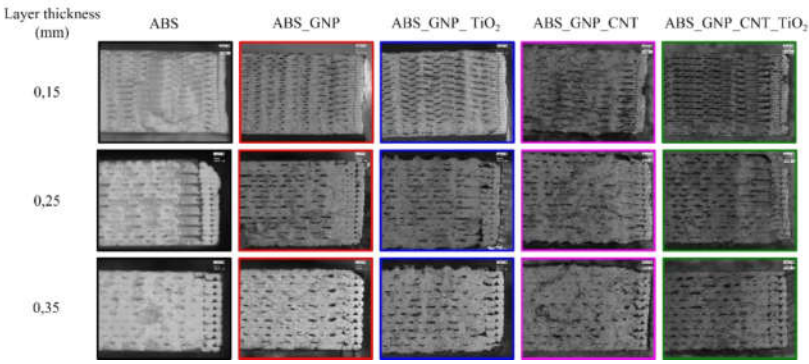

Figure 12: Influence of layer thickness and composition on the morphology of impact fractured specimens (impact strength data as last column in Table 9); 255°C and XYZ printing.

The last column of Table 7 contains data on impact strength. The impact strength of ABS slightly increases with the increase in LT, and this may be due to the presence of less voids in the part. For the nanocomposites, LT does not influence the impact strength and the addition of nanoparticles decreases the impact strength. The higher the loading, the lower the impact strength, as the nanoparticles will act as stress concentrators.

The morphology of impact fractured specimens has been assessed by means of optical microscopy, as shown in Figure 12. The micrographs show the presence of voids in all the specimens tested. With an increase in LT, the concentration of voids is reduced,

as there are less layers in the specimens printed at higher LT's. Therefore, there are fewer contact points and interfaces to undergo coalescence. Moreover, the specimens exhibit differences in the void distribution throughout the surface, which is related to the different thermal profiles each layer experiences during 3D printing. The layers printed first (bottom of micrographs) are heated up by the upcoming layers, so they will be for a longer time above T_g and may have more time for diffusion and neck growth than the upper layers [12]. Also, they support the weight of the top layers, making them likely denser. Even though the specimens produced with a LT of 0.35 mm have less void content, the size of the voids present in the specimens are usually larger than the ones in the specimens produced with LT of 0.15 mm.

The actual void content data for each composition is shown in Figure 13a. Unmodified ABS has a reduction for the void/pore content from 4% to 1% if LT is increased from 0.15 to 0.35 mm. ABS_GNP_CNT_TiO_2 is the specimen most affected by the LT variation in terms of void reduction going from 13.5% to 6% of void content, for a LT increase from 0.15 to 0.35 mm. However, the other nanocomposite compositions reach levels around 3% of void content at this LT of 0.35 mm. Overall it follows that the nanocomposites have a more difficult coalescence process than unmodified ABS, due to the restrictions in the movement of polymer chains. However, as such there is a reinforcing effect by the nanocomposites, which at larger LT is dominant overruling the presence of more voids with respect to unmodified ABS. The current work therefore demonstrates that is not recommended to only look at void contents as this could lead to a biased assessment of the mechanical properties.

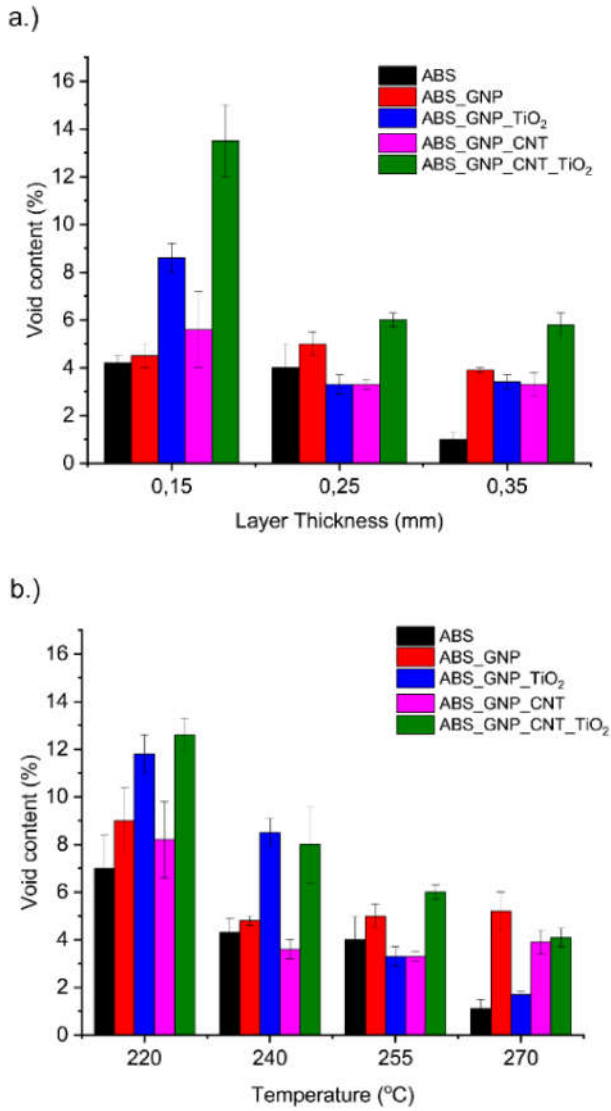

Figure 13: (a.) Influence of layer thickness (LT) on the void content of ABS and ABS based nanocomposites (255 °C). Combined with the data in Table 7 it is clear that at higher LT the reinforcing effect by the nanocomposites is dominant with respect to unmodified ABS; (b.) Influence of printing temperature on the void content. Combined with Table C3 of Appendix C.

Influence of printing temperature

The influence of the printing temperature on the mechanical properties of ABS and ABS-based nanocomposites is shown for a LT of 0.25 mm in Table C3 of Appendix C. Considering the standard deviations, the printing temperature variation leads on average to at most a little variation of the tensile properties. This is interesting from a technological point of view, as a lower printing temperature leads to less energy consumption and less material degradation in case repeated processing steps must be carried out. An increase of the tensile properties of ABS [77], PLA [78] and co-polyester [79] has although been reported as a result of an increased printing temperature, which propitiates a better bonding between layers. In this study, on average, the role of the nanoparticles is more important than the role of the printing temperature for improving the mechanical properties. One should although be careful with too generalized statements, as specific compositions can lead to significant changes upon a temperature variation. For instance, comparing unmodified ABS and ABS_GNP_CNT_TiO_2, the tensile modulus/strength increases by 16/20 and 4/18% if printed at 220 and 270 °C, respectively. Furthermore, ABS_GNP_CNT leads to an increased tensile strength by 15 and 9% at these two temperatures.

The influence of the printing temperature on the flexural modulus (Table C3 of Appendix C) is also not strong but with less trivial variations. Unmodified ABS displays an increase in the flexural modulus by 6% from 220 to 270 °C, probably due to a better coalescence, even though the specimen at 255 °C shows the worst flexural modulus value. The use of ABS_GNP, ABS_GNP_TiO_2, and ABS_GNP_CNT results in no variations in the flexural modulus with an increase in temperature. The use of ABS_GNP_CNT_TiO_2 results in an increase in the flexural modulus with an increase of the temperature up to 255 °C. Also, in many cases a decrease in the flexural

properties is observed. This is for instance very clear with ABS_GNP_TiO_2, which exhibits values of flexural modulus and strength up to 18% and 13% lower than the values for unmodified ABS.

The last column of Table C3 of Appendix C contains the impact strength data and Figure 14 shows the impact fractured specimens (LT of 0.25 mm). The impact strength of ABS is reduced with the addition of nanoparticles, and it is at first sight not majorly affected by the printing temperature. Figure 13b although shows significant decreases for the void content at higher printing temperature. The void content decreases with an increase in printing temperature and again the bottom parts of the micrographs show a denser structure. It should be reminded that a denser part with a (hybrid) nanocomposite does not mean that the material properties will be better, as the degree of dispersion and the interaction with the matrix are crucial as well.

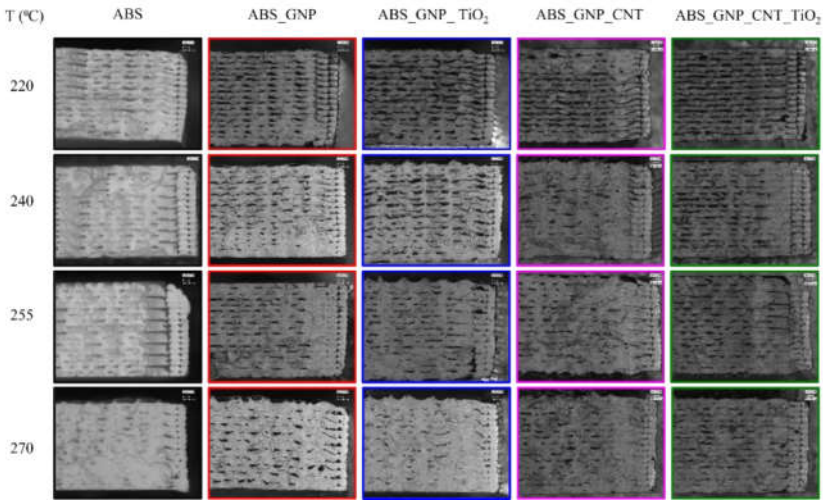

Figure 14: influence of temperature and composition on the morphology of impact fractured specimen. Layer thickness of 0.25 mm; XYZ printing.

More in detail, printing at 220 °C, leads to a higher void content in the part, especially in the nanocomposites, due to an increased viscosity and reduced mobility of the polymer chains. ABS_GNP_CNT_TiO_2 is the composition that is most sensitive to the temperature changes for the void content with a drop from 12,5 to 4% in Figure 13b. Amongst the nanocomposites, the use of ABS_GNP_TiO_2 allows to reach the lowest content of voids at 270 °C (1.5%), which is very close to unmodified ABS (1.1%). This indicates that the increase in temperature indeed creates denser parts and that indeed the sintering of specifically this composition is favorable. It should however be reminded that this does necessarily translates into improved quality in the bond or interface [80].

Influence of the printing orientation

Up to now all specimens have been printed in the XYZ direction. In the present work, ABS- and ABS-based nanocomposites have also been printed in the ZXY direction (see last entry in Table 3) to evaluate the influence of nanoparticle addition on the Z-strength. Specimens build in the ZXY-direction usually have lower mechanical properties than the ones printed in the XYZ direction. Such specimens usually undergo inter-layer bond failure [81], as the applied load is then perpendicular to the deposited layers. Hence, the interfacial region between layers and their adhesion will play an important role, as the bond will withstand most of the stress applied, instead of the bulk.

Table 8: Tensile properties of ABS and ABS-based nanocomposites printed in the ZXY direction and Degree of anisotropy results; LT of 0.25 mm; printing temperature of 255 °C; XYZ results in Table 7.

	Tensile modulus (MPa)	**Tensile strength (MPa)**	**Strain at break (%)**	**Degree of anisotropy (%)**
ABS	1970 ± 148	15.5 ± 3.4	1.1 ± 0.4	59.3
ABS_GNP	2032 ± 323	17.6 ± 2.8	1.3 ± 0.4	55.2
ABS_GNP_TiO_2	2107 ± 130	14.6 ± 2.4	0.8 ± 0.3	58.5
ABS_GNP_CNT	2220 ± 315	16.6 ± 3.7	1 ± 0.5	46.3
ABS_GNP_CNT_TiO_2	2206 ± 225	16 ± 2.5	0.9 ± 0.3	61.1

The results in Table 8 (LT of 0.25 mm and printing temperature of 255°C) show that all the compositions printed in the ZXY direction have a remarkable decrease in their tensile properties compared to the specimens printed in the XYZ direction (results in Table 7). Also, the standard variations are high in Table 8 and no major differences are noted between the different samples, indicating that the addition of nanoparticles has a limited effect on the overall bond formation. However, comparing the ZXY and XYZ results it follows that unmodified ABS shows a decrease of 30% in the tensile modulus, whereas for the other compositions a smaller drop is obtained with values ranging from 4 to 27%. With exception of ABS_GNP_CNT, the ultimate tensile strength (UTS) of ABS and compositions printed in the ZXY direction represents only around 40% of the strength of the parts printed in the XYZ direction. This can be further analyzed by the degree of anisotropy D_a [82]:

$$D_a = \left(\frac{UTS_{XYZ} - UTS_{ZXY}}{UTS_{XYZ}}\right) x100 , \qquad (2)$$

In this study, we report for ABS a value of anisotropy of 59.3 % which is somewhat higher than a reported value of 48% [82], likely due to other printing settings. For

most of the nanocomposites a slight drop of D_a is obtained, as shown in the last column of Table 8, especially for ABS_GNP_CNT which has a D_a of 46,3%. ABS_GNP_CNT_TiO_2 is the only nanocomposite that exhibits a D_a higher than ABS, and this may be due to its optimal dispersion and reinforcing effect in the XYZ direction.

Multidirectional analysis

To better outline the influence of nanoparticle addition and the printing parameters on the mechanical properties of ABS, correlation graphs have been made considering the mean results of the tensile and flexural testing. More in detail, the tensile strength is plotted against the tensile modulus in Figure 15a, and Figure 15b is the similar plot for the flexural testing results. Focus is on the influence of LT and the printing temperature for different compositions and the XYZ printing direction (each one region or color): ABS ("black/grey"), ABS_GNP ("red"), ABS_GNP_TiO_2 ("blue") ABS_GNP_CNT ("fuschia"), and ABS_GNP_CNT_TiO_2 ("green"). The extra tensile related results for the ZXY direction are represented via a "yellow" color.

It follows that globally the addition of nanoparticles to ABS influences the tensile properties more than the flexural properties. More specifically, under tension load the use of ABS_GNP and ABS_GNP_TiO_2 has little to no influence on the properties, whereas the use of ABS_GNP_CNT and ABS_GNP_CNT_TiO_2 lead to increased values for both the tensile strength and modulus, at least if the printing condition is XYZ.

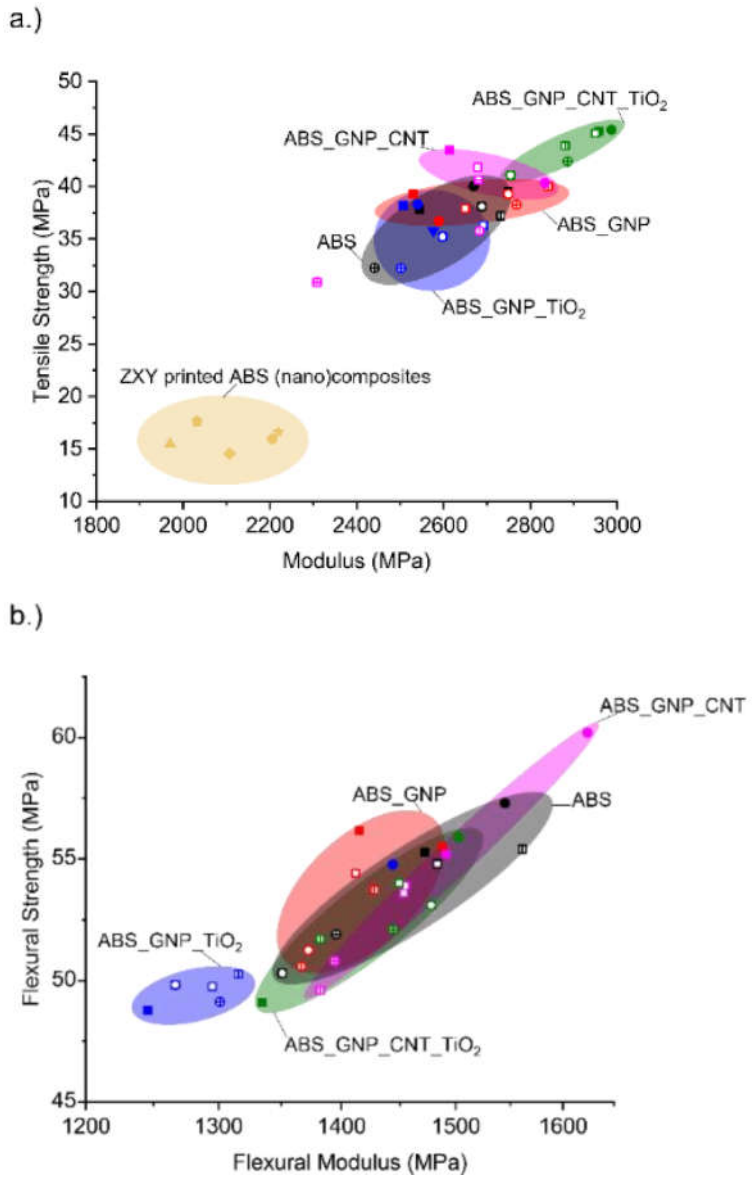

Figure 15: Main effects of the influence of layer thickness (LT), printing temperature, printing direction and nanoparticle addition on the tensile (a.) and flexural (b.) properties ; Circles represent the LT variation as: filled = 0.15 mm, hollow = 0.25 mm and cross = 0.35 mm.

Squares represent the printing temperature variation as: filled = 220 °C, hollow = 240 °C, cross = 255 °C, and vertical line = 270 °C (all XYZ data); for the ZXY printed tensile data (yellow group): △ = ABS; ⬠ = ABS_GNP; ◇ = ABS_GNP_TiO$_2$; ☆ = ABS_GNP_CNT, and ⬡ = ABS_GNP_CNT_TiO$_2$.

This positive tensile effect for ABS_GNP_CNT and ABS_GNP_CNT_TiO$_2$ can be related to the addition of CNT's to the mixture and their reinforcing effect. The use of ABS_GNP_CNT_TiO$_2$ results in the best tensile properties, what suggests that this composition possesses synergistic effects between the particles and displays the best dispersion state within the matrix. This composition improves the tensile modulus of ABS by 16% and the tensile strength up to 20%, with a total of 2,5 m% in loading. No improvements have been reported in the tensile strength of 3D printed ABS-based hybrid nanocomposites based on CNT and GNP [38], which indicates that the addition of TiO$_2$ is beneficial in improving the tensile properties.

As shown in Figure 15a, the specimens printed in the ZXY direction shows a dramatic decrease in the tensile properties, due to inter-layer bond failure. The addition of nanoparticles does not sufficiently improve the bond strength of the matrix. Hence, XYZ printing is preferred, as can be expected.

For the flexural tests in Figure 15b, most of the results fall in the same overall region, indicating limited effect of the particle addition on the flexural properties of ABS. However, the use of ABS_GNP_TiO$_2$ results in reduced mechanical properties, forming a separated group in the chart, which is due to the TiO$_2$ agglomeration in the matrix and the low interaction between GNP and TiO$_2$. A closer inspection reveals that printing with a low LT lead to the best flexural properties within each group. In addition, ABS_GNP_CNT printed with the smallest LT shows the best flexural results among all the compositions, regarding both modulus and strength.

5. 5. Conclusions

Several ABS-based mono- and hybrid nanocomposites have been first explored and submitted to dedicated analysis to evaluate their potential for 3D printing/FFF applications. The results for the addition of GNP, CNT and TiO_2 nanoparticles and their combination(s) on the linear viscoelastic properties indicate that the compositions with CNT display improved dispersion and interaction with the matrix. The qualitative printability tests indicate that all nanocomposites enable printing, but the ones containing GNP and/or TiO_2 show the best coalescence between deposited filaments. Combined the rheological and basic printing analysis allowed to select the most interesting compositions for further filament fabrication, namely ABS_GNP, ABS_GNP_TiO_2, ABS_GNP_CNT, and ABS_GNP_CNT_TiO_2.

The related filaments, alongside the unmodified ABS filament, have been characterized via thermal analysis, XRD, SEM, sintering, and further rheological analysis. It is shown that no major changes on the thermal properties of ABS are caused by the addition of the nanoparticles, indicating no stringent changes in the 3D printing processing parameters. The use of the composition ABS_GNP_CNT_TiO_2 results in the best dispersion, due to the good interaction between CNT and TiO_2 in the matrix, while the sintering analysis shows that the compositions with CNT reach lower levels of coalescence, due to an increased viscosity.

Modeling analysis reveals that the sintering mechanism is largely diffusional, in which the overall activation energy of sintering (E_a) correlates to the zero-shear viscosity (η_0), at least at higher temperatures.

The influence of layer thickness, printing temperature and build orientation on the mechanical properties of actually 3D printed samples has been assessed and

specifically rationalized into summary plots, highlighting the best compositions/settings for a control over tensile and/or flexural properties.

It is shown that the mechanical properties increase with the decrease in layer thickness, whereas the printing temperature has little influence on the mechanical properties. Changing the build orientation from XYZ to ZXY leads to an abrupt drop of the mechanical properties, indicating poor bond strength and high anisotropy in these materials. The combination of the nanoparticles with optimal printing parameters yields better properties for 3D printed ABS, which might increase the range of application of this material type. Notably the slower sintering and higher void degrees in the 3D printed parts play a secondary role as the nanoparticle incorporation provides strong reinforcement. In this context, a hybrid nanocomposite with GNP, CNT and TiO_2 is for the first time applied in FFF, indicating possible routes for new materials development for 3D printing.

REFERENCES

1. Cano-Vicent, A.; Tambuwala, M.M.; Hassan, S.S.; Barh, D.; Aljabali, A.A.A.; Birkett, M.; Arjunan, A.; Serrano-Aroca, Á. Fused deposition modelling: Current status, methodology, applications and future prospects. *Addit. Manuf.* **2021**, *47*, 102378, doi:10.1016/j.addma.2021.102378.
2. Penumakala, P.K.; Santo, J.; Thomas, A. A critical review on the fused deposition modeling of thermoplastic polymer composites. *Compos. Part B Eng.* **2020**, *201*, 108336, doi:10.1016/j.compositesb.2020.108336.
3. Lalegani Dezaki, M.; Mohd Ariffin, M.K.A.; Hatami, S. An overview of fused deposition modelling (FDM): research, development and process optimisation. *Rapid Prototyp. J.* **2021**, *27*, 562–582, doi:10.1108/RPJ-08-2019-0230.
4. Wang, S.; Daelemans, L.; D'hooge, D.R.; Couck, L.; Van Den Broeck, W.; Cornillie, P.; Gou, M.; De Clerck, K.; Cardon, L. Lifting the quality of fused filament fabrication of polylactic acid based composites. *Compos. Part B Eng.* **2021**, *210*, 108613, doi:10.1016/j.compositesb.2021.108613.
5. Van Waeleghem, T.; Marchesini, F.H.; Cardon, L.; D'hooge, D.R. Melt exit flow modelling and experimental validation for fused filament fabrication: From Newtonian to non-Newtonian effects. *J. Manuf. Process.* **2022**, *77*, 138–150, doi:10.1016/j.jmapro.2022.03.002.
6. La Gala, A.; Fiorio, R.; Ceretti, D.V.A.; Erkoç, M.; Cardon, L.; D'hooge, D.R. A Combined Experimental and Modeling Study for Pellet-Fed Extrusion-Based Additive Manufacturing to Evaluate the Impact of the Melting Efficiency. *Materials (Basel).* **2021**, *14*, 5566, doi:10.3390/ma14195566.
7. Tao, Y.; Kong, F.; Li, Z.; Zhang, J.; Zhao, X.; Yin, Q.; Xing, D.; Li, P. A review on voids of 3D printed parts by fused filament fabrication. *J. Mater. Res. Technol.* **2021**, *15*, 4860–4879, doi:10.1016/j.jmrt.2021.10.108.
8. Seppala, J.E.; Hoon Han, S.; Hillgartner, K.E.; Davis, C.S.; Migler, K.B. Weld formation during material extrusion additive manufacturing. *Soft Matter* **2017**, *13*, 6761–6769, doi:10.1039/c7sm00950j.
9. Coogan, T.J.; Kazmer, D.O. Prediction of interlayer strength in material extrusion additive manufacturing. *Addit. Manuf.* **2020**, *35*, 101368, doi:10.1016/j.addma.2020.101368.
10. Gurrala, P.K.; Regalla, S.P. Part strength evolution with bonding between filaments in fused deposition modelling: This paper studies how coalescence of filaments contributes to the strength of final FDM part. *Virtual Phys. Prototyp.* **2014**, *9*, 141–149, doi:10.1080/17452759.2014.913400.
11. Fernandez, E.; Ceretti, D.A.; Wang, S.; Jiang, Y.; Zhang, J.; D'hooge, D.R.; Cardon, L. Fused filament fabrication of copolyesters by understanding the balance of inter- and intra-layer welding. *Plast. Rubber Compos.* **2020**, *0*, 1–7, doi:10.1080/14658011.2020.1855386.
12. Sun, Q. Effect of processing conditions on the bonding quality of FDM polymer filaments. **2008**, *2*, 72–80, doi:10.1108/13552540810862028.
13. Gao, X.; Qi, S.; Kuang, X.; Su, Y.; Li, J.; Wang, D. Fused filament fabrication of polymer materials: A review of interlayer bond. *Addit. Manuf.* **2021**, *37*, 101658, doi:10.1016/j.addma.2020.101658.
14. Coogan, T.J.; Kazmer, D.O. Modeling of interlayer contact and contact pressure during fused filament fabrication. *J. Rheol. (N. Y. N. Y).* **2019**, *63*, 655–672, doi:10.1122/1.5093033.
15. Figueira, F.L.; Wu, Y.Y.; Zhou, Y.N.; Luo, Z.H.; Van Steenberge, P.H.M.;

D'Hooge, D.R. Coupled matrix kinetic Monte Carlo simulations applied for advanced understanding of polymer grafting kinetics. *React. Chem. Eng.* **2021**, *6*, 640–661, doi:10.1039/d0re00407c.

16. Dreval, V.E.; Vasil'ev, G.B.; Borisenkova, E.K.; Kulichikhin, V.G. Rheological and mechanical properties of ABS plastics prepared by bulk polymerization. *Polym. Sci. - Ser. A* **2006**, *48*, 338–345, doi:10.1134/S0965545X06030151.
17. Aoki, Y. Rheological properties of abs polymer melts having a good dispersion of rubber particles. *J. Nonnewton. Fluid Mech.* **1986**, *22*, 91–99, doi:10.1016/0377-0257(86)80005-2.
18. Bertin, M. -P; Marin, G.; Montfort, J. -P Viscoelastic properties of acrylonitrile-butadiene-styrene (ABS) polymers in the molten state. *Polym. Eng. Sci.* **1995**, *35*, 1394–1406, doi:10.1002/pen.760351711.
19. Takahashi, M.; Li, L.; Masuda, T. Nonlinear Viscoelasticity of ABS Polymers in the Molten State. *J. Rheol. (N. Y. N. Y).* **1989**, *33*, 709–723, doi:10.1122/1.550035.
20. Aoki, Y.; Hatano, A.; Watanabe, H. Chain relaxation time in ABS polymer melts. *Nihon Reoroji Gakkaishi* **2002**, *30*, 59–63, doi:10.1678/rheology.30.59.
21. Yu, W.; Wang, J.; You, W. Structure and linear viscoelasticity of polymer nanocomposites with agglomerated particles. *Polymer (Guildf).* **2016**, *98*, 190–200, doi:10.1016/j.polymer.2016.06.028.
22. Du, F.; Scogna, R.C.; Zhou, W.; Brand, S.; Fischer, J.E.; Winey, K.I. Nanotube networks in polymer nanocomposites: Rheology and electrical conductivity. *Macromolecules* **2004**, *37*, 9048–9055, doi:10.1021/ma049164g.
23. Wang, X.; Jiang, M.; Zhou, Z.; Gou, J.; Hui, D. 3D printing of polymer matrix composites: A review and prospective. *Compos. Part B Eng.* **2017**, *110*, 442–458, doi:10.1016/j.compositesb.2016.11.034.
24. Ahmadifar, M.; Benfriha, K.; Shirinbayan, M.; Tcharkhtchi, A. *Additive Manufacturing of Polymer-Based Composites Using Fused Filament Fabrication (FFF): a Review*; Springer Netherlands, 2021; Vol. 28; ISBN 0123456789.
25. Szeluga, U.; Kumanek, B.; Trzebicka, B. Synergy in hybrid polymer/nanocarbon composites. A review. *Compos. Part A Appl. Sci. Manuf.* **2015**, *73*, 204–231, doi:10.1016/j.compositesa.2015.02.021.
26. Waheed, Q.; Khan, A.N.; Jan, R. Investigating the reinforcement effect of few layer graphene and multi-walled carbon nanotubes in acrylonitrile-butadiene-styrene. *Polymer (Guildf).* **2016**, *97*, 496–503, doi:10.1016/j.polymer.2016.05.070.
27. Duan, L.; Spoerk, M.; Wieme, T.; Cornillie, P.; Xia, H.; Zhang, J.; Cardon, L.; D'hooge, D.R. Designing formulation variables of extrusion-based manufacturing of carbon black conductive polymer composites for piezoresistive sensing. *Compos. Sci. Technol.* **2019**, *171*, 78–85, doi:10.1016/j.compscitech.2018.12.009.
28. Duan, L.; D'hooge, D.R.; Cardon, L. Recent progress on flexible and stretchable piezoresistive strain sensors: From design to application. *Prog. Mater. Sci.* **2020**, *114*, 100617, doi:10.1016/j.pmatsci.2019.100617.
29. Jyoti, J.; Dhakate, S.R.; Singh, B.P. Phase transition and anomalous rheological properties of graphene oxide-carbon nanotube acrylonitrile butadiene styrene hybrid composites. *Compos. Part B Eng.* **2018**, *154*, 337–350, doi:10.1016/j.compositesb.2018.08.100.

30. Chatterjee, S.; Nafezarefi, F.; Tai, N.H.; Schlagenhauf, L.; Nüesch, F.A.; Chu, B.T.T. Size and synergy effects of nanofiller hybrids including graphene nanoplatelets and carbon nanotubes in mechanical properties of epoxy composites. *Carbon N. Y.* **2012**, *50*, 5380–5386, doi:10.1016/j.carbon.2012.07.021.
31. Yue, L.; Pircheraghi, G.; Monemian, S.A.; Manas-Zloczower, I. Epoxy composites with carbon nanotubes and graphene nanoplatelets - Dispersion and synergy effects. *Carbon N. Y.* **2014**, *78*, 268–278, doi:10.1016/j.carbon.2014.07.003.
32. Yang, S.Y.; Lin, W.N.; Huang, Y.L.; Tien, H.W.; Wang, J.Y.; Ma, C.C.M.; Li, S.M.; Wang, Y.S. Synergetic effects of graphene platelets and carbon nanotubes on the mechanical and thermal properties of epoxy composites. *Carbon N. Y.* **2011**, *49*, 793–803, doi:10.1016/j.carbon.2010.10.014.
33. Zhang, S.M.; Lin, L.; Deng, H.; Gao, X.; Bilotti, E.; Peijs, T.; Zhang, Q.; Fu, Q. Synergistic effect in conductive networks constructed with carbon nanofillers in different dimensions. *Express Polym. Lett.* **2012**, *6*, 159–168, doi:10.3144/expresspolymlett.2012.17.
34. Sun, Y.; Bao, H. Da; Guo, Z.X.; Yu, J. Modeling of the electrical percolation of mixed carbon fillers in polymer-based composites. *Macromolecules* **2009**, *42*, 459–463, doi:10.1021/ma8023188.
35. Liu, H.; Gao, J.; Huang, W.; Dai, K.; Zheng, G.; Liu, C.; Shen, C.; Yan, X.; Guo, J.; Guo, Z. Electrically conductive strain sensing polyurethane nanocomposites with synergistic carbon nanotubes and graphene bifillers. *Nanoscale* **2016**, *8*, 12977–12989, doi:10.1039/c6nr02216b.
36. Bilotti, E.; Zhang, H.; Deng, H.; Zhang, R.; Fu, Q.; Peijs, T. Controlling the dynamic percolation of carbon nanotube based conductive polymer composites by addition of secondary nanofillers: The effect on electrical conductivity and tuneable sensing behaviour. *Compos. Sci. Technol.* **2013**, *74*, 85–90, doi:10.1016/j.compscitech.2012.10.008.
37. Spinelli, G.; Kotsilkova, R.; Ivanov, E.; Petrova-Doycheva, I.; Menseidov, D.; Georgiev, V.; Di Maio, R.; Silvestre, C. Effects of filament extrusion, 3D printing and hot-pressing on electrical and tensile properties of poly(Lactic) acid composites filled with carbon nanotubes and graphene. *Nanomaterials* **2020**, *10*, doi:10.3390/nano10010035.
38. Dul, S.; Ecco, L.G.; Pegoretti, A.; Fambri, L. Graphene/carbon nanotube hybrid nanocomposites: Effect of compression molding and fused filament fabrication on properties. *Polymers (Basel).* **2020**, *12*, doi:10.3390/POLYM12010101.
39. Maiti, S.; Shrivastava, N.K.; Suin, S.; Khatua, B.B. Polystyrene/MWCNT/Graphite Nanoplate Nanocomposites: Efficient Electromagnetic Interference Shielding Material through Graphite Nanoplate–MWCNT–Graphite Nanoplate Networking. *ACS Appl. Mater. Interfaces* **2013**, *5*, 4712–4724, doi:10.1021/am400658h.
40. Yu, A.; Ramesh, P.; Sun, X.; Bekyarova, E.; Itkis, M.E.; Haddon, R.C. Enhanced Thermal Conductivity in a Hybrid Graphite Nanoplatelet – Carbon Nanotube Filler for Epoxy Composites. *Adv. Mater.* **2008**, *20*, 4740–4744, doi:10.1002/adma.200800401.
41. Ma, P.-C.; Liu, M.-Y.; Zhang, H.; Wang, S.-Q.; Wang, R.; Wang, K.; Wong, Y.-K.; Tang, B.-Z.; Hong, S.-H.; Paik, K.-W.; et al. Enhanced Electrical Conductivity of Nanocomposites Containing Hybrid Fillers of Carbon Nanotubes and Carbon Black. *ACS Appl. Mater. Interfaces* **2009**, *1*, 1090–1096, doi:10.1021/am9000503.

42. Prasad, K.E.; Das, B.; Maitra, U.; Ramamurty, U.; Rao, C.N.R. Extraordinary synergy in the mechanical properties of polymer matrix composites reinforced with 2 nanocarbons. *Proc. Natl. Acad. Sci.* **2009**, *106*, 13186–13189, doi:10.1073/pnas.0905844106.
43. Kumar, A.; Kumar, K.; Ghosh, P.K.; Yadav, K.L. MWCNT/TiO2 hybrid nano filler toward high-performance epoxy composite. *Ultrason. Sonochem.* **2018**, *41*, 37–46, doi:10.1016/j.ultsonch.2017.09.005.
44. Zhang, H.; Zhao, M.; Huang, Z.X.; Qu, J.P. Synergistic Effect Based on Enhanced Local Shear Forces in PVDF/TiO2/CNT Ternary Composites. *Ind. Eng. Chem. Res.* **2020**, *59*, 18887–18897, doi:10.1021/acs.iecr.0c03725.
45. Montgomery, D.C. *Design and Analysis of Experiments*; 5th ed.; John Wiley & Sons: New York, NY, 2001;
46. Zosel, A. Viskoelastisches Verhalten von ABS-Polymeren in der Schmelze. *Rheol. Acta* **1972**, *11*, 229–237, doi:10.1007/BF01993025.
47. Münstedt, H. Rheology of rubber-modified polymer melts. *Polym. Eng. Sci.* **1981**, *21*, 259–270, doi:10.1002/pen.760210503.
48. Gao, C.; Zhang, S.; Wang, F.; Wen, B.; Han, C.; Ding, Y.; Yang, M. Graphene networks with low percolation threshold in abs nanocomposites: Selective localization and electrical and rheological properties. *ACS Appl. Mater. Interfaces* **2014**, *6*, 12252–12260, doi:10.1021/am501843s.
49. Van Gurp, M.; Palmen, J. Time-Temperature superposition for polymeric blends. *Rheol. Bull.* **1998**, *6*, 5.
50. Dealy, J.M.; Larson, R.G. *Structure and Rheology of Molten Polymers*; Carl Hanser Verlag GmbH & Co. KG: München, 2006; ISBN 978-3-446-21771-3.
51. Aoki, Y. Dynamic viscoelastic properties of ABS polymers in the molten state. 5. Effect of grafting degree. *Macromolecules* **1987**, *20*, 2208–2213, doi:10.1021/ma00175a027.
52. Canales, J.; Muñoz, M.E.; Fernández, M.; Santamaría, A. Rheology, electrical conductivity and crystallinity of a polyurethane/graphene composite: Implications for its use as a hot-melt adhesive. *Compos. Part A Appl. Sci. Manuf.* **2016**, *84*, 9–16, doi:10.1016/j.compositesa.2015.12.018.
53. Serrano, C.; Cerrada, M.L.; Fernández-García, M.; Ressia, J.; Vallés, E.M. Rheological and structural details of biocidal iPP-TiO 2 nanocomposites. *Eur. Polym. J.* **2012**, *48*, 586–596, doi:10.1016/j.eurpolymj.2011.12.012.
54. Sukumaran, S.K.; Kobayashi, T.; Takeda, S.; Khosla, A.; Furukawa, H.; Sugimoto, M. Electrical Conductivity and Linear Rheology of Multiwalled Carbon Nanotube/Acrylonitrile Butadiene Styrene Polymer Nanocomposites Prepared by Melt Mixing and Solution Casting. *J. Electrochem. Soc.* **2019**, *166*, B3091–B3095, doi:10.1149/2.0171909jes.
55. McClory, C.; McNally, T.; Baxendale, M.; Pötschke, P.; Blau, W.; Ruether, M. Electrical and rheological percolation of PMMA/MWCNT nanocomposites as a function of CNT geometry and functionality. *Eur. Polym. J.* **2010**, *46*, 854–868, doi:10.1016/j.eurpolymj.2010.02.009.
56. Kota, A.K.; Cipriano, B.H.; Duesterberg, M.K.; Gershon, A.L.; Powell, D.; Raghavan, S.R.; Bruck, H.A. Electrical and rheological percolation in polystyrene/MWCNT nanocomposites. *Macromolecules* **2007**, *40*, 7400–7406, doi:10.1021/ma0711792.
57. Rostami, A.; Nazockdast, H.; Karimi, M. Graphene induced microstructural changes of PLA/MWCNT biodegradable nanocomposites: Rheological, morphological, thermal and electrical properties. *RSC Adv.* **2016**, *6*, 49747–49759, doi:10.1039/c6ra08345e.

58. Manap, A.; Mahalingam, S.; Vaithylingam, R.; Abdullah, H. Mechanical, thermal and morphological properties of thermoplastic polyurethane composite reinforced by multi-walled carbon nanotube and titanium dioxide hybrid fillers. *Polym. Bull.* **2021**, *78*, 5815–5832, doi:10.1007/s00289-020-03393-z.
59. Lertwimolnun, W.; Vergnes, B. Influence of compatibilizer and processing conditions on the dispersion of nanoclay in a polypropylene matrix. *Polymer (Guildf).* **2005**, *46*, 3462–3471, doi:10.1016/j.polymer.2005.02.018.
60. Kruth, J.P.; Levy, G.; Klocke, F.; Childs, T.H.C. Consolidation phenomena in laser and powder-bed based layered manufacturing. *CIRP Ann. - Manuf. Technol.* **2007**, *56*, 730–759, doi:10.1016/j.cirp.2007.10.004.
61. Berretta, S.; Wang, Y.; Davies, R.; Ghita, O.R. Polymer viscosity, particle coalescence and mechanical performance in high-temperature laser sintering. *J. Mater. Sci.* **2016**, *51*, 4778–4794, doi:10.1007/s10853-016-9761-6.
62. Benedetti, L.; Brulé, B.; Decraemer, N.; Evans, K.E.; Ghita, O. Evaluation of particle coalescence and its implications in laser sintering. *Powder Technol.* **2019**, *342*, 917–928, doi:10.1016/j.powtec.2018.10.053.
63. Bellehumeur, C.T.; Bisaria, M.K.; Vlachopoulos, J. An experimental study and model assessment of polymer sintering. *Polym. Eng. Sci.* **1996**, *36*, 2198–2207, doi:10.1002/pen.10617.
64. Batakliev, T.; Georgiev, V.; Angelov, V.; Ivanov, E.; Kalupgian, C.; Muñoz, P.A.R.; Fechine, G.J.M.; Andrade, R.J.E.; Kotsilkova, R. Synergistic Effect of Graphene Nanoplatelets and Multiwall Carbon Nanotubes Incorporated in PLA Matrix: Nanoindentation of Composites with Improved Mechanical Properties. *J. Mater. Eng. Perform.* **2021**, *30*, 3822–3830, doi:10.1007/s11665-021-05679-3.
65. Wang, W.K.; Chen, J.J.; Zhang, X.; Huang, Y.X.; Li, W.W.; Yu, H.Q. Self-induced synthesis of phase-junction TiO2 with a tailored rutile to anatase ratio below phase transition temperature. *Sci. Rep.* **2016**, *6*, 1–10, doi:10.1038/srep20491.
66. Wang, Z.; Wang, J.; Li, M.; Sun, K.; Liu, C.J. Three-dimensional printed acrylonitrile butadiene styrene framework coated with Cu-BTC metal-organic frameworks for the removal of methylene blue. *Sci. Rep.* **2014**, *4*, 4–10, doi:10.1038/srep05939.
67. Batakliev, T.; Petrova-Doycheva, I.; Angelov, V.; Georgiev, V.; Ivanov, E.; Kotsilkova, R.; Casa, M.; Cirillo, C.; Adami, R.; Sarno, M.; et al. Effects of graphene nanoplatelets and multiwall carbon nanotubes on the structure and mechanical properties of Poly(lactic acid) composites: A comparative study. *Appl. Sci.* **2019**, *9*, doi:10.3390/app9030469.
68. Skorski, M.R.; Esenther, J.M.; Ahmed, Z.; Miller, A.E.; Hartings, M.R. The chemical, mechanical, and physical properties of 3D printed materials composed of TiO2-ABS nanocomposites. *Sci. Technol. Adv. Mater.* **2016**, *17*, 89–97, doi:10.1080/14686996.2016.1152879.
69. Al-Saleh, M.H.; Al-Saidi, B.A.; Al-Zoubi, R.M. Experimental and theoretical analysis of the mechanical and thermal properties of carbon nanotube/ acrylonitrilee-styrenee-butadiene nanocomposites. *Polymer (Guildf).* **2016**, *89*, 12–17, doi:10.1016/j.polymer.2016.01.053.
70. Al-Saleh, M.H.; Sundararaj, U. Microstructure, electrical, and electromagnetic interference shielding properties of carbon nanotube/acrylonitrile-butadiene-styrene nanocomposites. *J. Polym. Sci. Part B Polym. Phys.* **2012**, *50*, 1356–1362, doi:10.1002/polb.23129.
71. D'Hooge, D.R.; Van Steenberge, P.H.M.; Reyniers, M.F.; Marin, G.B. The

strength of multi-scale modeling to unveil the complexity of radical polymerization. *Prog. Polym. Sci.* **2016**, *58*, 59–89, doi:10.1016/j.progpolymsci.2016.04.002.

72. McIlroy, C.; Olmsted, P.D. Deformation of an amorphous polymer during the fused-filament-fabrication method for additive manufacturing. *J. Rheol. (N. Y. N. Y).* **2017**, *61*, 379–397, doi:10.1122/1.4976839.
73. Razavi-Nouri, M.; Rezadoust, A.M.; Soheilpour, Z.; Garoosi, K.; Ghaffarian, S.R. Morphology and mechanical properties of poly (acrylonitrile-butadiene-styrene)/multi-walled carbon nanotubes nanocomposite specimens prepared by fused deposition modeling. *Polym. Compos.* **2021**, *42*, 342–352, doi:10.1002/pc.25829.
74. Dul, S.; Fambri, L.; Pegoretti, A. Filaments production and fused deposition modelling of ABS/carbon nanotubes composites. *Nanomaterials* **2018**, *8*, doi:10.3390/nano8010049.
75. Sezer, H.K.; Eren, O. FDM 3D printing of MWCNT re-inforced ABS nano-composite parts with enhanced mechanical and electrical properties. *J. Manuf. Process.* **2019**, *37*, 339–347, doi:10.1016/j.jmapro.2018.12.004.
76. Vidakis, N.; Maniadi, A.; Petousis, M.; Vamvakaki, M.; Kenanakis, G.; Koudoumas, E. Mechanical and Electrical Properties Investigation of 3D-Printed Acrylonitrile–Butadiene–Styrene Graphene and Carbon Nanocomposites. *J. Mater. Eng. Perform.* **2020**, *29*, 1909–1918, doi:10.1007/s11665-020-04689-x.
77. Abbott, A.C.; Tandon, G.P.; Bradford, R.L.; Koerner, H.; Baur, J.W. Process-structure-property effects on ABS bond strength in fused filament fabrication. *Addit. Manuf.* **2018**, *19*, 29–38, doi:10.1016/j.addma.2017.11.002.
78. Kuznetsov, V.E.; Solonin, A.N.; Tavitov, A.; Urzhumtsev, O.; Vakulik, A. Increasing strength of FFF three-dimensional printed parts by influencing on temperature-related parameters of the process. *Rapid Prototyp. J.* **2020**, *26*, 107–121, doi:10.1108/RPJ-01-2019-0017.
79. Abouzaid, K.; Guessasma, S.; Belhabib, S.; Bassir, D.; Chouaf, A. Printability of co-polyester using fused deposition modelling and related mechanical performance. *Eur. Polym. J.* **2018**, *108*, 262–273, doi:10.1016/j.eurpolymj.2018.08.034.
80. Cole, D.P.; Riddick, J.C.; Iftekhar Jaim, H.M.; Strawhecker, K.E.; Zander, N.E. Interfacial mechanical behavior of 3D printed ABS. *J. Appl. Polym. Sci.* **2016**, *133*, 1–12, doi:10.1002/app.43671.
81. Chacón, J.M.; Caminero, M.A.; García-Plaza, E.; Núñez, P.J. Additive manufacturing of PLA structures using fused deposition modelling: Effect of process parameters on mechanical properties and their optimal selection. *Mater. Des.* **2017**, *124*, 143–157, doi:10.1016/j.matdes.2017.03.065.
82. Torrado, A.R.; Shemelya, C.M.; English, J.D.; Lin, Y.; Wicker, R.B.; Roberson, D.A. Characterizing the effect of additives to ABS on the mechanical property anisotropy of specimens fabricated by material extrusion 3D printing. *Addit. Manuf.* **2015**, *6*, 16–29, doi:10.1016/j.addma.2015.02.001.

Chapter 6

Insights on the dispersion of nanofillers in ABS and the influence of filament production technique on the properties of filaments and 3D printed parts

6.1. Abstract

In this chapter, the dispersion state of nanofillers on acrylonitrile butadiene styrene (ABS) is assessed via transmission electron microscopy (TEM) and rheometry. Additionally, the effect of fabrication route of ABS_GNP material and printing temperature on the tensile properties of 3D printed specimens is evaluated. TEM analysis and van Gurp-Palmen plots reveal that the composition ABS_GNP_CNT_TiO_2 presents the best nanofiller dispersion state, as a result of synergy between nanofillers. It is also shown that ABS_GNP_CNT presents a good nanofiller dispersion state in the matrix, even though some agglomerates may be present. Manufacturing ABS_GNP via one-step twin-screw extrusion (TSE), may induce a slightly better dispersion state of the GNP in ABS, when compared to the two-step production via micro-extrusion followed by single-screw extrusion (ME + SSE). However, thermo-mechanical degradation occurs during TSE, decreasing the zero-shear viscosity of the material and the tensile properties of 3D printed parts.

6.2. Introduction

Polymer nanocomposites (PNC's) are a promising class of materials for tailoring the feedstock properties and to expand the range of materials available for FFF [1–3]. PNC's have attracted considerable interest because of the "nano-effect", perceived by the enhancement in properties, such as mechanical, thermal, electrical or chemical, achieved by small loadings of nanofillers [4]. These materials are multi-component and multiphase systems, with at least two different phases that interact with one another, the continuum polymer matrix (Figure 1a) and a solid dispersed phase (Figure 1b). The latter presenting, in at least one of its dimensions, a size equal or smaller than 100 nm. The improvements in the properties of the polymer and potential of materials to exhibit superior properties are related to the interface and interactions between the nanofillers and matrix [5,6].

Several nanofillers may be used in PNC's [7–12] and they may be characterized according to their geometry, as this may influence their interaction with the matrix and influence the final properties of the materials (aspect ratio) [13–15]. As shown in Figure 1b, two-dimensional (2D) nanofillers present at least one nanometric dimension such as lamellar nanofillers, including layered silicate clays and graphene. One-dimensional (1D) nanofillers present at least two nanometric dimensions, such as carbon nanotubes or nanofiber. Zero-dimensional (0D) nanofillers, in turn, present three nanometric dimensions, such as spherical nanofillers, including nanosilica and titanium dioxide [5].

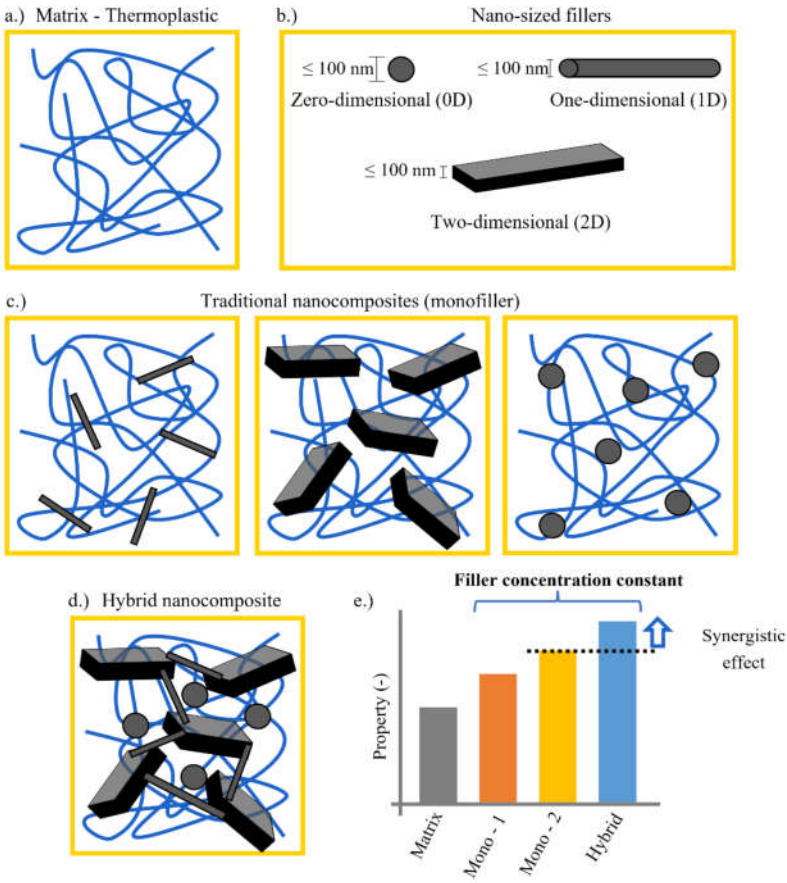

Figure 1: a.) polymer matrix, b.) types of nano-sized fillers according to their geometry, c.) mono-nanocomposites, d.) hybrid nanocomposites and e.) scheme of synergistic effect.

With promising properties, various compositions containing one nanoparticle (mono-nanocomposite) have been developed (scheme in Figure 1c) in the past decades [16–20]. Furthermore, hybrid nanocomposites (HNC's) have also been investigated [21–24]. HNC's are materials that consist of two or more nanofillers dispersed in a polymer matrix (Figure 1d), which show improved properties than their *mono-*

nanocomposites counterparts at the same nanofiller concentration. The improvement in the properties is related to a synergy effect between the nanofillers [25], as exemplified in (Figure 1e). These materials could be promising for 3D printing applications, due to their enhanced properties. For instance, as discussed in Chapter 5, we recently developed acrylonitrile butadiene styrene (ABS) hybrid nanocomposites with graphene nanoplatelets (GNP), carbon nanotubes (CNT) and titanium dioxide (TiO_2) which yield improved mechanical properties of 3D printed parts, with only 2.5 m.% loading [26].

One of the most economical and environmentally friendly method to produce PNC's is via melt blending, using common processing tools, such as a twin-screw extruder. Mechanical stresses generated in the processing leads to the breakdown of the nanoparticle agglomerates and subsequent individualization and dispersion of the nanofillers in the polymer matrix [27]. Still, this methodology may also induce degradation of the polymer, in case high screw speeds are used [28].

The final physical properties of the nanocomposite feedstock material are largely dependent of the degree of nanofillers dispersion in the polymer matrix [29]. Due to their small dimensions and high specific surface areas, nanofillers tend to form micron-sized aggregates. When a good dispersion state is not reached, the performance of nanocomposites may reduce significantly [30]. To assess the dispersion of nanofillers, electron microscopy tools are extremely valuable, especially transmission electron microscopy (TEM) [31]. The typical specimens for TEM measurements are ultra-thin sections of the material being analyzed, with thickness ranging from 50 to 100 nm. The obtained image is a 2D projection of the 3D specimen along the optic axis (Figure 2).

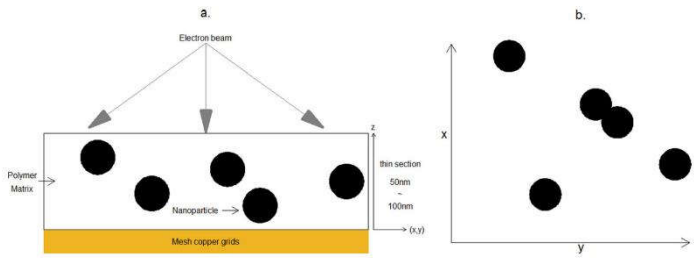

Figure 2: Projection view of TEM micrographs [30].

In Chapter 5, we demonstrated the potential and relevance of hybrid nanocomposites for FFF applications. Here, we further investigate the dispersion state of the nanofillers in ABS using transmission electron microscopy (TEM) and rheological analysis. In addition, we compare two processing routes for the manufacturing of ABS_GNP filaments for FFF on the dispersion state of the nanoparticle. We also assess the effect of processing route and printing temperature on the properties of 3D printed specimens.

6.3. Materials and methods

6.3.1. Materials

A general-purpose ABS (Terluran GP-22, INEOS) was used as a matrix. Graphene nanoplatelets (GNP's) (C-750-900407, Sigma Aldrich), multi-walled carbon nanotubes (MWCNT's, NC7000TM, Nanocyl) and titanium (IV) oxide (TiO_2) nano powder (634662, Sigma Aldrich) were used as nanofillers.

6.3.2. Characterization

ABS-based (nano)composite filaments for fused filament fabrication, obtained in Chapter 5, were manufactured via melt blending in a two-step procedure to reach the compositions described in Table 1. In the first step, masterbatches with a higher concentration of each nanofiller with respect to ABS were produced in a twin-screw micro-extruder (ME). The masterbatches were then pelletized and diluted into ABS using a single screw extruder (SSE). More details on the protocol may be found in Chapter 5 [26].

Table 1: Compositions assessed in this research.

Processing technique	Sample	Composition (m.%)			
		ABS	GNP	CNT	TiO_2
ME + SSE	**ABS**	100	0	0	0
ME + SSE	**ABS_GNP**	99.5	0.5	0	0
ME + SSE	**ABS_GNP_CNT**	98.5	0.5	1	0
ME + SSE	**ABS_GNP_TiO_2**	98.5	0.5	0	1
ME + SSE	**ABS_GNP_CNT_TiO_2**	97.5	0.5	1	1
TSE	**ABS_GNP_TSE**	99.5	0.5	0	0

In addition, the composition containing only GNP (see description in Table 1), was also produced in a one-step procedure, directly via larger scale twin-screw extrusion (TSE; Coperion ZSK18, co-rotating screws with 18 mm screw diameter and L/D of 40) with a temperature profile ranging from 145–220 °C, with a screw speed of 220 rpm. In both SSE and TSE, a rolling system and spooling device were used to pool the extrudates into a filament with a controlled (average) diameter of 1,75 mm and wind it into a spool for further FFF application.

The dispersion of nanofillers in ABS was assessed by means of transmission electron microscopy (TEM) in a JEM-1400 Plus (Jeol) at 100 kV on ultrathin sections (± 90 nm) of each specimen, cut with a ultramicrotome (Leica, EM UC6) using a diamond

knife (DIATOME, ultra 45°; 2,5mm) and collected on Formvar-coated copper grids (Formvar solution, EMS).

The linear viscoelastic behavior of the filaments was assessed by means of small amplitude oscillatory shear (SAOS) tests in a rheometer (MCR 702, Anton-Paar), using a parallel plate configuration with 25 mm of diameter and 1 mm gap, at 220 °C, under N_2 atmosphere. The filaments were chopped, and compression molded into a disk-like shape with 1 mm thickness and 25 mm diameter at 220 ◦C, using a hot press.

Specimens for tensile tests of ABS_GNP_TSE were produced using a Prusa printer (Prusa i3 MK3S+) with a 0.4 mm nozzle. The nozzle temperatures employed were 240, 255 and 270 °C, with 100% infill, 45° infill angle, 0.25 mm layer thickness and 110 °C bed temperature. The tensile properties of 3D printed materials were assessed in an Instron 5565 according to ISO 527, with 1BA specimens.

6.4. Results and discussion

6.4.1. Dispersion of nanofillers

Scanning electron microscopy (SEM) micrographs of ABS-based mono and hybrid nanocomposites were discussed in Chapter 5 [26]. They indicated that the samples ABS_GNP, ABS_GNP_TiO_2 and ABS_GNP_CNT exhibited regions with agglomerated nanofillers. While ABS_GNP_CNT_ TiO_2 exhibited an overall good nanofillers dispersion state, without occurrence of agglomerates.

To further assess the dispersion state of the nanofillers in ABS, a qualitative TEM analysis of the filaments was carried out. The TEM micrographs of ABS_GNP and ABS_GNP_TSE are shown in Figure 3, with aggregates or other interesting structures indicates by blue circles or arrows, respectively.

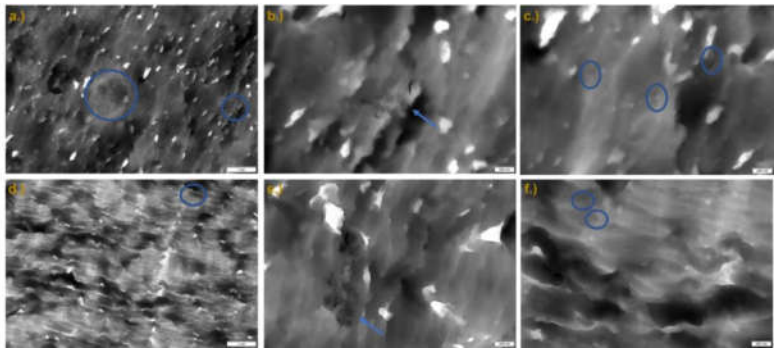

Figure 3: TEM micrographs of ABS_GNP (a.-c.) and ABS_GNP_TSE (d.-f.).

ABS_GNP (Figure 3a-c) presents big agglomerates (Figure 3a), smaller agglomerates (Figure 3b), and partially exfoliated structures with good distribution (Figure 3c). ABS_GNP_TSE (Figure 3d-f) also presents agglomerates (Figure 3d), however smaller and in less frequency than what was previously observed for ABS_GNP_SSE. Also, partially exfoliated structures can also be seen (Figure 3f). Less and smaller agglomerates observed for ABS_GNP_TSE indicates that TSE may have been more efficient in dispersing GNPs into ABS.

The TEM micrographs of ABS_GNP_TiO_2 composition (Figure 4) indicate the occurrence of agglomerates, corroborating the results of SEM. Some areas of high concentration of TiO_2 are also shown, however, TiO_2 particles seem to be more finely dispersed and distributed than GNPs. Uyor et al [32] reported good synergy between modified GNP and TiO_2, prepared via solution blending. This may indicate the potential of these materials when different routes of fabrication and chemical modification strategies are used. However, this still implies a less sustainable approach towards the manufacturing of filaments for FFF.

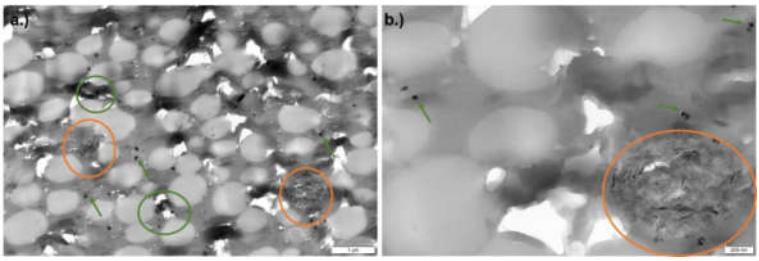

Figure 4: TEM micrographs of ABS_GNP_ TiO_2.

When it comes to ABS_GNP_CNT (Figure 5), the analyzed section indicates a more finely distribution of CNTs in the matrix (blue arrows), with few partially exfoliated GNP structures (orange arrows). Important to note that SEM investigations (see Chapter 5) indicated the occurrence of agglomerates for CNT. However, in the sections of the specimen analyzed via TEM, no agglomeration was seen.

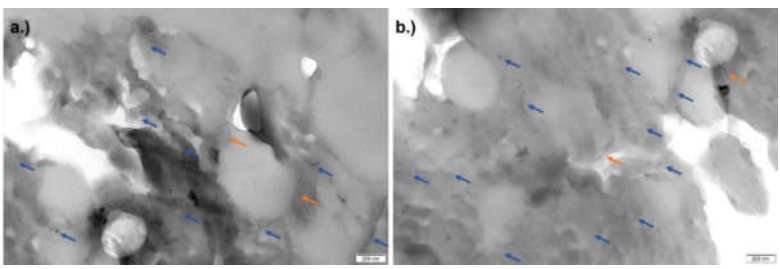

Figure 5: TEM micrographs of ABS_GNP_CNT.

The composition ABS_GNP_CNT_TiO_2 (Figure 6) shows the best dispersion and distribution state, as already discussed in Chapter 5. There are few small agglomerates of GNPs (Figure 6a, orange circles), however it is possible to see that the dispersion of TiO_2 and CNT occurred properly in the matrix, as indicated by green and blue arrows, respectively. This is due to synergistic interaction between the nanofillers, with TiO_2 assisting the dispersion of CNT in the matrix [33]. Furthermore, there are

also partially and fully exfoliated structures of GNPs, shown by the orange arrows. This composition exhibited the best dispersion levels due to the synergy between particles [34].

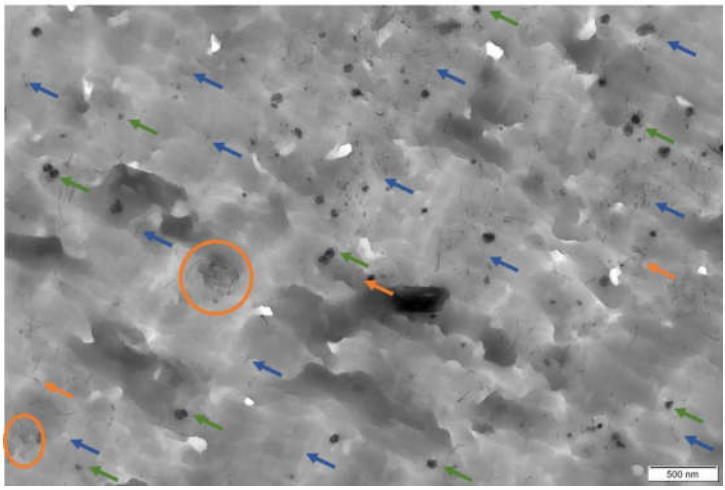

Figure 6: TEM micrograph of ABS_GNP_CNT_TiO_2.

To further corroborate the dispersion and structural analysis of hybrid composites, van Gurp-Palmen plots are presented for the mono and hybrid compositions (Figure 7). These plots represents the variation of phase angle (δ) with the complex modulus, and are often used to assess Time-Temperature Superposition (TTS) of polymers [35]. Nevertheless, they may give insight on the structural changes of polymer nanocomposites and an idea of their rheological percolation. When the polymer chains are completely relaxed, the value of δ is close to 90° in the low complex modulus region. For a heterogeneous composite, the response above 45° indicates viscous flow and below 45° indicates an elastic flow [36]. The ABS used in this research presents a high elastic behavior [26] and already exhibits δ below 45° in the low frequency region. The incorporation of GNP (via SSE and TSE), and GNP and TiO_2 combined

into ABS did not significantly alter the curve for ABS, indicating that no network formation between particles took place, because of their restricted level of dispersion, forming rather micro-composites. The incorporation of GNP and CNT and GNP, CNT and TiO_2 combined in ABS lead to a reduction in the phase angle, indicating a stronger elastic behavior. This drop in phase angle is related to the development of the elasticity due to the network structure formed [37]. This corroborates the results of TEM analysis, suggesting the particles were well dispersed.

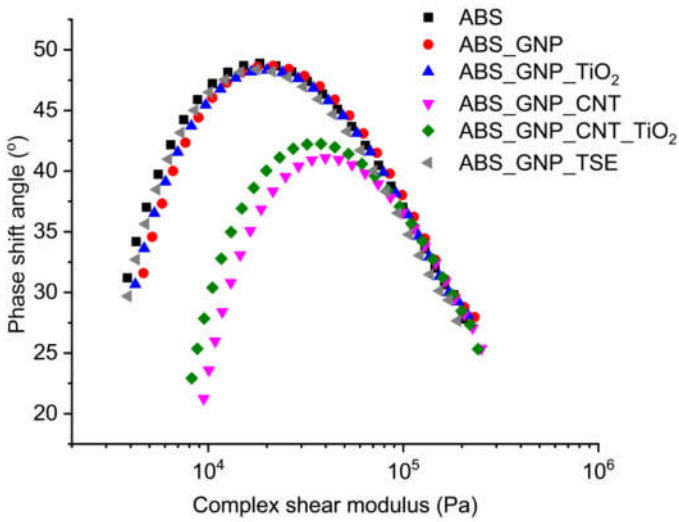

Figure 7: van Gurp-Palmen plots for raw ABS and ABS-based (nano)composites.

6.4.2. Influence of filament processing technique on the rheological behavior of filaments and on the properties of 3D printed parts

For the composition containing ABS and GNP, the influence of fabrication technique on the dispersion state of GNP and on macroscopic properties is assessed. From TEM

analysis (Figure 3), it is possible to see that the TSE process may have induced a slightly better nanofiller dispersion, when compared to ME + SSE. Rheological testing may also give further insights on the structure of these materials, as discussed in Chapters 3 and 4 [26]. The variation of storage modulus and the complex viscosity with the angular frequency for ABS, ABS_GNP and ABS_GNP_TSE filaments are shown in Figure 8. As discussed in Chapters 3 and 4, ABS displays a non-terminal behavior, seen by the plateau on the low frequency region of G', (Figure 8a) and consistent with the increase in the complex viscosity in the same region (Figure 8b), indicating an apparent yield stress. The non-terminal behavior is associated to the restriction in the molecular movement, resulting in incomplete relaxation of the polymer chains [38]. This behavior was not enhanced by the addition of GNP when ME fabrication route was employed, as discussed in Chapter 5, for the extrudates. From Figure 8a, it is possible to see that the fabrication of this compositions via ME + SSE and TSE also did not induce any enhancement on the ABS terminal behavior, indicating a poor dispersion state of the GNP in ABS.

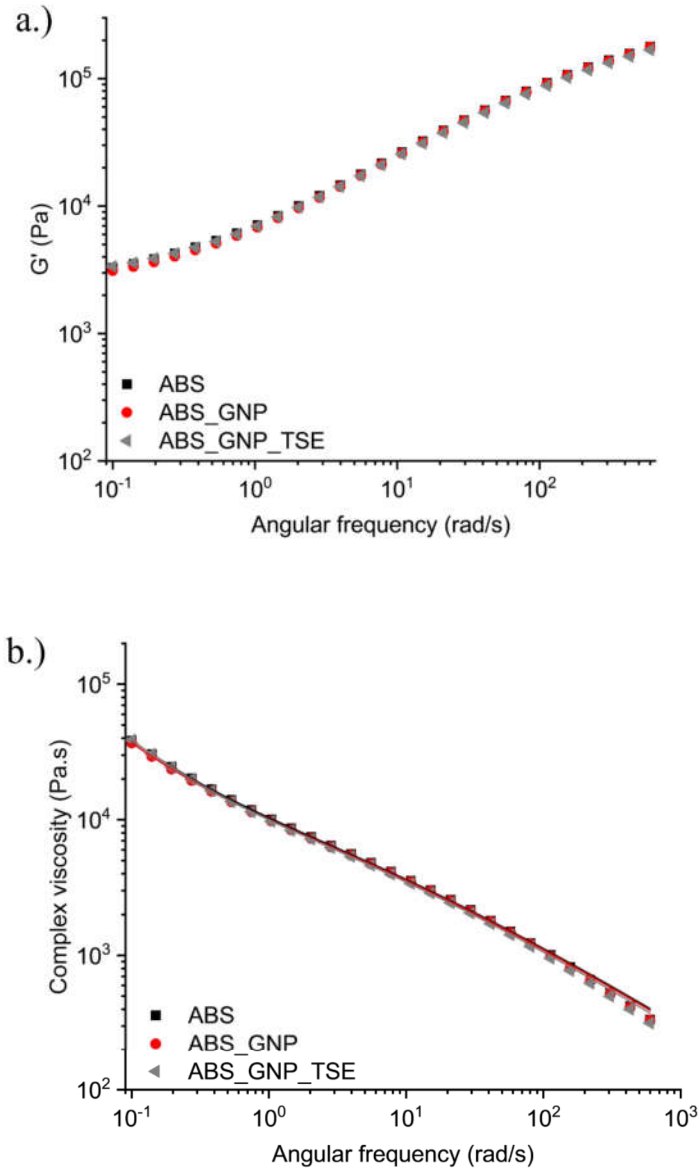

Figure 8: Storage modulus (a.) and complex viscosity (b.) of ABS and ABS/GNP nanocomposites feedstocks prepared via two different routes.

A qualitative assessment of the complex viscosity plots for ABS_GNP and ABS_GNP_TSE (Figure 8b) also indicate no major differences due to the addition of GNP. When fitting the plots to a modified Carreau-Yasuda equation, as described in Chapters 3 and 4 [26,39], important parameters to assess this effect are obtained (Table 2). Dispersing GNP into ABS via ME + SSE yields both melt yield stress and zero-shear rate viscosity lower than the ABS filament, indicating a poor dispersion of the nanoparticle in the matrix. For the ABS_GNP_TSE sample, the viscosity decreases even further, when compared to ABS, indicating that this material underwent thermo-mechanical degradation during twin-screw extrusion. The melt yield stress increases by 7% and this effect may be related to the strongest contribution of PB-g-SAN phase to the overall elastic response of the material, as discussed in Chapter 3.

Table 2: Parameters obtained from fitting the data to the modified Carreau-Yasuda model.

Sample	Manufacturing technique	σ_0	η_0	λ (s)	a (-)	n (-)
ABS	SSE	2516	22452	0.63	0.37	0.35
ABS_GNP_SSE	ME + SSE	2416	20356	0.57	0.39	0.35
ABS_GNP_TSE	TSE	2700	17543	0.51	0.42	0.35

The effects of feedstock processing route and printing temperature on the tensile properties of 3D printed specimen are shown in Figure 9 (results for ABS and ABS_GNP are repeated from Chapter 5 for comparison with ABS_GNP_TSE). Processing the material via TSE induced a pronounced thermo-mechanical degradation of the matrix, which can be seen by a significant decrease on the tensile modulus, around 30%, when compared to the filaments processed via ME + SSE. The

reduction in tensile strength is also noticed, but it is less pronounced (around 7%). These results corroborate the rheological analysis.

The changes in printing temperature did not affect the mechanical properties of ABS_GNP_TSE, indicating that improving the properties by tuning printing parameters may not be possible when degradation takes place. Interesting to notice that ABS_GNP (produced via ME + SSE) yields increased properties with the increase in printing temperature. For instance, the tensile modulus and strength increase by 6% and 5% when printed at 270 °C, respectively, in comparison with 220 °C. Still, the properties of the matrix are not improved for this composition, at any of the temperatures tested.

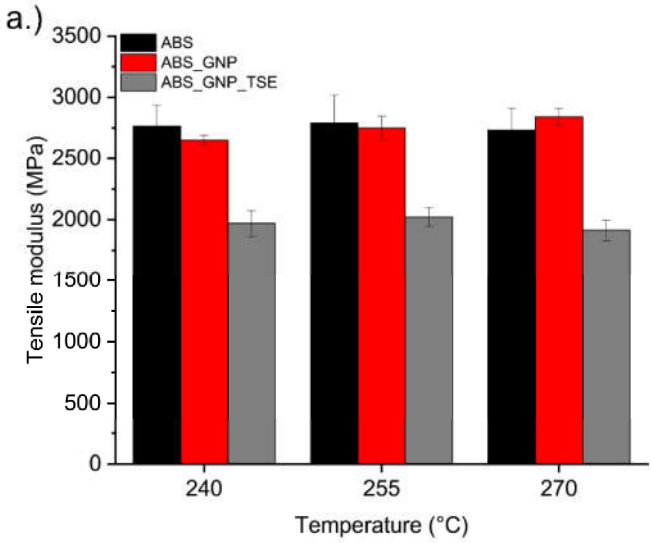

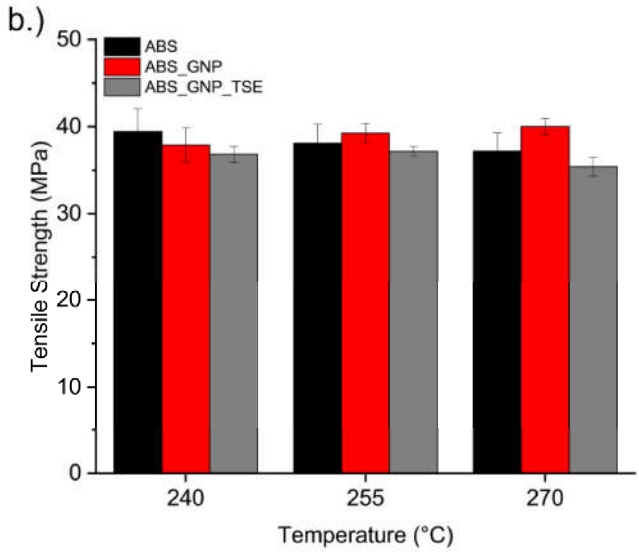

Figure 9: Tensile modulus (a.) and tensile strength (b.) of 3D printed ABS, ABS_GNP and ABS_GNP_TSE.

6.5. Conclusions

In this chapter, the dispersion of nanoparticles in ABS for the filaments obtained in Chapter 5 was further evaluated by means of TEM and van Gurp-Palmen plots. Furthermore, filaments based on ABS and GNP were also obtained via twin-screw extrusion (ABS_GNP_TSE) and 3D printed. The morphological and rheological properties of this filament and the tensile properties of 3D printed parts were compared to ABS and ABS_GNP obtained via micro-extrusion followed by single-screw extrusion (ME + SSE).

The TEM micrographs confirms that the dispersion state of the composition ABS_GNP_CNT_TiO_2 is the best amongst samples, due to the improved synergy

between the nanofillers. The van Gurp-Palmen plots indicate that no network formation occurred for the samples ABS_GNP, ABS_GNP_TSE and ABS_GNP_ TiO_2, due to their restricted level of dispersion. For ABS_GNP_CNT and ABS_GNP_CNT_ TiO_2, the drop in the phase angle indicates that a network between the nanofillers is formed.

The sample produced via twin-screw extruder (ABS_GNP_TSE) seems to have a slightly improved dispersion of the GNP in ABS, when compared to ABS_GNP. However, the twin-screw extrusion process induced thermo-mechanical degradation on this specimen, as seen by the reduction in the zero-shear rate viscosity and the dramatic decrease in the mechanical properties of 3D printed specimen. Furthermore, tuning the properties by adjusting the printing temperature may not be possible for degraded materials.

REFERENCES

1. Berretta, S.; Davies, R.; Shyng, Y.T.; Wang, Y.; Ghita, O. Fused Deposition Modelling of high temperature polymers: Exploring CNT PEEK composites. *Polym. Test.* **2017**, *63*, 251–262, doi:10.1016/j.polymertesting.2017.08.024.
2. Ahmadifar, M.; Benfriha, K.; Shirinbayan, M.; Tcharkhtchi, A. *Additive Manufacturing of Polymer-Based Composites Using Fused Filament Fabrication (FFF): a Review*; Springer Netherlands, 2021; Vol. 28; ISBN 0123456789.
3. Patel, A.; Taufik, M. Nanocomposite materials for fused filament fabrication. *Mater. Today Proc.* **2021**, *47*, 5142–5150, doi:10.1016/j.matpr.2021.05.438.
4. Wu, H.; Fahy, W.P.; Kim, S.; Kim, H.; Zhao, N.; Pilato, L.; Kafi, A.; Bateman, S.; Koo, J.H. Recent developments in polymers/polymer nanocomposites for additive manufacturing. *Prog. Mater. Sci.* **2020**, *111*, doi:10.1016/j.pmatsci.2020.100638.
5. Ajayan, P.M.; Schadler, L.S.; Braun, P. V. *Nanocomposite Science and Technology*; Wiley-VCH Verlag GmbH & Co. KGaA: Weinheim, FRG, 2003; ISBN 3527303596.
6. Dasari, A.; Njuguna, J. *Functional and Physical Properties of Polymer Nanocomposites*; Wiley, 2016; ISBN 9781118542323 A.
7. Seydibeyoğlu, Ö.M.; İşçi, S.; Güngör, N.; Ece, I.O.; Güner, F.S. Preparation of polyurethane/hectorite, polyurethane/montmorillonite and polyurethane/laponite nanocomposites without organic modifiers. *J. Appl. Phys.* **2010**, *116*, 832–837, doi:10.1002/app.
8. Paszkiewicz, S.; Szymczyk, A.; Špitalský, Z.; Mosná, J.; Ros, Z. Influence of expanded graphite (EG) and graphene oxide (GO) on physical properties of PET based nanocomposites. **2014**, *16*, 45–50.
9. Dintcheva, N.T.; Arrigo, R.; Gambarotti, C.; Carroccio, S.; Coiai, S.; Filippone, G. Advanced ultra-high molecular weight polyethylene/antioxidant-functionalized carbon nanotubes nanocomposites with improved thermo-oxidative resistance. *J. Appl. Polym. Sci.* **2015**, *132*, n/a-n/a, doi:10.1002/app.42420.
10. Mishra, A.K.; Mushtaq, S.; Nando, G.B.; Chattopadhyay, S. Effect of Cloisite and modified Laponite clays on the rheological behavior of TPU–clay nanocomposites. *Rheol. Acta* **2010**, *49*, 865–878, doi:10.1007/s00397-010-0458-5.
11. Jo, J.O.; Saha, P.; Kim, N.G.; Chang Ho, C.; Kim, J.K. Development of nanocomposite with epoxidized natural rubber and functionalized multiwalled carbon nanotubes for enhanced thermal conductivity and gas barrier property. *Mater. Des.* **2015**, *83*, 777–785, doi:10.1016/j.matdes.2015.06.045.
12. Bilotti, E.; Duquesne, E.; Deng, H.; Zhang, R.; Quero, F.; Georgiades, S.N.; Fischer, H.R.; Dubois, P.; Peijs, T. In situ polymerised polyamide 6/sepiolite nanocomposites: Effect of different interphases. *Eur. Polym. J.* **2014**, *56*, 131–139, doi:10.1016/j.eurpolymj.2014.04.004.
13. Kutvonen, A.; Rossi, G.; Puisto, S.R.; Rostedt, N.K.J.; Ala-NissilaTapio Influence of nanoparticle size, loading, and shape on mechanical properties of polymer nanocomposites. *J. Chem. Phys.* **2012**, *137*.
14. Papageorgiou, D.G.; Chrissafis, K.; Pavlidou, E.; Deliyanni, E.A.; Papageorgiou, G.Z.; Terzopoulou, Z.; Bikiaris, D.N. Effect of nanofiller's size and shape on the solid state microstructure and thermal properties of

poly(butylene succinate) nanocomposites. *Thermochim. Acta* **2014**, *590*, 181–190, doi:10.1016/j.tca.2014.06.030.
15. Nelson, J.K. *Dielectric polymer nanocomposites*; Nelson, J.K., Ed.; Springer, 2010; ISBN 9781441915900.
16. Hu, K.; Kulkarni, D.D.; Choi, I.; Tsukruk, V. V. Graphene-polymer nanocomposites for structural and functional applications. *Prog. Polym. Sci.* **2014**, *39*, 1934–1972, doi:10.1016/j.progpolymsci.2014.03.001.
17. Faupel, F.; Zaporojtchenko, V.; Strunskus, T.; Elbahri, M. Metal-polymer nanocomposites for functional applications. *Adv. Eng. Mater.* **2010**, *12*, 1177–1190, doi:10.1002/adem.201000231.
18. Zeng, Q.H.; Yu, A.B.; Lu, G.Q.; Paul, D.R. Clay-based polymer nanocomposites: Research and commercial development. *J. Nanosci. Nanotechnol.* **2005**, *5*, 1574–1592, doi:10.1166/jnn.2005.411.
19. Bitinis, N.; Hernandez, M.; Verdejo, R.; Kenny, J.M.; Lopez-Manchado, M.A. Recent advances in clay/polymer nanocomposites. *Adv. Mater.* **2011**, *23*, 5229–5236, doi:10.1002/adma.201101948.
20. Carey, M.; Barsoum, M.W. MXene polymer nanocomposites: a review. *Mater. Today Adv.* **2021**, *9*, 100120, doi:10.1016/j.mtadv.2020.100120.
21. Kumar, A.; Kumar, K.; Ghosh, P.K.; Yadav, K.L. MWCNT/TiO2 hybrid nano filler toward high-performance epoxy composite. *Ultrason. Sonochem.* **2018**, *41*, 37–46, doi:10.1016/j.ultsonch.2017.09.005.
22. Aghadavoudi, F.; Golestanian, H.; Zarasvand, K.A. Elastic behaviour of hybrid cross-linked epoxy-based nanocomposite reinforced with GNP and CNT: experimental and multiscale modelling. *Polym. Bull.* **2019**, *76*, 4275–4294, doi:10.1007/s00289-018-2602-9.
23. Hu, X.; Zhao, H.; Li, T.; He, X.; Wang, X.; Pellerin, C.; Zhang, R. Acrylonitrile–butadiene rubber reinforced by graphene oxide/halloysite nanotubes hybrid nanofillers through mechanical blending method. *Plast. Rubber Compos.* **2020**, *49*, 141–149, doi:10.1080/14658011.2020.1718324.
24. Len, T.A.; Vovchenko, L.L.; Turkov, O. V.; Lozitsky, O. V.; Matzui, L.Y. Electrical and thermal properties of epoxy composites filled with carbon nanotubes and inorganic particles. *Mol. Cryst. Liq. Cryst.* **2021**, *717*, 109–120, doi:10.1080/15421406.2020.1860536.
25. Szeluga, U.; Kumanek, B.; Trzebicka, B. Synergy in hybrid polymer/nanocarbon composites. A review. *Compos. Part A Appl. Sci. Manuf.* **2015**, *73*, 204–231, doi:10.1016/j.compositesa.2015.02.021.
26. Ceretti, D.V.A.; Fiorio, R.; Van Waeleghem, T.; Desmet, A.; Florizoone, B.; Cardon, L.; D'hooge, D.R. Exploiting mono- and hybrid nanocomposite materials for fused filament fabrication with <scp>acrylonitrile butadiene styrene</scp> as polymer matrix. *J. Appl. Polym. Sci.* **2022**, *139*, 1–21, doi:10.1002/app.52922.
27. Krishnamoorti, R. Strategies for Dispersing Nanoparticles in Polymers. *MRS Bull.* **2007**, *32*, 341–347, doi:10.1557/mrs2007.233.
28. Barbas, J.M.; MacHado, A. V.; Covas, J.A. In-line near-infrared spectroscopy: A tool to monitor the preparation of polymer-clay nanocomposites in extruders. *J. Appl. Polym. Sci.* **2013**, *127*, 4899–4909, doi:10.1002/app.38106.
29. Šupová, M.; Martynková, G.S.; Barabaszová, K. Effect of nanofillers dispersion in polymer matrices: A review. *Sci. Adv. Mater.* **2011**, *3*, 1–25, doi:10.1166/sam.2011.1136.
30. Li, X.; Zhang, H.; Jin, J.; Huang, D.; Qi, X.; Zhang, Z.; Yu, D. Quantifying dispersion of nanoparticles in polymer nanocomposites through transmission

electron microscopy micrographs. *J. Micro Nano-Manufacturing* **2014**, *2*, 1–11, doi:10.1115/1.4027339.

31. Khare, H.S.; Burris, D.L. A quantitative method for measuring nanocomposite dispersion. *Polymer (Guildf).* **2010**, *51*, 719–729, doi:10.1016/j.polymer.2009.12.031.
32. Uyor, U.O.; Popoola, A.P.I.; Popoola, O.M.; Aigbodion, V.S. Nanomechanical evaluation of poly (vinylidene fluoride) nanocomposites reinforced with hybrid graphene nanoplatelets and titanium dioxide. *Polym. Bull.* **2022**, *79*, 2345–2361, doi:10.1007/s00289-021-03604-1.
33. Manap, A.; Mahalingam, S.; Vaithylingam, R.; Abdullah, H. Mechanical, thermal and morphological properties of thermoplastic polyurethane composite reinforced by multi-walled carbon nanotube and titanium dioxide hybrid fillers. *Polym. Bull.* **2021**, *78*, 5815–5832, doi:10.1007/s00289-020-03393-z.
34. Shah, R.; Kausar, A.; Muhammad, B.; Shah, S. Progression from Graphene and Graphene Oxide to High Performance Polymer-Based Nanocomposite: A Review. *Polym. - Plast. Technol. Eng.* **2015**, *54*, 173–183, doi:10.1080/03602559.2014.955202.
35. Van Gurp, M.; Palmen, J. Time-Temperature superposition for polymeric blends. *Rheol. Bull.* **1998**, *6*, 5.
36. Jyoti, J.; Dhakate, S.R.; Singh, B.P. Phase transition and anomalous rheological properties of graphene oxide-carbon nanotube acrylonitrile butadiene styrene hybrid composites. *Compos. Part B Eng.* **2018**, *154*, 337–350, doi:10.1016/j.compositesb.2018.08.100.
37. Abdel-Goad, M.; Potschke, P.; Zhou, D.; Mark, J.E.; Heinrich, G. Preparation and rheological characterization of polymer nanocomposites based on expanded graphite. *J. Macromol. Sci. Part A Pure Appl. Chem.* **2007**, *44*, 591–598, doi:10.1080/10601320701284840.
38. Yue, L.; Pircheraghi, G.; Monemian, S.A.; Manas-Zloczower, I. Epoxy composites with carbon nanotubes and graphene nanoplatelets - Dispersion and synergy effects. *Carbon N. Y.* **2014**, *78*, 268–278, doi:10.1016/j.carbon.2014.07.003.
39. Ceretti, D.V.A.; Marien, Y.W.; Edeleva, M.; La Gala, A.; Cardon, L.; D'hooge, D.R. Thermal and Thermal-Oxidative Molecular Degradation of Polystyrene and Acrylonitrile Butadiene Styrene during 3D Printing Starting from Filaments and Pellets. *Sustainability* **2022**, *14*, 15488, doi:10.3390/su142315488.

Chapter 7

Conclusions and outlook

This chapter summarizes the most important findings regarding this doctoral research and gives an outlook on future research.

In this PhD thesis, the rheological behavior of polymer melts, printing parameters, processing techniques, polymer degradation during printing and material formulations were successfully investigated in view of extrusion-based additive manufacturing (EAM) of styrene-based materials. Main insights are related to rheological behavior of polystyrene melts undergoing degradation, degradation processes during EAM, and the design of new material formulations for EAM applications. This was done with support of various characterization techniques to establish structure-processing-properties relationships of the investigated materials.

The literature review, presented in Chapter 2, discussed the degradation during processing, including conventional processing, mechanical recycling and extrusion-based additive manufacturing. The most important degradation pathways for polymers were reviewed, including thermal, thermal-oxidative and thermo-mechanical degradation, and hydrolysis. It was highlighted how the combination of experimental techniques and modeling tools can further underpin specific degradation pathways of polymers and to contribute for the understanding of the behavior of materials undergoing structural breakdown. This aspect was further investigated in Chapter 3 of the thesis. Furthermore, this chapter also indicated that the literature regarding degradation during EAM is currently limited, suggesting that further studies on the topic may be needed, which served as an input for Chapter 4.

A step towards structural rheokinetic modelling of polymer melts undergoing degradation is discussed in Chapter 3. First, an experimental protocol was defined to study the rheological behavior during thermal degradation of polystyrene in the rheometer. Then, a group of parameters for the model validation was estimated based on rheological tests (time sweep, frequency sweep and constant shear rate tests) and size-exclusion chromatography (SEC). In addition, the nonlinear viscoelastic behavior of virgin and aged samples was assessed via constant shear rate tests. Both samples exhibited an overshoot on the transient response of viscosity. Nevertheless, the onset of disentanglement occurred at lower shear rates for the aged sample, due to its reduced average molar mass. In addition, the transient response of viscosity of the aged sample showed an undershoot following the overshoot. This was attributed to the *tumbling* effect, which is for the first time reported for aged polymer melts. This observation may implicate on novel characterization pathways for polymer degradation via rheometry and it is an interesting topic for future research, including other types of polymers and different degradation conditions.

The influence of printing parameters and printing technique on the degradation of ABS and PS has been assessed in Chapter 4. For PS, a reduction on the zero-shear viscosity of 3D printed parts produced via fused filament fabrication (FFF) and pellet-based additive manufacturing (PBAM), also perceived by a decrease in the (average) molar mass indicated that chain fission occurred. This was more pronounced for the FFF process, as this technique also includes a prior filament fabrication via single-screw extrusion (SSE). In addition, the print temperature plays a role on the degradation extent, and printing PS at a higher temperature induce a higher level of degradation. PBAM is an interesting alternative to additively manufacture PS with lower degradation extent, and the same level of mechanical properties when compared to the FFF counterpart. For ABS, manufacturing samples via FFF with prior filament

production (SSE) induces a different degradation mechanism (more fission) than manufacturing samples via PBAM (more cross-linking). This happens because of the reduced mechanical stresses in PBAM, inducing a more thermally driven degradation. In addition, samples produced via both techniques presented yellowing upon processing, indicating a certain level of oxidation, with FFF samples exhibiting the highest values of yellowness index (YI). A follow-up of this study should consider further optimization of PBAM conditions for ABS to improve the inter and intralayer adhesion between deposited filaments. In addition, the procedure assessed here for ABS and PS may be tested for other types of materials in order to obtain more insights on the degradation during EAM.

One possibility to improve the final properties of 3D printed parts is by the design of material formulations. This can be a time-consuming process, with a high amount of samples to be tested. In Chapter 5, a methodology to assess possible formulations of polymer (nano)composites for EAM applications was proposed. Specifically, mono and hybrid ABS-based (nano)composites were assessed, using graphene nanoplatelets (GNPs), carbon nanotubes (CNTs) and titanium dioxide (TiO_2) as nanoparticles. The methodology accounts for linear viscoelastic measurements and printability tests. It was discussed how rheological tests can indicate the level of synergy between nanoparticles, which may be a good indicative for improved properties after 3D printing, due to the synergistic effect. The printability tests indicated that all the compositions were printable and that compositions containing GNP and TiO_2 seemed to have an improved coalescence. Based on these results, promising compositions for FFF were produced into filaments for further microscopical and sintering analysis and 3D printing. Scanning electron microscopy indicated that with exception of the composition containing GNP, CNT and TiO_2, all the others exhibited a certain level of agglomeration. The sintering analysis shows that the compositions with CNT reach

lower levels of coalescence, due to an increased viscosity. For the actual 3D printing, the influence of material composition, printing direction, printing temperature and layer thickness on tensile, flexural and impact properties were assessed. A multidirectional analysis revealed that the best compositions discussed in step one (ABS_GNP_CNT and ABS_GNP_CNT_TiO_2), were the ones that generated the best final properties of 3D printed parts, especially under tensile loads of XYZ printed specimens. This is due to the synergy between nanoparticles, creating a synergistic effect. In case the build orientation is set to ZXY, an abrupt drop of the mechanical properties is perceived, indicating poor bond strength and high anisotropy in these materials. In addition, the mechanical properties increase with the decrease of layer thickness, whereas the printing temperature has a little influence of the properties of 3D printed parts. For the first time a triple composition containing GNPs, CNTs and TiO_2 was used for FFF applications. The full potential of this material is yet to be investigated, and preliminary results already show an increase on its electrical conductivity. The effect of 3D printing parameters on this property must also be assessed, including layer thickness, build orientation and raster angle. In addition, the screening strategy proposed here may be employed for the development of new (nano)composites for EAM applications.

To confirm insights obtained via SEM analysis, the materials studied in Chapter 5 were subjected to TEM analysis and the results were discussed in Chapter 6. It is shown that the composition containing GNPs, CNTs and TiO_2 presents the better dispersion state amongst the materials assessed. Furthermore, in Chapter 6, the mono-composition containing GNPs was also produced via twin-screw extrusion to assess the dispersion effects and filament processing technique on the final properties of 3D printed parts. Even though the dispersion of GNP in the matrix seemed to slightly improve, the mechanical properties of the final part were reduced because of

degradation. This indicates that further optimization of the extrusion parameters should be carried out to benefit from the improved dispersion of GNPs in the matrix.

Overall, the results of this thesis indicate several perspectives for future studies, and for the application of concepts developed here. Concerning the structural rheokinetic model, after its validation, it may be employed to study the polymer degradation during actual processing. Additionally, it may be used to study the rheological behavior of materials undergoing reactive extrusion. Both applications could have a big impact on the polymer industry.

The possibilities to strategically study polymer degradation via constant-shear rate tests has been put forward. However, a broader range of materials, with different molecular properties, that underwent different degradation processes must be tested. By doing so, more straightforward relationships between molecular properties, the extent and type of degradation on the tumbling effect could be obtained. In addition, from a modelling perspective, improved models accounting for the undershoot must be developed.

The potential of PBAM technique in producing materials with improved properties and lower levels of degradation may be further investigated. The technique may be assessed for a broader range of materials and optimization in terms of processing parameters and machine design must be carried out. The use of this technique could potentially be used to design parts with complex shapes, without the needs of molds and reduced extent of degradation.

To create lightweight, high-strength parts for structural applications in aerospace and automotive industry, the methodology performed to design formulations for FFF is very promising. Other formulations may be assessed at different concentration ratios

to obtain improved final parts of 3D printed materials. In addition, because of the use of the nanoparticles chosen, possibilities of increased thermal and electrical properties may also enable the use of these materials for advanced applications, such as electromagnetic interference shielding for electronic materials, energy storage devices and radiation shielding. To fully exploit such applications, a complete analysis on the influence of printing parameters and composition on electrical and thermal properties of the materials must be carried out.

Appendix A - Supporting Information for Chapter 3

A.1 Structural rheokinetic model details

To describe the evolution of time-dependent rheological behavior of polymer melts undergoing degradation, a modified version of the model proposed by Marchesini et al. [28] was carried out by Professor. Dr. Flávio H. Marchesini and is briefly described in this section.

The constitutive equation of the model (Equation A1) relates the shear rate ($\dot{\gamma}$) and shear stress (σ), and it is based on a modified Jeffreys model:

$$\dot{\gamma} + \theta_2 \ddot{\gamma} = \frac{\theta_2}{\eta_\infty}\left(\frac{\sigma}{\theta_1} + \dot{\sigma}\right), \tag{A1}$$

in which η_∞ is the infinite shear viscosity, θ_1 and θ_2 are the relaxation and retardation times, described by equations A2 and A3, respectively.

$$\theta_1(\lambda_s) = \left(1 - \frac{\eta_\infty}{\eta_\upsilon(\lambda_s)}\right)\frac{\eta_\upsilon(\lambda_s)}{G_s(\lambda_s)}, \tag{A2}$$

$$\theta_2(\lambda_s) = \left(1 - \frac{\eta_\infty}{\eta_\upsilon(\lambda_s)}\right)\frac{\eta_\infty}{G_s(\lambda_s)}, \tag{A3}$$

in which λ_s is the structural parameter, η_υ is the purely viscous part of viscosity and G_s is the shear modulus. Equations A4 and A5 describe G_s and η_υ, respectively.

$$G_s(\lambda_s) = G_0\left(\frac{1}{\lambda_s}\right)^\kappa, \tag{A4}$$

$$\eta_\upsilon(\lambda_s) = \eta_\infty\left(\frac{\eta_0}{\eta_\infty}\right)^{\lambda_s}, \tag{A5}$$

in which G_0 is the shear modulus of the virgin material, η_0 is the zero-shear rate viscosity and κ is a fitting parameter of the model.

Equations A6 and A7 describe the variation of G_0 and η_0 with the mass average molar mass (M_m) of the polymer, and k_1, k_2, α_1, α_2 are fitting parameters.

$$G_0(M_m) = k_1 M_m^{\alpha_1}, \tag{A6}$$

$$\eta_0(M_m) = k_2 M_m^{\alpha_2}, \tag{A7}$$

Equation A8 describes the evolution of the irreversible process (degradation) in which k_{app} is the apparent rate constant and t is time.

$$\zeta(t) = 1 - exp[-k_{app}t], \tag{A8}$$

The variation of the average molar mass with the irreversible process is described in Equation A9, in which $M_{m,initial}$ is the initial mass average molar mass and $M_{m,final}$ is the final one.

$$M_m(\zeta) = M_{m,initial} - [M_{m,initial} - M_{m,final}]\zeta, \tag{A9}$$

The evolution of the structure of polystyrene melts based on the structural parameter (λ_s) is obtained by Equation A10.

$$\frac{d\lambda_s}{dt} = \frac{1}{t_{eq}}\left[(1-\lambda_s) - (1-\lambda_{s,eq})\left(\frac{\lambda_s}{\lambda_{s,eq}}\right)\right] - \left(\frac{\lambda_{s,final}}{\lambda_{s,eq}}\right)\dot{\zeta}(t), \tag{A10}$$

in which, t_{eq} is a characteristic time for equilibrium, $\lambda_{s,final}$ represents the breakdown level of the structure at the final state, $\lambda_{s,eq}$ is the structural parameter at t_{eq}. Equations A11 and A12 describe $\lambda_{s,final}$ and $\lambda_{s,eq}$, with ξ being a model parameter

$$\lambda_{s,final} = \left(\frac{M_{m,final}}{M_{m,initial}}\right)^{\xi} \lambda_{s,eq}, \tag{A11}$$

$$\lambda_{s,eq}(\dot{\gamma}) = \frac{\ln \eta(\dot{\gamma}) - \ln \eta_{\infty}}{\ln \eta_0 - \ln \eta_{\infty}}, \tag{A12}$$

The Carreau-Yasuda equation (Equation A13) is used to fit the flow curves and describes the steady state behavior of virgin and aged polystyrene.

$$\eta(\dot{\gamma}) = [\eta_0 - \eta_{\infty}]\left[1 + \left(\frac{\dot{\gamma}}{\dot{\gamma}_0}\right)^{a}\right]^{\frac{n-1}{a}} + \eta_{\infty}, \tag{A13}$$

in which $\dot{\gamma}_0$ is the characteristic shear rate that marks the transition from the zero-shear viscosity to the power-law region, a is the Yasuda parameter and n is the power law index.

The variations on the Yasuda parameter (a) and on the characteristic shear rate ($\dot{\gamma}_0$) with the mass average molar mass are described by equations A14 and A15, respectively, with k_3, k_4, α_3, α_4 being model parameters.

$$a(M_m) = k_3 M_m^{\alpha_3}, \tag{A14}$$

$$\dot{\gamma}_0(M_m) = \frac{1}{k_4 M_m^{\alpha_4}}, \tag{A15}$$

A.2 Osawa/Flynn/Wall method for the calculation of apparent activation energy of PS - 240

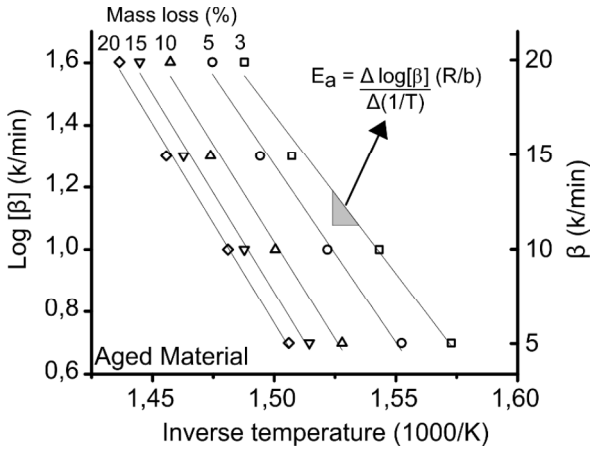

Figure A1: Isoconversional approach for calculating apparent activation energies of PS-240 (raw data for Figure 2d)

Appendix B - Supporting Information for Chapter 4

B.1. Mass variation obtained in isothermal TGA tests for ABS and PS

Table B1: Mass variation obtained in isothermal TGA tests.

Material	Temperature (ºC)	Mass variation (%): mass percentage at time t (m_t) – initial mass percentage (m_i)						
		300 s	600 s	900 s	1200 s	1500 s	1800 s	2000 s
ABS	220	-0.37	-0.55	-0.69	-0.69	-0.74	-0.79	-0.82
	270	-0.58	-0.94	-1.12	-1.23	-1.32	-1.38	-1.43
PS	240	-0.03	-0.11	-0.16	-0.18	-0.2	-0.25	-0.27
	270	-0.1	-0.31	-0.44	-0.54	-0.64	-0.74	-0.8

B.2. ANOVA results

Table B2: p-values obtained from ANOVA.

Variation source	*p*-values		
	ABS		PS
	Melt yield stress	Zero-shear viscosity	Zero-shear viscosity
Temperature	0,6	0,1	0,0
Layer thickness	0,6	0,1	0,3
Printing velocity	0,3	0,0	0,2
Temperature, Layer thickness	0,9	0,7	0,8
Temperature, Printing velocity	0,7	0,7	0,7
Layer thickness, Printing velocity	0,6	0,9	0,4
Temperature, Layer thickness, printing velocity	0,6	0,1	0,6

B.3. FTIR spectra

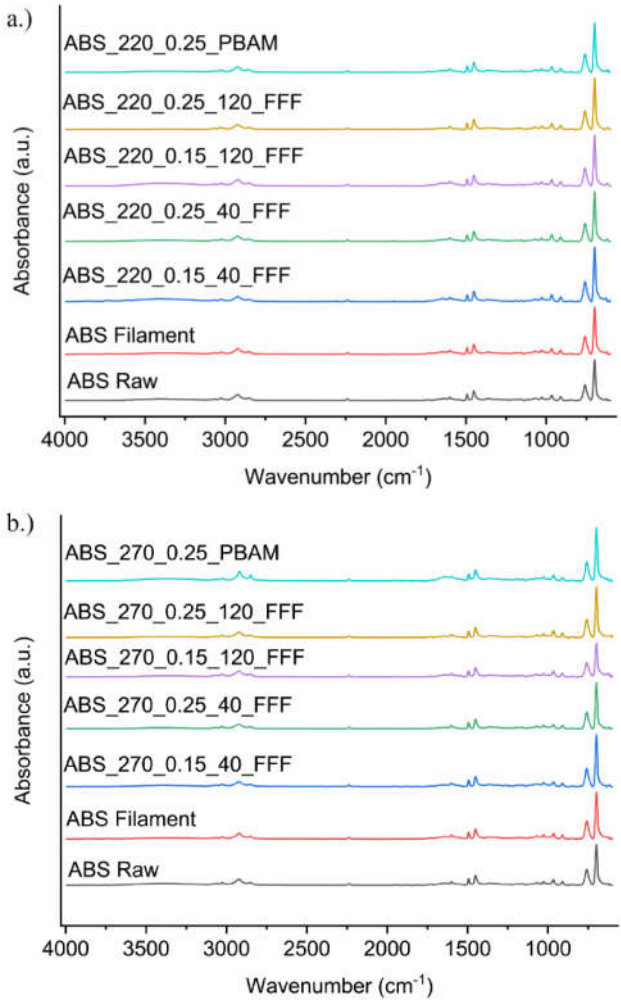

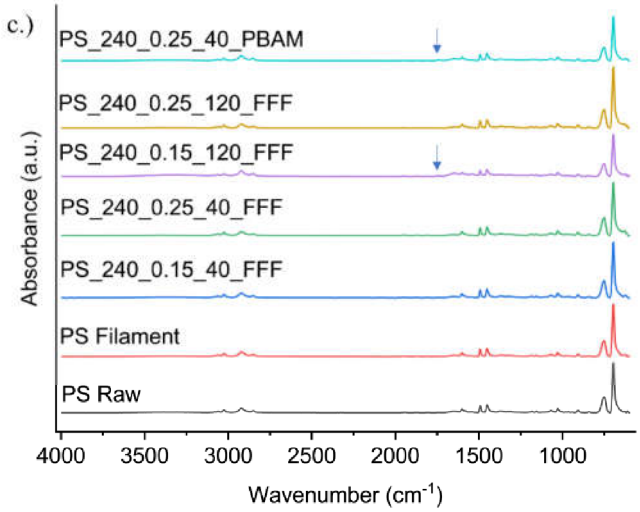

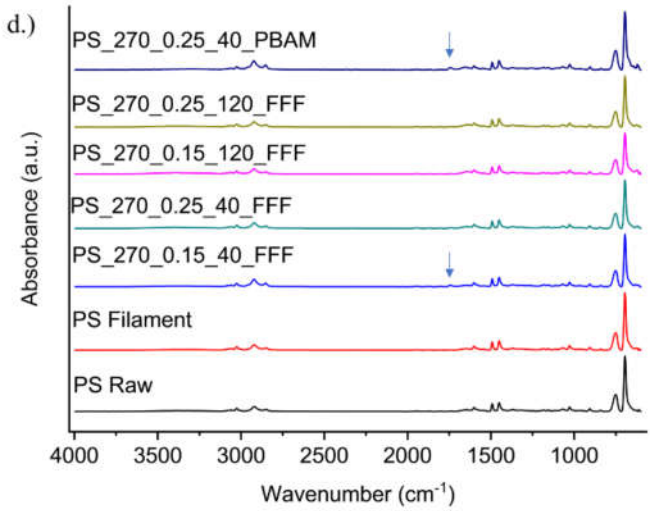

Figure B1: FTIR spectra of ABS samples printed at a.) 220 °C and b.) 270 °C and FTIR spectra of PS samples printed at c.) 240 °C and d.) 270 °C. Arrows were added in the most prominent peaks that appeared as a result of degradation of PS. The spectra for raw material and filament are repeated in each graph for comparison.

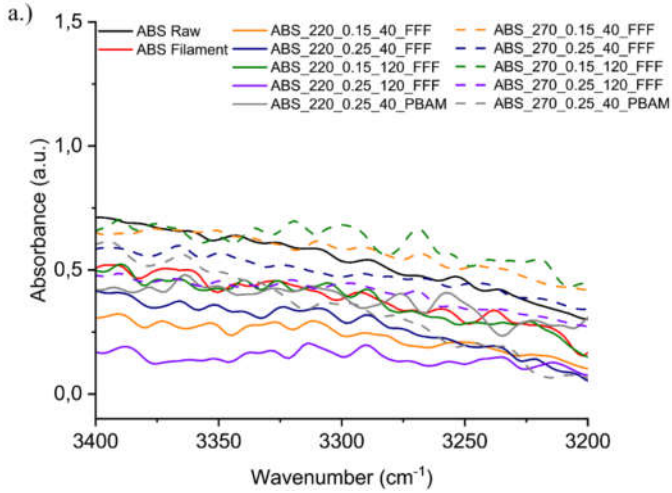

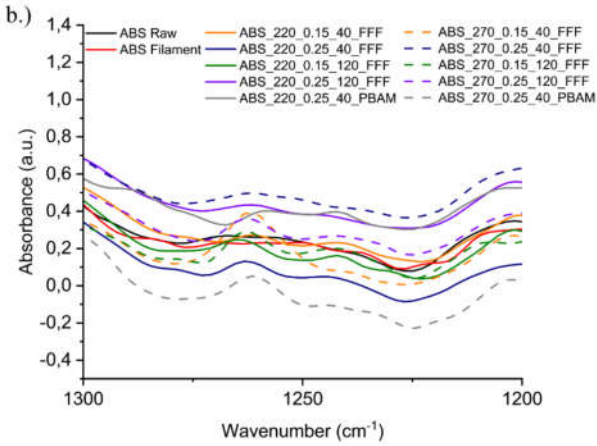

Figure B2: Regions of interest for FTIR degradation analysis of ABS: a.) hydroxyl and b.) C-O stretches region.

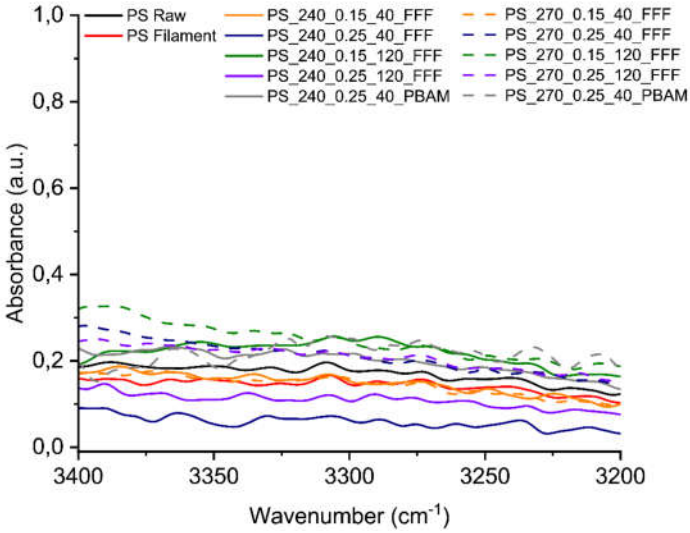

Figure B3: Hydroxyl region of FTIR spectra of PS samples.

B.4. Color variation of PS specimens

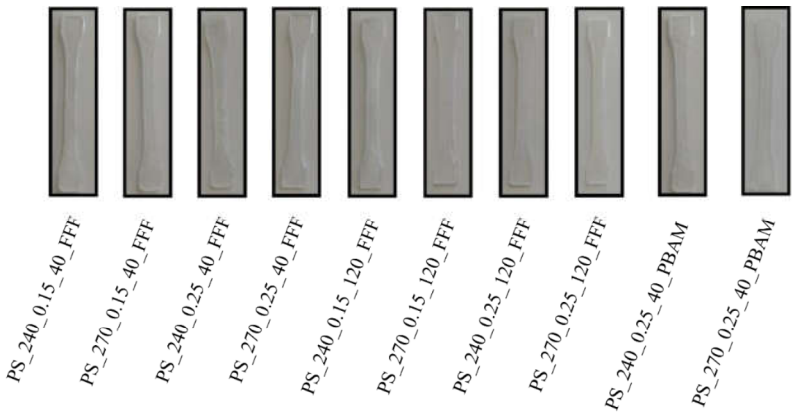

Figure B4: Variation in the color of PS specimens produced via FFF and PBAM.

B.5. Tensile properties of ABS and PS samples

Table B3: Tensile tests results for ABS and PS samples printed via FFF and PBAM.

Processing technique	Sample	Tensile modulus (MPa)	Tensile strength (MPa)	Strain at break (%)
FFF	**ABS_220_0.15_40_FFF**	2351 ± 155	42.2 ± 1.4	6.9 ± 1.4
	ABS_270_0.15_40_FFF	2389 ± 106	40.6 ± 0.7	7.1 ± 3.4
	ABS_220_0.25_40_FFF	2323 ± 97	38.5 ± 0.5	7.0 ± 1.9
	ABS_270_0.25_40_FFF	2347 ± 205	37.9 ± 0.8	6.8 ± 1.7
	ABS_220_0.15_120_FFF	2413 ± 100	41.5 ± 1.0	5.8 ± 1.0
	ABS_270_0.15_120_FFF	2379 ± 65	40.8 ± 1.2	5.9 ± 1.6
	ABS_220_0.25_120_FFF	2299 ± 131	38.6 ± 1.2	6.4 ± 1.2
	ABS_270_0.25_120_FFF	2284 ± 107	38.2 ± 0.4	5.0 ± 1.7
PBAM	**ABS_220_0.25_40_PBAM**	2268 ± 206	33.3 ± 1.6	3.5 ± 0.5
	ABS_270_0.25_40_PBAM	2166 ± 80	31.5 ± 1.7	3.6 ± 0.4
FFF	**PS_240_0.15_40_FFF**	2952 ± 142	42.0 ± 3.1	2.7 ± 0.5
	PS_270_0.15_40_FFF	2829 ± 137	39.3 ± 2.1	2.2 ± 0.4
	PS_240_0.25_40_FFF	2616 ± 300	34.6 ± 4.7	1.9 ± 0.4
	PS_270_0.25_40_FFF	2796 ± 212	37.5 ± 2.7	2.8 ± 0.3
	PS_240_0.15_120_FFF	2674 ± 289	41.4 ± 2.8	2.6 ± 0.3
	PS_270_0.15_120_FFF	2993 ± 154	39.6 ± 1.4	2.2 ± 0.4
	PS_240_0.25_120_FFF	2574 ± 333	37.5 ± 2.9	2.4 ± 0.2
	PS_270_0.25_120_FFF	3063 ± 199	40.6 ± 2.6	2.3 ± 0.4
PBAM	**PS_240_0.25_40_PBAM**	2621 ± 261	32.1 ± 4.0	1.9 ± 0.3
	PS_270_0.25_40_PBAM	2726 ± 412	27.7 ± 5.0	1.5 ± 0.3

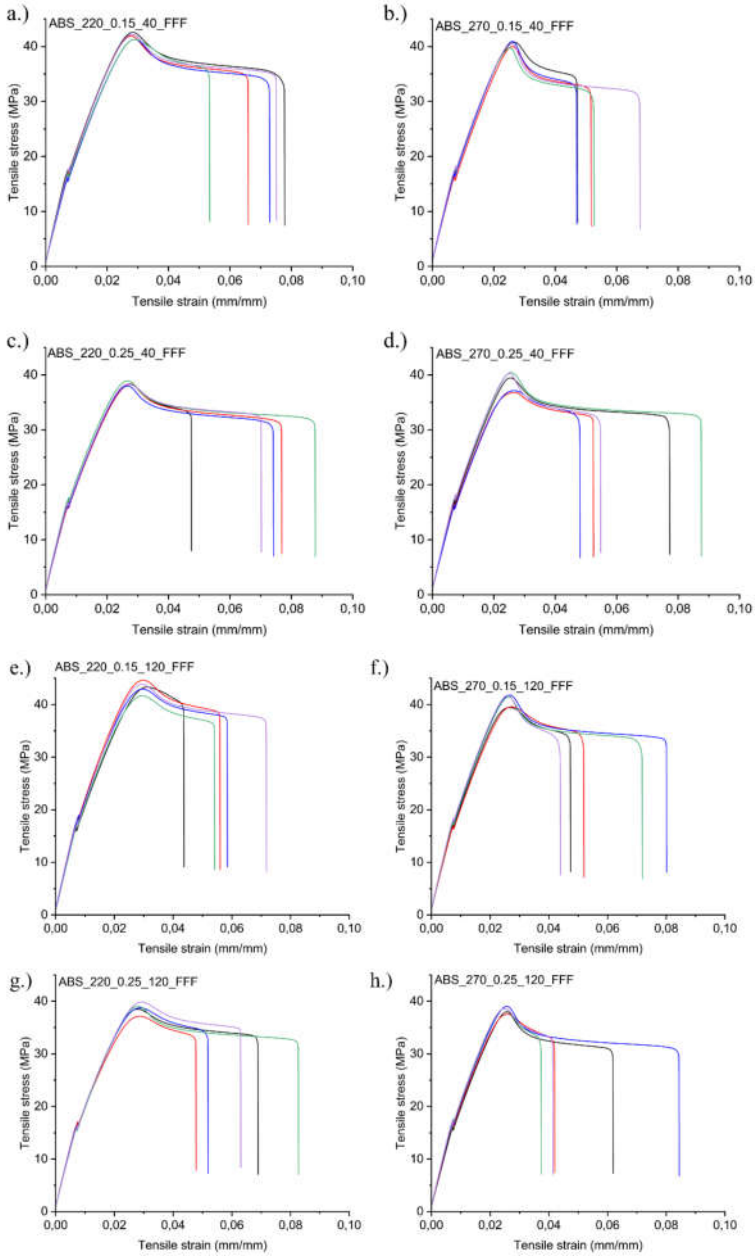
a.)
ABS_220_0.15_40_FFF
b.)
ABS_270_0.15_40_FFF
c.)
ABS_220_0.25_40_FFF
d.)
ABS_270_0.25_40_FFF
e.)
ABS_220_0.15_120_FFF
f.)
ABS_270_0.15_120_FFF
g.)
ABS_220_0.25_120_FFF
h.)
ABS_270_0.25_120_FFF
Tensile stress (MPa)
Tensile strain (mm/mm)
0
10
20
30
40
0,00
0,02
0,04
0,06
0,08
0,10

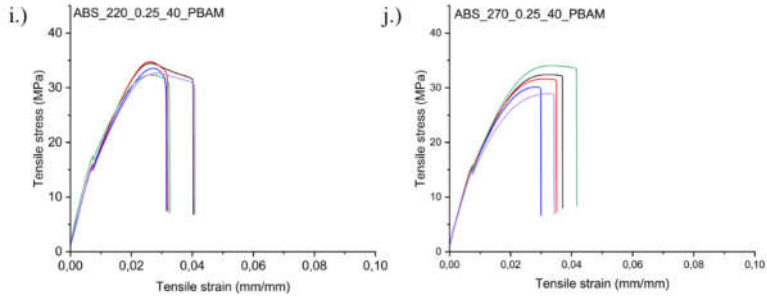

Figure B5: Stress-strain curves of ABS samples: a.) ABS_220_0.15_40_FFF, b.) ABS_270_0.15_40_FFF, c.) ABS_220_0.25_40_FFF, d.) ABS_270_0.25_40_FFF, e.) ABS_220_0.15_120_FFF, f.) ABS_270_0.15_120_FFF, g.) ABS_220_0.25_120_FFF, h.) ABS_270_0.25_120_FFF, i.) ABS_220_0.25_40_PBAM and j.) ABS_270_0.25_40_PBAM. Each color represents the curves of one out of five different specimens.

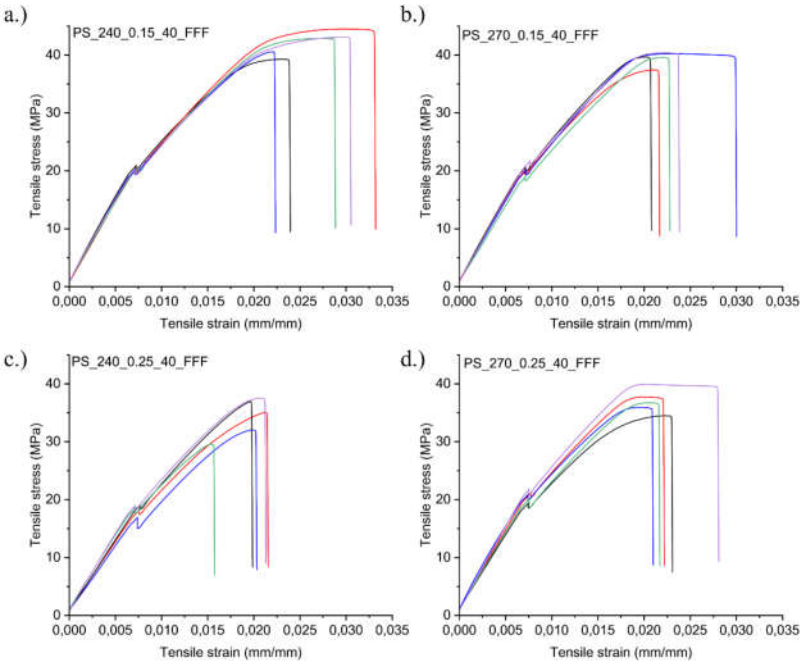

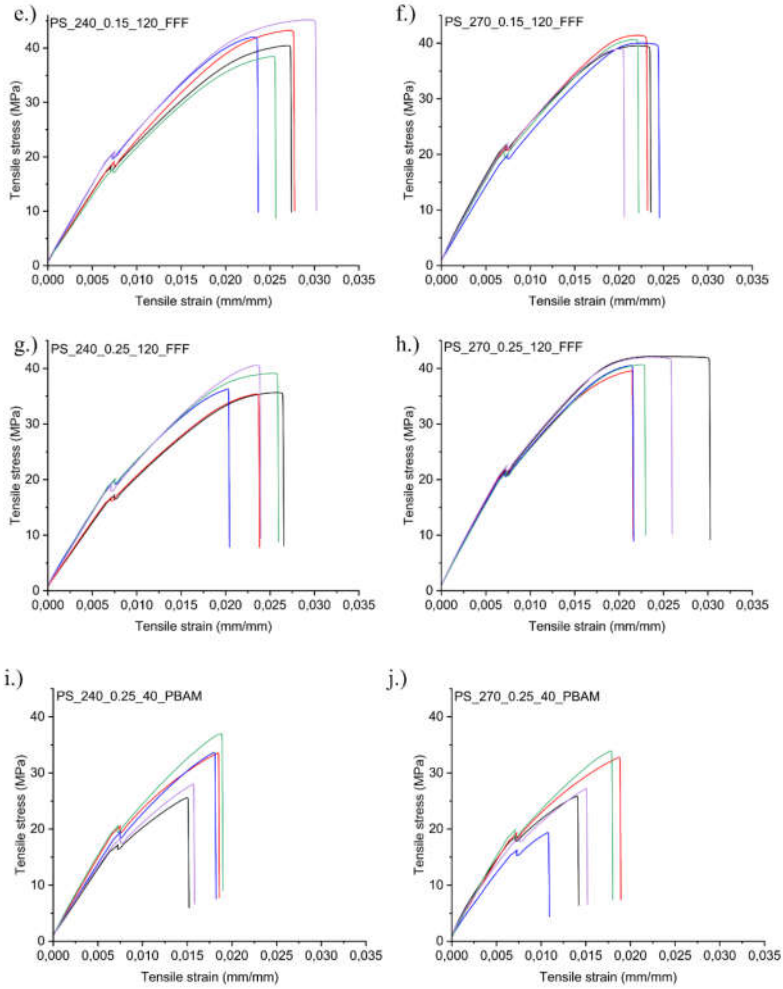

Figure B6: Stress-strain curves of PS samples: a.) PS_240_0.15_40_FFF, b.) PS_270_0.15_40_FFF, c.) PS_240_0.25_40_FFF, d.) PS_270_0.25_40_FFF, e.) PS_240_0.15_120_FFF, f.) PS_270_0.15_120_FFF, g.) PS_240_0.25_120_FFF, h.)PS_270_0.25_120_FFF, i.) PS_240_0.25_40_PBAM and J.) PS_270_0.25_40_PBAM. Each color represents the curves of one out of five different specimens.

Appendix C - Supporting Information for Chapter 5

C.1. Evaluation of Time-Temperature Superposition (TTS)

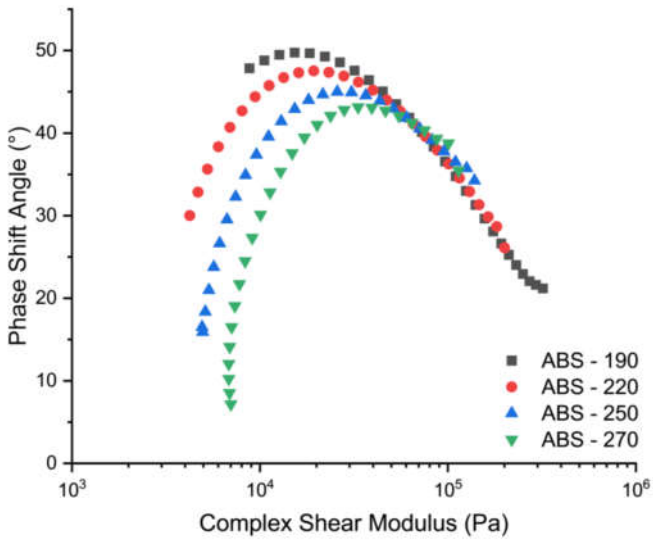

Figure C1: Van Gurp-Palmen plots indicating the TTS is invalid for the ABS used in this study in the range of temperatures evaluated (190 to 270 °C).

C.2. Modeling of sintering

The isothermal neck growth between two cylinders has been modeled by counting for the balance of work of surface tension and the viscous dissipation involved during the coalescence process [1,2]. In these models [1,2], a dimensionless neck radius, x/a_0 = 1.414 is predicted for full coalescence, which is obtained from mass conservation. As shown in Figure 10b in the main text, considering the isothermal case, the maximum neck growth is ~0,6, for pure ABS at 270 °C, way lower than the model predictions. For the dynamic case, the non-isothermal model proposed by Polychronopoulos *et al.*

[2] indicates that coalescence during heating reaches full coalescence values in very short times, which also does not predict well the coalescence behavior of the materials used in this study. This indicates that further studies should be carried out in models to predict sintering of cylinders.

The sintering results obtained via the dynamic mode may be used to obtain the overall activation energy of sintering for the materials studied. The Coats and Redfern method [3] is very versatile and easy to employ. It has been e.g. used to calculate kinetic parameters of the degradation process of poly(butylene succinate) [4]. By carrying dynamic experiments at a specific heating rate, one can identify the overall reaction mechanism and kinetic parameters by comparing the fitting of the model predicting each mechanism (see Table C1) with the data [5]. Their method is based on the following equation:

$$log\left[\frac{g(\alpha)}{T^2}\right] = log\left(\frac{AR}{\beta \mathrm{Ea}}\right) - \frac{\mathrm{Ea}}{2.3R},$$

with

$$g(\alpha) = \int_0^{\alpha} \frac{d\alpha}{f(\alpha)},$$

and A is the pre-exponential, E is the (apparent/overall) activation energy, T is the temperature, R is the universal gas constant, $f(\alpha)$ is the reaction model (Table C1), α is the extent of conversion and β is the heating rate. Here we used the full coalescence dimensionless neck growth of 1.414 to normalize the data and to obtain the α, as α = dimensionless neck growth/full dimensionless neck growth.

Table C1: Classification of mathematical expressions of (overall) reaction mechanisms.

Kinetic classification		**$g(\alpha) = \int d\alpha/f(\alpha) = kt$**	**$f(\alpha) = (d\alpha/dt)/k$**
		Based on nucleus growing	
N1		$[-\ln(1-\alpha)]^{1/4}$	$4(1-\alpha)[-\ln(1-\alpha)]^{3/4}$
N2		$[-\ln(1-\alpha)]^{1/3}$	$3(1-\alpha)[-\ln(1-\alpha)]^{2/3}$
		Based on geometrical models	
R1	Plane symmetry	α	1
R2	Cylindrical symmetry	$1-(1-\alpha)^{1/2}$	$2(1-\alpha)^{1/2}$
R3	Spherical symmetry	$1-(1-\alpha)^{1/3}$	$2(1-\alpha)^{1/3}$
		Based on diffusion mechanisms	
D1	Plane symmetry	α^2	$(1/2\alpha)$
D2	Cylindrical symmetry	$(1-\alpha)\ln(1-\alpha)+\alpha$	$[-\ln(1-\alpha)]^{-1}$
D3	Three dimensional	$[1-(1-\alpha)^{1/3}]^2$	$(3/2)(1-\alpha)^{2/3}[1-(1-\alpha)^{1/3}]^{-1}$
D4	Spherical symmetry	$(1-2\alpha/3)-(1-\alpha)^{2/3}$	$(3/2)[(1-\alpha)^{-1/3}-1]^{-1}$
		Based on reaction "order"	
F1	First order	$[-\ln(1-\alpha)]$	$(1-\alpha)$
F2	Second order	$[-1+(1-\alpha)^{-1}]$	$(1-\alpha)^2$
F3	Third order	$[-1+(1-\alpha)^{-2}]/2$	$(1-\alpha)^3$

The calculated activation energies based on the proposed method are shown in Table C2. A threshold coefficient of determination R^2 higher than 0.80 was used to define which models fits our process best. All the compositions showed a good fit for the mechanisms D3, D4, F2, F3, which regards to diffusion or reaction order mechanisms. All the other models tested showed unsuitable to fit the data for the coalescence.

Table C2: Calculated overall activation energy for sintering process via Coats and Redfern method.

Kinetic Classification	**ABS**		**ABS_GNP**		**ABS_GNP_TiO_2**	
	E_a (kJ/mol)	R^2	E_a (kJ/mol)	R^2	E_a (kJ/mol)	R^2
N1	-1.9	0.42	-2.2	0.54	-1.0	0.22
N2	0.1	0.00	-0.4	0.02	1.3	0.24
R1	9.2	0.63	7.3	0.54	11.2	0.74
R2	12.3	0.73	10.6	0.69	**15.0**	**0.84**
R3	13.4	0.75	11.8	0.72	**16.4**	**0.86**
D1	26.3	0.79	22.4	0.74	**30.2**	**0.84**
D2	**30.0**	**0.81**	26.4	0.79	**34.9**	**0.88**
D3	**34.5**	**0.85**	**31.3**	**0.83**	**40.7**	**0.91**
D4	**31.5**	**0.82**	**28.0**	**0.80**	**36.8**	**0.89**
F1	**15.7**	**0.80**	14.4	0.78	**19.5**	**0.90**
F2	**24.0**	**0.88**	**23.8**	**0.89**	**30.7**	**0.96**
F3	**33.9**	**0.92**	**35.3**	**0.94**	**44.3**	**0.98**

Continuation of Table C2: Calculated overall activation energy for sintering process via Coats and Redfern method.

Kinetic Classification	ABS_GNP_CNT		ABS_GNP_CNT_TiO_2	
	E_a (kJ/mol)	R^2	E_a (kJ/mol)	R^2
N1	-1.6	0.36	-1.4	0.35
N2	0.4	0.02	0.8	0.10
R1	10.8	0.70	12.3	0.78
R2	13.5	0.76	**15.1**	**0.83**
R3	14.4	0.78	**16.1**	**0.85**
D1	**29.3**	**0.81**	**32.5**	**0.86**
D2	**32.6**	**0.83**	**36.0**	**0.88**
D3	**36.4**	**0.85**	**40.0**	**0.90**
D4	**33.9**	**0.84**	**37.3**	**0.89**
F1	**16.4**	**0.81**	**18.2**	**0.88**
F2	**23.2**	**0.87**	**25.3**	**0.93**
F3	**31.2**	**0.91**	**33.6**	**0.96**

C.3. Extra information on the intralayer

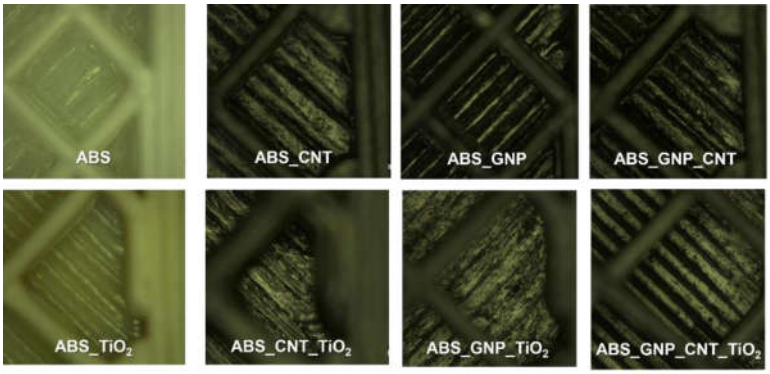

Figure C2: Intralayer adhesion in the inner part of the specimen used for the printability tests.

C.4. Neck radius evolution

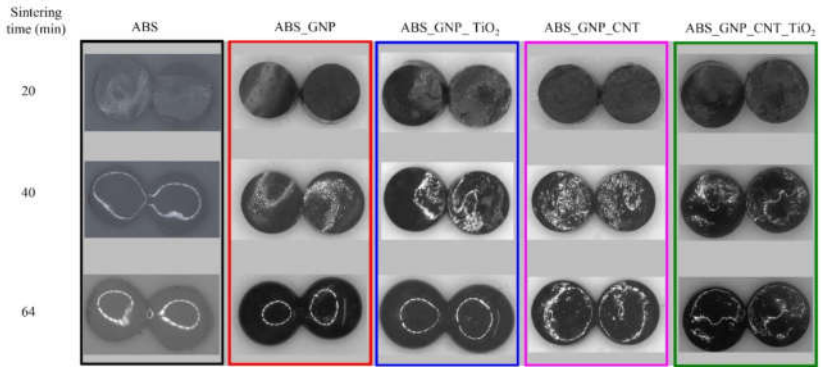

Figure C3: Radius evolution in the dynamic mode for the compositions.

C.5. Effect of printing temperature on the mechanical properties of ABS

Table C3: Influence of temperature on the mechanical properties of ABS and ABS based nanocomposites.

Composition	Temperature (°C)	Tensile properties		
		Modulus (MPa)	Strength (MPa)	Strain at break (%)
ABS	220	2544 ± 150	37.8 ± 1.5	5 ± 2
	240	2765 ± 170	39.5 ± 2.6	4.9 ± 1.1
	255	2789 ± 228	38.1 ± 2.2	5.5 ± 1
	270	2732 ± 179	37.2 ± 2.1	6.0 ± 0.9
ABS_GNP	220	2530 ± 211	39.3 ± 2.3	5.4 ± 1
	240	2650 ± 116	37.9 ± 2	5 ± 0.8
	255	2749 ± 96	39.3 ± 1.1	5.1 ± 1.4
	270	2842 ± 69	40 ± 0.9	5.2 ± 1.9
ABS_GNP_TiO_2	220	2507 ± 160	38.2 ± 0.9	6.5 ± 0.4
	240	2692 ± 94	36.3 ± 1.7	5.4 ± 1.3
	255	2598 ± 128	35.2 ± 0.8	5.8 ± 1.3
	270	2576 ± 54	35.8 ± 1	4.9 ± 1.3
ABS_GNP_CNT	220	2614 ± 274	43.5 ± 1.3	4.8 ± 1.1
	240	2679 ± 231	41.8 ± 0.7	4.5 ± 0.8
	255	2309 ± 163	30.9 ± 3.7	4.2 ± 0.7
	270	2680 ± 295	40.6 ± 1	4.7 ± 0.9
ABS_GNP_CNT_TiO_2	220	2958 ± 141	45.3 ± 1.4	4.2 ± 0.6
	240	2950 ± 159	45.1 ± 1.4	4.1 ± 0.3
	255	2754 ± 102	41.1 ± 1.3	3.6 ± 0.4
	270	2880 ± 269	43.9 ± 1.8	4.1 ± 0.5

Continuation of Table C3: Influence of temperature on the mechanical properties of ABS and ABS based nanocomposites.

Composition	Temperature (°C)	Flexural properties		Impact Strength (kJ/m^2)
		Modulus (MPa)	Strength (MPa)	
ABS	220	1472 ± 36	55.3 ± 1	15.4 ± 1.9
	240	1483 ± 40	54.8 ± 1	16.3 ± 2.5
	255	1351 ± 28	50.3 ± 0.7	15.1 ± 1.7
	270	1561 ± 41	55.4 ± 1	13.7 ± 2.5
ABS_GNP	220	1415 ± 32	56.2 ± 1.7	10.7 ± 0.8
	240	1412 ± 27	54.4 ± 0.9	9.6 ± 0.8
	255	1372 ± 35	51.3 ± 1.1	11.1 ± 1.3
	270	1428 ± 37	53.7 ± 0.7	9.1 ± 0.7
ABS_GNP_TiO_2	220	1245 ± 50	48.8 ± 1.6	7.6 ± 0.5
	240	1295 ± 25	49.8 ± 1.7	6.8 ± 0.5
	255	1267 ± 37	49.8 ± 1.5	7.6 ± 0.5
	270	1316 ± 19	50.3 ± 0.4	7.1 ± 0.4
ABS_GNP_CNT	220	1491 ± 15	55.2 ± 0.6	7.4 ± 0.4
	240	1453 ± 63	53.6 ± 2.5	7.8 ± 0.6
	255	1455 ± 66	53.9 ± 3.2	7.9 ± 0.5
	270	1382 ± 75	49.6 ± 2.8	7 ± 0.6
ABS_GNP_CNT_TiO_2	220	1334 ± 46	49.1 ± 1.9	8 ± 0.9
	240	1449 ± 52	54 ± 1.3	7.2 ± 0.5
	255	1478 ± 46	53.1 ± 1	6.6 ± 0.5
	270	1382 ± 38	51.7 ± 1.3	6.4 ± 0.4

REFERENCES

1. Hopper, R.W. Coalescence of Two Equal Cylinders: Exact Results for Creeping Viscous Plane Flow Driven by Capillarity. *J. Am. Ceram. Soc.* **1984**, *67*, C-262-C-264, doi:10.1111/j.1151-2916.1984.tb19692.x.
2. Polychronopoulos, N.D.; Vlachopoulos, J. The role of heating and cooling in viscous sintering of pairs of spheres and pairs of cylinders. *Rapid Prototyp. J.* **2020**, *26*, 719–726, doi:10.1108/RPJ-06-2019-0162.
3. Coats, A.W.; Redfern, J.P. Kinetic Parameters from Thermogravimetric Data. *Nature* **1964**, *201*, 68–69, doi:10.1038/201068a0.
4. Shih, Y.F.; Chieh, Y.C. Thermal degradation behavior and kinetic analysis of biodegradable polymers using various comparative models, 1 Poly(butylene succinate). *Macromol. Theory Simulations* **2007**, *16*, 101–110, doi:10.1002/mats.200600059.
5. Moens, E.K.C.; De Smit, K.; Marien, Y.W.; Trigilio, A.D.; Van Steenberge, P.H.M.; Van Geem, K.M.; Dubois, J.L.; D'hooge, D.R. Progress in reaction mechanisms and reactor technologies for thermochemical recycling of poly(methyl methacrylate). *Polymers (Basel).* **2020**, *12*, doi:10.3390/POLYM12081667.

3D printed part based on polymer composites.